1237

UNIVERSITÉ DE NEUCHÂTEL
INSTITUT DE MICROTECHNIQUE
SUISSE

DETERMINATION OF THE DEEP DEFECT DENSITY IN AMORPHOUS HYDROGENATED SILICON BY THE CONSTANT PHOTOCURRENT METHOD: A CRITICAL VERIFICATION

THÈSE

Présentée à la Faculté des Sciences

pour obtenir le grade de docteur ès sciences

par

ANDREAS METTLER

DETERMINATION OF THE DEEP DEFECT DENSITY IN AMORPHOUS HYDROGENATED SILICON BY THE CONSTANT PHOTOCURRENT METHOD:

A CRITICAL VERIFICATION

A dissertation
submitted to the
FACULTY OF SCIENCES
UNIVERSITY OF NEUCHÂTEL
SWITZERLAND

for the degree of
Doctor of Natural Sciences
(docteur ès science)

presented by
ANDREAS METTLER
Dipl. Phys. ETH
born February 9, 1962
citizen of Herrliberg ZH and St.Gallen.

Accepted on the recommendation of
Prof. Dr. A.V.Shah, Institute of Microtechnology, Neuchâtel,
Prof. Dr. H.Beck, Institute of Physics, Neuchâtel,
Prof. Dr. H.Fritzsche, James Franck Institute, Chicago,
Dr. M.Vanecek, Czechoslovak Academy of Sciences, Prague,
PD Dr. H.von Känel, Swiss Federal Institute of Technology, Zürich.

Date of examination June 7, 1994

IMPRIMATUR POUR LA THÈSE

Determination of deep defect density in amorphous silicon by the Constant Photocurrent Method (CPM) : a critical verification

de Monsieur Andreas Mettler

UNIVERSITÉ DE NEUCHÂTEL

FACULTÉ DES SCIENCES

La Faculté des sciences de l'Université de Neuchâtel
sur le rapport des membres du jury,

Messieurs A. Shah, H. Beck, H. von Känel (EPF-Zurich), H. Fritzsche (Chicago) et M. Vanecek (Prague)

autorise l'impression de la présente thèse.

Neuchâtel, le 31 octobre 1994

Le doyen

Nägeli

H.-H. Nägeli

For R. and M.

PROLOGUE - for non-specialists

Silicon was identified in 1823 by the Swede Jöns Jacob Berzelius; it is the second most common element on earth. In 1930 scientists "decided" that **crystalline silicon** is a metal and not an insulator; at that time the electrical properties of this material were governed by the present strong contaminations. After 20 years of intensive research, pure crystalline silicon was recognised as a **semiconductor** and the first transistor was developed at the Bell Laboratories (New Jersey) in December 1947. Today, crystalline silicon is the core material for all computers. In 1989 the semiconductor market had a total turnover of $ 62'000'000'000.

In Scotland in 1954, a group of scientists working on the production of high purity single crystal silicon, using thermal decomposition of silane by r.f. heating, noticed a deposit of a non-crystalline form of silicon on the unheated parts of their reaction vessel: **Amorphous hydrogenated silicon** was discovered - as published in 1969 by Chittick et al. A big break-through for amorphous silicon was the substitutional introducing of impurities, as published in a famous paper by Spear LeComber in 1975. This opened the fabrication of semiconductor devices such as transistors and solar cells with amorphous hydrogenated silicon.

The significant advantage of amorphous hydrogenated silicon - in comparison to crystalline silicon - is that this semiconductor can be directly produced in a form that can cover a **very large area**. Today, amorphous hydrogenated silicon is a key material, e.g. for the electronic parts of liquid crystal displays as used in portable computers; it also has great potential for photocopy machines (the photoconductive layer on the cylinder) and laser printers.

The first **solar cell** based on amorphous hydrogenated silicon was developed in the RCA laboratories in 1976. In contrast to crystalline silicon solar cells, amorphous solar cells are easy to produce in the form of panels with a surface of up to 1 m x 1 m; the production of such amorphous cells also uses much less energy and material for a given installed power rating. The thickness of a crystalline solar cell is (usually) several 100 µm and is produced at very high temperatures, whereas amorphous solar cells are only about 0.5 µm thick and are deposited at about 200 °C.

Industries all over the world have started to produce amorphous silicon solar panels, however, it was reported by Staebler and Wronski in 1977 that **this material is unstable** when exposed to light: i.e., it exhibits an initial light-induced degradation effect and stabilises, therefore, at a lower performance value. The initial cell efficiency is 8% to 10% (in the most simple configuration) and decreases to a **stabilised** value which is about 30% lower than the initial value. More complex cell structures lead to about **10% stabilised** cell efficiencies. The panel efficiency is generally a bit lower.

For several years now, an important topic in amorphous silicon research has been the understanding of the instability of the amorphous hydrogenated silicon; the ulterior motive was to avoid this instability or at least reduce its effect. Nowadays, it is more or less proven that this instability is related to an increase of defects located within the amorphous semiconductor. The **Constant Photocurrent Method** was introduced by Vanecek et al. in 1981, in order to measure such defects (by measuring the optical absorption). In the following study, the **Constant Photocurrent Method** is intensively used and, thereby, critically analysed.

* * *

ABSTRACT - for specialists

The **Constant Photocurrent Method** (CPM) is one of the experiments most commonly used for measuring the sub-band-gap absorption spectrum of **amorphous hydrogenated silicon** (a-Si:H). The original form of the theory underlying the CPM technique was developed for "n-type" a-Si:H material. However, CPM is also often used to characterise intrinsic or "p-type" material. Therefore, it is of basic interest to know in which cases CPM detects the "true" absorption spectrum of a-Si:H.

The study presented here consists of three chapters: **CPM measurements** are presented in chapter 1, **analytical studies and definitions for the numerical calculations** in chapter 2 and a **numerical analysis** in chapter 3.

In chapter 1, CPM spectra of different samples and configurations are presented and discussed: CPM spectra were measured on different, slightly doped layers in the annealed and in the light-soaked state. It was found experimentally that CPM spectra measured on slightly "p-type" samples often do not correspond to the absorption spectrum in the annealed state: Moreover, the correspondance is better in the light-soaked state. Based on this observation, **three CPM measurement conditions**, which quite generally need to be fulfilled during the measurement of a CPM spectrum, and the concept of the **CPM "working point"** are introduced and discussed. Further, CPM spectra were measured on PIN diodes in sandwich-contacted and in coplanar-contacted configurations. Also, CPM spectra were measured on "partial", coplanar-contacted diodes in different, inhomogeneously degraded states. These spectra were compared with CPM spectra measured on slightly doped, inhomogeneousely degraded layers.

In chapter 2, the so-called "standard model" of a-Si:H is recapitulated; based on this well-known model photo conductivity, carrier generation rate and optical absorption are discussed. It is found that a defect with a finite correlation energy (e.g. dangling bond defects) can - as a matter of principle - not be replaced by a combination of a donor-like and an acceptor-like defect. The occupation functions of a defect with a finite correlation energy are analysed at steady-state equilibrium; certain specific "recombination" levels are introduced as a new concept: between these levels, the occupation functions are constant. Further, "generation" levels are introduced to describe the **defect-to-band generation mechanisms** (localised-to-delocalised transitions and vice versa) which are present in the case of sub-band-gap illumination as well as in the case of band-gap illumination.

In chapter 3, conductivity and generation rate are analysed numerically, as a function of the incident photon flux and of the photon energy. This allows one to numerically calculate CPM spectra at steady-state equilibrium and to compare them with the absorption spectra at thermal equilibrium. As a cross check, absorption spectra pertaining to the Photothermal Deflection Spectroscopy (PDS) method were also numerically analysed at steady-state equilibrium. It is

found that CPM spectra at steady-state equilibrium are sensitive to the ratio of the capture cross sections (of the defects) and also to the Fermi level position; furthermore, it can be thereby illustrated that the **three CPM measurement conditions** are not always fulfilled.

* * *

* WHAT IS NEW *

a) CPM Measurements (chapter 1):

The CPM technique is connected with the relation between conductivity and generation rate (a relation that is well known for band-gap illumination). Based on this relation three CPM measurement conditions are introduced here. Only if all these CPM measurement conditions are fulfilled, will the CPM technique detect the absorption spectrum. Here, some cases were experimentally identified where these CPM measurement conditions are not fulfilled: in fact in these cases the CPM spectra are distorted and cannot be used for the determination of defect density.

So far, either undoped or strongly doped samples were analysed with the CPM technique. Here, for the first time slight "n-type" or "p-type" samples are analysed with CPM. It is found that the deep defect absorption values of slightly "n-type", annealed samples are related in a "strict" way to the gas dopant ratio. In the case of slightly "p-type", annealed samples, it is found that the CPM deep defect absorption values are higher than the corresponding PDS values: but the CPM measurement conditions are not fulfilled in this case and the CPM spectra are, therefore, distorted.

The origin of the relation between the CPM deep defect absorption value and the Fermi level position is contradictional. Here, it is found that a simple, but not very "strict" relation between them exists for slightly "n-type" samples as well as for undoped samples deposited at different temperatures. In the case of slightly "p-type", annealed samples, the relation between the CPM deep defect absorption value and the Fermi level position is meaningless due to the failure of the CPM technique for such samples.

The comparison between annealed and light-soaked states of a-Si:H, as well as the degradation kinetics for the transition between the two states, are of fundamental interest. Here, it is found for the first time that slightly doped samples show different degradation kinetics than undoped samples. Further, it is demonstrated that the defect density in the light-soaked state should be characterised by the CPM technique and not by photo-conductivity measurements, as the latter method can lead to significant errors.

The interpretation of CPM measurements on thin PIN diodes is contradictional. Here, it is shown that CPM spectra of thin and thick PIN diodes are much more similar than assumed so far. As a new tentative, thin PIN diodes where measured not only in sandwich configuration but also in coplanar configurations.

The influence of inhomogeneous defect distributions on CPM spectra has so far hardly been studied. In order to know more about this problem, layers were light-soaked inhomogeneously and analysed by "front" and "back" CPM.

Finally, some coplanar-contacted "n-i" and "p-i" multilayer structures (called "partial diodes" here) are analysed by the CPM technique. The results of these new configurations are discussed in the term of charge carrier accumulation in the i-layer.

b) Analytical studies and definitions for numerical calculations (chapter 2):

The analysis presented in chapters 2 and 3 is based on the so-called "standard DOS model" and "standard transport model". The "standard DOS" of a-Si:H consists of parabolic band states, exponential tail states and a Gaussian shaped defect distribution of defects with a finite correlation energy (dangling bonds). The standard transport model is based on multiple trapping theory and is related to the concept of a mobility gap.

It is generally assumed that the CPM technique operates under fixed "recombination levels" (see e.g. Taylor and Simmons). Here, for the fist time, recombination levels for a defect with a finite correlation energy (dangling bonds) are introduced.

It is generally assumed that the occupation functions prevailing during CPM measurements are approximately equal to the occupation functions prevailing in thermal equilibrium. Here, for the fist time, the occupation functions of a defect with a finite correlation energy (dangling bonds) are investigated under different values of steady-state illumination intensity.

Concerning the possible optical transitions from a defect with a finite correlation energy (dangling bonds), it is found that certain of these have been underestimated by a factor 2 so far.

Mittiga et al. introduced a new concept in order to describe localised-to-delocalised transitions (sub-band-gap statistics). This concept is analysed here with help of some new "generation levels" and adapted to a defect with a finite correlation energy (dangling bonds).

c) Numerical analysis (chapter 3):

So far, a-Si:H models are either discussed at thermal equilibrium (i.e. sub-band-gap absorption) or at steady-state equilibrium (i.e. photo conductivity under band-gap illumination). Here, for the first time, a complete numerical model is presented which describes both thermal equilibrium and steady-state equilibrium. To the author's knowledge, this numerical model is at present the most complete available. The thermal emission rates as well as the optical transition rates are, thereby, taken into account.

At thermal equilibrium a new deconvolution approach is presented which allows to determine some of the parameters of the model. It is found, however, that the value of the optical matrix element cannot be determined by this approach. For the first time, bands with asymmetrical parabolic densities of states for a-Si:H are discussed here.

At steady-state equilibrium this numerical model allows to compare CPM spectra at steady-state equilibrium with the "true" absorption at thermal equilibrium for the first time. Additionally, PDS spectra at steady-state equilibrium are analysed here for the first time. Furthermore, it is possible to analyse the conductivity as a function of the photon energy and as a function of the incident photon flux. It is found that even in the case where the photon energy is equal to the mobility gap, the conductivity of a-Si:H can still be determined by transitions from localised-to-delocalised states.

* * *

TABLE OF CONTENTS

1. CPM Measurements

In this chapter the Constant Photocurrent Method (CPM) will be presented within the framework of the measurement of optical absorption spectra of amorphous hydrogenated silicon (a-Si:H). Some "strong" measurement conditions that are necessary in the case of CPM will be presented; these conditions must be fulfilled in order to measure the absorption spectrum correctly with the CPM technique. CPM spectra of undoped and doped layers will be presented in the annealed and the light-soaked state as well as CPM spectra measured on PIN diodes with sandwich and coplanar contacts. Further, CPM spectra of "n-i" and "p-i" configurations with coplanar contacts will be presented. The influence, e.g. of measurement temperature, of Fermi level position, of layer thicknesses, of dopants and of deposition temperature on the CPM spectra, will be discussed, analysed and compared to the behaviour of other absorption measurement techniques.

1.1. Introduction

A typical absorption spectrum for **amorphous hydrogenated silicon** (a-Si:H) is shown in Fig.1a. Generally, such an absorption spectrum consists of three parts: the **deep defect absorption range**, the **exponential tail range** and the **band absorption range**. In this chapter these three ranges will be analysed, while their detailed, microscopic interpretation will be discussed in chapter 2.

The band absorption range is interpreted - in terms of crystalline semiconductor - to correspond to optical transitions from the valence band to the conduction band. The exponential tail - also called Urbach tail (as it was originally observed by Urbach [53] in AgBr) - is characterised by its slope (indicated as a dashed line in fig.1a). In the case of a-Si:H, the Urbach slope is independent of the layer's temperature over a wide range. The deep defect absorption range is of basic interest in the case of a-Si:H: in the annealed state, the deep defect absorption is low, but it increases over more than one order of magnitude, as e.g. under light soaking. This increase in the deep defect absorption range is called degradation of the material. One can distinguish between the initial state (annealed state) and the light-soaked state (degraded state). The deep defect absorption range is interpreted as the result of transitions from localised deep defect states within the bandgap to delocalised band states: these deep defects act as recombination centres and their increase leads to a decrease of the photo conductivity. However, not only is the photo conductivity lower in the degraded state than in the annealed state, but also the dark conductivity. The decrease of the dark conductivity is interpreted to be related to a shift of the Fermi energy E_F.

Recent research efforts have been centred on finding new preparation techniques for a-Si:H to produce layers which do not show such degradation behaviour (or, at least, show less degradation). Therefore, experimental tools are required to measure the absorption spectrum in the absolute scale, especially in the deep defect absorption range. In this study the **Constant Photocurrent Method** (CPM) - introduced by Vanecek et al. [81] for a-Si:H - and the

Photothermal Deflection Spectroscopy (PDS) - proposed by Jackson et al. [81] for a-Si:H - will be used to measure the optical absorption spectrum of a-Si:H. Besides this, the **dual-beam method** - proposed by Wronski et al. [82] for a-Si:H - will also be discussed.

The **Constant Photocurrent Method** (CPM) measures the conductivity and detects a relative spectrum (called the CPM spectrum here), whereas PDS operates contactless and detects (in a certain sense, see section 1.3.2.) an **absolute** spectrum (called the PDS spectrum here). The relative CPM spectrum can be calibrated in the range of the exponential tail with the absolute PDS spectrum. If no PDS spectrum is available (especially in the case of device configurations), it will be shown hereunder that the relative CPM spectrum can be calibrated in the range of the band absorption with **optical transmission measurements**. Fig.1b shows the CPM and PDS spectrum of the same a-Si:H layer: the relative CPM spectrum is calibrated in the exponential tail range by the absolute PDS spectrum. CPM only works under the uniform absorption condition ($\alpha d << 1$), whereas PDS also works under slightly non-uniform absorption: this is the origin of the differences between the two spectra as observed in the band absorption range. The differences in the deep defect absorption range are of capital interest and will be discussed here: in comparison to the PDS method, CPM seems to be more sensitive in the deep defect absorption range than PDS and generally shows lower deep defect absorption values than PDS.

The Constant Photocurrent Method CPM and the Photothermal Deflection Spectroscopy PDS method, which are well established tools to determine the optical absorption spectra of a-Si:H layers in the annealed or light-soaked states, will be analysed here to decide which method detects the "true" absorption spectrum of a-Si:H.

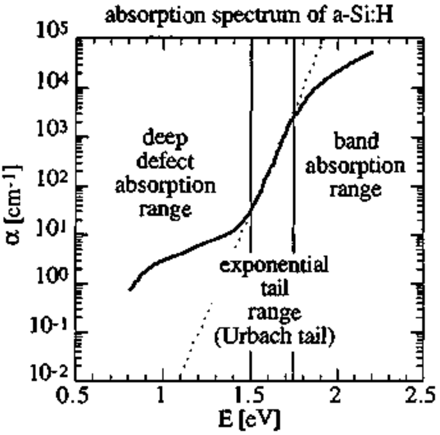

Fig.1a: absorption spectrum $\alpha(\hbar\omega)$ of a-Si:H (hypothetical).

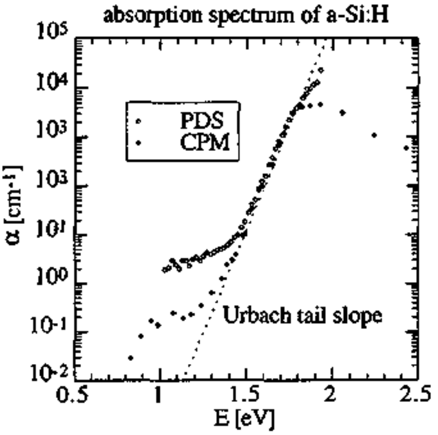

Fig.1b: measured CPM and PDS spectrum $\alpha(\hbar\omega)$ of an annealed, undoped a-Si:H layer. (sample D190393)

1.2. The Constant Photocurrent Method CPM and the conductivity

This analysis is independent of a possible microscopic DOS model of a-Si:H. This analysis is based only on photo conductivity, the generation rate, the incident photon flux and the absorption.

1.2.1. The original CPM measurement approach

It has been observed experimentally that the photo conductivity σ_{ph} of a semiconductor is often connected with the generation rate G by a power law [Rose 63]:

$$\sigma_{ph} \propto G^{\gamma}$$

The main feature of the power law exponent γ (Rose factor) is to characterise the recombination behaviour. For uniform absorption ($\alpha\, d << 1$) the generation rate G can be approximated by $G = \alpha\, \Phi_0$ where Φ_0 corresponds to the total incident photon flux. Thus, one can write

$$\sigma_{ph} \propto \{\alpha\, \Phi_0\}^{\gamma}$$

In the case of amorphous hydrogenated silicon (a-Si:H) the power law exponent γ can vary with the generation rate, and the proportionality $\sigma_{ph} \propto G^{\gamma}$ is only defined in a small range. This fact was the main motivation for Vanecek et al. [81] to introduce the **Constant Photocurrent Method** CPM for a-Si:H in 1981. While keeping the photocurrent constant, they found that the absorption α is simply inversely-proportional to the total incident photon flux Φ_0 [Vanecek 81]:

$$\sigma_{ph} = \text{const} \qquad => \qquad \alpha \propto \frac{1}{\Phi_0} \qquad \text{for } \alpha\, d << 1$$

With this approach the power law exponent γ does not vary any longer with the generation rate, and it is possible to measure the **relative** absorption spectrum of a-Si:H. The relative CPM spectra, which will be presented in this chapter, have been calculated with this approach ($\alpha \propto 1/\Phi_0$).

1.2.2. Critical analysis of the CPM measurement approach

Starting from the differences measured in the deep defect absorption range between CPM and PDS (see e.g. fig.1b), the author has analysed the CPM measurement approach of Vanecek et al. [81] in a more detailed way. This analysis will not give any microscopic interpretation of the CPM spectra, but lead to some strong, restrictive CPM measurement conditions which have to be fulfilled in order to identify the CPM spectra as the optical absorption spectra of a-Si:H.

a) Non-linear photo conductivity

One can either measure the photo conductivity σ_{ph} (with the lock-in technique) or the total conductivity σ_{tot} (with a multimeter / electrometer). For an arbitrary, but small range of the generation rate G, one can write:

$$\sigma_{ph} \propto G^{\gamma} \qquad \text{or} \qquad \sigma_{tot} \propto G^{\gamma^*}$$

The power law exponent γ^* - introduced by the author et al. [Mettler 93/2] - differs in general from the Rose factor γ; however, it differs significantly only in the range of low generation rates G if the principle of superposition is valid:

$$\sigma_{ph} << \sigma_d \qquad => \qquad \gamma \neq \gamma^* = 0$$
$$\sigma_{ph} >> \sigma_d \qquad => \qquad \gamma = \gamma^*$$

The principle of superposition means that total conductivity σ_{tot} is equal to the sum of dark conductivity σ_d and photo conductivity σ_{ph} ($\sigma_{tot} = \sigma_d + \sigma_{ph}$). Note that the analysis presented in this section is valid, independent of the principle of superposition. The term "non-linear photo conductivity" means that the power law exponent γ (Rose factor) is not equal to one ($\gamma \neq 1$).

For uniform absorption ($\alpha\, d << 1$) the generation rate can be approximated by $G = \alpha\, \Phi_0$ where Φ_0 corresponds to the total incident photon flux. Thus, one can write for an arbitrary, but small range of the generation rate G:

$$\sigma_{ph} \propto G^{\gamma} \propto \{\alpha\, \Phi_0\}^{\gamma} \qquad \text{or} \qquad \sigma_{tot} \propto G^{\gamma^*} \propto \{\alpha\, \Phi_0\}^{\gamma^*}$$

In the case of a-Si:H the power law exponents γ and γ^* can vary with the generation rate G. When either photo conductivity σ_{ph} or total conductivity σ_{tot} is kept constant, the power law exponents and the generation rate are fixed. The author has described this condition of having a fixed conductivity as a **CPM "working point"** (σ_{CPM}, G_{CPM}) [Mettler 93/3]:

$$\sigma_{CPM} \propto (G_{CPM})^{\gamma_{CPM}} \propto \{\alpha\, \Phi_0\}^{\gamma_{CPM}} \quad \text{with } \sigma_{CPM} = \sigma_{ph}$$

$$\sigma_{CPM} \propto (G_{CPM})^{\gamma^*_{CPM}} \propto \{\alpha\, \Phi_0\}^{\gamma^*_{CPM}} \quad \text{with } \sigma_{CPM} = \sigma_{tot}$$

The description of the photo conductivity of a semiconductor by a power law ($\sigma_{ph} \propto G^{\gamma}$) was originally introduced for photon energies $\hbar\omega$ **larger** than the bandgap and for photo conductivities larger than the dark conductivity. One can assume that this power law dependency can also be used to describe the photo conductivity for photon energies $\hbar\omega$ **smaller** than the bandgap - at least for a small range of generation rates. But the author would like to point out that a priori **there is no evidence that these power law dependencies are identical for different photon energies** $\hbar\omega$. The conductivity, the generation rate and the power law exponent can all be a function of the photon energies. Therefore, one has to write:

$$\sigma_{ph}(\hbar\omega) \propto G(\hbar\omega)^{\gamma(\hbar\omega)} \propto \left\{\alpha(\hbar\omega)\,\Phi_0(\hbar\omega)\right\}^{\gamma(\hbar\omega)}$$

or

$$\sigma_{tot}(\hbar\omega) \propto G(\hbar\omega)^{\gamma^*(\hbar\omega)} \propto \left\{\alpha(\hbar\omega)\,\Phi_0(\hbar\omega)\right\}^{\gamma^*(\hbar\omega)}$$

If the conductivity is kept constant while the photon energy $\hbar\omega$ is changed, the conductivity is no longer a function of the photon energy $\hbar\omega$. But the generation rate, as well as the power law exponent, are - a priori - still functions of the photon energies. One can write in terms of the CPM "working point" (σ_{CPM}, G_{CPM}):

lm-mode: $\sigma_{CPM} \propto G_{CPM}(\hbar\omega)^{\gamma_{CPM}(\hbar\omega)} \propto \left\{\alpha(\hbar\omega)\,\Phi_0(\hbar\omega)\right\}^{\gamma_{CPM}(\hbar\omega)}$ with $\sigma_{CPM} = \sigma_{ph}$

cw-mode: $\sigma_{CPM} \propto G_{CPM}(\hbar\omega)^{\gamma^*_{CPM}(\hbar\omega)} \propto \left\{\alpha(\hbar\omega)\,\Phi_0(\hbar\omega)\right\}^{\gamma^*_{CPM}(\hbar\omega)}$ with $\sigma_{CPM} = \sigma_{tot}$

These two equations describe the situation of the Constant Photocurrent Method CPM: the upper equation corresponds to the **lm-mode** (light-modulated CPM mode), whereas the lower equation corresponds to the **cw-mode** (continuous-wave CPM mode). In both cases, one gets a **relative** CPM spectrum $\alpha_{CPM}(\hbar\omega)$ by using the relationship

$$\alpha_{CPM}(\hbar\omega) \propto \frac{1}{\Phi_0(\hbar\omega)}.$$

The following two conditions are necessary (but not sufficient) conditions to ensure that the relative CPM spectrum $\alpha_{CPM}(\hbar\omega)$ corresponds to the relative absorption spectrum $\alpha(\hbar\omega)$ [Mettler 93/2]:

First CPM condition: the power law exponent γ_{CPM} or γ^*_{CPM} has to be spectrally-independent:

$\gamma_{CPM}(\hbar\omega) = \gamma_{CPM}$ for all $\hbar\omega$ (lm-mode).
$\gamma^*_{CPM}(\hbar\omega) = \gamma^*_{CPM}$ for all $\hbar\omega$ (cw-mode).

Second CPM condition: the CPM generation rate G_{CPM} and the CPM "working point" (σ_{CPM}, G_{CPM}) have to be spectrally-independent:

$G(\hbar\omega) = G_{CPM}$ for all $\hbar\omega$.

If the first and the second CPM conditions are fulfilled, the original CPM approach (see section 1.2.1.) is valid in the following manner:

lm-mode: $\sigma_{CPM} \propto G_{CPM}{}^{\gamma_{CPM}} \propto \left\{\alpha(\hbar\omega)\, \Phi^0_{ph}(\hbar\omega)\right\}^{\gamma_{CPM}}$ with $\sigma_{CPM} = \sigma_{ph}$

cw-mode: $\sigma_{CPM} \propto G_{CPM}{}^{\gamma^*_{CPM}} \propto \left\{\alpha(\hbar\omega)\, \Phi^0_{ph}(\hbar\omega)\right\}^{\gamma^*_{CPM}}$ with $\sigma_{CPM} = \sigma_{tot}$

So much for CPM analysis for the case where photo conductivity is larger than dark conductivity ($\sigma_{ph} > \sigma_d$), corresponding to the original CPM measurement approach (see section 1.2.1.).

The following figures illustrate the meaning of the CPM "working point" and of the two CPM measurement conditions. Fig.2 shows the results of an undoped a-Si:H layer where the first and the second CPM conditions are fulfilled. Fig.3 shows the results of a slightly "p-type" layer where neither of the two CPM conditions are fulfilled. Note that the spectral calibration of the generation rate G requires to know the exact optical absorption values. Details and a discussion of these measurements are given in appendix A2.3.

b) Spectrally independent, linear photo conductivity

In this subsection the author will discuss the special case where the power law exponent is spectrally-independent and equal to one (linear photo conductivity). This can be the case for layers measured in the lm-mode with $\sigma_{ph} << \sigma_{tot}$ where total conductivity is equal to dark conductivity or where total conductivity is equal to the conductivity of an additional cw-mode bias light (dual-beam technique). Further, this can be the case for diodes (primary photo current).

In this special case one can write

$$\sigma_{ph}(\hbar\omega) \propto G(\hbar\omega) \propto \alpha(\hbar\omega)\, \Phi_0(\hbar\omega) \qquad \text{for } \gamma(\hbar\omega) = \gamma = 1$$

$$\sigma_{tot}(\hbar\omega) \propto G(\hbar\omega) \propto \alpha(\hbar\omega)\, \Phi_0(\hbar\omega) \qquad \text{for } \gamma^*(\hbar\omega) = \gamma^* = 1$$

Therefore, the absorption spectrum $\alpha(\hbar\omega, G(\hbar\omega))$ is given as

lm-mode: $\alpha(\hbar\omega, G(\hbar\omega)) \propto \dfrac{G(\hbar\omega)}{\Phi_0(\hbar\omega)} \propto \dfrac{\sigma_{ph}(\hbar\omega)}{\Phi_0(\hbar\omega)}$ for $\gamma(\hbar\omega) = \gamma = 1$

cw-mode: $\alpha(\hbar\omega, G(\hbar\omega)) \propto \dfrac{G(\hbar\omega)}{\Phi^0_{ph}(\hbar\omega)} \propto \dfrac{\sigma_{tot}(\hbar\omega)}{\Phi^0_{ph}(\hbar\omega)}$ for $\gamma^*(\hbar\omega) = \gamma^* = 1$

One can conclude from these relations that it is no longer necessary now to keep the conductivity constant (as in the case of CPM) in order to measure the absorption spectrum. The author came to this conclusion for the specific case where photo conductivity is below dark conductivity ($\sigma_{ph} << \sigma_d$) [Mettler 93/2]. Furthermore, this is the standard approach of the dual-beam technique ($\sigma_{ph} << \sigma_{tot}$) [Wronski 82]. However, it is still possible to measure CPM spectra in this specific case of a spectrally independent, linear photo conductivity. The author will show CPM spectra measured with a bias light in section 1.6.2.

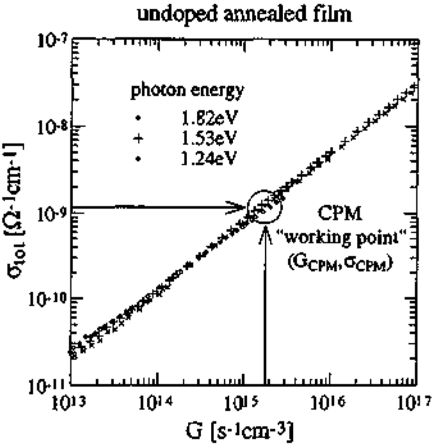

Fig.2a: the conductivity σ_{tot} as a function of the generation rate G for three different photon energies: a typical CPM "working point" is indicated where the **second CPM condition is fulfilled** (undoped, annealed layer [Mettler 93/3]).

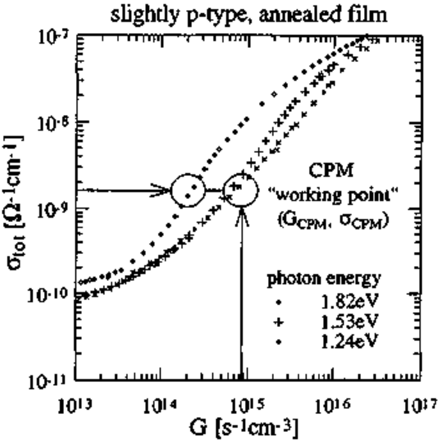

Fig.3a: the conductivity σ_{tot} as a function of the generation rate G for three different photon energies: a typical, spectrally dependent CPM "working point" is indicated where the **second CPM condition is <u>not</u> fulfilled** (slightly "p-type", annealed layer [Mettler 93/3]).

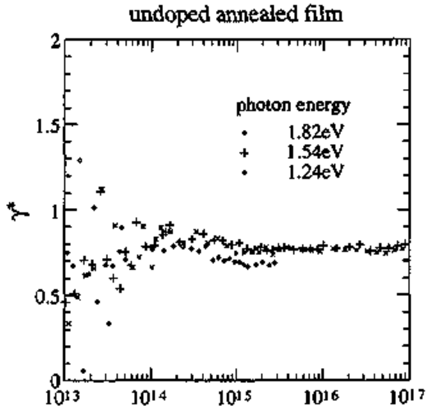

Fig.2b: the power law exponent γ^* (which corresponds to fig.2a) as a function of the generation rate G for three different photon energies: here the **first CPM condition is fulfilled** (undoped, annealed layer [Mettler 93/3]).

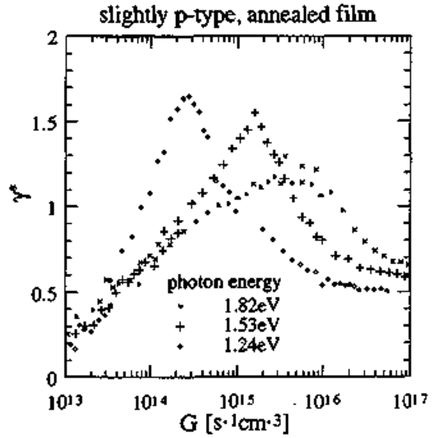

Fig.3b: the power law exponent γ^* (which corresponds to fig.3a) as a function of the generation rate G for three different photon energies: here the **first CPM condition is <u>not</u> fulfilled** (slightly "p-type", annealed layer [Mettler 93/3]).

Fig.4 shows two spectra of a slightly "p-type" layer (CPM1: $\sigma_{CPM} >> \sigma_d$ and CPM2: $\sigma_{CPM} << \sigma_d$) as calibrated by PDS. One recognises that the PDS spectrum is higher than the CPM1 spectrum in the deep defect absorption range. This fact is related to the failure of the first and the second CPM condition for $\sigma_{tot} >> \sigma_d$ (as shown in fig.3 for this layer). In contrast, the PDS spectrum is approximately identical to the CPM2 spectrum when the two CPM conditions remain fulfilled for $\sigma_{ph} << \sigma_d$ (spectrally independent, linear photo conductivity).

From these measurements one can see that if the CPM measurement conditions are not fulfilled for one CPM conductivity σ_{CPM} (CPM1), it is still possible that the CPM measurement conditions are fulfilled for another CPM conductivity σ_{CPM} (CPM2).

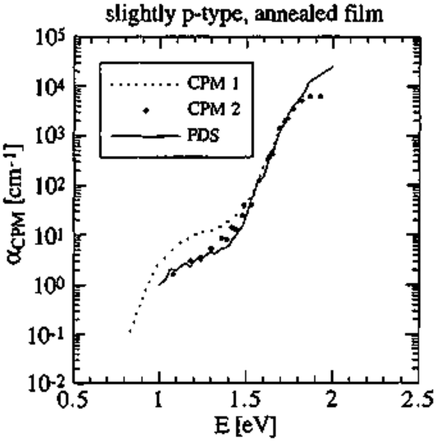

Fig.4: the CPM spectra $\alpha_{CPM}(\hbar\omega)$ of a slightly "p-type", annealed layer as calibrated by PDS spectrum. The CPM1 spectrum was measured in the cw-mode with $\sigma_{CPM} >> \sigma_d$ and the CPM2 spectrum was measured in the lm-mode with $\sigma_{CPM} << \sigma_d$.
[Mettler 93/3]

c) The third CPM condition

If the first and the second CPM condition are fulfilled, one can write

	non-linear photo conductivity	linear photo conductivity
lm-mode:	$\sigma_{CPM} \propto G_{CPM}^{\gamma_{CPM}}$	$\sigma_{CPM} \propto G_{CPM}$
cw-mode:	$\sigma_{CPM} \propto G_{CPM}^{\dot{\gamma}_{CPM}}$	$\sigma_{CPM} \propto G_{CPM}$

In order to be more precise, one has to note that the proportionality factors of these relations also has to be spectrally-independent. The author will call this the "third CPM condition" here. This proportionality factor could change if e.g. the majority charge carrier (or alternatively its mobility value), as related to the conductivity σ_{CPM}, changes as a function of the photon energy $\hbar\omega$.

If the first, the second and the third CPM condition are fulfilled, the CPM spectrum should correspond to the absorption spectrum of the a-Si:H:

$$\alpha(\hbar\omega) = \alpha_{CPM}(\hbar\omega) \propto \frac{1}{\Phi_0(\hbar\omega)}.$$

One can conclude that the CPM spectrum $\alpha_{CPM}(\hbar\omega)$ can, in principle, always be measured but that this CPM spectrum does not a priori correspond to the optical absorption spectrum. Only if the first, the second and the third CPM conditions are fulfilled does the Constant Photocurrent Method CPM measure the absorption spectrum. In this section no assumption at all has been made about the material itself and therefore the author notes that CPM spectra can be measured on any material with a measurable photo conductivity (see e.g. µc-Si layers analysed by CPM, section 1.4.5.).

c) The absorption and the deep defect occupation

From an **experimental** point of view three different spectra will be distinguished here: CPM spectrum $\alpha_{CPM}(\hbar\omega)$, PDS spectrum $\alpha_{PDS}(\hbar\omega)$ and dual-beam spectrum $\alpha_{DB}(\hbar\omega)$. Each of these experiments claim to detect the "true" absorption spectrum $\alpha(\hbar\omega)$ of a-Si:H. However, it bas been shown that these measurements operate under different conditions, especially under different illuminations. From a theoretical point of view, the author bas noticed that the absorption spectrum at thermal equilibrium need not be identical to the absorption spectrum under experimental illumination because the illumination of the layer can - in principle - influence the occupation of the deep defects in such a way that the possible optical transitions change. Such effects are a possible origin for the different deep defect absorption values found in the three different experiments (discussion see section 1.7.3d).

1.3. Measurement set-ups

1.3.1. The CPM detection mechanism

With the CPM measurement set-up used here, the dark current, the total current and the pbotocurrent of a sample can be measured as a function of the temperature (T = 0 - 250°C), as a function of the incident light intensity (I_0 = 0 - 4 mWcm^{-2}) for a specific photon energy ($\hbar\omega$ = 0.83 - 2.43eV) or as a function of the applied voltage (U = 0-100V). Fig.5a illustrates the CPM detection mechanism. Details of this CPM measurement set-up are given in appendix A1.

In this CPM set-up it is possible to use samples deposited on a glass substrate with coplanar contacts or any kind of multilayer structure (e.g. diodes) with sandwich or coplanar contacts. The sample can either be illuminated from the front or from the back by a monochromatic, spectrally dependent pump beam. Basically it is possible to measure CPM spectra $\alpha_{CPM}(\hbar\omega)$ in the lm- or cw-mode with this set-up, but also annealing curves $\sigma(T)$, current-voltage dependencies (I-V curves) and photo conductivity characteristics $\sigma(G, \hbar\omega)$. If, additionally, a second monochromatic pump beam illuminates the sample (bias light), it is also possible to measure dual-beam spectra $\alpha_{DB}(\hbar\omega)$ in the lm-mode. Experimental details concerning the CPM measurement techniques are given in the appendix, sections A1.1. to A1.4.

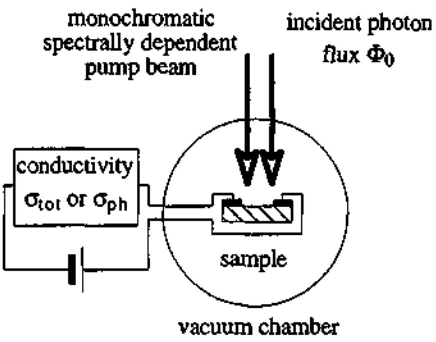

Fig.5a: CPM detection mechanism.

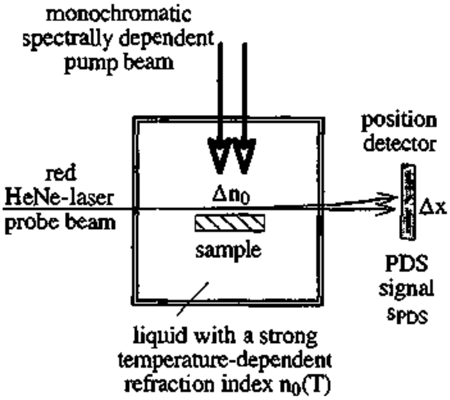

Fig.5b: PDS detection mechanism.

1.3.2. The PDS detection mechanism

The PDS method was analysed in detail by Curtins et al. [89] and Favre [94/1]. Fig.5b shows the PDS detection mechanism: the surface of a homogeneously grown layer of a-Si:H is illuminated by a monochromatic, spectrally dependent pump beam. Parallel and close to the layer surface, a red HeNe-laser probe beam passes the layer and its light is detected by a position detector. In order to measure the absorption of the layer, it has to be in a liquid (here: CCl_4) with a strongly temperature-dependent refraction index $n_0(T)$. The red HeNe-laser probe beam passes through this liquid. Depending on the spectral absorption of the a-Si:H layer, the liquid is heated in a different way, leading to a change in its refraction index Δn_0. Due to the change in the refraction index Δn_0 of the liquid, the deflection of the red HeNe-laser probe beam also changes. This deflection Δx is detected as a function of the photon energy of the pump beam. The detected PDS signal $s_{PDS}(\hbar\omega)$ is proportional to the total generation rate $G_{tot}(\hbar\omega)$:

$$s_{PDS}(\hbar\omega) \propto G_{tot}(\hbar\omega)$$

The PDS signal $s_{PDS}(\hbar\omega)$ is detected with the help of a lock-in technique. The incident photon flux $\Phi_0(\hbar\omega)$ of the monochromatic light is generally kept constant - in contrast to the CPM technique. The **absolute** PDS spectrum is given as

$$\alpha_{PDS}(\hbar\omega) = \frac{G(\hbar\omega)}{\Phi_0(\hbar\omega)} = \frac{\Phi_{ph}^0(\hbar\omega_c)}{d\, s_{PDS}(\hbar\omega_c)} \frac{s_{PDS}(\hbar\omega)}{\Phi_0(\hbar\omega)}$$

$$\text{with } \alpha(\hbar\omega)\, d << 1 \qquad \text{and} \qquad \alpha(\hbar\omega_c)\, d >> 1$$

The PDS spectrum is calibrated at a specific photon energy $\hbar\omega_c$ with $\alpha d>>1$ (full absorption).

1.3.3. Transmission measurements

If no PDS spectrum is available, the relative CPM spectrum can be calibrated by a transmission measurement. The averaged transmission $\overline{T}$ depends on the absorption α, the sample thicknesses d, the refraction coefficient R_0 of the a-Si:H / air interface and on the refraction coefficient R_1 of the a-Si:H / substrate interface [Swanepoel 83]:

$$\overline{T} = \frac{(1-R_0)\,(1-R_1)\,e^{-\alpha d}}{1-R_0R_1e^{-2\alpha d}} \text{ with } \overline{T} = \sqrt{T_{max}T_{min}}\,,$$

The absorption $\alpha(\hbar\omega)$ can be calculated from this transcendent equation by assuming two spectrally independent refraction coefficients R_0(a-Si:H / air) = 0.3 and R_1(a-Si:H / substrate) = 0.16 and by determining the sample thickness d (which can be measured for example with an α-step).

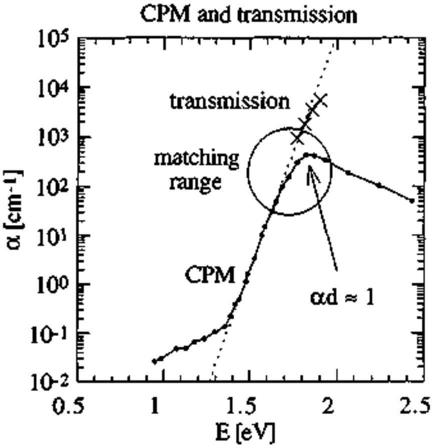

Fig.6: Calibration of a relative CPM spectrum by transmission measurements (sample A121090A2 as calibrated by Vanecek [91/1]). Especially for thick samples, the matching range (indicated by a circle) can cause some problems. In this case it is helpful to draw the exponential tail range (dashed line) which connects the transmission absorption with the CPM absorption. However, it remains easier to calibrate the relative CPM spectrum by the PDS spectrum (see fig.2).

1.3.4. I-V measurements and the electrical contacts

The current-voltage dependency (I-V measurement) contains some information about the physical nature of the contacts. In this section I-V measurements are presented for a coplanar-contacted layer. The dark current is measured with an electrometer. Under illumination the current can be measured in the cw-mode (electrometer) and in the lm-mode (lock-in technique). One can distinguish between dark current I_d, total current I_{tot} and photo current I_{ph}. The author has introduced the following notation in order to describe the I-V characteristics by a power law for an arbitrary but small voltage range U:

$$I_d \propto U^{\xi_d^*} \qquad I_{tot} \propto U^{\xi^*} \qquad I_{ph} \propto U^{\xi}$$

$$\xi_d^* \equiv \frac{\log(I_d)}{\log(U)} \qquad \xi^* \equiv \frac{\log(I_{tot})}{\log(U)} \qquad \xi \equiv \frac{\log(I_{ph})}{\log(U)}$$

The exponents with a star correspond to measurements with an electrometer. As already mentioned, the principle of superposition ($I_{tot} = I_{ph} + I_d$) need not be a priori valid. The following classification of the voltage power law factors is well known for the <u>dark current</u>:

Ohmic contacts:	$I = R^{-1} U$	$\xi_d^*=1$	and R = const
Charge carrier injection:	$I_d \propto U^{\xi_d^*}$	$\xi_d^*>1$	
Ideal blocking contact:	$I = \text{const}$	$\xi_d^*=0$	

In the case of the <u>photo current</u>, the following classification seems reasonable:

Ohmic-like:	$I \propto U$	$\xi=1$
Ideal collection:	$I = \text{const}$	$\xi=0$

Fig.7 shows the I-V characteristics of a coplanar-contacted layer (0.5mm x 8mm). Fig.7a shows the dark current I_d, fig.7b shows the total current I_{tot} and fig.7c shows the photo current I_{ph}. The layers were illuminated with a constant intensity ($I_0 \approx 4\text{mW cm}^{-2}$ and $\hbar\omega$ = 1.1eV and 1.3eV). One can recognise that the contacts show an Ohmic behaviour in all three cases at 10V corresponding to an electric field of 200V/cm. Vanecek [91/1] supports the hypothesis that an electric field of 200V/cm will generally lead to Ohmic contacts which are required for CPM measurements on layers. Hereafter, an applied voltage of 10V has been chosen with a coplanar contact configuration of 0.5mm x 8mm.

The I-V measurements shown in fig.7 and the CPM spectra shown in fig.8 correspond to the same sample. The observed difference in the deep defect absorption range of these CPM spectra - as measured in the **cw-mode** and in the **lm-mode** - seems not to be related to the Omic behaviour measured in both cases (see notes at the end of this section).

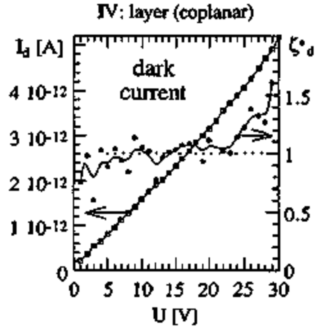

Fig.7a: dark I-V characteristics ($I_d(U)$ and $\xi_d^*(U)$) of a layer with coplanar contacts in the dark. (sample A121090)

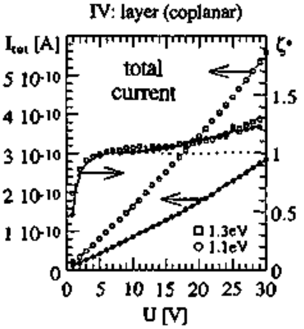

Fig.7b: cw I-V characteristics ($I_{tot}(U)$ and $\xi^*(U)$) of a layer with coplanar contacts under illumination.(sample A121090)

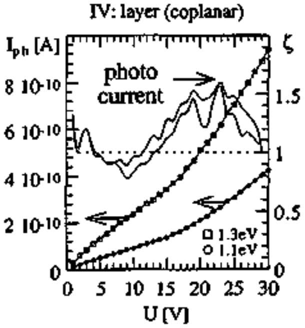

Fig.7c: lm I-V characteristics ($I_{ph}(U)$ and $\xi(U)$) of a layer with coplanar contacts under illumination.(sample A121090)

I-V measurements characterise the **contact behaviour**. Fig.8b indicates that Cr and Al contacts lead to the same CPM deep defect absorption values (the author used basically Al contacts for this study). This means that these metals show no spectrally dependent Ohmic behaviour. However, Hoheisel et al. [91] reported that the CPM deep defect absorption values (undoped, annealed layers) are very sensitive to the material of the contacts.

In principle, metallic contacts on a-Si:H can lead to band bendings, related to charge carrier injection or to charge carrier depletion, maybe not only in the dark, but also under illumination. But as a further aspect of the contacts, the distance between the two coplanar contacts also influences the CPM spectrum of a-Si:H: the larger the distance between the two coplanar contacts, the higher the deep defect absorption values (see e.g. [Vanecek 91/2], [Hoheisel 91]). Such effects have been analysed and interpreted as light scattering effects within the layer (see e.g. [Vanecek 91/2]). In order to keep such effects small [Vanecek 91/1], the distance between the two coplanar contacts has been chosen as 0.5mm for this study.

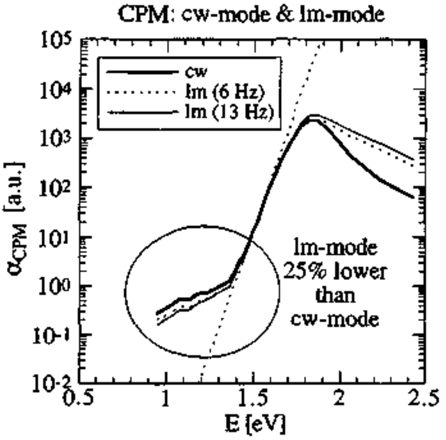
CPM: cw-mode & lm-mode

Fig.8a: relative CPM spectra $\alpha_{CPM}(\hbar\omega)$ (calibrated at 1.6eV) of an undoped, annealed layer, as measured in the cw-mode and in the lm-mode. (sample A121090)

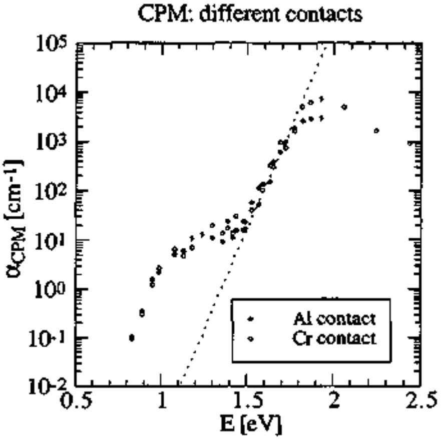
CPM: different contacts

Fig.8b: relative cw-CPM spectra $\alpha_{CPM}(\hbar\omega)$ (calibrated at 1.6eV) of a "p-type" layer with Al and Cr contacts. (sample C270991)

Note: Even if the Ohmic condition is fulfilled, the CPM spectra - as measured in the **cw-mode** and in the **lm-mode** - can be different (see fig.7 and fig.8a). One can recognise that the deep defect absorption values decrease with increasing chopper frequencies. The cw-mode CPM shows a higher deep defect absorption than the lm-mode CPM (also reported e.g. by Sladek et al. [92]). Nevertheless, the differences in the deep defect absorption between the cw-mode and the lm-mode are small if the chopper frequency is low. Note that the dualbeam-technique shows similar trends: J.Z.Liu et al. [93] reported that the deep defect absorption values decrease with increasing chopper frequencies.

The author assumes that this behaviour is caused by a spectrally dependent response time: the occupation of the deep defects in the lm-mode has to change between two different states (illuminated / non-illuminated). If the chopper frequency is so high that the requested time to change between these states is not given, the lock-in technique underestimates the true signal. If the layer is doped, generally no differences between the lm-mode CPM spectra and the cw-mode CPM spectra are observed.

1.4. Absorption measurements on layers

1.4.1. Thickness dependency of CPM and PDS

Fig.9a shows CPM spectra of undoped, annealed a-Si:H layers as a function of the layer thickness. No changes in the deep defect absorption range can be detected for the chosen thicknesses (d = 0.6 - 40μm), except for the layer with d = 1μm (dashed line). For the thin layer with d = 0.6μm (dots), the inference fringes can clearly be seen (limiting spectral resolution of the measurement set-up, see appendix A1). Thick layers show little interference fringes, but the CPM spectra are reduced in the upper part due to the uniform absorption condition ($\alpha d<<1$) and they are difficult to calibrate (see section 1.3.3.) - especially in the light-soaked state. From fig.9a and fig.9b the author concludes that **CPM is almost insensitive to the layer thicknesses** in the range of d = 0.6 - 40μm. The situation appears to be quite different for lower thicknesses: Fiorini et al. [93] observed a pronounced increase in the CPM deep defect absorption values for d = 0.3μm and Sasaki et al. [93] for d < 0.25μm. In contrast to CPM, Favre et al. [91] observed that **PDS is very sensitive to layer thicknesses** in the range of d = 0.01 - 100μm. Fig.9c indicates that the PDS deep defect absorption values of undoped, annealed a-Si:H layers are sensitive to the layer thicknesses over four orders of magnitude.

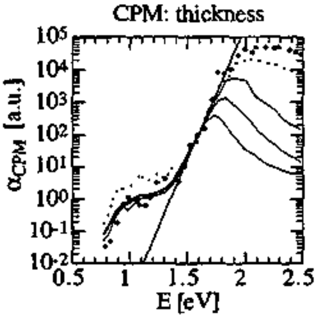

Fig.9a: CPM spectra $\alpha_{CPM}(\hbar\omega)$ of samples[*] with different thicknesses d (see fig.8b).

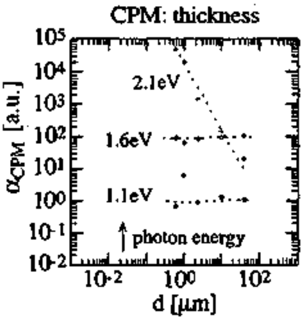

Fig.9b: CPM absorption values as a function of layer thicknesses d (details of fig.8a).

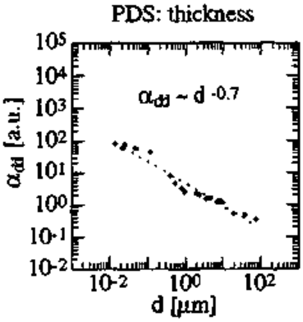

Fig.9c: PDS deep defect absorption values α_{dd} as a function of layer thicknesses d. [Favre 91]

[*] samples: C091189/1, A160689/1, A300687, A290687/1, A160287/2

It is assumed that these changes in the deep defect absorption range are caused by some surface / interface states - in the case of PDS [Curtins 89] as well as in the case of CPM [Fiorini 93]. In this context, the author checked if the non-uniformly absorbed, red HeNe laser probe beam of the PDS set-up (shown in fig.5a) influences the occupation of the deep defects in such a way that the PDS technique shows thickness-dependent deep defect absorption values; it is experimentally not found that the probe beam influences the PDS spectrum (cf. fig.10).

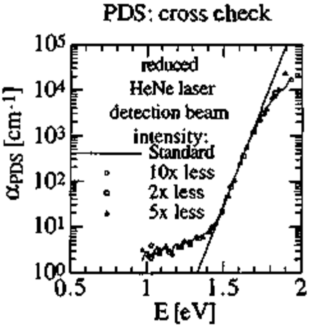

Fig.10: PDS spectra $\alpha_{PDS}(\hbar\omega)$ of an annealed, undoped layer (d = 2.34μm), were the HeNe-laser light intensity was reduced by a factor of 2, 5 and 10. The light intensity was alternatively reduced after passing the sample in order to check the sensitivity of the position detector. The sensitivity limit of the position detector was reached for intensity reductions higher than 10. (sample D190393)

One has to conclude from this section that PDS spectra of different layers can only be compared if their thicknesses are identical, whereas the relative CPM spectra are thickness insensitive over a wide range and can, therefore, be compared more easily.

1.4.2. Dopants dependency of CPM and PDS

Basically three reasons are the motivation to study slightly doped a-Si:H layers: (1) analysis of the Fermi level dependency of CPM, (2) analysis of the degradation behaviour and (3) analysis of the photo conductivity. The results of two independent series of annealed, slightly doped layers will be presented here. Details are given in appendix A2 (see also [Sauvain 93], [Mettler 93/2] and [Mettler 93/3]).

Fig.11 shows the smoothed CPM spectra of the "n-type" and the "p-type" layers of series 2 which are calibrated by PDS and transmission measurements. The Urbach tail is indicated as a straight line with a slope of 51meV. The 50ppm and 100ppm boron-doped layers show a change in the Urbach tail (slope of ~72meV) and a change in the band absorption range as compared to the lower doped layers. Similar results to those in fig.11 are reported for much higher gas dopant ratios in published literature (see e.g. [Street 91]).

In general, a deconvolution (see chapter 3) of the absorption spectra of annealed "n-type" layers leads to the conclusion that the deep defect peak of the standard DOS (see chapter 2) is shifted towards the valence band, whereas for annealed, "p-type" layers the deep defect peak of the standard DOS is shifted towards the conduction band. Different interpretations are given in the published literature for the dopant mechanism and for these deep defect peak shifts (see e.g. [Street 82], [Stutzmann 87], [Kocka 89] and for ref. of the defect pool model see section 2.1.1.).

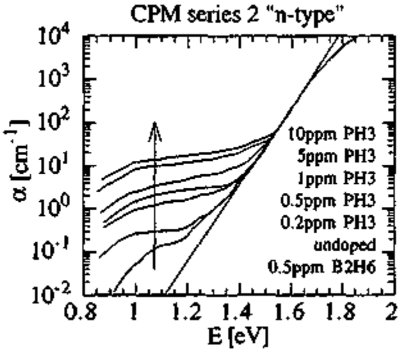

Fig.11a: smoothed CPM spectra $\alpha(\hbar\omega)$ of annealed, "n-type" layers, calibrated by PDS and by transmission measurements. [Mettler 93/3]

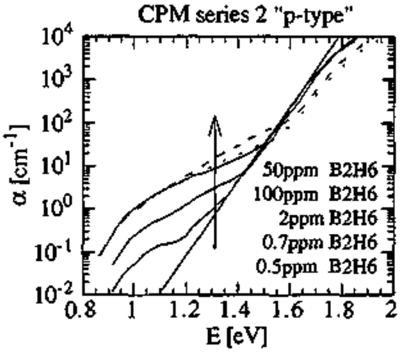

Fig.11b: smoothed CPM spectra $\alpha(\hbar\omega)$ of annealed, "p-type" layers, calibrated by PDS and by transmission measurements. [Mettler 93/3]

There is no direct indication from the CPM spectra of fig.11 whether these spectra are valid or not. However, a comparison to the corresponding PDS spectra indicates that the deep defect absorption values of slightly "p-type" layers - as measured by CPM - are surprisingly high. Fig.12a shows the deep defect absorption values of both series measured by CPM and PDS where the deep defect absorption was measured at a photon energy of 1.2eV for "n-type" layers and at 1.3eV for "p-type" layers. Fig.12b shows the same information schematically. As can be seen in fig.12, CPM **yields a higher deep defect absorption than PDS in the range of slightly "p-type" layers**. For higher doped "p-type" layers, for compensated layers or for "n-type" layers the deep defect absorption values measured by PDS are larger or identical to those measured by CPM. From these measurements one can note that CPM indicates, in a reproducible manner, higher deep defect absorption values than PDS in the range of 2 - 10ppm B_2H_6 doping.

For **"n-type" layers** of both series, the **CPM deep defect absorption value is proportional to the square root of the gas dopant ratio C** (indicated with a straight line in fig.12a). This square root dependency is similar to the one discussed by Street [91] (For the time being, the physical origin of this square-root law is unknown).

The main motivation to carry out an extensive test of CPM measurement conditions (introduced in section 1.2.2.) in the present study, were these annealed, slightly "p-type" layers, where the deep defect absorption values measured by CPM are higher than the corresponding values of PDS. Based on this anomalous situation, the author proceeded to measure the conductivity σ_{tot} and the power law factor γ^* as a function of the generation rate G for three annealed layers: an undoped one, an "n-type" one and a "p-type" layer). Details and results are presented in appendix A2.3. and in section 1.2.2.

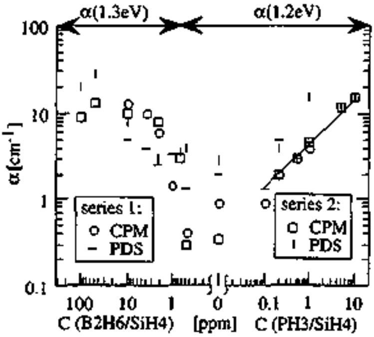

Fig.12a: deep defect absorption values α(1.2eV) for "n-type" layers and α(1.3eV) for "p-type" layers measured by CPM and PDS as a function of the gas dopant ratio C. [Mettler 93/3]

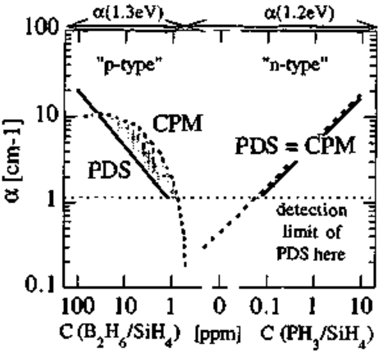

Fig.12b: schematical information of fig.12a.

Concerning the annealed **"p-type" layer**, one has to conclude from these conductivity measurements that **the first and the second CPM condition are not fulfilled** and its CPM spectrum therefore does **not** correspond to the absorption spectrum. However, section 1.2.1b indicates that it is indeed possible to measure the "proper" CPM spectrum of the annealed "p-type" layer if one changes the measurement situation to ensure that $\sigma_{ph} << \sigma_d$ (see fig.4).

Concerning the annealed, undoped and the annealed, **"n-type"** layers, one can note that **the first and the second CPM condition are fulfilled here**, and that the CPM spectrum, in fact, corresponds to the absorption spectrum.

Is it, therefore, necessary to check the CPM measurement condition for each layer? *For practical reasons, the author proposes as a general rule to do this detailed check (regarding the first and the second CPM measurement conditions) only on layers where a large difference in the deep defect absorption values between CPM and PDS has been detected.*

1.4.3. Fermi level dependency of CPM

Firstly, one may note that it is assumed here based on the so-called "standard transport model for a-Si:H" (see chapter 2) that the conductivity at thermal equilibrium (also called dark conductivity σ_d) is related to the Fermi level position E_F - in the same manner as for intrinsic, crystalline semiconductors. One can write: $\sigma_d = \sigma_0 \exp\{-E_a / [kT]\}$.

A value of the prefactor $\sigma_0 = 150$ is claimed to have been found for a-Si:H, both by experiments and by theoretical transport studies [Overhof 89]. With this prefactor it is possible to determine the Fermi level position E_F of any kind of a-Si:H layers after measuring the dark conductivity σ_d.

E_a is the activation energy, which is for "n-type" material $E_a = E_{Cmob} - E_F$ and for "p-type" material $E_a = E_F - E_{Vmob}$ (notation see chapter 2).

Secondly, the standard CPM deconvolution approach assumes that only optical transitions to the band of the majority charge carrier determine the CPM spectrum (see e.g. [Wyrsch 91]). If one uses the standard DOS (see chapter 2), one has to conclude that CPM spectra are indeed very sensitive to the Fermi level position E_F - in contrast to the standard PDS deconvolution approach where "all" optical transitions determine the PDS spectrum (see e.g. [Wyrsch 92]).

Thirdly, the defect pool model (ref. see section 2.1.1.) assumes that the deep defect absorption values depend mainly on the Fermi level position E_F. Indeed, Pierz's CPM measurements [90] on (interstitial?) Li-doped layers have been interpreted in this way. This is in strong contrast to the substitutional dopant theory in a-Si:H (see [Street 82] and [Stutzmann 87]), which shows that the deep defect density is equal to the substitutional dopant density.

Here the author will present the CPM deep defect absorption values of three independent series of layers as a function of the dark conductivity in fig.13a and as a function of the activation energy in fig.13b. "PH_3 series 1" corresponds to the first series of "n-type" layers and "PH_3 series 2" corresponds to the second series of "n-type" layers, both introduced in section 1.4.2. In fig.13 the "n-type" layers of these two series with the lowest dark conductivity, i.e. with the highest activation energy are undoped. "T_S series" corresponds to a series of undoped layers, where the substrate temperature T_S varies between 200°C and 400°C during deposition (see [Kroll 93] and appendix A3).

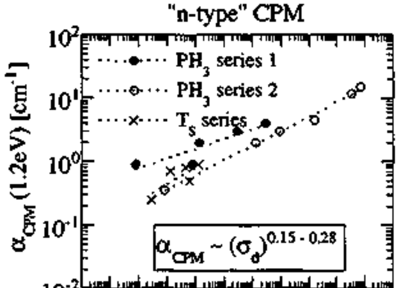

Fig.13a: CPM deep defect absorption values $\alpha_{CPM}(1.2eV)$ for annealed, "n-type" layers as a function of the dark conductivity σ_d.

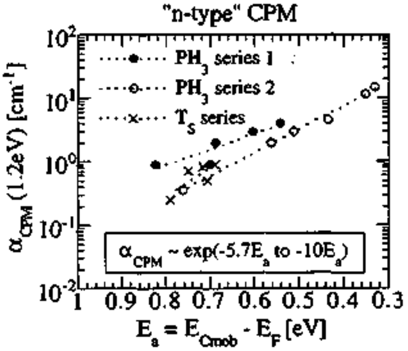

Fig.13b: CPM deep defect absorption values $\alpha_{CPM}(1.2eV)$ for annealed, "n-type" layers as a function of the activation energy E_a, while using $\sigma_d\left[(\Omega\,cm)^{-1}\right] = 150\ \exp(-E_a/[kT])$.

One can observe that an increase in dark conductivity (and a decrease in activation energy) is related to an increase in deep defect absorption values. Further, one recognises that each series can be fitted in a reasonable way (approximately by the law $\alpha(1.2eV) \propto (\sigma_d)^{1/5}$). However, for the two series of "n-type" layers, a substantial shift with respect to each other was observed in fig.13a, whereas no shift with respect to each other was observed in fig.12a ($\alpha(1.2eV) \propto \sqrt{C}$). The "$T_S$ series" on **undoped** layers indicates that dark conductivity and the Fermi level position E_F are also related in a similar way to the CPM deep defect absorption values (shown in fig.13) as they are to the slightly doped samples.

1.4.4. Degradation studies analysed by CPM

As mentioned in the introduction 1.1., the basic aim of the present research on a-Si:H is to determine the deep defect absorption values in the light-soaked, degraded state: Light soaking of an annealed layer leads to an increase in the deep defect absorption and to a decrease in the dark conductivity and in the photo conductivity. There are different physical models which attempt to explain this degradation behaviour (e.g. weak-bond to dangling-bond conversion model by Stutzmann et al. [87] or Street's Hydrogen-induced metastability model [91]), but in fact, the precise physical and chemical mechanisms of the degradation process are not yet understood in such a way that these degradation processes of a-Si:H could be stopped or even eliminated.

a) Selected doped layers

The results of these degradation studies are based on four layers already introduced in section 1.4.2. (series 1: undoped, "n-type" and "p-type" layers). Details on the light soaking procedure and the measured CPM spectra are given in appendix A2.4.

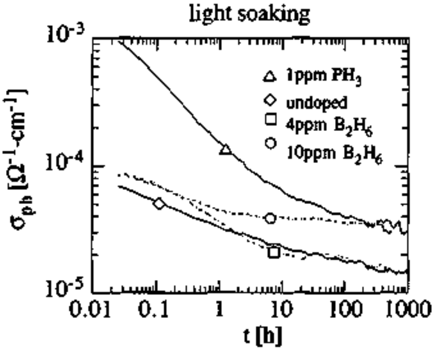

Fig.14a: "photo conductivity" σ_{ph} (under the illumination of a sodium lamp with $I_0 \approx 500 mWcm^{-2}$) as a function of time t (averaged cw-measurement, 50Hz ac-power supply). [Mettler 93/3]

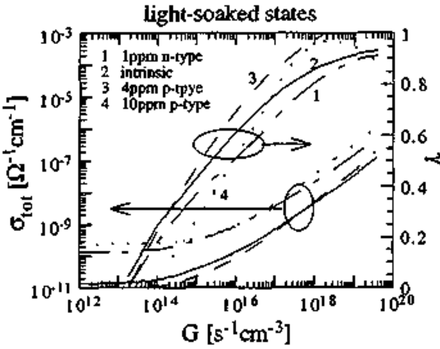

Fig.14b: conductivity σ_{tot} and factor γ^* as a function of the generation rate G of the light-soaked layer (smoothed curves). [Mettler 93/2]

Fig.14a shows the "photo conductivity", as a function of time, under strong illumination by a sodium lamp with I_0 = 500mWcm^{-2} (averaged cw-measurement, 50Hz ac-power supply). One can recognise that **no correlation exists between the first minute degradation kinetics and the final (light-soaked) state** after 1000h. Further, one can see that even after hundreds of hours of light exposure the photo conductivity still decreases. Note that the so-called "saturated state" is related to an equilibrium between annealing and degradation processes, and it is, therefore, dependent on the temperature of the layer and dependent on the intensity of the illumination [Santos 91].

In order to measure the CPM spectra in the final (light-soaked) state, the author first checked the CPM measurement conditions (c.f. section 1.2.2.) remembering that they were not fulfilled for these "p-type" layers in the annealed state (c.f. section 1.4.2.). Fig.14b shows total conductivity and the corresponding power law factor as a function of the generation rate for the four light-soaked layers. Whereas each of these layers showed an **individual "finger print"** for this type of measurements **in the annealed state** (shown in appendix A2.3.), the curves in fig.14b look quite **identical** for these layers **in the light-soaked state**. It seems that the dopant atoms do not influence the power law factor dependency $\gamma^*(G)$ any longer. However, fig.15 indicates that dark conductivity is not identical for these layers in the light-soaked state and that, at least, dark conductivity is still influenced by the dopant atoms. Further, one can note that the first and the second **CPM measurement conditions are fulfilled in the light-soaked state** and that, therefore, the CPM spectra correspond now to the absorption spectra in the light-soaked state.

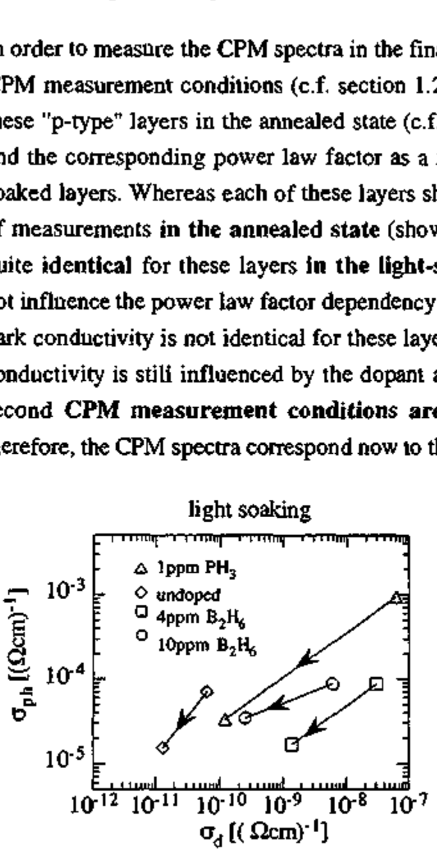

Fig.15a: "photo conductivity" σ_{ph} (deduced from fig.14a) as a function of dark conductivity σ_d in the initial (annealed) and in the final (light-soaked) state. The arrows go from the annealed to the light-soaked state. [Mettler 93/3]

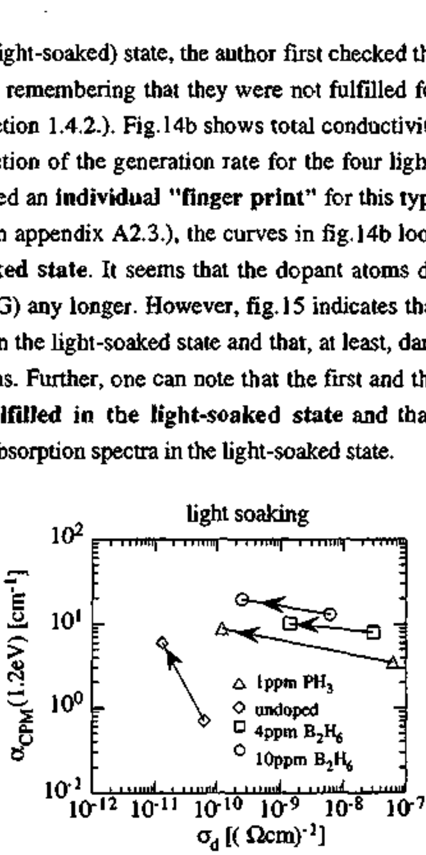

Fig.15b: CPM deep defect absorption values $\alpha_{CPM}(1.2eV)$ as a function of dark conductivity σ_d in the initial (annealed) and in the final (light-soaked) state. The arrows go from the annealed to the light-soaked state. [Mettler 93/3]

Fig.15a shows the "photo conductivity" values (under the illumination of a sodium lamp with I_0 = 500mWcm^{-2}, as deduced from fig.14a) as a function of dark conductivity in the initial (annealed) and the final (light-soaked) state. The corresponding CPM deep defect absorption values as a function of dark conductivity, in the initial (annealed) and the final (light-soaked) state, are shown in fig.15b. Concerning the light-soaked states one can note the following: Fig.15a indicates that the **higher doped layers show a higher photo conductivity** than the other two layers: this observation may (at first sight) give rise to the hope that these doped layers are "better". But fig.15b indicates that the **CPM deep defect absorption value of the undoped layer is lower** than the CPM deep defect absorption value of the doped layers, which indicates that the undoped layer is "better".

In fact, the author argues that the **CPM deep defect absorption values are a better indicator** for the quality of the light-soaked material than photo conductivity. The photo conductivity can be influenced by mono-molecular and bi-molecular recombination processes (see [Stutzmann 91] and [Brandt 91]) at these high intensities and, furthermore, it depends strongly on the occupation of the deep defects [Shah 93]. This explains that the photo conductivity of these layers (c.f. fig.15) is not simply inversely-proportional to the deep defect density nor to the CPM deep defect absorption value (see chapter 2).

Is it even possible to study the **degradation kinetics by CPM**? From the experimental point of view the problems are that the temperature and the occupation during the light soaking process (strong illumination) and during the CPM measurement ("dark conditions") are different. Therefore, a long stabilisation time before measuring CPM remains necessary. Alternatively, Santos et al. [91] introduced a fast in-situ CPM technique (detecting $\alpha_{CPM}(1.15eV) / \alpha_{CPM}(2eV)$) for the study of the CPM degradation kinetics. As an even easier approach, Brandt and Stutzmann [91] introduced the Constant Degradation Method CDM for the study of the degradation kinetics where photo conductivity is kept constant during the light soaking. In fact, the author supposes that these techniques ([Brandt 91] and [Santos 91]) are indeed more reasonable approaches to study degradation kinetics than would be an approach involving the analysis of photo conductivity kinetics: photo conductivity is a "bad" monitor for the degradation kinetics because it is very sensitive to the deep defect occupation [Shah 93].

b) Series with different substrate temperatures during deposition

The results of this degradation study is based on the layers of the substrate temperature series ("T_S series") introduced in section 1.4.2. These layers were light-soaked in the same way as the doped layers (in section 1.4.4.a). Details on the light soaking procedure and the measured absorption spectra are given in appendix A2.4.

Fig.16a shows the CPM and PDS deep defect absorption values of the "T_S series" as a function of dark conductivity in the initial (annealed) and the final (light-soaked) state. The arrow corresponds to the undoped layer shown in fig.15b and goes from the annealed to the light-soaked state. Fig.16b shows the same information as fig.16a, but as a function of the activation energy E_a.

From these figures one can note that (here, at least) the **Fermi level dependency of CPM** in the annealed state (discussed in section 1.4.3.) **disappears in the light-soaked state** (this statement may not necessarily be generally true). Further, one can see that the undoped layer of series 1 shows the same CPM deep defect absorption value as the layers of the "T_S series" whenever these layers were deposited in different deposition chambers. Finally, it has to be noted that **PDS shows, in the light-soaked state, slightly higher deep defect absorption values than CPM** (by a factor of about 2, see fig. A3-4 in appendix A3). Helpful information for further analysis of interpretation of the differences between CPM and PDS (as in the case of annealed layers, see 1.4.1.) would be the thickness dependency of PDS spectra measured on light-soaked layers.

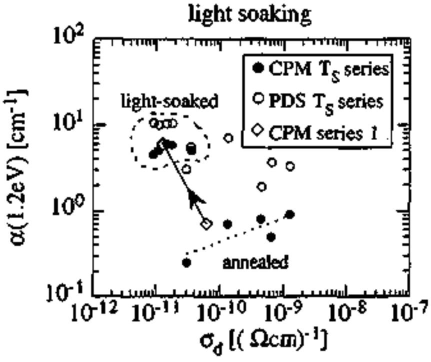

Fig.16a: CPM and PDS deep defect absorption values $\alpha(1.2eV)$ as a function of dark conductivity σ_d in the initial (annealed) and the final (light-soaked) state. The arrow goes from the annealed to the light-soaked state and corresponds to the undoped layer shown in fig.15b.

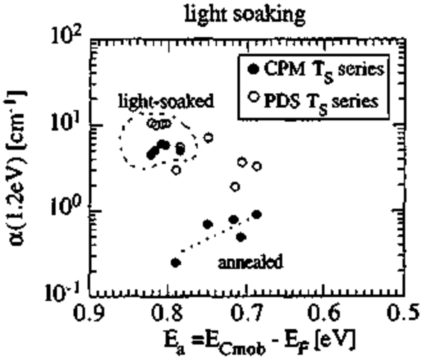

Fig.16b: CPM and PDS deep defect absorption values $\alpha(1.2eV)$ in the initial (annealed) and the final (light-soaked) state as a function of the activation energy E_a, while using $\sigma_d\left[(\Omega\,\mathrm{cm})^{-1}\right] = 150\ \exp\{-E_a / [kT]\}$.

1.4.5. μc-Si layers analysed by CPM

H.N.Liu et al. [93] presented the first CPM measured on an annealed, undoped μc-Si layer and explained the results by a multilayer approach (a-Si:H / c-Si). Here, CPM and PDS spectra of a doped layer of micro-crystalline silicon (μc-Si) will be presented.

Fig.17a shows the PDS spectrum and the transmission measurements of an annealed μc-Si:B layer ("p-type", d = 0.58μm, details see [Prasad 91]), as measured by Prasad and the corresponding

CPM spectrum (measured at $\nu = 13\text{Hz}$ with $I_{CPM} = 76\text{pA}$ and $U = 40\text{V}$ in the lm-mode). Note that the CPM current is more than 10^5 times lower than the dark current ($I_d = 10\mu\text{A}$ at $U = 40\text{V}$).

One recognises a **difference between CPM and PDS** for photon energies below 1.3eV and above 1.8eV, similar to the case of a-Si:H. But **no exponential Urbach tail** is observed for this layer. Fig.17b shows the corresponding Cody-plot, indicating an optical bandgap of 1.5eV (the Cody-plot and the optical bandgap will be introduced in chapter 2). Fig.17c compares the CPM spectrum of fig.17a with the CPM spectrum of H.N.Liu et al. [93] of an undoped μc-Si layer. Below a photon energy of 1.3eV several differences can be observed. However, only further systematic measurements can decide if such spectra are helpful for the understanding of μc-Si.

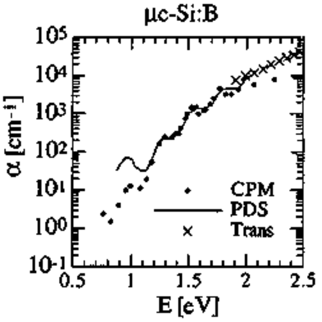

Fig.17a: PDS and CPM spectra $\alpha(\hbar\omega)$ of a μc-Si:B layer calibrated by transmission measurement.
(sample I100890)

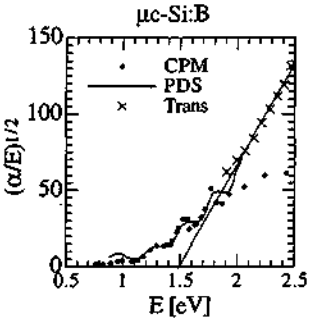

Fig.17b: Cody-plot $\sqrt{\alpha/\hbar\omega}(\hbar\omega)$ of the measurements shown in fig.17a.

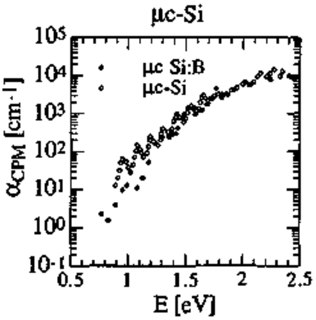

Fig.17c: CPM spectrum $\alpha_{CPM}(\hbar\omega)$ of fig.17a compared to the CPM spectrum $\alpha_{CPM}(\hbar\omega)$ of an undoped μc-Si layer [H.N.Liu 93].

1.5. Absorption measurements on PIN diodes

CPM remains one of the very few possibilities to measure the absorption spectrum on PIN diodes. Especially for the development of solar cells it is of basic interest to have a tool which measures the deep defect absorption values. The main goal of the following analysis is to come to a preliminary decision on whether CPM on PIN diodes has the potential to become a useful tool for the determination of the deep defect absorption in the intrinsic layer of PIN diodes, as in the case of layers. The author will analyse PIN diodes in the annealed state only, as measured under different conditions. Based on the contradictional results of CPM on sandwich-contacted PIN diodes, the author proposes a further CPM configuration for the measurements on PIN diodes, which is closer to the measurements on layers.

1.5.1. Introduction

A PIN diode consists of an undoped a-Si:H layer (i-layer), which is contacted on one side by a heavily doped "n-type" layer (n-layer) and on the other side by a heavily doped "p-type" layer (p-layer). Here, in the case of a thin undoped i-layer (up to 1µm), one will speak of a **PIN solar cell**, and in the case of a thicker undoped i-layer, one will simply speak of a **thick PIN diode**. In a more general way, they will be called PIN diodes here. The following illustrations show the different contact configurations for CPM on a layer and for CPM on a PIN diode:

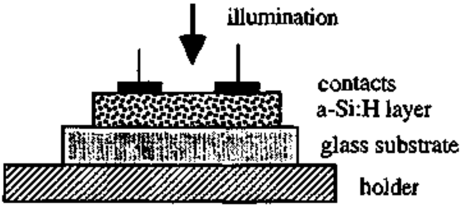

CPM configuration for a layer

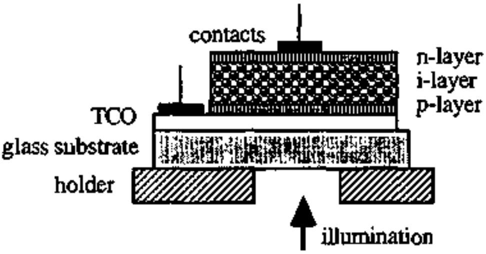

CPM configuration for a PIN diode

One can see that the standard CPM configuration for measurements on a layer is coplanar-contacted, whereas the CPM configuration for the measurements on a PIN diode is sandwich-contacted. The coplanar-contacted standard CPM measurements of layers operate under Ohmic conditions with an electric field of 200V/cm, whereas the sandwich-contacted PIN diodes operate under non-Ohmic conditions with an internal electric field of about 20'000V/cm (typical built-in potential of 1eV). The general complexity of PIN diodes is not discussed here (see e.g. [Fischer 94]). The author restricts himself here to comparing the CPM spectra of PIN diodes to the CPM spectra of layers.

First, the author analysed the current-voltage dependency (I-V measurements) of a thin PIN diode under reverse voltages as in the case of a layer (see section 1.3.4.). Following the notation of section 1.3.4., fig.18a indicates that the <u>dark current</u> I_d does not block ideally: $\xi_d^* = 1$ at 0V (i.e. it is Ohmic-like, rather than blocking) and there is a slight decrease in ξ_d^* with increasing negative voltage. Fig.18b indicates that the <u>total current under illumination</u> I_{tot} is approximately proportional to the square root of the reverse voltage U (this means $\xi^* \approx 0.5$). Therefore, neither the dark current nor the total current under illumination can be described with the help of Ohmic behaviour, nor with the ideal diode equation ($I_d \propto \exp[eU/(kT)] - 1$). Fig.18c indicates that the <u>photo current</u> I_{ph} is voltage independent (Ideal collection: $\xi = 0$).

From these measurements one can conclude that the I-V measurements of a thin PIN diode are different - as measured with lock-in technique (lm-mode: I_{ph} and ξ) or as measured with an electrometer (cw-mode: I_{tot} and ξ^*). But it will be shown that the corresponding CPM spectra - as measured in the cw-mode or in the lm-mode - are identical for an applied voltage of 0V.

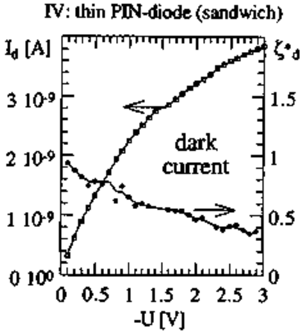

Fig.18a: dark I-V characteristics ($I_d(U)$ and $\xi^*_d(U)$) of a thin PIN-diode. (sample C220590)

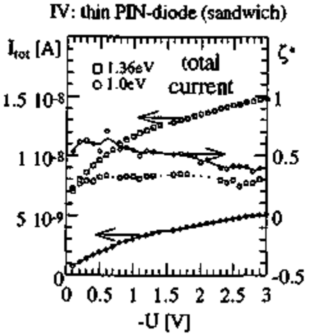

Fig.18b: cw I-V characteristics ($I_{tot}(U)$ and $\xi^*(U)$) of a thin PIN-diode under illumination. (sample C220590)

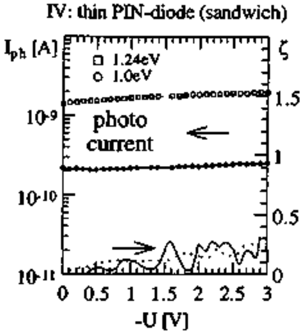

Fig.18c: Im I-V characteristics ($I_{ph}(U)$ and $\xi(U)$) of a thin PIN-diode under illumination. (sample C220590)

1.5.2. CPM measurements on PIN diodes (sandwich configuration)

Fig.19a illustrates a typical CPM spectrum of an annealed solar cell (thin PIN diode with d = 0.7µm) measured at 0V. As in the case of a standard CPM spectrum on a layer one recognises a "band absorption range", an exponential tail absorption range and a deep defect absorption range. No interferences are observed because the substrate (TCO) is strongly textured. Fig.19b shows the same CPM spectrum compared to the standard CPM spectra of three annealed, undoped layers and one annealed, very slightly boron-doped layer ("compensated" sample). One recognises that the three undoped layers show about the same relative CPM spectra whenever they are deposited in three different deposition systems. Further, one can see that a **CPM spectrum of a sandwich-contacted PIN with a buffer-layer is identical to the standard CPM spectrum of a very slightly boron-doped layer** ("compensated" sample).

Can this result be interpreted in a simple way? In a compensated layer electrons and holes contribute to the CPM current, whereas in an undoped or more strungly doped layer only the majority charge carrier determines the CPM current. In a PIN diode both charge carriers also contribute to the CPM current. It looks as if this fact determines the CPM spectrum. But is there an indication that the CPM spectrum - as measured on PIN diodes - corresponds to the absorption spectrum?

In order to test the reliability of such a CPM spectrum on thin PIN diodes, many different measurements were carried out. The corresponding CPM spectra are presented in appendix A5.1. to A5.3. The main results are the following:

CPM on thin PIN diodes with a buffer layer (sandwich configuration):

- Varying the applied voltage from 0V to -3V leads to a slight increase in the deep defect absorption range.
- Varying the applied voltage from 0V to 0.3V leads to identical spectra.
- cw-mode and lm-mode CPM lead to identical spectra at 0V.
- a variation in the chopper frequency between 7 and 33Hz leads to identical spectra.
- CPM-like spectra and PPC ("primary photocurrent") spectra are identical.
- the "band absorption range" measured depends strongly on the CPM current.
- thin PIN diodes all show approximately identical CPM spectra (d = 0.08-0.3μm).

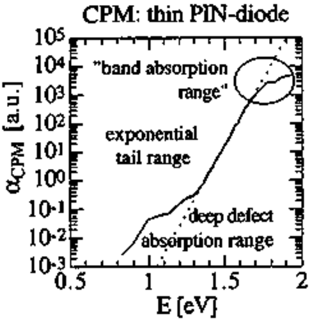

Fig.19a: CPM spectra $\alpha_{CPM}(\hbar\omega)$ measured at 0V of a thin PIN diode with sandwich configuration contacts and with a buffer layer. (sample C220690)

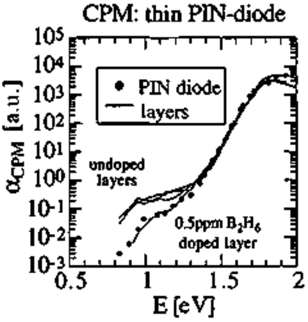

Fig.19b: CPM spectra $\alpha_{CPM}(\hbar\omega)$ of fig.19a compared to different CPM spectra on layers* (all spectra calibrated at $\alpha_{CPM}(1.59eV)=100$ cm^{-1}). (* samples A121090, C021091, D190393, C1803931)

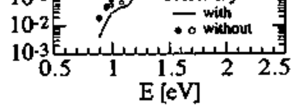

Fig.20a: CPM spectra $\alpha_{CPM}(\hbar\omega)$ measured at 0V of annealed thin PIN diodes* (d = 0.7μm) with and without a buffer layer. (* samples C060891, C090191, C220590)

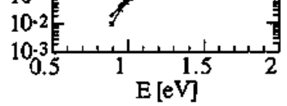

Fig.20b: CPM spectra $\alpha_{CPM}(\hbar\omega)$ measured at 0V of a thin and a thick PIN diode* without a buffer layer. (* samples C060891, B080692)

Fig.20a shows CPM spectra measured at 0V of an annealed, thin PIN diode (d = 0.7μm) with and without a buffer layer. One recognises a slight change in the deep defect absorption range. Further, it can be seen in fig.20a that the CPM spectra in the "band absorption range" are split: therefore the relative CPM spectra of PIN diodes shown here are calibrated in the Urbach tail ($\alpha_{CPM}(1.59eV) = 100\ cm^{-1}$). Fig.20b shows the relative CPM spectra of a thick and a thin PIN diode without a buffer layer, as measured at 0V. One can see that **CPM spectra measured at 0V of two annealed PIN diodes without a buffer layer are identical, independent of their thicknesses** (one is 0.7μm thick and one is 15μm thick).

Can this result be interpreted in a simple way? The fact that the CPM spectra are thickness independent at 0V could mean that they are not related to the internal electrical field. Mittiga et al. [90] showed in their numerical analysis of CPM spectra on thin PIN diodes that the bulk recombination can be neglected. In fact, if the bulk recombination can be neglected, CPM spectra are thickness-independent.

In order to test the reliability of CPM on thick PIN diodes, different measurements were carried out. The corresponding CPM spectra are presented in appendix A5.4. The main results are the following:

CPM on thick PIN diodes (sandwich configuration):

* Increasing the applied voltage from 0V to -100V leads to a pronounced increase in the deep defect absorption range.

* Varying the applied voltage from 0V to 0.2V leads to identical spectra.

* Varying the applied voltage from 0.6V to 1V leads to identical spectra.

* The deep defect absorption values are higher for an applied voltage of 0.6V to 1V than for an applied voltage of 0V to 0.2V.

The origin of this behaviour can be related to the accumulation or the depletion of charge carriers in the i-layer and to the corresponding change in the occupation functions in the i-layer (see section 1.7.).

Remarks:

From an experimental point of view, Rübel et al. [91] found a correlation between the CPM deep defect absorption values on thin PIN diodes and the corresponding fill factor in the annealed state as well as during degradation processes (light-soaking and current injection). Further, CPM deep defect absorption values of thin PIN diodes increase in a similar way to the case of a layer (see published results in fig.A5-5b of appendix A5.5). From this the author concludes that the CPM deep defect absorption value seems to be a reasonable parameter for the characterisation of a PIN diode - independent of the thicknesses - as measured at 0V, whenever the correlation between CPM deep defect absorption values and the corresponding spin density has not been measured yet. In the case of absorption measurements on layers, such correlations allow one to estimate the deep defect density by measuring the deep defect absorption range (see chapter 3).

However, there have been two basic arguments against CPM on PIN diodes lately: Zhou et al. [91] could not find an interdependence between the hydrogen content and the deep defect absorption value measured by CPM with a bias-light. He concluded that CPM was not a useful tool for the characterisation of PIN diodes. But this is not an argument against CPM on thin PIN diodes because CPM and PDS on layers can equally show no dependency on the hydrogen content (see [Kroll 93] and appendix A3). Mittiga et al. [90] argued that CPM on solar cells could underestimate the deep defect absorption value by a factor 2 and he came to the same negative conclusions about CPM on solar cells as Zhou et al. [91]. But the effect of a factor of 2 is only valid if the optical matrix element is very large (see generation mechanisms in chapter 2).

1.5.3. CPM measurements on PIN diodes (coplanar configuration)

Here, the author will introduce a new experimental approach which allows one to measure the absorption spectrum of the i-layer of a thin PIN diode in a similar way to a regular layer.

A thin PIN diode was alternatively contacted on the top with TiAg or on the back with Al. A configuration with flat, non-textured TCO and, alternatively, without TCO was studied. The following illustrations show the different contact configurations for CPM on a coplanar-contacted PIN diode:

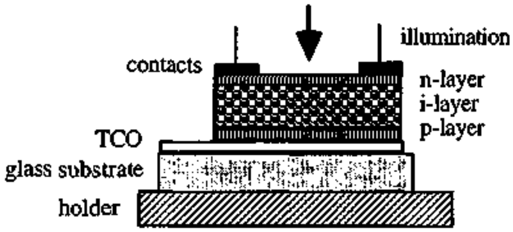

top contacts

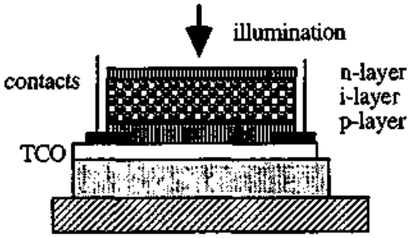

back contacts

Distances of 0.2 and 0.5mm were chosen between the contacts. The doped layers of the PIN diode are so thin (100-200Å) that the coplanar conductivity of the doped layers can be neglected. Furthermore, the doped layers of the PIN are so highly doped that the photo conductivity of the doped layer can also be neglected. The CPM spectra, measured in the lm-mode or in the cw-mode, should, therefore, only be determined by the i-layer.

Fig.21a shows the CPM spectra of a thin PIN diode without TCO with top contacts and with back contacts, measured in the cw-mode with a contact gap of 0.2mm. The applied voltage and the corresponding CPM currents are both indicated. **The CPM spectra measured with coplanar, top and back contacts are approximately identical.**

Fig.21b shows, for the same sample, but with TCO, the CPM spectrum measured in the lm-mode. Here, the contact configuration is identical to the one used for CPM measurements on layers (top contacts: 0.5 x 8mm). This CPM spectrum is compared to the CPM spectrum of a thin undoped layer (shown in fig.12a). The undoped i-layers of these two samples are approximately identical (d = 0.6µm). These figures indicate that the **CPM spectra measured with coplanar contacts are approximately identical for undoped layers and for PIN diodes**. But these spectra do not correspond to the CPM spectra of thin PIN diodes measured in a sandwich configuration.

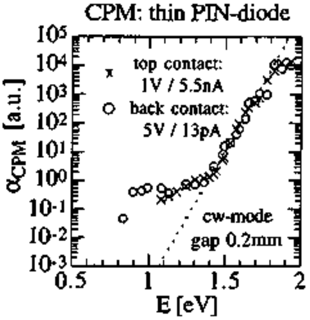

Fig.21a: coplanar CPM spectra $\alpha_{CPM}(\hbar\omega)$ of a thin PIN diode with top or back contacts (no TCO). (sample C120990)

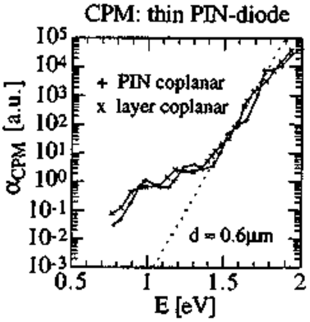

Fig.21b: coplanar CPM spectra $\alpha_{CPM}(\hbar\omega)$ of fig.21a compared to CPM of a thin undoped layer. (samples C120990, C091189)

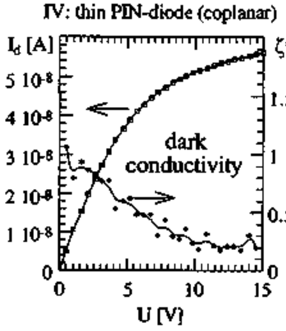

Fig.22a: dark I-V characteristics ($I_d(U)$ and $\xi^*_d(U)$) of a thin PIN-diode with coplanar contacts. (sample C120990)

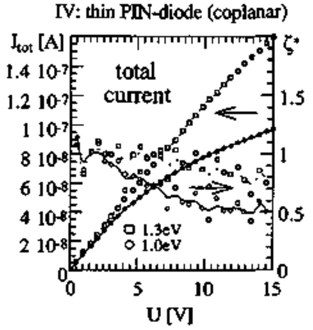

Fig.22b: cw I-V characteristics ($I_{tot}(U)$ and $\xi^*(U)$) of a thin PIN-diode with coplanar contacts under illumination. (sample C120990)

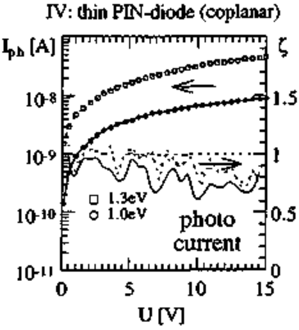

Fig.22c: lm I-V characteristics ($I_{ph}(U)$ and $\xi(U)$) of a thin PIN-diode with coplanar contacts under illumination. (sample C120990)

In order to understand this result, the author analysed the current-voltage dependency (I-V measurements) of this thin, coplanar-contacted PIN diode. Following the notation of 1.3.4., fig.22a indicates that the dark current I_d does not block ideally: $\xi^*_d = 1$ at 0V (Ohmic-like) and, furthermore, ξ^*_d decreases with increasing voltage U. Fig.22b indicates that the total current under illumination I_{tot} is approximately Ohmic-like for low voltages U (this means $\xi^* \approx 1$) and, furthermore, ξ^* decreases with increasing voltage U. Fig.22c indicates that the photo current I_{ph} is Ohmic-like (this means $\xi = 1$) over a wide voltage range, in strong contrast to a sandwich-contacted PIN diode with $\xi = 0$ (= ideal collection).

The author gives the following interpretation on these I-V measurements. The dark current I_d of a thin, coplanar-contacted PIN diode (fig.22a) is identical to a thin PIN diode with sandwich contacts (fig.18a). Therefore, the coplanar part of the dark current can be neglected, whereas the transversal part of the dark current dominates. The thin, coplanar-contacted PIN diode works, in this voltage range, without illumination just as two diodes would, one of which alternatively being "blocked". The following two possibilities correspond to the front and back contact configurations:

dark:

or

In contrast, the photo current I_{ph} of a thin, coplanar-contacted PIN diode (fig.22c) is approximately identical to a coplanar-contacted layer (Ohmic-like, c.f. fig.7c). Therefore, the coplanar part of the photo current dominates, whereas the transversal part of the photo current can be neglected. The thin, coplanar-contacted PIN diode can be described as an intensity-dependent photo resistance:

illumination:

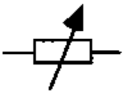

A possible interpretation for the behaviour of the photo current I_{ph} is that the internal field is screened under illumination by photo generated charge carriers in the i-layer located close to the interface of the doped layers (see section 1.7.).

Concerning CPM measurements on a coplanar-contacted PIN diode in the lm-mode, one can understand that this spectrum corresponds to the CPM spectrum of a coplanar-contacted layer because both configurations show an Ohmic behaviour under illumination (see fig.22a and fig.7c). Note that Vanecek [91/1] has pointed out that CPM measurements operate only under Ohmic conditions in a reliable manner.

The author intuitively concludes that CPM spectra measured on coplanar-contacted PIN diodes are less related to the internal field than CPM spectra measured on sandwich contacted PIN diodes, and that CPM spectra measured on coplanar-contacted PIN diodes are much closer to the original CPM approach than CPM spectra measured on sandwich contacted PIN diodes. However, some further measurements are required in order to examine this approach.

1.6. Absorption measurements on layers and on PIN diodes

Section 1.4. presented absorption measurements on layers, whereas section 1.5. introduced absorption measurements on PIN diodes. In contrast, this section will present CPM measurements as a function of the measurement temperature, in the presence of a bias light and while illuminating the sample with the pump beam from the front side or the back side. All these measurements are traced out on layers and on PIN diodes in order to compare them.

1.6.1. Temperature dependency of CPM

It is an established practice to study the absorption spectrum of a-Si:H layers at different temperatures. What is reported in published literature are mainly CPM measurements at temperatures below room temperature: Nonomura et al. [93] analysed PDS spectra at T = 77K and found that the absorption of the substrate (Corning 7059) limits the deep defect absorption range of PDS. Pierz et al. [87] measured CPM spectra on doped samples at T = 100K, with the result that the CPM deep defect absorption values are much lower than the corresponding PDS values measured at T = 300K. Sladek et al. [93] measured CPM values of $\alpha_{CPM}(\hbar\omega = 0.6\text{eV}) \approx 10^{-4}\text{cm}^{-1}$ at T = 77K. Stradins et al. [93] found identical CPM deep defect absorption values at T = 4K and at T = 300K, but also much lower values at T = 80K. The physical meaning of the CPM deep defect absorption minimum measured at around T≈80K on annealed a-Si:H is contradictional. Checking the CPM measurement conditions (introduced in section 1.2.2.) remains necessary for these CPM spectra, but also for the CPM measurements presented hereunder.

The author analysed CPM spectra measured at temperatures above room temperature. The measurement set-up used here did not allow him to determine CPM spectra at low temperatures in a reasonable way. CPM spectra measured at high temperatures contain information about the annealing mechanism.

a) Layers

Three layers (i.e. an undoped, an "n-type" and a "p-type" layer) were selected for these measurements. Details of these measurements and all CPM spectra are presented in appendix A4. Unfortunately, there was no possibility to calibrate the CPM spectrum of each sample in the absolute scale with transmission measurements at different temperatures. Fig.23a shows the CPM spectra of the undoped, annealed sample as "calibrated" in the Urbach tail ($\alpha_{CPM}(1.59\text{eV}) = 100$ cm^{-1}) and fig.23b shows the same CPM spectra as "calibrated" in the deep defect absorption range ($\alpha_{CPM}(1.13\text{eV}) = 0.075\ \text{cm}^{-1}$). Fig.23a would correspond to a decrease in the deep defect absorption range with increasing temperatures. Fig.23b would correspond to a shrinkage of the band gap with increasing temperatures and to a constant deep defect absorption range. A shrinkage of the band gap with increasing temperatures is expected for undoped a-Si:H (see e.g. [Street 91]). The doped samples show similar behaviour patterns but the missing, absolute calibration of these CPM spectra prevents a detailed analysis (especially for doped samples).

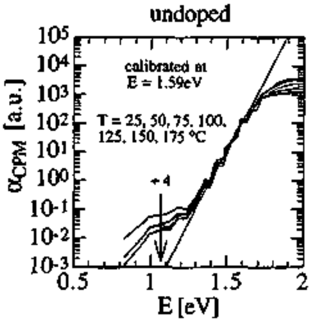

Fig.23a: CPM spectra $\alpha_{CPM}(\hbar\omega)$ of an annealed, undoped layer as "calibrated" in the Urbach tail (α_{CPM}(1.59eV) = 100 cm^{-1}). (sample C021091)

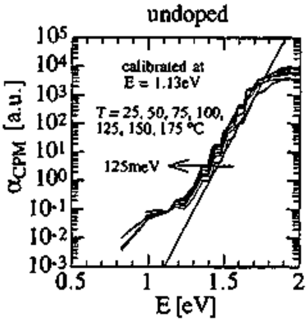

Fig.23b: CPM spectra $\alpha_{CPM}(\hbar\omega)$ of an annealed, undoped layer as "calibrated" in the deep defect absorption range (α_{CPM}(1.13eV) = 0.075 cm^{-1}). (sample C021091)

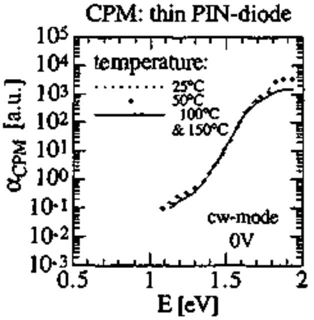

Fig.24a: CPM spectra $\alpha_{CPM}(\hbar\omega)$ of a thin, sandwich-contacted PIN diode at U = 0V as "calibrated" in the Urbach tail (α_{CPM}(1.59eV] = 100 cm^{-1}). (sample C220690)

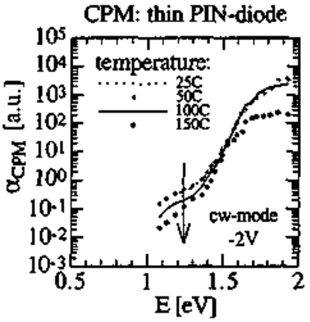

Fig.24b: CPM spectra $\alpha_{CPM}(\hbar\omega)$ of a thin, sandwich-contacted PIN diode at U = -2V as "calibrated" in the Urbach tail (α_{CPM}(1.59eV) = 100 cm^{-1}). (sample C220690)

b) A thin, sandwich-contacted PIN diode

A thin, sandwich-contacted PIN diode was selected for these measurements. Here, there was also no possibility to calibrate the CPM spectrum in the absolute scale with transmission measurements at different temperatures. Fig.24 shows the CPM spectra of the thin, sandwich-contacted PIN diode as "calibrated" at α_{CPM}(1.59eV) = 100 cm^{-1}. Fig.24a was measured at U = 0V and fig.24b at U = -2V. Fig.24b would correspond to a decrease in the deep defect absorption range with increasing temperatures, as in the case of a layer (fig.23a). Alternatively, the measurements at U = -2V of fig.24b could also be "calibrated" in the deep defect absorption range (e.g. α_{CPM}(1.13eV) = 0.075 cm^{-1}), with the result that the situation would correspond to a shrinkage of the band gap with increasing temperatures and to a constant deep defect absorption range, as in the case of a layer (fig.23b). But - completely surprising - **the CPM spectra of the thin, sandwich-contacted PIN diode at U = 0V shows no change in the CPM spectra with increasing temperatures** (fig.24a). This may indicate that the argument of a shrinkage of the bandgap is not very helpful here. The missing absolute calibration also precludes a detailed analysis here.

1.6.2. CPM measurements with a bias light

As an additional experiment, CPM spectra have been measured by the author with a monochromatic bias light of 1.85eV photon energy. These measurements correspond to the dual-beam technique, but the photo current is kept constant here (the set-up used here operates in the CPM-mode). The motivation to use the dual-beam technique was mentioned in section 1.2.2. The influence of a bias-light on CPM and on PDS is analysed for different configurations.

Whereas the PDS spectra measured on a layer are insensitive to a bias-light (fig.25b), all CPM spectra measured on different configurations are sensitive to a bias-light: the CPM deep defect absorption range changes due to the bias-light in the case of an undoped layer (fig.25a), in the case of a thin, sandwich-contacted PIN diode (fig.26a) and in the case of a thin, coplanar-contacted PIN diode (fig.26b).

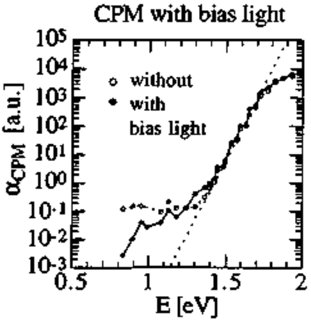

Fig.25a: CPM spectra $\alpha_{CPM}(\hbar\omega)$ of the same annealed, undoped **layer** measured with and without a red bias light: cw-mode and lm-dual beam-mode (ν = 13Hz). (sample C021091)

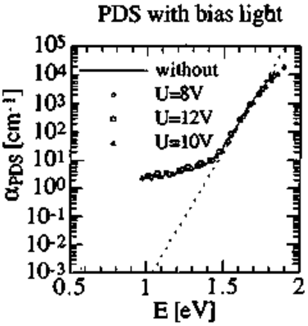

Fig.25b: PDS spectra $\alpha_{PDS}(\hbar\omega)$ of the same annealed, undoped **layer** measured with and without a red bias light. U correspond to the voltage of the 100W halogen lamp. (sample C021091)

Basically, the origin of these changes can be caused by a change in the deep defect occupation (= different optical transitions = different absorption) or by a change in the generation-recombination paths (see also section 1.7.3d). PDS measurements could, in principle, help decide which mechanism dominates. Indeed, if one could exclude that the PDS spectrum of fig.25b is determined by surface states, one could then conclude that the differences observed between CPM without and with bias light are only caused by different recombination paths. Unfortunately, this cannot be excluded here (i.e. one is not sure whether the PDS spectra of fig.25b are partially influenced by surface states or not; to clarify this point, PDS measurements on a whole thickness series would be required).

However, the author still suggests that a change in the recombination paths - which is also related to a change in the occupation [Shah 93] - is the origin of the changes in the CPM spectra: It seems to be **an experimental fact that a bias-light leads to an increase in the deep defect absorption range - independent of the sample configuration.**

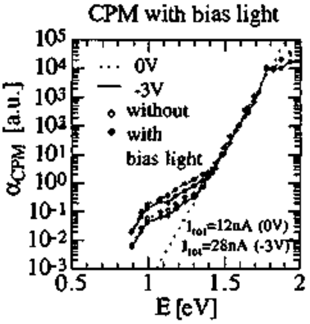

Fig.26a: CPM spectra $\alpha_{CPM}(\hbar\omega)$ of a thin, **sandwich-contacted PIN diode** measured with and without a red bias light. (textured TCO). (sample C220590)

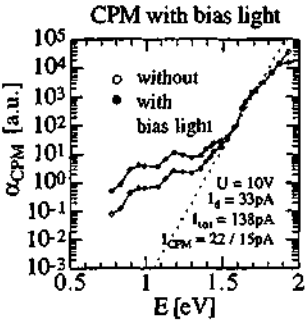

Fig.26b: CPM spectra $\alpha_{CPM}(\hbar\omega)$ of a thin, **coplanar-contacted PIN diode** measured with and without a red bias light. (flat TCO). (sample C120990)

1.6.3. "Front" and "Back" CPM spectra

One normally measures CPM spectra on layers by illuminating the sample from the front side ("front" CPM) with the monochromatic light of the pump beam. The author additionally measured CPM spectra illuminating the sample from the back side ("back" CPM) with monochromatic light. The configurations of "front" CPM and "back" CPM are the following (for a layer):

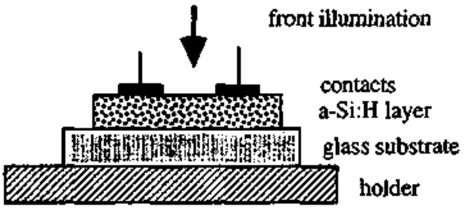

"front" CPM

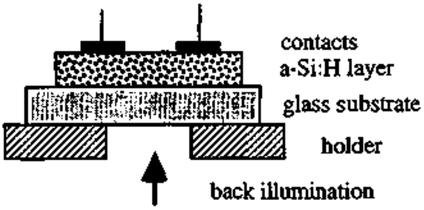

"back" CPM

a) Layers

Four layers introduced in section 1.4.2. (series 1: undoped, "n-type" and "p-type") were chosen. In the annealed state, no changes in the deep defect absorption range are found between "front" and "back" CPM, also for doped samples. This result is in contrast to the prediction of Hoheisel et al. [91] that the reflection of the contacts in the "front" CPM mode influence the deep defect absorption range. Note that because of this "prediction", Hoheisel et al. [91] proposed to measure CPM in the "back" CPM mode. On the other hand, Asano et al. [93] observed changes in the deep defect absorption range between "front" and "back" CPM, which they interpreted as the influence of surface states on the CPM spectrum.

As will be shown in section 1.7.2., some differences in the deep defect absorption range between "front" and "back" CPM could be observed, but only during the non-uniform degradation of these samples. This means, as far as the author is concerned, that a **non-uniform defect distribution** (e.g. non-uniformly grown layer) may be at the origin of the differences, observed here and elsewhere [Asano 93].

In contrast to the deep defect absorption range, the "band absorption range" shows a strong variation between "front" and "back" CPM, as can be seen in fig.27a. As mentioned in 1.4.1., the "band absorption range" is limited by the uniform absorption condition $\alpha d \approx 1$. De Vore [56] showed that the range of non-uniform absorption ($\alpha d \geq 1$) is in general determined by diffusion processes and by surface recombination. A detailed analysis of these measurements observed would, therefore, be complex.

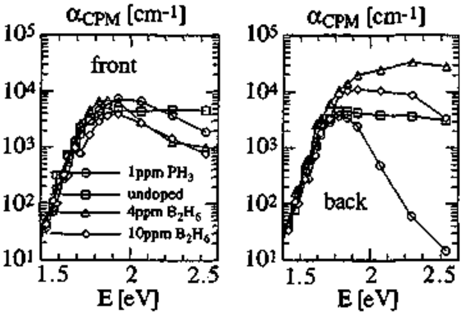

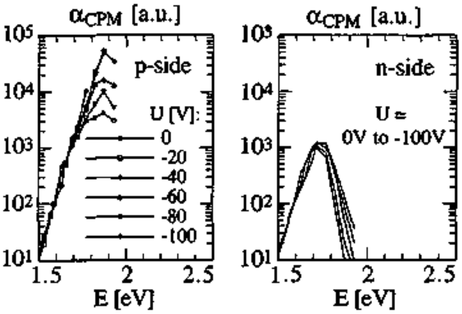

Fig.27a: "Front" and "back" CPM spectra $\alpha_{CPM}(\hbar\omega)$ ($\hbar\omega$ = 1.5 - 2.5eV) for four annealed, slightly doped and undoped layers (notation identical for both graphics). (samples C270991, C211091, C021091, C041291)

Fig.27b: "Front" and "back" CPM spectra $\alpha_{CPM}(\hbar\omega)$ ($\hbar\omega$ = 1.5 - 2.5eV) of an annealed, thick PIN diode as a function of the applied voltage U. (sample B080692)

b) A thick, sandwich-contacted PIN diode

Further, the author measured the "front" and "back" CPM spectra on a thick PIN diode as a function of different reverse voltages U (see appendix A5.4.). The most surprising result appears in the "band absorption range". Fig.27b shows this range, where all CPM spectra are "calibrated" at $\alpha_{CPM}(1.59eV) = 100\ cm^{-1}$. Illumination from the n-layer side of this PIN diode leads to a pronounced maximum at 1.7eV (corresponding to $\alpha d = 1.5$), which is quite independent of the applied voltage. Illumination from the p-layer side also leads to a maximum at 1.7eV but it is not related to αd. One of the reasons for this could be that the "calibration" was wrong here. Another reason could be instead that this variation (between "front" and "back" CPM spectra) under non-uniform illumination is related to the difference in the mobility values and in the charge carrier collection (the author tends to favour this second explanation). However, the detection of an **exponential Urbach tail** at $U = -20V$ **over 5 orders of magnitude** (as found here) is indeed surprising (see also appendix A5.4.).

The author concludes from these measurements on layers and on a thick PIN diode that "front" and "back" CPM spectra should in principle be identical in the deep defect absorption range and in the exponential tail range up to $\alpha d \approx 1$. Otherwise there seem to be some problems with the CPM technique, which may be caused by non-uniform defect distributions (e.g. non-uniformly grown layers).

1.7. CPM measurements on "partial" diodes

As new configurations, the author analysed some "partial" diodes (i.e. a part of a PIN diode). An i-layer was alternatively contacted by an n-layer or by a p-layer and these configurations were coplanar-contacted, as in the case of a single layer. The two configurations used are called "n-i" and "p-i" and look as follows:

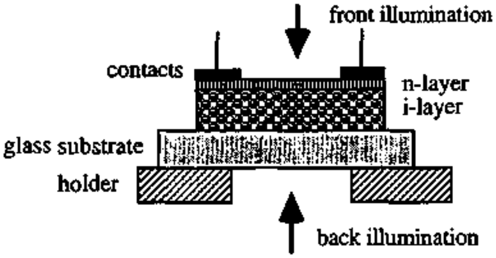

"n-i" configuration

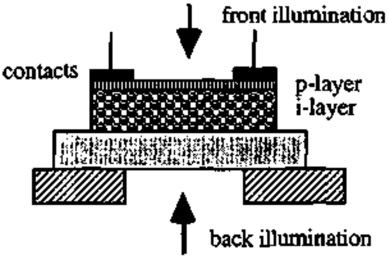

"p-i" configuration

The elements of these configurations are identical to the elements of a PIN diode. Nevertheless, the configurations resemble some Thin Film Transistor structures (TFT) without a Gate-electrode and "channel effects" may also be expected. Details of these samples are given in appendix A6.

1.7.1. CPM measurements on annealed "partial" diodes

Fig.28a shows the calibrated CPM spectra of the "partial" diodes with two different i-layer thicknesses. No differences can be observed between the two i-layer thicknesses. Some cross check measurements are presented in appendix A6. One can recognise that the "n-i" configuration shows higher deep defect absorption values than the "p-i" configuration.

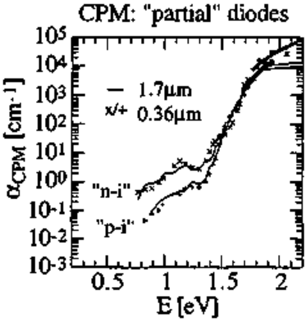

Fig.28a: "front" CPM spectra $\alpha_{CPM}(\hbar\omega)$ of the annealed, "n-i" and "p-i" configuration with different i-layer thicknesses.

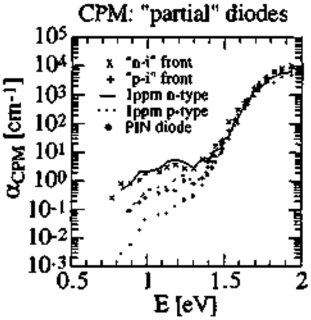

Fig.28b: "front" CPM spectra $\alpha_{CPM}(\hbar\omega)$ of the annealed, "n-i" and "p-i" configuration compared to other CPM spectra (see text).

Fig.28b compares the CPM spectra of these configurations with other CPM spectra. It can be seen that the CPM spectra of these configurations are not related to the CPM spectra of a sandwich-contacted PIN diode measured at U = 0V. But it can be found that the CPM spectrum of the **"n-i" configuration is almost identical to the CPM spectrum of a slightly "n-type" layer** (1ppm PH_3). Further, the CPM spectrum of the **"p-i" configuration is also almost identical to the CPM spectrum of a slightly "p-type" layer** (1ppm B_2H_6). Before proceeding to analyse these results, the author proposes to present the results of inhomogeneous degradation experiments.

1.7.2. Inhomogeneous degradation studies

As a next step, the inhomogeneous degradation behaviour of these "n-i" and "p-i" configurations will be studied. As a cross check, an "n-type" layer and an undoped layer were also degraded with the same procedure. The samples were degraded **from the back side** successively with blue, green, orange and red light of a filtered 100W halogen lamp (48 hours for each wavelength). The corresponding CPM spectra were measured between each change in the wavelength in the "front" CPM mode as well as in the "back" CPM mode. The following illustration shows the inhomogeneous degradation cycle:

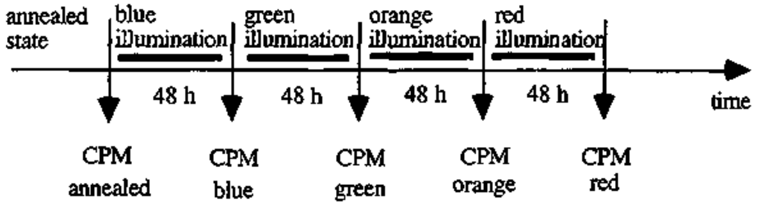

The "inhomogeneous degradation cycle"

a) Layers

Fig.29a shows the "front" and "back" CPM deep defect absorption values of an "n-type" and an undoped layer as a function of the inhomogeneous degradation cycles. One can recognise a pronounced difference between "front" and "back" CPM after the blue degradation. After the red degradation the differences between "front" and "back" CPM have disappeared. This confirms that a **non-uniform defect distribution** can indeed be the origin for differences between "front" and "back" CPM spectra (discussed in section 1.6.3.).

Further, one can see in fig.29a that the "n-type" sample shows a lower relative change in the deep defect absorption values than the undoped sample. But the absolute deep defect absorption values of the "n-type" layer are higher before and after this degradation procedure than that of the undoped layer. This result corresponds to the degradation behaviour of these samples with a sodium lamp (c.f. fig.15b and discussion in section 1.4.4.a).

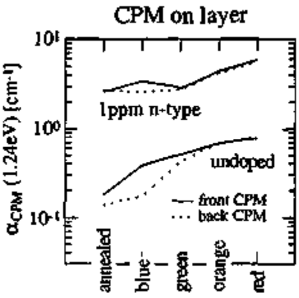

Fig.29a: "front" and "back" CPM deep defect absorption values α_{CPM}(1.2eV) of an "n-type" and an undoped layer as a function of the inhomogeneous degradation cycle (see text).

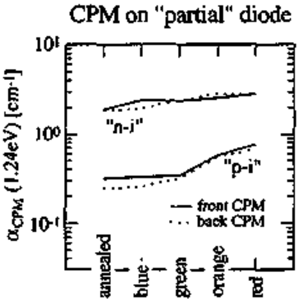

Fig.29b: "front" and "back" CPM deep defect absorption values α_{CPM}(1.2eV) of "n-i" and "p-i" configurations as a function of the inhomogeneous degradation cycle (see text).

b) "Partial" diodes ("n-i" and "p-i" configuration)

Fig.29b shows the "front" and "back" CPM deep defect absorption values of "n-i" and "p-i" configurations as a function of the inhomogeneous degradation cycle. One can recognise a slight difference between "front" and "back" CPM after the blue degradation. After the red degradation, these differences have also disappeared. **The "n-i" configuration shows no important increase in the CPM deep defect absorption value** - in contrast to the "n-type" layer in fig.29a. The "p-i" configuration shows a similar increase in the CPM deep defect absorption value as the undoped layer in fig.29a.

1.7.3. Interpretations

The author will present a very simple picture, which can explain in a qualitative way some results observed on "partial" diodes and on coplanar-contacted PIN diodes.

a) "Partial" diodes ("n-i" and "p-i" configuration)

An i-layer on top of a heavily doped layer is expected to act as a diode here. However, a diode is usually contacted in a sandwich configuration. The way of contacting the samples presented here leads, therefore, to something like a "transversally contacted diode". Because the doped layers are very thin, one can expect the doped layers to be depleted (fixed atomic space charge of the dopants). The corresponding charge carriers (electrons in the case of the "n-i" configuration and holes in the case of the "p-i" configuration) can diffuse into the i-layer as driven by the internal field of the diode. The expected behaviour can be shown as follows:

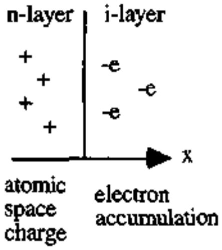

"n-i" configuration

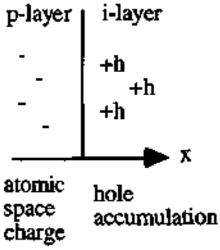

"p-i" configuration

In this picture, the CPM spectra of the "n-i" ("p-i") configuration is measured in the bulk of the undoped i-layer, which is accumulated by the electrons (holes) of the doped layers. These electrons (holes) act as majority charge carriers of the CPM current. At the same time, these electrons (holes) change the occupation of the deep defects and the optical transition behaviour, both of which can influence the CPM spectrum. **In this picture the CPM spectra measured on these "partial" diodes are determined by the accumulation of electrons or of holes in the i-layer.** It is assumed here that a change in the occupation leads to a change in the recombination paths in such a way that the CPM spectra change. Note that the author argued in the same way for the case of dual beam-CPM spectra (see section 1.6.2.).

Note: Hoheisel et al. [91] observed an increase in the CPM deep defect absorption values while using a heavily doped n-layer between the coplanar metal contacts and the undoped i-layer. This behaviour may also be understood in terms of the picture proposed for the "partial diodes": the n-layers of the contacts lead to an accumulation of electrons in the bulk material between the contacts.

b) Coplanar-contacted PIN diode

This simple picture can also explain why the accumulation of electrons and holes is much less pronounced in the case of thin, coplanar-contacted PIN diodes:

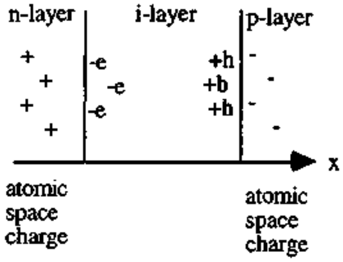

PIN configuration A

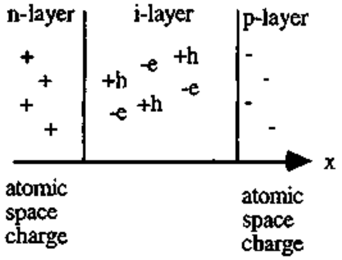

PIN configuration B

In a PIN diode the internal electrical field is large. Therefore, the accumulation of electrons and holes is located close to the interface (PIN configuration A). This could explain that the CPM spectrum of a coplanar-contacted PIN diode is identical to the CPM spectrum of an undoped layer. Alternatively, the accumulation of electrons could also be compensated by the accumulation of holes (PIN configuration B) in such a way that the i-layer looks undoped.

c) Limits of this simple picture

It is clear that an accumulation of charge carriers influences the Fermi level position E_F (at thermal equilibrium). In this sense, CPM spectra are expected to be sensitive to the Fermi level position E_F. Instead of an accumulation of charge carriers in the i-layer, a contamination by dopant atoms in the i-layer might also be possible, but would influence the Fermi level position E_F (at thermal equilibrium) in a similar way.

However, this simple picture cannot explain why the "n-i" configuration does not degrade under light-soaking (fig.29b) and also why the conductivity dependency $\sigma_{tot}(G)$ of both "partial" diodes in the annealed state (fig.A6-3 in appendix A6) looks similar to the conductivity dependency $\sigma_{tot}(G)$ of strongly light-soaked layers (fig.14b).

d) Homogeneous material without dopant atoms

The experimental part of this study ends here. The following, theoretical and numerical parts (chapter 2 and chapter 3) are based on a homogeneous material without dopant atoms and effects of charge carrier accumulation are neglected in principle. It will generally be assumed that the material is neutral. But for some specific cases, the Fermi level position E_F will be taken as a free parameter - with the result that the charge neutrality is hurt for a given DOS. In a certain sense, these specific cases correspond to the accumulation of charge carriers (or to a contamination by dopant atoms).

One of the questions to be answered will be whether the measured absorption spectra corresponds to the absorption spectra at thermal equilibrium. Even for a homogeneous material without dopant atoms the author sees **two main situations which can cause problems**:

situation (1): different optical transitions:
absorption spectrum at thermal equilibrium ≠
absorption spectrum at steady-state equilibrium =
measured spectrum

situation (2): sensitivity to the generation - recombination paths:
absorption spectrum at thermal equilibrium =
absorption spectrum at steady-state equilibrium ≠
measured spectrum

Situation (1) corresponds to the influence of the pump beam and can in principle be present for any absorption measurement techniques (here: CPM, dualbeam technique or PDS), whereas situation (2) is related to absorption measurement techniques which detect a photo current (here: CPM and dualbeam technique).

In chapter 2 the model of a-Si:H for a numerical analysis will be presented and the generation-recombination mechanisms for sub-band-gap illumination will be discussed, whereas in chapter 3 a numerical analysis of CPM and PDS will be presented and discussed. It will be found (for the case of a homogeneous material without dopant atoms) that PDS is not touched by these two situations (1 and 2) and detects the absorption spectrum, whereas CPM can quite simply correspond to situation (2) - corresponding to the violation of the CPM measurement conditions introduced in section 1.2. It is evident that these results will be related to the a-Si:H model used.

2. Analytical studies and definitions for numerical calculations

The main goal of this chapter is to introduce the elements for the numerical calculations of conductivity and of absorption at thermal equilibrium as well as of conductivity and generation rate at the steady-state equilibrium. This will lead to the numerical analysis of CPM and PDS in chapter 3. Further, some important questions pertaining to the analytical analysis of a-Si:H will be discussed here.

2.1. The standard density of states (DOS)

In this section the standard density of states (DOS) of amorphous hydrogenated silicon (a-Si:H) is introduced, since it will be used in the following study. It consists of a parabolic conduction band (CB) and a parabolic valence band (VB), an exponential conduction band tail (CBT), an exponential valence band tail (VBT) and one Gaussian-shaped defect peak. These deep defects are usually called "dangling bonds" (DB) in amorphous semiconductors. The parabolic bands (in the DOS) are described by effective DOS masses, which are helpful parameters to define the band bending. The connection between the parabolic bands and the exponential tails is discussed explicitly, and some new conditions for this connection are proposed.

2.1.1. General remarks

The following analysis is based on the standard DOS of a-Si:H (see e.g. [Overhof 91]). However, some more complex DOS models exist, as e.g. the defect pool model, which contains several peaks of deep defects with a finite correlation energy (see e.g. [Bar-Yam 86], [Smith 89], [Winer 90], [Schumm 93]). In order to analyse CPM and PDS, not only the deep defects, but also the tail states are of importance. Concerning the tail states in a-Si:H, Street [91] writes: "The precise relation between the structural disorder and the band tail shape remains unclear." In the standard DOS model of a-Si:H - used here - the exponential tails are part of the DOS.

Fig.1 shows a general picture of the standard DOS of a-Si:H in the logarithmic scale: one recognises the parabolic conduction band (CB) and the parabolic valence band (VB), the exponential conduction band tail (CBT) and the exponential valence band tail (VBT) and the Gaussian peak of the deep defects ("dangling bonds" DB). So far, the mobility gap as well as the connection between the band states and the band tail states has not been discussed very clearly in published literature (see e.g. [Cody 84]). Fig.2 shows the standard DOS of a-Si:H in the linear scale where the (optical) bandgap is indicated. The different elements of the standard DOS will be introduced in the following sections and are shown in fig.1 and fig.2; their mathematical formulations are given in appendix B1.

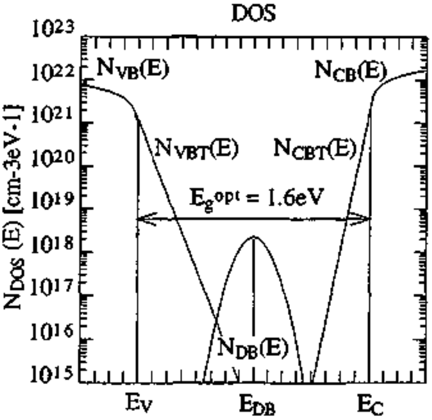

Fig.1: the standard DOS of a-Si:H in the logarithmic scale.

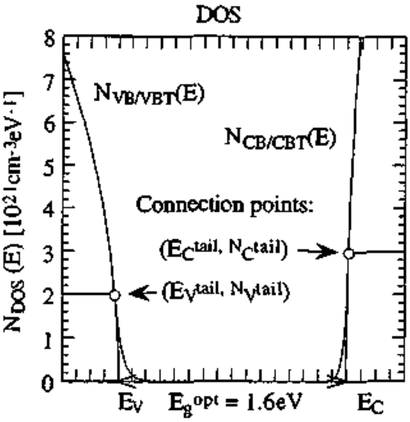

Fig.2: the standard DOS of a-Si:H in the linear scale.

2.1.2. The parabolic conduction and valence bands

Describing the conduction band and the valence band of amorphous semiconductors by parabolic bands is quite established. In order to describe the bending of these parabolic bands, the author suggests using the effective DOS masses because, when parabolic bands are used, the effective DOS masses are defined a priori. The advantage is that a comparison to the case of crystalline semiconductors is possible although the parabolic band approach in crystalline semiconductors is only valid near the band edges and although the general theoretical meaning of effective masses in amorphous semiconductors is still a topic of research [Kivelson 79]. A further advantage of these effective DOS masses in amorphous semiconductors is that asymmetrical bands can be studied in a simple way. In order to describe the conduction and the valence bands the author has followed the terminology of crystalline semiconductor physics (see e.g. [Kireev 75]):

The DOS of the parabolic conduction band $N_{CB}(E)$ and the DOS of the parabolic valence band $N_{VB}(E)$ have the same parabolic behaviour as the DOS of the free electrons N(E). But the electron rest mass m_e is replaced by the so-called effective DOS mass for electrons $\breve{m}_e^*$ in the conduction band and for holes $\breve{m}_h^*$ in the valence band (not to be confounded with the effective transport mass or the effective cyclotron mass also present in crystalline semiconductor physics). The bandgap is defined as $E_g \equiv E_C - E_V$. In the case of amorphous semiconductors it corresponds to the so-called "optical bandgap" E_g^{opt}. E_C is the edge of the parabolic conduction band and E_V is the edge of the parabolic valence band as shown in fig.2. N_C^0 and N_V^0 control the bending of the parabolas (c.f. appendix B1). In this sense, one may call N_C^0 and N_V^0 the bending parameters of the parabolic bands. The bending parameter is a function of the effective DOS mass and vice versa.

2.1.3. The exponential conduction and valence band tails

The DOS of the exponential conduction band tail $N_{CBT}(E)$ and the DOS of the exponential valence band tail $N_{VBT}(E)$ are determined by the characteristic tail slopes E_C^0 and E_V^0. The point (E_C^{tail}, N_C^{tail}) of the CBT and the point (E_V^{tail}, N_V^{tail}) are the connection points where the exponential tails are connected to the parabolic bands (see fig.2). The author suggests here that the slope of the parabolic band and the exponential tail should be identical at the connection points. This condition is, at least for the valence band, supported by absorption measurements, where so far no discontinuity has been observed between the band absorption range and the Urbach tail range. Together with this second condition, the connection point can be expressed in terms of the characteristic tail slope and the bending parameters. The DOS of the exponential valence band tail $N_{CBT}(E)$ and the DOS of the exponential conduction band tail $N_{VBT}(E)$ can then be expressed in terms of the characteristic tail slopes (E_C^0 and E_V^0) and the bending parameters of the parabolic bands (N_C^0 and N_V^0).

2.1.4. The DOS of the conduction and valence band

The DOS of the conduction band $N_{CB/CBT}(E)$ and the DOS of the valence band $N_{VB/VBT}(E)$ are either parabolic or exponential, depending on the energy (see fig.2). Hereafter, these states will also be called (delocalised) band states and (localised) band tail states (c.f. section 2.2.2.).

2.1.5. The dangling bond peak

In the standard DOS model, the deep defects (dangling bonds) are distributed in the form of a Gaussian curve. This deep defect peak $N_{DB}(E)$ is defined by the total (integrated) density of **defects** N_{DB}^{tot}, by the middle energy of this peak E_{DB} and by the half-width of this peak W_{DB}. Other functions have also been proposed in order to describe this peak (e.g. Lorentz-functions). Other DOS models of amorphous silicon use two independent (donor-like and acceptor-like) defect peaks. Here it is assumed that these deep defects correspond to dangling bond defects with a finite correlation energy U, which have three possible electron states: non-occupied, single-occupied or double-occupied.

2.2. Transport and charge neutrality at thermal equilibrium

This section introduces the standard transport model of amorphous hydrogenated silicon (a-Si:H), which will be used hereafter. Further, the mobility gap and the effective DOS are introduced and defined. Finally, it has been found that the charge neutrality of the dangling bonds is only fulfilled if the Fermi level is located at $E_F = E_{DB} + U/2$.

2.2.1. Introduction

The two basic transport mechanisms in amorphous semiconductors are multiple trapping and hopping. The overview below shows, on the left, the multiple trapping mechanism of an electron in an electrical field: the localised (immobile) electron can be emitted into a delocalised (mobile) state above a mobility edge (defined in section 2.2.2.). In a delocalised state, the electron can move in the electrical field until it is captured by another localised state. Note that the mobility edge is neither necessarily identical to the band edge (E_C or E_V) nor necessarily identical to the connection points (E_C^{tail} or E_V^{tail}). For electrons at thermal equilibrium, the localised states above the Fermi level E_F act as trapping states and below as recombination states (vice versa for holes at thermal equilibrium). The concept of the mobility edge is typical for amorphous semiconductors (see [Mott 79]).

The overview below shows, on the right, the hopping transport mechanism for electrons. The electrons jump from one localised state to another localised state (tunnelling). The energy of the electron is always lower than the mobility edge energy. By symmetry, one finds the same situation for holes, as shown for electrons in the figure below.

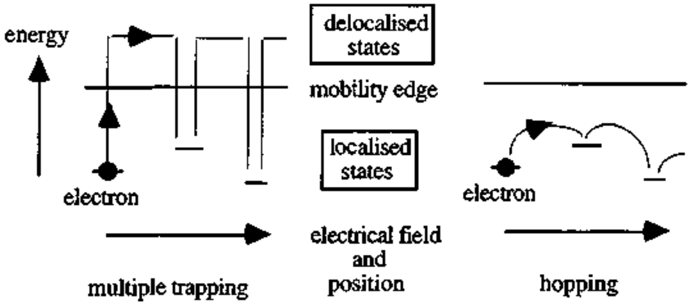

Overview: multiple trapping and hopping transport mechanism.

The mechanism which dominates in amorphous semiconductors has led to a controversy. Mott and Davis [79] assume that at room temperature the multiple trapping mechanism is valid for both charge carriers, whereas at low temperature the hopping mechanism is valid for both charge carriers. Overhof and Thomas [89] as well as Thomas [93] predict that at room temperature the electrons follow the multiple trapping mechanism, whereas the holes follow the hopping mechanism: in this theory the slope of the exponential tails is the parameter which allows to distinguish between the two mechanisms. As a third possibility, Kosarev [93] thinks that even at room temperature the hopping mechanism is dominant for both charge carriers.

Conductivity at thermal equilibrium is only defined for Ohmic conditions. In the case of carrier injection, of asymmetrical illumination, of diffusion processes or of any kind of time-dependent currents, the classical form of Ohm's law is violated. The Ohmic conductivity in amorphous semiconductors is assumed here to have the same structure as in a classical, non-degenerated crystalline semiconductor $\sigma = e\{\mu_e n + \mu_h p\}$.

In the case of multiple trapping, n and p are the charge carrier densities in the bands outside the mobility gap and μ_e and μ_h are the average mobilities at the mobility edges. In the case of hopping, n and p are the charge carrier densities at the average hopping energy ("hopping edge"), with the average hopping mobilities at the average hopping energy [Thomas 93].

At room temperature the experimentally deduced mobilities (at the mobility edges) of a-Si:H are some orders of magnitude lower than in c-Si, e.g. approx. $\mu_e = 10\ \mathrm{cm}^2/(\mathrm{Vs})$ and $\mu_h = 1\ \mathrm{cm}^2/(\mathrm{Vs})$ [Vaillant 86].

This asymmetry can have many origins, but is not surprising considering the asymmetry of the exponential tails or even considering some asymmetrical parabolic bands - as in a crystalline semiconductor. But this asymmetry is not supported by the disorder theory of amorphous materials [Anderson 75] where a full symmetry of the conduction and valence band DOS, of the mobilities at the mobility edges and of the charge carrier masses ($\breve{m}_e = \breve{m}_h = m_e$) is predicted [Thomas 93]. The low mobility values are assumed to be caused by the disorder in the amorphous structure, in strong contrast to crystalline semiconductor physics.

In this study, which is restricted to room temperature, the multiple trapping mechanism is assumed to be present and dominant for both charge carriers. The different elements of the conductivity are introduced in the following sections and are shown in fig.3 and fig.4; the mathematical formulations are given in appendix B2.

2.2.2. The mobility gap and the conductivity

The DOS introduced in 2.1. can be split into three parts: above the mobility edge of the conduction band E_{Cmob}, the electron states are delocalised and the corresponding charge carriers (density n) contribute to the current with a finite mobility $\mu_e > 0$. Below the mobility edge of the valence band E_{Vmob}, the hole states are also delocalised and the corresponding charge carriers (density p) also contribute to the current with a finite mobility $\mu_h > 0$. Thus, the conductivity is given as $\sigma = e\{\mu_e n + \mu_h p\}$. The mobilities are assumed to be constant for the delocalised charge carriers. The energy difference in the two mobility edges is called mobility gap $E_g^{mob} \equiv E_{Cmob} - E_{Vmob}$. Within the mobility gap, the mobility of both charge carriers is assumed to be zero ($\mu_e = \mu_h = 0$) because these states are localised and because hopping is neglected.

The mobility edge of the conduction band is defined to be relative to the origin of the parabolic conduction band as $E_{Cmob} \equiv E_C + \varepsilon_c$. The mobility edge of the valence band is defined to be relative to the origin of the parabolic valence band as $E_{Vmob} \equiv E_V - \varepsilon_v$. The parameters ε_c and ε_v are called threshold energies here. Thus, the difference between the mobility gap and the optical bandgap is given as $E_g^{mob} - E_g^{opt} = \varepsilon_c + \varepsilon_v$.

The DOS at the mobility edges are noted as N_{Cmob} and N_{Vmob}. The DOS of the delocalised conduction band states are noted as $N_C(E)$ and the DOS of the localised conduction band tail states as $N_c(E)$. The DOS of the delocalised valence band states are noted as $N_V(E)$ and the DOS of the localised valence band tail states as $N_v(E)$. The deep defect states with $N_{DB}(E)$ are assumed to be always localised. In the approach studied here, the mobility edges can be different from the connection points of the DOS, which distinguish between parabolic band states and the exponential tail states.

It is assumed here that the threshold energies (ε_c, ε_v) and the mobilities (μ_e, μ_h) are each identical in the case of thermal equilibrium conductivity and in the case of steady-state conductivity.

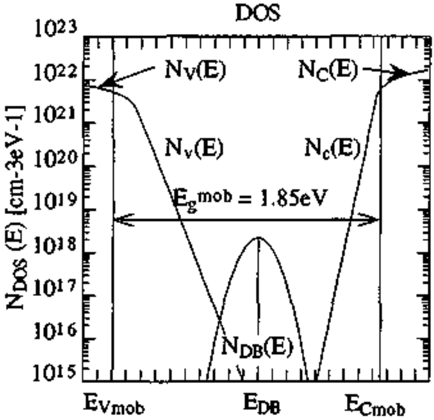

Fig.3: notations for the mobility gap in the DOS (logarithmic scale).

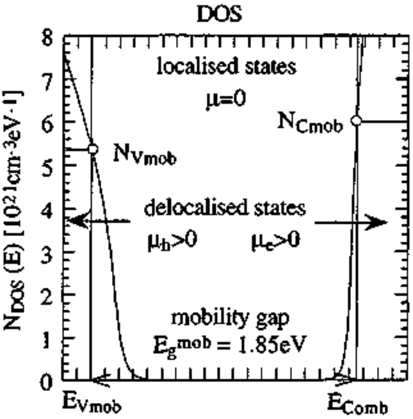

Fig.4: notations for the mobility gap in the DOS (linear scale).

2.2.3. The conductivity at thermal equilibrium

The conductivity is given as $\sigma = e\{\mu_e n + \mu_h p\}$. At thermal equilibrium, the charge carrier densities n and p are determined by the Fermi function f(E). If the threshold energies (ε_c, ε_v) are positive, the charge carrier densities are proportional to the effective DOS N_{Cmob}^{eff} and N_{Vmob}^{eff}, which are related to the parameters of the parabolic bands in a simple way. The corresponding equations are shown in appendix B4. For the numerical calculations the charge carrier densities at thermal equilibrium are calculated by the approach shown in approach B2.

2.2.4. The charge neutrality at thermal equilibrium

The total charge density $Q_{tot}(E_F)$ of a given DOS at thermal equilibrium is only a function of the Fermi level E_F. The combination of the standard DOS with the mobility gap leads to six partial charge densities:

$$Q_{tot}(E_F) = p + p_t + N_{DB}^{+} - n - n_t - N_{DB}^{-}$$

n and p are the charge carrier densities of the delocalised band states, n_t and p_t are the charge densities of the localised band tail states, N_{DB}^- and N_{DB}^+ are the charged dangling bond densities. The charge densities of the localised band tail states (n_t and p_t) are calculated by the Fermi function f(E) here. The charge densities of the dangling bonds are calculated by the occupation functions $f^+(E)$, $f^0(E)$ and $f^-(E)$, which were introduced by Schweitzer et al. [81] for the case of thermal equilibrium. The author would like to point out that the charge neutrality of the dangling bonds is fulfilled only if

$$N_{DB}^+ = N_{DB}^- \quad \Leftrightarrow \quad f^+(E) = f^-(E) \quad \Leftrightarrow \quad E_F = E_{DB} + U/2$$

This means that the position E_{DB} of the dangling bond peak and the corresponding finite correlation energy U determine the Fermi level E_F (details see appendix B5). If the charge neutrality of the dangling bonds is fulfilled, the total charge density is determined by the charge in the exponential valence band tail: $Q_{tot}(E_F) \cong p_t$. On the other hand, if the charge neutrality of the dangling bonds is not fulfilled, the total charge density can be larger by several orders of magnitude (details see appendix B5).

On the one hand, the Fermi level E_F is assumed to be a free parameter in published literature's discussion of the dangling bond occupation functions (see e.g. [Adler 76]) as well as in the analysis of the standard DOS occupation at thermal equilibrium (see e.g. [Wyrsch 92], [Favre 94/1]). On the other hand, the total charge density Q_{tot} has to be zero from the physical point of view. If this is not the case, it indicates that the standard DOS model is incomplete. In fact, a lot of impurities, which may act as dopants, are present in "undoped" a-Si:H (see e.g. [Kroll 93]). The case of charge carrier accumulation is discussed in section 1.7.3., corresponding to an inhomogeneous situation. However, the author has kept the standard DOS as simple as possible (no additional dopant peaks; homogeneous material without dopant atoms).

2.3. The absorption

This section introduces the absorption concept based on the joint density of states (JDOS). Here, the case is studied where localised-to-localised state transitions are suppressed. This leads to several new aspects for the determination of the optical bandgap. For the case of defects with a finite correlation energy (dangling bonds), the equivalence of the one-peak picture and the two-peak picture is shown. Further, it has been found that the transitions pertaining to the charged dangling bond states have to be multiplied by a factor of 2, while using their occupation functions.

2.3.1. Introduction

The absorption $\alpha(\hbar\omega)$ of a photon $\hbar\omega$ leads to a change in the quantum mechanical electron state. In terms of the momentum operator **P** or of the dipole operator **R** one can write (see e.g. [Ley 84]):

$$\alpha(\hbar\omega) \propto \sum_i \sum_j \left|\langle i|\mathbf{P}|j\rangle\right|^2 \delta\left(E_i - E_j - \hbar\omega\right) \qquad \text{with } \mathbf{P} = \frac{im}{\hbar}[\mathrm{H},\mathrm{R}]$$

(E_i energy of the occupied electron states; E_j energy of the non-occupied electron states)

In amorphous material, the absorption coefficient $\alpha(\hbar\omega)$ is then given in terms of the joint density of states (JDOS) $J(\hbar\omega)$ (see e.g. [Jackson 85]):

$$\alpha(\hbar\omega) = C_0\, \hbar\omega\, R^2\, J(\hbar\omega) \qquad \text{with } C_0 \equiv \frac{(2\pi)^2}{n_0} \frac{e^2}{\hbar c_0} \frac{1}{3\rho_A}$$

or

$$\alpha(\hbar\omega) = C_1 \frac{P^2}{\hbar\omega} J(\hbar\omega) \qquad \text{with } C_1 = C_0 \frac{\hbar^4}{m_e^2}$$

with

$$J(\hbar\omega) \equiv \int N_{occ}(E)\, N_{non}(E + \hbar\omega)\, dE \propto \sum_i \sum_j \delta\left(E_i - E_j - \hbar\omega\right)$$

n_0 is the refraction index, ρ_A is the atomic density and $e^2 / \hbar c_0 = 1/137$ is the fine structure constant. Because of different transitions, the proportional factors C_0 and C_1 are different in the case of c-Si [Jackson 85]. $N_{occ}(E)$ corresponds to the occupied electron states and $N_{non}(E)$ to the non-occupied electron states.

Which of the two optical matrix elements should be assumed to be constant in energy? Tauc et al. [66] suggested to fix the average square momentum matrix element P^2, whereas Cody [84] and Jackson et al. [85] proposed to set the average square dipole matrix element R^2. As long as no reasonable microscopic model exists, which can explain the absorption physics of a-Si:H, one may use either of them. But if for any reason the effective DOS masses, which describe the bending of the parabolic bands, act in a-Si:H in a similar way to crystalline semiconductors, these effective DOS masses have to be introduced into the proportional factor C_1. Due to this uncertainty, the author will use the average square dipole matrix element R^2 and the proportional factor C_0 hereafter. The different elements of the absorption will be introduced in the following sections, their mathematical formulations are given in appendix B2.

2.3.2. The transition types

The mobility edges E_{Cmob} and E_{Vmob} split the DOS into three regions with "alternatively" delocalised or localised states. Depending on the photon energy $\hbar\omega$, four different transition types are possible, here called A, B, C, D:

transition A:	delocalised valence band state $N_V(E)$	->	delocalised conduction band state $N_C(E)$
transition B:	delocalised valence band state $N_V(E)$	->	localised state
transition C:	localised state	->	delocalised conduction band state $N_C(E)$
transition D:	localised state	->	localised state

Each of these transitions increases the energy of an electron by the energy of one photon (direction of the arrows). Jackson et al. [85] have shown that transitions A, B and C have the same probability in a-Si:H. **Hereafter, the author will drop transition** D, because it can be assumed that **localised-to-localised transitions are much less probable** than the other transition types. Further, it is assumed that the charge carrier densities (n and p) are much smaller than the DOS of the delocalised conduction and valence bands ($N_C(E)$ and $N_V(E)$).

The following picture shows these transition types:

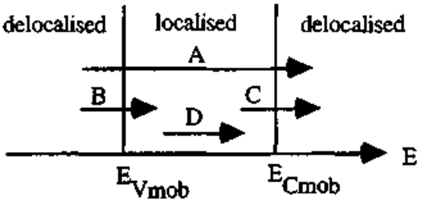

2.3.3. The band absorption and the optical bandgap

In this section, only the parabolic bands $N_{CB}(E)$ and $N_{VB}(E)$ are assumed to be present, which are each split into delocalised states ($N_C(E)$, $N_V(E)$) and localised states ($N_c(E)$, $N_v(E)$), as shown in fig.5.

If the optical bandgap is equal to the mobility gap ($E_g^{opt} = E_g^{mob}$ with $\varepsilon_c = \varepsilon_v = 0$), only the transitions of type A are possible and the JDOS $J(\hbar\omega)$ is given as:

$$J(\hbar\omega) = J_A(\hbar\omega) = \int_{E_C-\hbar\omega}^{E_V} dE\, N_V(E)\, N_C(E+\hbar\omega) = N_C^0\, N_V^0\, \frac{\pi}{8}(E_g^{opt} - \hbar\omega)^2$$

In this case, the JDOS $J(\hbar\omega)$ is proportional to the square of the difference between the optical bandgap and the photon energy: $J(\hbar\omega) \propto (E_g^{opt} - \hbar\omega)^2$. For a crystalline semiconductor with an indirect bandgap one gets the same dependency when replacing the photon energy by either the sum of the photon energy and the phonon energy or their difference [Kireev 75].

With an experimental measurement of the absorption spectrum $\alpha(\hbar\omega)$, the optical bandgap E_g^{opt} can then be determined with the help of $z_0(\hbar\omega) \equiv \sqrt{\alpha(\hbar\omega)/\hbar\omega}$:

$$z_0(\hbar\omega) \propto E_g^{opt} - \hbar\omega \qquad \text{and } E_g^{opt} = \hbar\omega \;\Leftrightarrow\; z_0(\hbar\omega) = 0$$

$z_0(\hbar\omega)$ is called the Cody-plot in the case of a-Si:H [Cody 84]. If the mobility gap is larger than the optical bandgap ($E_g^{mob} > E_g^{opt}$) and if the optical matrix elements of all transitions A, B, C and D are equal, one gets the same result for the JDOS $J(\hbar\omega)$ and $z_0(\hbar\omega)$.

In contrast, the author points out that, if the mobility gap is larger than the optical bandgap ($E_g^{mob} > E_g^{opt}$) but the transitions D are suppressed (see fig.5), the band absorption is proportional to the square of the difference between the optical bandgap and the photon energy **only** for $\hbar\omega \geq E_g^{mob}$:

$$\alpha(\hbar\omega) \propto (E_g^{opt} - \hbar\omega)^2 \qquad \text{for } \hbar\omega \geq E_g^{mob}$$

$$z_0(\hbar\omega) \propto E_g^{opt} - \hbar\omega \qquad \text{for } \hbar\omega \geq E_g^{mob}$$

The energy E_g^* with $z_i(\hbar\omega) = 0$ does not correspond in this case to the optical bandgap E_g^{opt} (see fig.6). But the measured curve $z_0(\hbar\omega)$ with $\hbar\omega \geq E_g^{mob}$ can be extrapolated in order to determine the optical bandgap E_g^{opt}, as shown in fig.6.

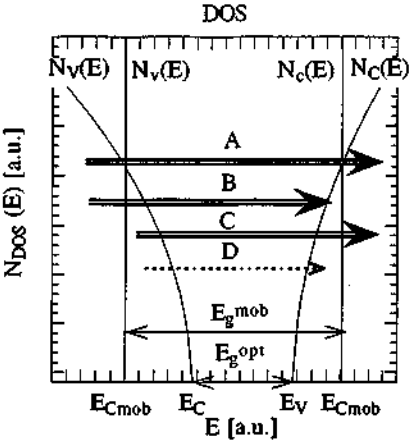

Fig.5: the two parabolic bands in the linear scale and transitions A, B, C and D for a specific situation.

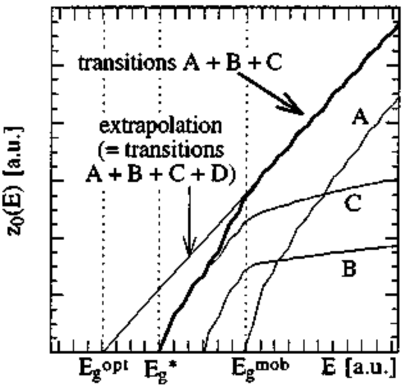

Fig.6: function $z_0(\hbar\omega)$ and transitions A, B and C for a specific case.

2.3.4. The transitions of the dangling bonds

For a defect **with** a finite correlation energy, four transitions of types B and C are possible, whereas for a defect without a finite correlation energy, two transitions of types B and C are possible only. In the case of dangling bond defects with one (Gaussian) DOS peak $N_{DB}(E)$ at E_{DB}, it is usual to use a two-peak picture in order to describe the following four transitions [Okamoto 77] and the corresponding chemical reactions:

		D → CB:	VB → D:
peak $D^{0/+}$ at E_{DB}	with $N_{DB}(E)$:	$D^0 + \hbar\omega \rightarrow D^+ + e$	$D^+ + \hbar\omega \rightarrow D^0 + h$
peak $D^{0/-}$ at E_{DB}+U	with $N_{DB}(E-U)$:	$D^- + \hbar\omega \rightarrow D^0 + e$	$D^0 + \hbar\omega \rightarrow D^- + h$

Transition: two-peak picture: one-peak picture:

$D^0 \rightarrow CB$:

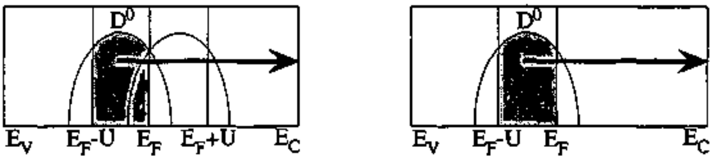

$$J^{C0}(\hbar\omega) = \int_{E_C-\hbar\omega>E_F-U}^{E_F} dE\, N_{DB}(E)\, N_C(E+\hbar\omega)$$

$VB \rightarrow D^+$:

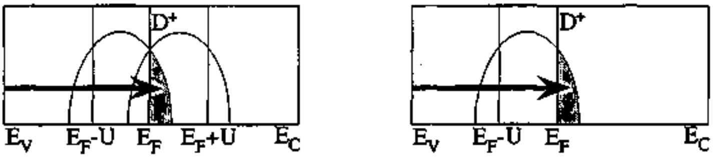

$$J^{V+}(\hbar\omega) = 2\int_{E_F}^{E_V+\hbar\omega} dE\, N_{DB}(E)\, N_V(E-\hbar\omega)$$

$D^- \rightarrow CB$:

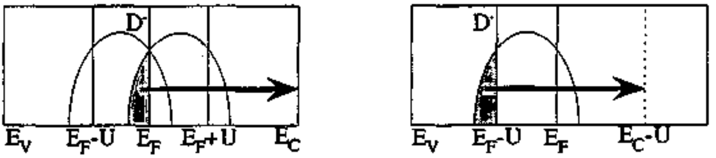

$$J^{C-}(\hbar\omega) = 2\int_{E_C-\hbar\omega}^{E_F} dE\, N_{DB}(E-U)\, N_C(E+\hbar\omega) = 2\int_{E_C-\hbar\omega-U}^{E_F-U} dE\, N_{DB}(E)\, N_C(E+\hbar\omega+U)$$

$VB \rightarrow D^0$:

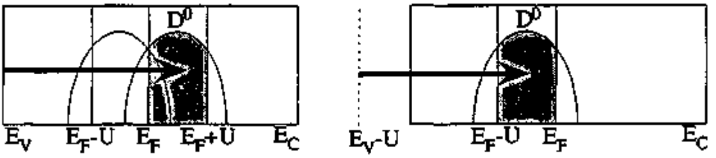

$$J^{C0}(\hbar\omega) = \int_{E_F}^{E_V+\hbar\omega<E_F+U} dE\, N_{DB}(E-U)\, N_V(E-\hbar\omega) = \int_{E_F-U}^{E_V+\hbar\omega-U<E_F} dE\, N_{DB}(E)\, N_V(E-\hbar\omega+U)$$

Overview 1: two-peak picture and one-peak picture (equations for T=0K).

The advantage of the one-peak picture, which is proposed hereafter, is obvious when one uses the occupation functions of the dangling bonds:

$$N^{+}_{DB}(E) = f^{+}(E)\, N_{DB}(E) \quad N^{0}_{DB}(E) = f^{0}(E)\, N_{DB}(E) \quad N^{-}_{DB}(E) = f^{-}(E)\, N_{DB}(E)$$

Overview 1 shows the one-peak picture and the two-peak picture. The JDOS values of the four possible transitions are independent of these two pictures and are presented in overview 1 for the case of T=0K at thermal equilibrium, where the dangling bond occupation functions turn out to be step functions. The first two transitions are independent of the picture chosen, whereas the second two transitions depend on it: in the two-peak picture, the defect peak is shifted by the finite correlation energy, whereas in the one-peak picture, it is not the defect peak which is shifted, but the border of the bands.

Note that the joint DOS of the charged dangling bonds $J^{V+}(\hbar\omega)$ and $J^{V-}(\hbar\omega)$ have to be multiplied by a factor of 2 because the occupation functions of the dangling bonds $f^{+}(E)$, $f^{0}(E)$ and $f^{-}(E)$ vary only between 0 and 1 (probability), but the dangling bond defects are occupied by 0, 1 or 2 electrons (see overview 1). **In published literature, this factor 2 has been omitted erroneously so far in the determination of the absorption.**

2.3.5. The absorption of the standard DOS

In the case of the standard DOS (introduced in section 2.1.), while taking into account a mobility gap (introduced in section 2.2.), the absorption coefficient $\alpha(\hbar\omega)$ is given as

$$\alpha(\hbar\omega) = C_0\, \hbar\omega\, R^2\, J(\hbar\omega) \qquad \text{with } J(\hbar\omega) = \sum_{ij \neq vc} J^{ij}(\hbar\omega)$$

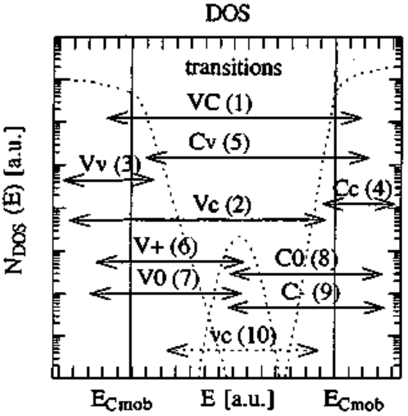

Fig.7: the standard DOS with the transitions which are taken into account for the numerical calculations.

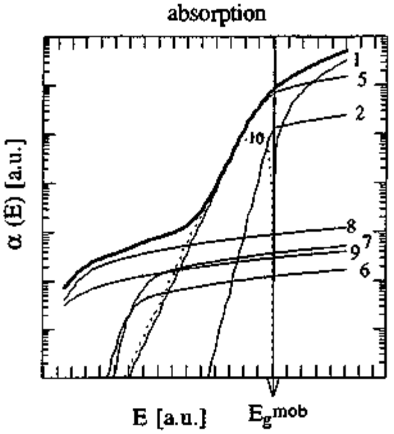

Fig.8: a possible absorption spectrum at thermal equilibrium corresponding to the transitions of fig.7.

There are nine partial joint DOS to be taken into account; they correspond to transitions of types A, B and C. The localised-to-localised transitions of type D are suppressed. Fig.7 shows these transitions and the corresponding notation ("V" and "C" correspond to delocalised band states, "v" and "c" to localised band tail states and "+", "0", "-" to the dangling bond states). Fig.8 shows the corresponding absorption spectrum where the suppressed transition "vc" (10) is indicated by a dashed line. The transitions "Vv" or "Cc" can dominate the deep defect absorption range in the case where the Fermi level E_F is close to one of the mobility edges. The equations of the partial joint DOS for the numerical calculations are shown in appendix B2.4. These partial joint DOS are defined in the same way at steady-state equilibrium, only the occupation functions themselves change.

2.4. The steady-state equilibrium

This section introduces the statistics at steady-state equilibrium. For a defect with a finite correlation energy (dangling bonds), "recombination" levels are introduced, between which the occupation is energy independent. Further, the total generation rate is introduced and analysed in the case of sub-bandgap illumination, while introducing "generation" levels. Finally, the rate equations are analysed in terms of generation rates, thermal emission rates and recombination rates.

2.4.1. Introduction

At steady-state equilibrium, the rate equation of the conduction band is zero ($\partial n / \partial t = 0$), as well as the rate equation of the valence band ($\partial p / \partial t = 0$). In this section, it is also assumed that any transition from localised-to-localised states can be neglected. Thus, the occupation functions at steady-state equilibrium can be expressed in a simple way.

The statistics of one defect level in crystalline semiconductors have been developed by Shockley and Read [52]. These statistics have been expanded to more complex defect distributions in crystalline semiconductors by Sah and Shockley [58], with the result of complex equations for the case of the steady-state and even at thermal equilibrium (see e.g. [Milnes 73]). Taylor and Simmons [72] found that the statistics of one defect level [Shockley 52] are also valid for certain energy distributions of one defect type in the case of crystalline semiconductors, while neglecting the spin degeneracy factor. The approach of Taylor and Simmons [72] is generally applied to amorphous semiconductors and has been expanded to the case of defects with a finite correlation energy U (dangling bonds) by Vaillant and Jousse [86]. Defects with an infinite correlation energy, well known as donor-like and acceptor-like defects, follow the formalism of Taylor and Simmons [72] if one takes into account the spin degeneracy factors. In a-Si:H, the defects with a finite correlation energy U (dangling bonds) are often approximated by a donor-like defect peak at E and an acceptor-like defect peak at E+U (see tab.3 in chapter 3). The author will show in this section that this approximation is not valid: for some specific cases the author found that a defect with a finite correlation energy U (dangling bonds) can be approximated **either** by a donor-like defect peak at E **or** by an acceptor-like defect peak at E+U.

2.4.2. The occupation function at steady-state equilibrium

One can express the occupation function at steady-state equilibrium f(E) of a defect without a finite correlation energy in terms of the thermal emission and capture probabilities ([Shockley 52] and [Taylor 72]):

$$f(E)=\frac{\tilde{n}+e_p^{th}}{\tilde{p}+e_n^{th}+\tilde{n}+e_p^{th}}$$

The capture probability ($\tilde{n}$ and $\tilde{p}$) of the charge carriers are given in terms of the charge carrier densities (n and p) in terms of the capture cross-sections (σ_n and σ_p) and in terms of the thermal velocity of the charge carriers (v_n and v_p). The thermal emission probabilities (e_n^{th} and e_p^{th}) additionally depend on the energy E (of the defect), on the effective DOS (here on the effective DOS at the mobility edges N_{Cmob}^{eff} and N_{Vmob}^{eff}) and on the border of the bands (here the mobility edges E_{Cmob} and E_{Vmob}). While neglecting the spin degeneracy factors, one gets:

$$\tilde{n}\equiv v_n\,\sigma_n\,n \qquad\qquad \tilde{p}\equiv v_p\,\sigma_p\,p$$

$$e_n^{th}=v_n\,\sigma_n\,N_{Cmob}^{eff}\exp\left[-\beta(E_{Cmob}-E)\right] \qquad\qquad e_p^{th}=v_p\,\sigma_p\,N_{Vmob}^{eff}\exp\left[-\beta(E-E_{Vmob})\right]$$

The following picture shows the notation used:

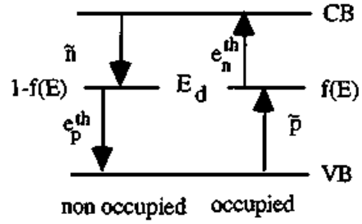

For the case of a-Si:H, Mittiga et al. [90] suggested to replace the thermal emission probabilities in the occupation function of the statistics of Taylor and Simmons [72] with the sum of the thermal emission probabilities and the defect-to-band generation probabilities (which are also called optical emission probabilities) in order to additionally describe the optical transitions of types B and C:

$$e_n^{th}\rightarrow e_n^{th}+e_n^{ph} \qquad\qquad e_p^{th}\rightarrow e_p^{th}+e_p^{ph}$$

The author points out that the approach of Mittiga et al. [90] is only valid if the thermal ionisation energy is equal to the optical "ionisation" energy (definition see section 2.4.6.). In crystalline semiconductors, the energy position of the localised states is different for thermal or for optical transitions because of the uncertainty relation [Kireev 75] and, thus, the localised state position can be overestimated in the optical determination by as much as 10% for dopants in crystalline silicon. Here, such effects are neglected and one can follow the approach of Mittiga et al. [90].

The following picture shows the notation used (the double arrows correspond to the optical transitions):

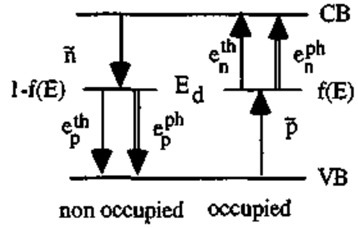

These defect-to-band generation probabilities (e_n^{ph} and e_p^{ph}) can be calculated from the JDOS $J(\hbar\omega)$ of the absorption $\alpha(\hbar\omega)$ and they have the following form [Mittiga 90]:

$$e_n^{ph} = C_0\, \hbar\omega\, R^2\, \Phi_0\, N_C(E+\hbar\omega) \qquad\qquad e_p^{ph} = C_0\, \hbar\omega\, R^2\, \Phi_0\, N_V(E-\hbar\omega)$$

These defect-to-band generation probabilities are proportional to the optical matrix element R^2 and to the incident photon flux Φ_0. The defect-to-band generation probability e_n^{ph} corresponds to a transition of a localised state to a delocalised conduction band state $N_C(E+\hbar\omega)$ (transition of type C), and the defect-to-band generation probability e_p^{ph} corresponds to a transition of a localised state to a delocalised valence band state $N_V(E-\hbar\omega)$ (transition of type B).

Thus, the occupation function at steady-state equilibrium f(E) of a defect without a finite correlation energy can be expressed in terms of a parameter K which determines the occupation function f(E):

$$f(E) = \frac{1}{1+K} \qquad\qquad \text{with } K \equiv \frac{\tilde{p} + e_n^{th} + e_n^{ph}}{\tilde{n} + e_p^{th} + e_p^{ph}}$$

Based on the results of Vaillant and Jousse [86], while taking the optical transitions into account, the occupation function at steady-state equilibrium of a defect with a finite correlation energy U (dangling bonds) can be expressed in terms of two parameters K and K_U which determine the occupation functions:

$$f^+(E) = \frac{1}{1+K^{-1}\left(1+K_U^{-1}\right)} \qquad\qquad f^0(E) = K^{-1}\, f^+(E) \qquad\qquad f^-(E) = K^{-1}\, K_U^{-1}\, f^+(E)$$

$$\text{with} \qquad K \equiv \frac{\tilde{p} + e_n^{th} + e_n^{ph}}{\tilde{n} + e_p^{th} + e_p^{ph}} \qquad \text{and} \qquad K_U \equiv \frac{\tilde{p}_U + e_{nU}^{th} + e_{nU}^{ph}}{\tilde{n}_U + e_{pU}^{th} + e_{pU}^{ph}}$$

The following picture shows the notation used (the double arrows correspond to the optical transitions):

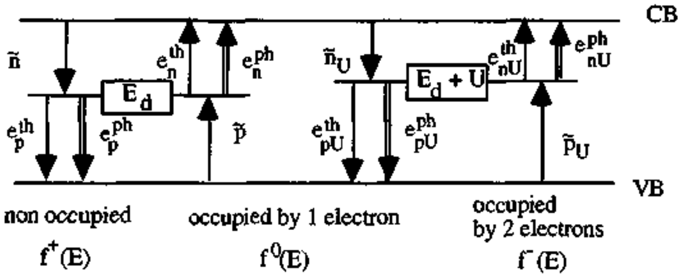

The occupation function $f^+(E)$ corresponds to an ionised atom, the occupation function $f^0(E)$ corresponds to a neutral dangling bond, and the occupation function $f^-(E)$ corresponds to a dangling bond occupied by two electrons. K and K_U determine these occupation functions, which depend on four capture probabilities ($\tilde{n}$, $\tilde{p}$, $\tilde{n}_U$, $\tilde{p}_U$), on four thermal emission probabilities (e_n^{th}, e_p^{th}, e_{nU}^{th}, e_{pU}^{th}) and on four defect-to-band generation probabilities (e_n^{ph}, e_p^{ph}, e_{nU}^{ph}, e_{pU}^{ph}). These terms are defined in appendix B3.5: the spin degeneracy factors are taken into account for the thermal emission probabilities (in contrast to [Taylor 72]); factors 2 - introduced in section 2.3.4. - are also taken into account for the defect-to-band generation probabilities (in contrast to [Mittiga 91]).

The author rewrites these occupation functions in terms of <u>correlation factors</u> z_d and z_{dU} introduced here:

$$f^+(E) = \frac{1}{1 + K^{-1}\, z_{dU}} \qquad f^0(E) = \frac{K^{-1}}{1 + K^{-1}\, z_{dU}} = \frac{K_U}{1 + K_U\, z_d} \qquad f^-(E) = \frac{1}{1 + K_U\, z_d}$$

with $\quad z_d \equiv (1 + K) \quad$ and $\quad z_{dU} \equiv \left(1 + K_U^{-1}\right)$

If the correlation factor z_{dU} is equal to one ($K_U^{-1} = 0$), the defect acts as a <u>donor-like defect</u> at the energy E:

$$f^+(E) = \frac{K}{1 + K} \qquad f^0(E) = \frac{1}{1 + K} \qquad f^-(E) = 0$$

If the correlation factor z_d is equal to one ($K = 0$), the defect acts as a <u>acceptor-like defect</u> at the energy E + U:

$$f^+(E) = 0 \qquad f^0(E) = \frac{K_U}{1 + K_U} \qquad f^-(E) = \frac{1}{1 + K_U}$$

It is not possible that the two correlation factors z_d and z_{dU} are both equal to 1 (never $K_U = K^{-1} = 0$) and, therefore, it is not possible to approximate a defect with a finite correlation energy U by a donor-like defect at the energy E and an acceptor-like defect at the energy E+U. A defect with a finite correlation energy U can either act as a donor-like defect ($z_{dU} = 1$) or as an acceptor-like defect ($z_d = 1$). This note is also valid if the thermal emission probabilities and/or the defect-to-band generation probabilities are neglected.

2.4.3. Analysis of the occupation functions

For the analysis of the occupation functions in this section, the defect-to-band generation probabilities are neglected, whereas in chapter 3 they will be taken into account. This will allow one to study the influence of the defect-to-band generation probabilities. In a-Si:H the defect-to-band generation probabilities are, in general, neglected for the study of photo conductivity with $\hbar\omega \geq E_g^{mob}$.

Taylor and Simmons [72] have shown that the occupation function of a defect without a finite correlation energy depends only on the ratio $\hat{K}$ of capture probabilities between two "recombination" levels (E_{tn} and E_{tp}), which is considered energy-independent by them:

$$f(E) \approx \frac{\tilde{n}}{\tilde{p}+\tilde{n}} = \frac{1}{1+\hat{K}} \equiv \hat{k} \qquad \text{for } E_{tp} < E < E_{tn} \qquad \text{with } \hat{K} = \frac{\tilde{p}}{\tilde{n}},$$

with

$$E_{tn} = E_{Cmob} + kT \ln\left(\frac{\tilde{n}+\tilde{p}}{v_n \sigma_n N_{Cmob}^{eff}}\right) \quad \text{from } e_n^{th} = \tilde{n}+\tilde{p}$$

$$E_{tp} = E_{Vmob} - kT \ln\left(\frac{\tilde{n}+\tilde{p}}{v_p \sigma_p N_{Vmob}^{eff}}\right) \quad \text{from } e_p^{th} = \tilde{n}+\tilde{p}$$

The "recombination" level E_{tn} is called quasi-Fermi-level for trapped electrons and the "recombination" level E_{tp} quasi-Fermi-level for trapped holes, by Taylor and Simmons [72].

In a similar way, the author presents here the result for the occupation function of a defect with a finite correlation energy U (dangling bonds). The complete occupation functions (calculated by Vaillant and Jousse [86]) can be approximated, provided that they lie between two "recombination levels" (E_{Rn} and E_{Rp}) introduced by the author hereafter; in this case they depend only on the ratio of the capture probabilities ($\hat{K}$ and $\hat{K}_U$). They are energy-independent between these two "recombination levels" (E_{Rn} and E_{Rp}).

$$f^+(E) \approx \frac{\tilde{p}\,\tilde{p}_U}{\tilde{p}\,\tilde{p}_U + \tilde{n}\,\tilde{p}_U + \tilde{n}\,\tilde{n}_U} = \frac{1}{1+\hat{K}^{-1}\left(1+\hat{K}_U^{-1}\right)} \equiv \hat{k}^+$$

$$f^0(E) \approx \frac{\tilde{n}\,\tilde{p}_U}{\tilde{p}\,\tilde{p}_U + \tilde{n}\,\tilde{p}_U + \tilde{n}\,\tilde{n}_U} = \frac{1}{1+\hat{K}+\hat{K}_U^{-1}} \equiv \hat{k}^0$$

$$f^-(E) \approx \frac{\tilde{n}\,\tilde{n}_U}{\tilde{p}\,\tilde{p}_U + \tilde{n}\,\tilde{p}_U + \tilde{n}\,\tilde{n}_U} = \frac{1}{1+\hat{K}_U\left(1+\hat{K}\right)} \equiv \hat{k}^-$$

$$\text{for } E_{Rp} < E < E_{Rn} \qquad \text{with } \hat{K} = \frac{\tilde{p}}{\tilde{n}} \qquad \text{and} \qquad \hat{K}_U = \frac{\tilde{p}_U}{\tilde{n}_U}$$

with $$E_{Rn} = E_{Cmob} + kT\ln\left(\frac{\tilde{n}+\tilde{n}_U+\bar{p}+\bar{p}_U}{\nu_n N_{Cmob}^{eff}\left(\frac{1}{2}\sigma_n + 2\,\sigma_{nU}\exp\left(\frac{U}{kT}\right)\right)}\right)$$

$$E_{Rp} = E_{Vmob} - kT\ln\left(\frac{\tilde{n}+\tilde{n}_U+\tilde{p}+\tilde{p}_U}{\nu_p N_{Vmob}^{eff}\left(2\,\sigma_p + \frac{1}{2}\sigma_{pU}\exp\left(-\frac{U}{kT}\right)\right)}\right)$$

The "recombination level" E_{Rn} is calculated from the condition $e_n + e_{nU} = \tilde{n} + \tilde{n}_U + \tilde{p} + \tilde{p}_U$ and the "recombination level" E_{Rp} from the condition $e_p + e_{pU} = \tilde{n} + \tilde{n}_U + \bar{p} + \bar{p}_U$. If the deep defect peak $N_{DB}(E)$ is located between these "recombination levels", the occupation functions are energy-independent.

In the case of a-Si:H, the following approximation may be valid:

$$1 \ll \frac{\sigma_n}{\sigma_{nU}}, \frac{\sigma_{pU}}{\sigma_p} \ll 4\exp\left(\frac{U}{kT}\right) \text{ and } \nu_n = \nu_p \qquad \text{e.g. for } U > 0.1\text{eV}, \ \frac{\sigma_n}{\sigma_{nU}} \approx \frac{\sigma_{pU}}{\sigma_p} \approx 100$$

Provided that this condition is valid, one can approximate the "recombination levels" as:

$$E_{Rn} = E_{Cmob} - U + kT\ln\left(\frac{n\,\sigma_n + p\,\sigma_{pU}}{2\,N_{Cmob}^{eff}\,\sigma_{nU}}\right); \qquad E_{Rp} = E_{Vmob} - kT\ln\left(\frac{n\,\sigma_n + p\,\sigma_{pU}}{2\,N_{Vmob}^{eff}\,\sigma_p}\right)$$

The author distinguishes the following five specific cases, which simplify the energy-independent occupation values $\hat{k}^+$, $\hat{k}^0$ and $\hat{k}^-$ between the two general "recombination" levels (E_{Rn} and E_{Rp}):

Case (1): $\hat{K} = \hat{K}_U = 1 \quad \Rightarrow \quad \hat{k}^+ = \hat{k}^0 = \hat{k}^- = 1/3$

Case (2): $\hat{K} \approx 0 \quad \Rightarrow \quad \hat{k}^+ = 0 \quad \hat{k}^0 = \frac{1}{1+\hat{K}_U^{-1}} \quad \hat{k}^- = \frac{1}{1+\hat{K}_U}$

Case (3): $\hat{K}_U^{-1} \approx 0 \quad \Rightarrow \quad \hat{k}^+ = \frac{1}{1+\hat{K}^{-1}} \quad \hat{k}^0 = \frac{1}{1+\hat{K}} \quad \hat{k}^- = 0$

Case (4): $\hat{K} \approx \hat{K}_U \approx 0 \quad \Rightarrow \quad \hat{k}^+ = 0 \quad \hat{k}^0 = 0 \quad \hat{k}^- = 1$

Case (5): $\hat{K}^{-1} \approx \hat{K}_U^{-1} \approx 0 \quad \Rightarrow \quad \hat{k}^+ = 1 \quad \hat{k}^0 = 0 \quad \hat{k}^- = 0$

In cases (2) and (4) the defect acts as an acceptor-like defect, in cases (3) and (5) the defect acts as a donor-like defect. Case (4) corresponds to an n-type material, case (5) to a p-type material. Note that it is also possible to define some other specific cases (see e.g. [Hubin 94]).

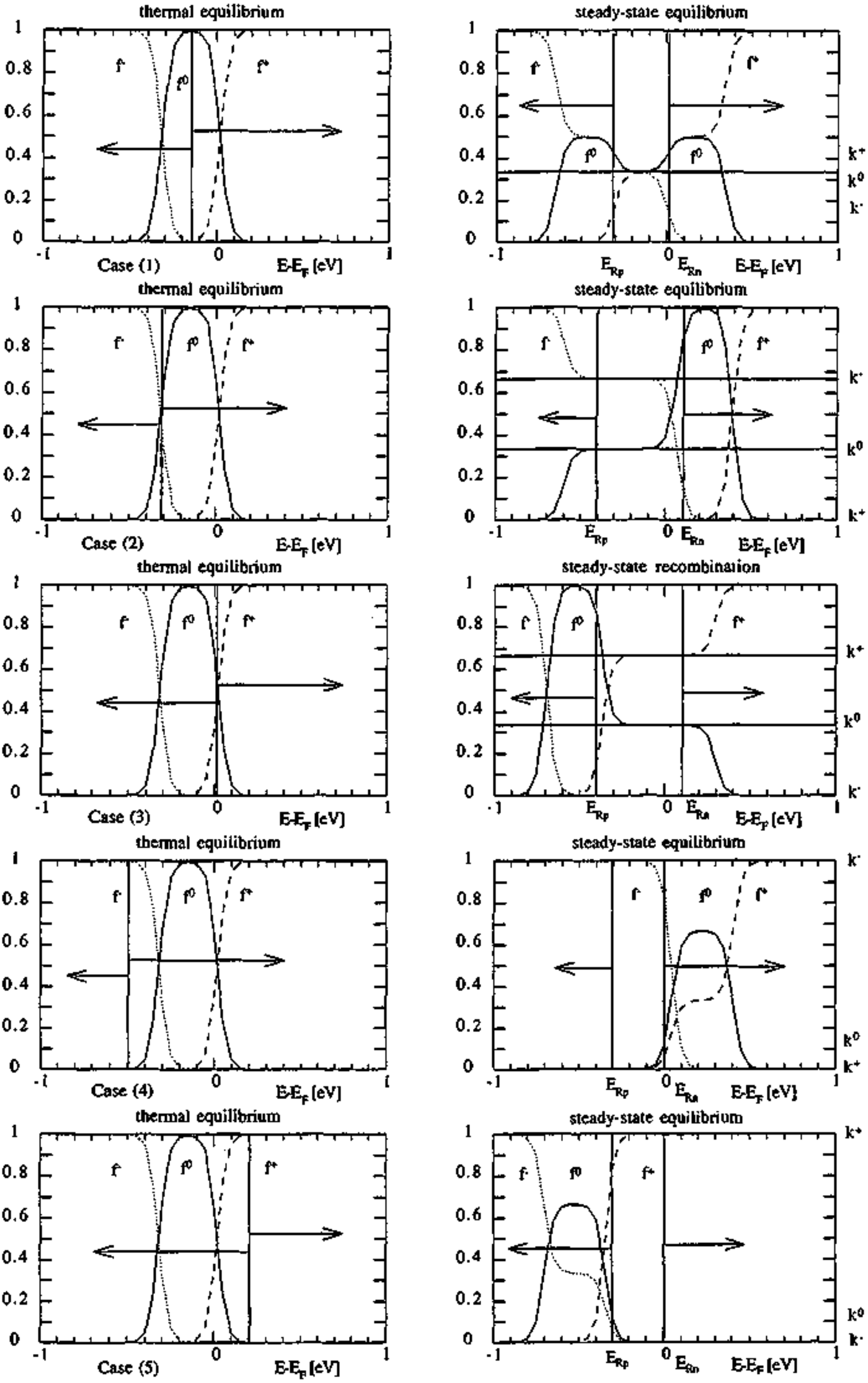

Fig.9: occupation functions: top to bottom: case(1) to (5): details see text.

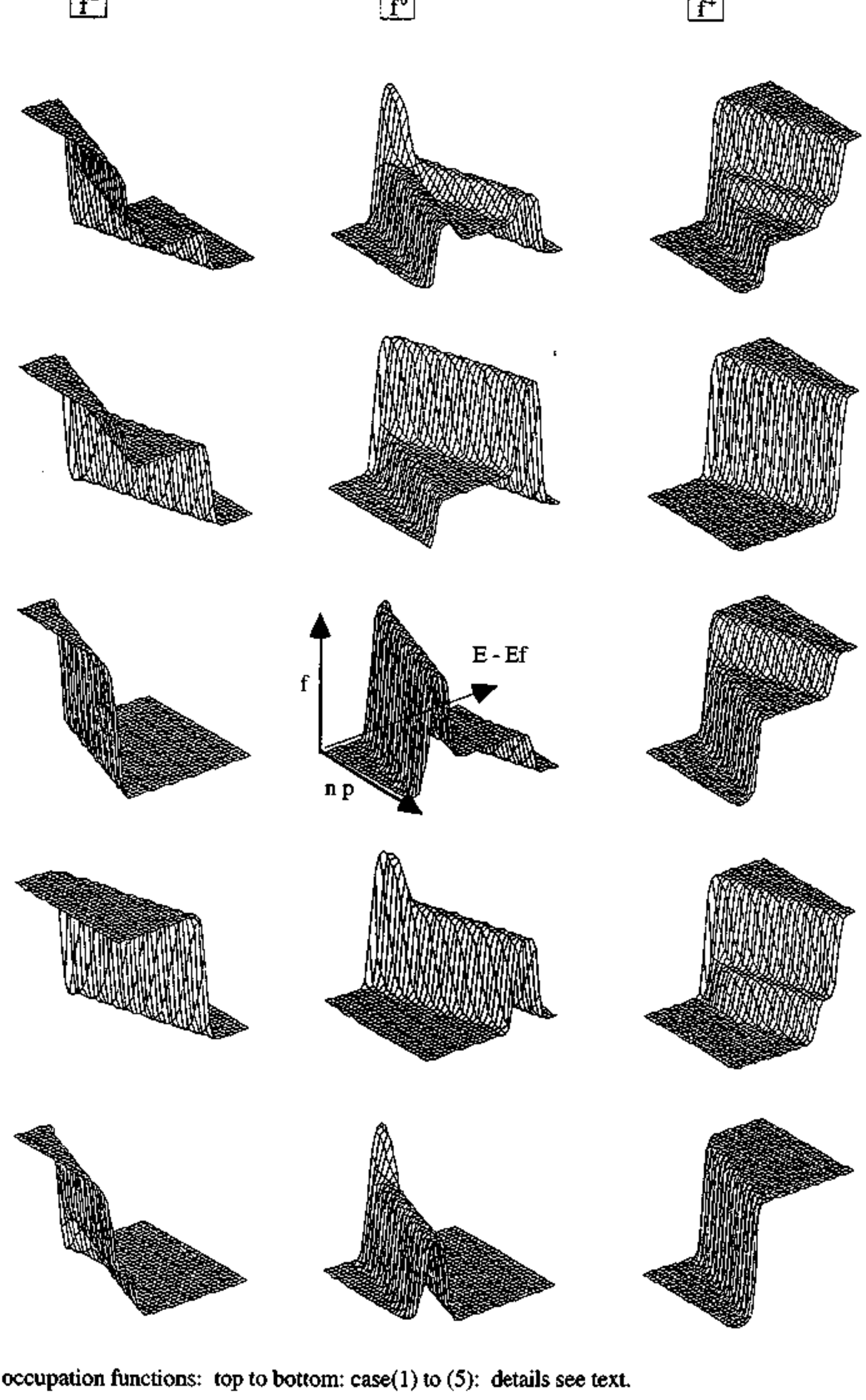

Fig.10: occupation functions: top to bottom: case(1) to (5): details see text.

In order to prove the validity of the "recombination levels" introduced here for a defect with a finite correlation energy and the approximations between them, the author has numerically calculated the occupation functions introduced by Vaillant and Jousse [86] for dangling bonds for the five cases introduced above.

The following values have been chosen as general input values: a correlation energy of U=0.3eV, a temperature of T=300K, identical thermal velocities $v_n = v_p$, identical capture cross-sections $\sigma_{nU} = \sigma_p$ for the neutral state, identical charge carrier densities at thermal equilibrium $n' = p'$ (intrinsic semiconductor) and a ratio of the charge carrier densities at steady-state equilibrium to the charge carrier densities at thermal equilibrium of $(n\ p)/(n'\ p') = 10^{10}$ (corresponding to the mass action law $n\ p > n_i^2 = n'\ p'$). The following table shows some further input parameters:

	Case (1)	Case (2)	Case (3)	Case (4)	Case (5)
n / p	1	100	1/100	100	1/100
$\frac{\sigma_n}{\sigma_p} = \frac{\sigma_{pU}}{\sigma_{nU}} =$	1	50	50	1/50	1/50

Fig.9 shows the numerical results: the left column shows the occupation function at thermal equilibrium. For each case the energy level is indicated where the split of the "recombination levels" will take place at steady-state equilibrium. The right column shows the corresponding occupation functions at steady-state equilibrium where the "recombination levels" E_{Rn} and E_{Rp} are indicated as well as the energy-independent occupation values $\hat{k}^+$, $\hat{k}^0$ and $\hat{k}^-$ between them. The five cases are numbered from top (1) to bottom (5). The arrows correspond to the shift in the "recombination levels" due to higher charge carrier density products (n p).

Fig.9 confirms that the occupation functions are energy-independent between the "recombination levels" E_{Rn} and E_{Rp}. In the intervals (E_{Rn} and E_{Rn}+ U) and (E_{Rp}- U and E_{Rp}), the occupation functions can be energy-independent or more complex, depending on the chosen parameters.

Fig.10 shows the occupation functions $f^-(E)$ (left column), $f^0(E)$ (middle column) and $f^+(E)$ (right column), from top to bottom case (1) to case (5) as a function of an increasing charge carrier density product (n p). In the energy intervals (E_{Rn} and E_{Rn}+ U) and (E_{Rp}- U and E_{Rp}), one finds a rather complex behaviour of the occupation functions depending on the parameters chosen.

From these figures one can estimate that the occupation functions are determined by the following probabilities:

Interval (E_{Rn} and E_{Rp}):	only capture probabilities
Intervals (E_{Rn} and E_{Rn}+ U) and (E_{Rp}- U and E_{Rp}):	capture and/or thermal emission probabilities
Outside interval (E_{Rp}- U and E_{Rn}+ U):	only thermal emission probabilities

CPM and PDS operate at low light intensities. This means that the "recombination levels" (E_{Rn} and E_{Rp}) are not necessarily split in such a way that the defect peak is located between them and that, therefore, the thermal emission probabilities can be neglected. Naturally, the defect-to-band generation probabilities (e_n^{ph}, e_p^{ph}, e_{nU}^{ph}, e_{pU}^{ph}) cannot be neglected for the case of $\hbar\omega < E_g^{mob}$ (CPM and PDS). But - a priori - it is not even evident that the defect-to-band generation probabilities can be neglected for the case of $\hbar\omega \geq E_g^{mob}$.

2.4.4. The generation rate

The generation rate G corresponds to the electron-hole pair creation due to the absorption of photons per second and per volume. The local generation G(x) is defined in general as

$$G(x) \equiv \eta\, \alpha(x)\, \Phi(x) \qquad \text{with} \qquad \Phi(x) = \Phi_0\, e^{-\alpha(x)x}$$

Thus, the total generation rate G_{tot} is a function of the incident photon flux Φ_0, the local absorption coefficient $\alpha(x)$, the thickness d of the material and the microscopic quantum efficiency η given as

$$G_{tot} = \frac{1}{d}\int_0^d dx\, G(x) = \frac{\Phi_0\, \eta}{d}\int_0^d dx\, \alpha(x)\, e^{-\alpha(x)x}$$

Hereafter it is assumed that the microscopic quantum efficiency η is 1 and it will, therefore, be omitted in the following equations. If the material is homogeneous, the absorption coefficient α can be assumed to be position-independent and the total generation rate G_{tot} is given as

$$G_{tot} = \frac{\Phi_0}{d}\left\{1 - e^{-\alpha d}\right\} \qquad \text{for } \alpha \text{ position-independent}$$

The special case $\alpha d \ll 1$ of this equation is called the "uniform absorption condition" here, and the total generation rate G_{tot} is given as

$$G_{tot} = \Phi_0\, \alpha \qquad \text{for } \alpha d \ll 1$$

Only this case will be analysed hereafter. In fact, CPM as well as PDS mostly operate under uniform absorption condition and are, thus, related in a direct way to the total generation rate G_{tot}. Further, the conductivity at steady-state equilibrium is also related to the total generation rate (see chapter 1 and chapter 3). Therefore, it is important to analyse the total generation rate G_{tot}.

The absorption coefficient $\alpha(\hbar\omega)$ in the expression $G_{tot} = \Phi_0\, \alpha$ is still a function of the photon energy $\hbar\omega$ and is determined by the transitions of types A, B, C or D as introduced in section 2.3.2. Transitions of type D are, once again, droped here. Thus, the total generation rate $G_{tot}(\hbar\omega)$ is given as a sum:

$$G_{tot}(\hbar\omega) = G_{bb}(\hbar\omega) + G_d(\hbar\omega)$$

The band-to-band generation rate $G_{bb}(\hbar\omega)$ is cansed by delocalised-to-delocalised band transitions (transitions of type A). The defect-to-band generation rate $G_d(\hbar\omega)$ is caused by localised-to-delocalised transitions (transitions of types B and C). *The total generation rate is related to the absorption of photons which generate electron-hole pairs.* The band-to-band generation rate $G_{bb}(\hbar\omega)$ creates pairs of delocalised electrons and holes. The defect-to-band generation rate $G_d(\hbar\omega)$ creates electron-hole pairs, where one of them is localised and the other delocalised.

The following picture shows the notation used (the double arrows correspond to the optical transitions):

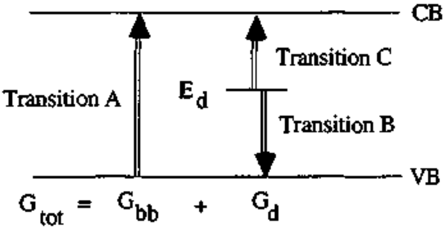

In general, the total generation rate $G_{tot}(\hbar\omega)$ is controlled by the transitions which dominate the total absorption $\alpha_{tot}(\hbar\omega)$. For a crystalline semiconductor with a defect located within the bandgap, it is evident that the total generation rate $G_{tot}(\hbar\omega)$ is equal to the band-to-band generation rate $G_{bb}(\hbar\omega)$ for a photon energy equal to the bandgap ($\hbar\omega = E_g^{opt}$). But in the case of a-Si:H with a mobility gap and with some exponential tails as DOS, the total generation rate $G_{tot}(\hbar\omega)$ can be dominated by transitions of types B and C and not by transitions of type A for photon energy equal to the mobility gap ($\hbar\omega = E_g^{mob}$), as shown in fig.8. This means that the defect-to-band generation rate $G_d(\hbar\omega)$ cannot be neglected for the calculation of the total generation rate $G_{tot}(\hbar\omega)$ in the case of a-Si:H for photon energies comparable to the energy of the mobility gap. If the photon energies are smaller than the mobility gap ($\hbar\omega < E_g^{mob}$), the band-to-band generation rate is zero ($G_{bb}(\hbar\omega)$=0) and the total generation rate $G_{tot}(\hbar\omega)$ is always controlled by the defect-to-band generation rate $G_d(\hbar\omega)$.

The band-to-band generation rate $G_{bb}(\hbar\omega)$ is given as

$$G_{bb}(\hbar\omega) = \Phi_0\, C_0\, \hbar\omega\, R^2\, J_A(\hbar\omega) = \Phi_0\, C_0\, \hbar\omega\, R^2 \int_{E_{Cmob}-\hbar\omega}^{E_{Vmob}} dE\, N_V(E)\, N_C(E+\hbar\omega)$$

or $$G_{bb}(\hbar\omega) = \int_{E_{Cmob}-\hbar\omega}^{E_{Vmob}} dE\, N_V(E)\, e_{bb}^{ph} \qquad \text{with} \qquad e_{bb}^{ph} \equiv \Phi_0\, C_0\, \hbar\omega\, R^2\, N_C(E+\hbar\omega)$$

The band-to-band generation probability e_{bb}^{ph} of transition A has the same form as the defect-to-band generation probabilities introduced in section 2.4.2. for the description of the occupation functions.

If the optical bandgap is equal to the mobility gap ($E_g^{opt} = E_g^{mob}$), the band-to-band generation rate $G_{bb}(\hbar\omega)$ is given as (see section 2.3.3.):

$$G_{bb}(\hbar\omega) = \Phi_0\, C_0\, \hbar\omega\, R^2\, N_C^0\, N_V^0\, \frac{\pi}{8}(E_g^{opt} - \hbar\omega)^2 \qquad \text{for } E_g^{opt} = E_g^{mob}$$

The <u>defect-to-band generation rate</u> $G_d(\hbar\omega)$ depends on the defect type. For the defect type analysed by Taylor and Simmons [72], Mittiga et al. [90] found the following <u>defect-to-band generation rate</u> $G_d(\hbar\omega)$:

$$G_d(\hbar\omega) = \frac{e_n^{ph} e_p^{th} + e_n^{th} e_p^{ph} + e_n^{ph} e_p^{ph}}{\left(\tilde{n} + e_p^{th} + e_p^{ph}\right) + \left(\tilde{p} + e_n^{th} + e_n^{ph}\right)} N_d$$

N_d is the defect density at the energy E_d within the bandgap. This result of the defect-to-band generation rate $G_d(\hbar\omega)$ for a defect without a finite correlation energy will be discussed in section 2.4.6..

The author found the following expression for the defect-to-band generation rate $G_d(\hbar\omega)$ of a defect **with** a finite correlation energy U:

$$G_d(\hbar\omega) = \left\{ \frac{e_n^{ph} e_p^{th} + e_n^{th} e_p^{ph} + e_n^{ph} e_p^{ph}}{\left(\tilde{p} + e_n^{th} + e_n^{ph}\right) + \left(\tilde{n} + e_p^{th} + e_p^{ph}\right) z_{dU}} + \frac{e_{nU}^{ph} e_{pU}^{th} + e_{nU}^{th} e_{pU}^{ph} + e_{nU}^{ph} e_{pU}^{ph}}{\left(\tilde{n}_U + e_{pU}^{th} + e_{pU}^{ph}\right) + \left(\bar{p}_U + e_{nU}^{th} + e_{nU}^{ph}\right) z_d} \right\} N_d$$

with $\qquad z_d \equiv (1 + K) \qquad$ and $\qquad z_{dU} \equiv \left(1 + K_U^{-1}\right)$

$$K \equiv \frac{\tilde{p} + e_n^{th} + e_n^{ph}}{\bar{n} + e_p^{th} + e_p^{ph}} \qquad \text{and} \qquad K_U \equiv \frac{\tilde{p}_U + e_{nU}^{th} + e_{nU}^{ph}}{\bar{n}_U + e_{pU}^{th} + e_{pU}^{ph}}$$

From the formal point of view, the terms of this expression look similar to those contained in the result of Mittiga et al. [90], but the two correlation factors z_d and z_{dU} do not allow a simple interpretation.

Regardless of the defect type, one can see that the defect-to-band generation rate $G_d(\hbar\omega)$ is proportional to the defect density N_d.

In general, if the defect-to-band generation probabilities (e_n^{ph}, e_p^{ph} or e_n^{ph}, e_p^{ph}, e_{nU}^{ph}, e_{pU}^{ph}) are neglected, the defect-to-band generation rate $G_d(\hbar\omega)$ is zero. In contrast, if the band-to-band generation probability e_{bb}^{ph} is neglected, the band-to-band generation rate $G_{bb}(\hbar\omega)$ is zero.

2.4.5. The steady-state equilibrium

At steady-state equilibrium, the total generation rate $G_{tot}(\hbar\omega)$ is equal to the total recombination rate R_{tot} minus the total thermal emission rate T_{tot}:

$$G_{tot}(\hbar\omega) = R_{tot} - T_{tot}$$

with $\quad G_{tot}(\hbar\omega) = G_{bb}(\hbar\omega) + G_d(\hbar\omega) \qquad R_{tot} = R_{bb} + R_d \qquad T_{tot} = T_{bb} + T_d$

The total generation rate $G_{tot}(\hbar\omega)$ consists of the band-to-band generation rate $G_{bb}(\hbar\omega)$ and the defect-to-band generation rate $G_d(\hbar\omega)$ (see section 2.4.4.). The total recombination rate R_{tot} consists of the <u>band-to-band recombination rate</u> R_{bb} and the <u>defect recombination rate</u> R_d. The total thermal emission rate T_{tot} consists of the <u>band-to-band thermal emission rate</u> T_{bb} and the <u>defect thermal emission rate</u> T_d.

The following picture shows the notation used (the double arrows correspond to the optical transitions):

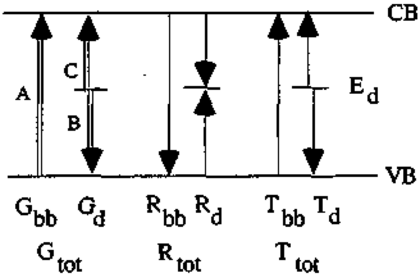

Here the band-to-band recombination rate R_{bb} is neglected because the defect recombination rate R_d is assumed to be dominating the total recombination rate R_{tot}. For very high generation rates, this assumption is not valid. Further, the band-to-band thermal emission rate T_{bb} is neglected because the defect thermal emission rate T_d is assumed to be dominating the total thermal emission rate T_{tot}. For very low generation rates, this assumption is not valid.

The author analysed the steady-state equilibrium for a defect without and with a finite correlation energy U by solving the rate equations, while using the correlation factors z_d and z_{dU} (introduced in section 2.4.2.).

The author has found the following expression for the defect recombination rate R_d and the defect thermal emission rate T_d.

For a defect without a finite correlation energy:

$$R_d = \frac{\tilde{n}\,\tilde{p}}{\left(\tilde{n} + e_p^{th} + e_p^{ph}\right) + \left(\tilde{p} + e_n^{th} + e_n^{ph}\right)} N_d \text{ and } T_d = \frac{e_n^{th}\,e_p^{th}}{\left(\tilde{n} + e_p^{th} + e_p^{ph}\right) + \left(\tilde{p} + e_n^{th} + e_n^{ph}\right)} N_d$$

For a defect **with** a finite correlation energy U:

$$R_d = \left\{ \frac{\tilde{n}\,\tilde{p}}{\left(\tilde{p} + e_n^{th} + e_n^{ph}\right) + \left(\tilde{n} + e_p^{th} + e_p^{ph}\right) z_{dU}} + \frac{\tilde{n}\,\tilde{p}}{\left(\tilde{n}_U + e_{pU}^{th} + e_{pU}^{ph}\right) + \left(\tilde{p}_U + e_{nU}^{th} + e_{nU}^{ph}\right) z_d} \right\} N_d$$

$$T_d = \left\{ \frac{e_n^{th}\,e_p^{th}}{\left(\tilde{p} + e_n^{th} + e_n^{ph}\right) + \left(\tilde{n} + e_p^{th} + e_p^{ph}\right) z_{dU}} + \frac{e_{nU}^{th}\,e_{pU}^{th}}{\left(\tilde{n}_U + e_{pU}^{th} + e_{pU}^{ph}\right) + \left(\tilde{p}_U + e_{nU}^{th} + e_{nU}^{ph}\right) z_d} \right\} N_d$$

One can see that the presence of the correlation factors z_d and z_{dU} does not allow one to approximate a defect (**with** a finite correlation energy U) with two defects (without a finite correlation energy) - even if the defect-to-band generation probabilities are neglected.

Further, the author has found the following expression of the band-to-band generation rate $G_{bb}(\hbar\omega)$ at steady-state equilibrium.

For a defect without a finite correlation energy:

$$G_{bb}(\hbar\omega) = R_d - T_d - G_d(\hbar\omega) = \left\{ \frac{\tilde{n}\,\tilde{p} - \left(e_n^{th} + e_n^{ph}\right)\left(e_p^{th} + e_p^{ph}\right)}{\left(\tilde{p} + e_n^{th} + e_n^{ph}\right) + \left(\tilde{n} + e_p^{th} + e_p^{ph}\right)} \right\} N_d$$

For a defect **with** a finite correlation energy U:

$$G_{bb}(\hbar\omega) = R_d - T_d - G_d(\hbar\omega) =$$

$$\left\{ \frac{\tilde{n}\,\tilde{p} - \left(e_n^{th} + e_n^{ph}\right)\left(e_p^{th} + e_p^{ph}\right)}{\left(\tilde{p} + e_n^{th} + e_n^{ph}\right) + \left(\tilde{n} + e_p^{th} + e_p^{ph}\right) z_{dU}} + \frac{\tilde{n}_U\,\tilde{p}_U - \left(e_{nU}^{th} + e_{nU}^{ph}\right)\left(e_{pU}^{th} + e_{pU}^{ph}\right)}{\left(\tilde{n}_U + e_{pU}^{th} + e_{pU}^{ph}\right) + \left(\tilde{p}_U + e_{nU}^{th} + e_{nU}^{ph}\right) z_d} \right\} N_d$$

If the photon energy is smaller than the mobility gap ($\hbar\omega < E_g^{mob}$), the band-to-band generation rate $G_{bb}(\hbar\omega)$ is zero and these two expressions, which determine the steady-state equilibrium, are equal to zero. The interpretation remains complex (see section 2.4.6.).

In contrast, the expression of the band-to-band generation rate $G_{bb}(\hbar\omega)$ at steady-state equilibrium can be simplified if the defect-to-band generation probabilities and the thermal emission probabilities can be neglected. For this specific case and for a defect **with** a finite correlation energy U the author has found the following simple expression for the band-to-band generation rate G_{bb} :

$$G_{bb} = R_d = \left(\frac{\tilde{n}}{1 + \hat{K}^{-1}\left\{1 + \hat{K}_U^{-1}\right\}} + \frac{\tilde{p}_U}{1 + \hat{K}_U\left\{1 + \hat{K}\right\}} \right) N_d \qquad \text{for } E_{Rp} < E_d < E_{Rn}$$

with $\hat{K} = \frac{\tilde{p}}{\tilde{n}}$ $\hat{K}_U = \frac{\tilde{p}_U}{\tilde{n}_U}$

The thermal emission probabilities can be neglected if the defect is located between the two "recombination levels", introduced in section 2.4.3. ($E_{Rp} < E_d < E_{Rn}$). In this case the occupation functions are energy-independent and also determined by $\hat{K}$ and $\hat{K}_U$ (see section 2.4.3.).

Corresponding to the five specific cases of the occupation functions under these conditions (see section 2.4.3.), the author found the following five cases for the band-to-band generation rate G_{bb}:

$$\text{Case (1):} \quad \hat{K} = \hat{K}_U = 1 \qquad \Rightarrow \quad G_{bb} = R_d \approx \frac{1}{3}(\tilde{n} + \tilde{p}_U)\,N_d$$

$$\text{Case (2):} \quad \hat{K} \approx 0 \qquad \Rightarrow \quad G_{bb} = R_d \approx \frac{\tilde{n}_U\,\tilde{p}_U}{\tilde{n}_U + \tilde{p}_U}\,N_d$$

$$\text{Case (3):} \quad \hat{K}_U^{-1} \approx 0 \qquad \Rightarrow \quad G_{bb} = R_d \approx \frac{\tilde{n}\,\tilde{p}}{\tilde{n} + \tilde{p}}\,N_d$$

$$\text{Case (4):} \quad \hat{K} = \hat{K}_U \approx 0 \qquad \Rightarrow \quad G_{bb} = R_d \approx \tilde{p}_U\,N_d$$

$$\text{Case (5):} \quad \hat{K}^{-1} \approx \hat{K}_U^{-1} \approx 0 \qquad \Rightarrow \quad G_{bb} = R_d \approx \tilde{n}\,N_d$$

In cases (2) and (4) the defect acts as an acceptor-like defect, in cases (3) and (5) the defect acts as a donor-like defect. Cases (2) - (5) correspond to the recombination behaviour of a defect analysed by Taylor and Simmons [72]. In cases (4) and (5) the recombination is limited by the minority carrier. Case (1) looks like a combination of cases (4) and (5) and the factor 1/3 is related to the occupation function of case (1) (see section 2.4.3.). Note: it is also possible to define some other specific cases (see e.g. [Hubin 94]).

The following picture shows the five cases (the double arrow corresponds to the optical transition):

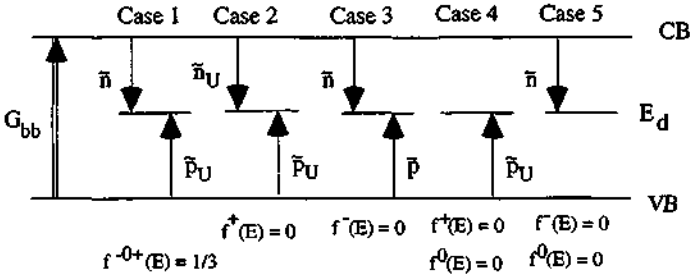

These five main recombination paths may also be present for the case where the band-to-band generation $G_{bb}(\hbar\omega)$ is replaced by the defect-to-band generation rate $G_d(\hbar\omega)$. Therefore, the defect-to-band generation rate $G_d(\hbar\omega)$ will have to be analysed next.

2.4.6. The defect-to-band generation rate and the "generation" levels

Any kind of experiment which operates with photon energies lower than the mobility gap ($\hbar\omega < E_g^{opt}$) is controlled by the defect-to-band generation rate $G_d(\hbar\omega)$. The following analysis of the defect-to-band generation rate $G_d(\hbar\omega)$ remains necessary in order to understand CPM and PDS.

The defect-to-band generation rate $G_d(\hbar\omega)$ depends on the defect type. The defect-to-band generation rate $G_d(\hbar\omega)$ of a defect with a finite correlation energy U is a complicated function, due to the correlation factors z_d and z_{dU} (see section 2.4.4.). Therefore, only the defect-to-band generation rate $G_d(\hbar\omega)$ of a defect without a finite correlation energy will be analysed in this section (see section 2.4.4.). The main defect-to-band generation mechanism will be similar for a defect with or without a finite correlation U.

Mittiga et al. [90] found the following defect-to-band generation rate $G_d(\hbar\omega)$ at steady-state equilibrium for the defect type analysed by Taylor and Simmons [72]:

$$G_d(\hbar\omega) = \frac{e_n^{ph} e_p^{th} + e_n^{th} e_p^{ph} + e_n^{ph} e_p^{ph}}{\tilde{n} + e_n^{th} + e_n^{ph} + \tilde{p} + e_p^{th} + e_p^{ph}} N_d$$

This result can be written as

$$G_d(\hbar\omega) = \left(G_n + G_p + G_{pn}\right) k_d^{-1}$$

with $\quad G_n \equiv e_n^{ph}\, e_p^{th} \qquad G_p \equiv e_n^{th}\, e_p^{ph} \qquad G_{np} \equiv e_n^{ph}\, e_p^{ph}$

$$k_d \equiv \left(\tilde{n} + \tilde{p} + e_n^{th} + e_n^{ph} + e_p^{th} + e_p^{ph}\right) N_d^{-1}$$

The following picture shows the notation used (the double arrows correspond to the optical transitions):

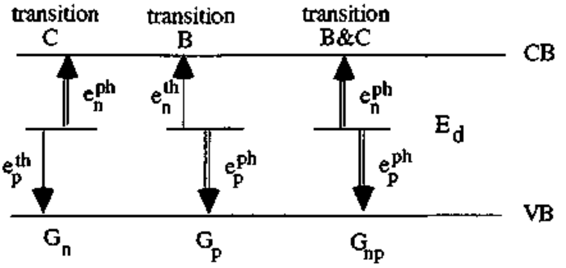

G_n corresponds to a transition of type C and is proportional to the thermal emission probability e_p^{th} (thermal emission of a hole), G_p corresponds to a transition of type B and is proportional to the thermal emission probability e_n^{th} (thermal emission of an electron). Finally, G_{np} corresponds to a transition of type B plus a transition of type C and is independent of the thermal emission probabilities e_n^{th} and e_p^{th}.

The three defect-to-band generation mechanism each produce a **delocalised** electron-hole pair, similar to the band-to-band generation rate $G_{bb}(\hbar\omega)$. Here, only one defect level at the energy E_d is assumed to be present. Therefore, the recombination of such a delocalised electron-hole pair takes place by the same defect (a discussion of a system with two defect levels will be given in chapter 3).

Concerning the photon energy $\hbar\omega$ one can distinguish between four cases which depend on the <u>optical "ionisation" energies</u> (E_{In}, E_{Ip}) of the defect at the energy E_d:

$$E_{In} \equiv E_{Cmob} - E_d \quad \text{and} \quad E_{Ip} \equiv E_d - E_{Vmob}$$

These cases are determined by the photon energy $\hbar\omega$ for a fixed defect at the energy E_d:

Case (a): Transitions B and C possible: $G_d(\hbar\omega) = \left(G_n + G_p + G_{pn}\right) k_d^{-1}$ for $\hbar\omega \geq E_{In}, E_{Ip}$

Case (b): Only transition B possible: $G_d(\hbar\omega) = G_p\, k_d^{-1}$ for $E_{In} > \hbar\omega \geq E_{Ip}$

Case (c): Only transition C possible: $G_d(\hbar\omega) = G_n\, k_d^{-1}$ for $E_{In} \leq \hbar\omega < E_{Ip}$

Case (d): no transition possible: $G_d(\hbar\omega) = 0$ for $\hbar\omega < E_{In}, E_{Ip}$

This means that only the transitions marked above as "possible" contribute to the defect-to-band generation rate $G_d(\hbar\omega)$ as in the case of the absorption at thermal equilibrium (see fig.8). However, the absorption at thermal equilibrium does not necessarily have to be identical to the absorption at steady-state equilibrium; a change in the occupation functions from the thermal equilibrium to the steady-state equilibrium can, in principle, lead to a change in the absorption, especially in the deep defect absorption range (see section 1.7.3d and chapter 3).

In order to estimate the dominating generation mechanism (G_{np}, G_n or G_p) of case (a), the author introduces "<u>generation" levels</u>" E_{Gn} and E_{Gp} in the following way :

$$e_n^{th} = e_n^{ph} \quad \rightarrow \quad E_{Gn} = E_{Cmob} + kT \ln\left(Z_n \frac{N_C(E_d + \hbar\omega)}{N_{Cmob}^{eff}} \right) \qquad Z_n \equiv \theta_n \frac{C_0\, \hbar\omega}{v_n} \Phi_0 \qquad \theta_n \equiv \frac{R^2}{\sigma_n}$$

$$e_p^{th} = e_p^{ph} \quad \rightarrow \quad E_{Gp} = E_{Vmob} - kT \ln\left(Z_p \frac{N_V(E_d - \hbar\omega)}{N_{Vmob}^{eff}} \right) \qquad Z_p \equiv \theta_p \frac{C_0\, \hbar\omega}{v_p} \Phi_0 \qquad \theta_p \equiv \frac{R^2}{\sigma_p}$$

These levels depend on the incident photon flux Φ_0, on the photon energy $\hbar\omega$ and on the ratio θ_i of the optical matrix element R^2 and the capture cross-section σ_i (i =n, p). Fig.11 shows the two "generation levels" E_{Gn} and E_{Gp} as a function of the incident photon flux Φ_0. One can see that the mobility gap E_g^{mob} is split into four regions I, II, III and IV, depending on the incident photon flux

Φ_0. For a fixed defect position E_d within the mobility gap E_g^{mob} the defect-to-band generation rate $G_d(\hbar\omega)$ passes up to three regions as a function of the incident photon flux Φ_0. Further, Fig.12 indicates that for a fixed incident photon flux Φ_0 the dominating defect-to-band generation mechanism depends on the defect position E_d.

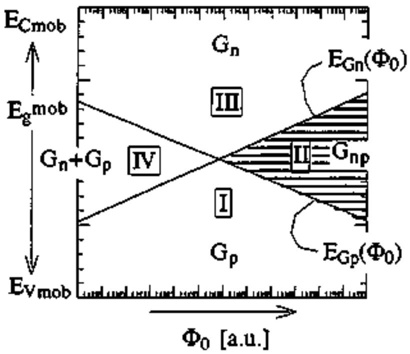

Fig.11: the "generation levels" E_{Gn} and E_{Gp} as a function of the incident photon flux Φ_0 and the corresponding regions I, II, III and IV of case (a).

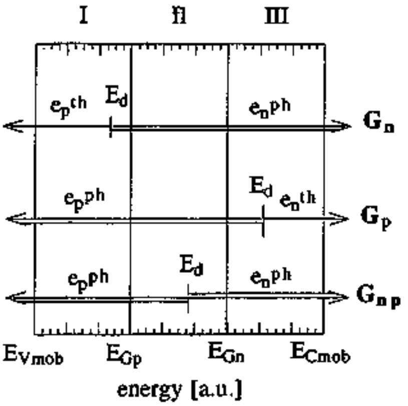

Fig.12: the three generation mechanisms G_{np}, G_n and G_p, depending on the defect energy position E_d within the mobility gap E_g^{mob}.

The four regions I - IV of case (a) are defined as follows and the defect-to-band generation rate $G_d(\hbar\omega)$ is given for each region in terms of the three generation mechanism (G_{np}, G_n or G_p):

region I:	$E_{Vmob} < E_d < E_{Gn}, E_{Gp}$	$e_n^{th} < e_n^{ph}$	$e_p^{th} > e_p^{ph}$	$G_d(\hbar\omega) \approx G_n\, k_d^{-1}$
region II:	$E_{Gp} < E_d < E_{Gn}$	$e_n^{th} < e_n^{ph}$	$e_p^{th} < e_p^{ph}$	$G_d(\hbar\omega) \approx G_{pn}\, k_d^{-1}$
region III:	$E_{Gn}, E_{Gp} < E_d < E_{Cmob}$	$e_n^{th} > e_n^{ph}$	$e_p^{th} < e_p^{ph}$	$G_d(\hbar\omega) \approx G_p\, k_d^{-1}$
region IV:	$E_{Gp} > E_d > E_{Gn}$	$e_n^{th} > e_n^{ph}$	$e_p^{th} < e_p^{ph}$	$G_d(\hbar\omega) \approx \left(G_n + G_p\right) k_d^{-1}$

It is evident that the ratio θ_i of the optical matrix elements and the capture cross-sections govern the selection between the different generation mechanism G_n, G_p and G_{np}. For very large ratios θ_i the two-photon generation mechanism G_{np} (region II) can dominate the defect-to-band generation rate at a high incident photon flux Φ_0; otherwise the one-photon generation mechanisms G_n and G_p (region I, III, IV) dominate the defect-to-band generation rate $G_d(\hbar\omega)$. In appendix B6 a numerical estimation of the "generation levels" E_{Gn} and E_{Gp} is given for the case of a-Si:H.

The defect-to-band generation rate $G_d(\hbar\omega)$ and the occupation function f(E) can then be expressed for the four regions I - IV of case (a):

region I:
$$G_d(\hbar\omega) \approx \frac{e_n^{ph} e_p^{th}}{\tilde{n} + e_n^{ph} + \tilde{p} + e_p^{th}} N_d \qquad f(E) = \frac{\tilde{n} + e_p^{th}}{\tilde{p} + e_n^{ph} + \tilde{n} + e_p^{th}}$$

region II:
$$G_d(\hbar\omega) \approx \frac{e_n^{ph} e_p^{ph}}{\tilde{n} + e_n^{ph} + \tilde{p} + e_p^{ph}} N_d \qquad f(E) = \frac{\tilde{n} + e_p^{ph}}{\tilde{p} + e_n^{ph} + \tilde{n} + e_p^{ph}}$$

region III:
$$G_d(\hbar\omega) = \frac{e_n^{th} e_p^{ph}}{\tilde{n} + e_n^{th} + \tilde{p} + e_p^{ph}} N_d \qquad f(E) = \frac{\tilde{n} + e_p^{ph}}{\tilde{p} + e_n^{th} + \tilde{n} + e_p^{ph}}$$

region IV:
$$G_d(\hbar\omega) \approx \frac{e_n^{ph} e_p^{th} + e_n^{th} e_p^{ph}}{\tilde{n} + e_n^{th} + \tilde{p} + e_p^{th}} N_d \qquad f(E) = \frac{\tilde{n} + e_p^{th}}{\tilde{p} + e_n^{th} + \tilde{n} + e_p^{th}}$$

One can see that the occupation function f(E) in region IV does not depend on the defect-to-band generation probabilities (e_n^{ph} and e_p^{ph}). Here, the capture probabilities ($\tilde{n}$ and $\tilde{p}$) will, therefore, determine the occupation functions. In contrast, the occupation function f(E) in region II depends on both defect-to-band generation probabilities (e_n^{ph} and e_p^{ph}). In this case one can expect a change in the absorption at steady-state equilibrium (for PDS and CPM) in comparison to the absorption at thermal equilibrium.

One can conclude that the defect-to-band generation rate $G_d(\hbar\omega)$ depends on the possible transitions and that all three generation mechanisms are proportional to the defect density N_d, but that G_n and G_p are additionally proportional to the thermal emission probabilities which are strongly dependent of the defect position E_d, whereas G_{np} depends much less on the defect position E_d. Whether G_{np} dominates the defect-to-band generation rate $G_d(\hbar\omega)$ depends basically on the ratio θ_i of the optical matrix element and the capture cross-sections and can be determined with the help of the "generation levels" (E_{Gn} and E_{Gp}) introduced here.

2.4.7. CPM and PDS theory at steady-state equilibrium

At this point in the study, it remains necessary to compare the approaches of Mittiga et al. [90] and of Vanecek et al. [81] (original CPM approach), which both describe the CPM at steady-state equilibrium.

Vanecek et al. [81] calculated the steady-state equilibrium only for transitions of type C ($E_{In} \le \hbar\omega < E_{Ip}$) - corresponding to an n-type material - and found the following result for a defect with a defect density N_d and with a defect position E_d:

$$\frac{\partial n}{\partial t} = 0 = e_n^{ph}\, f\, N_d - \tilde{n}\,(1-f)\, N_d$$

Based on this rate equation, it is generally assumed that CPM is controlled by the majority charge carrier, that CPM is independent of the thermal emission probabilities and that the occupation function f corresponds to the occupation function at thermal equilibrium.

In contrast, Mittiga et al. [90] considered both rate equations ($\partial n / \partial t = 0$ and $\partial p / \partial t = 0$) with the result that the occupation function f(E) (see section 2.4.2.) and the defect-to-band generation rate $G_d(\hbar\omega)$ (see section 2.4.5.) can be determined. Further, in the approach of Mittiga et al. [90], the defect position E_d can be located anywhere within the bandgap (transitions of type B and C possible).

Based on the analysis of the defect-to-band generation rate in 2.4.6. (approach of Mittiga et al. [90]), one has to conclude for CPM that the minority charge carrier and the thermal emission probabilities cannot be neglected and that the occupation functions and the defect-to-band generation rates $G_d(\hbar\omega)$ can be photon energy dependent! Therefore, CPM will be analysed numerically.

In general it is assumed that PDS can be described as a system at thermal equilibrium. An interesting consequence of the approach of Mittiga et al. [90] is that PDS can be analysed at steady-state equilibrium. The detected deflection of PDS is simply proportional to the total generation rate $G_{tot}(\hbar\omega)$:

$$\alpha_{PDS}(\hbar\omega) = \frac{G_{tot}(\hbar\omega)}{\Phi_0(\hbar\omega)} \quad \text{with} \quad G_{tot}(\hbar\omega) = G_{bb}(\hbar\omega) + G_d(\hbar\omega)$$

The incident photon flux $\Phi_0(\hbar\omega)$ of PDS is approximately constant (in strong contrast with CPM). But it can influence the occupation functions and this can - in principle - lead to a change in the absorption $\alpha(\hbar\omega)$ (see section 1.7.3d and chapter 3). Therefore, PDS will also be analysed numerically.

2.4.8. The basis of the numerical analysis at steady-state equilibrium

The goal of a numerical analysis is to calculate the total generation rate $G_{tot}(\hbar\omega)$ and the conductivity $\sigma = e\{\mu_e n + \mu_h p\}$ at steady-state equilibrium. This will allow one to numerically study PDS and CPM, which are both functions of the incident photon flux Φ_0 and the photon energy $\hbar\omega$. Here, the basis for the numerical analysis at steady-state equilibrium is presented, whereas the numerical results will be shown in chapter 3. The mathematical formulations of the different elements at steady-state equilibrium are given in appendix B3.

At steady-state equilibrium the localised conduction and valence band states of the standard DOS (introduced in section 2.1.) are described by the statistics of Taylor and Simmons [72], taking into account the defect-to-band generation probabilities of Mittiga et al. [90]. The occupation function of the dangling bond peak of the standard DOS is described by the statistics of Vaillant and Jousse [86], while using the corresponding defect-to-band generation probabilities additionally.

In the case of the standard DOS with a mobility gap (introduced in section 2.2.) the rate equation at steady-state equilibrium and the total generation rate $G_{tot}(\hbar\omega)$ is given as

Rate equation of the CB: $$\frac{\partial}{\partial t} n = 0 = G_{VC}(\hbar\omega) + \sum_j \left\{ G_{Cj}(\hbar\omega) + T_{Cj} - R_{Cj} \right\}$$

Rate equation of the VB: $$\frac{\partial}{\partial t} p = 0 = G_{VC}(\hbar\omega) + \sum_j \left\{ G_{Vj}(\hbar\omega) + T_{Vj} - R_{Vj} \right\}$$

Total generation rate: $$G_{tot}(\hbar\omega) = G_{VC}(\hbar\omega) + \sum_j \left\{ G_{Cj}(\hbar\omega) + G_{Vj}(\hbar\omega) \right\}$$

with $j = v, c, +, 0, -$

The transitions of types A, B and C are taken into account whereas the localised-to-localised transitions of type D are suppressed. The following overview illustrates all partial rates and the corresponding notations ("R_{ij}" correspond to the recombination rates, "T_{ij}" to the thermal emission rates and "G_{ij}" to the generation rates. The indices "V" and "C" correspond to delocalised band states, "v" and "c" to localised band tail states and "+", "0", "-" to dangling bond states). The thermal emission rate of the transition of type A and the corresponding capture rate are not taken into account here. The equations of the partial rates for the numerical calculations are shown in appendix B3.4. Overview 2 shows the partial rates (recombination R_{ij}, generation G_{ij} and thermal emission T_{ij}).

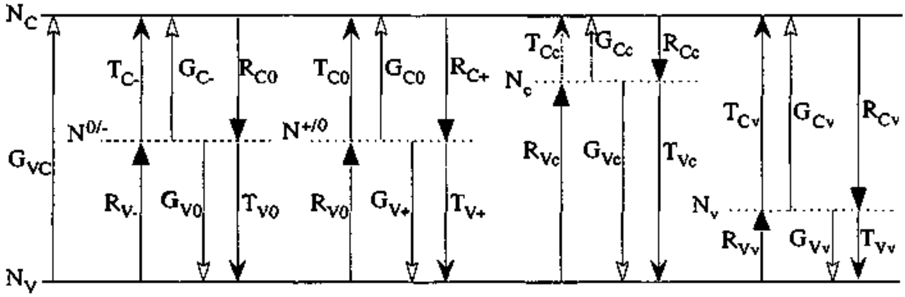

Overview 2: notation of all partial rates used for the numerical analysis.

It is assumed that the standard DOS, the mobility gap, the optical matrix element and the mobilities are equal at thermal equilibrium as well as at steady-state equilibrium. For a given set of parameters of the standard DOS and of the mobility gap, the only "free" parameter at thermal equilibrium is the Fermi level E_F, which determines the total charge $Q_{tot}(E_F)$ and the effective DOS N^{eff}_{Cmob} and N^{eff}_{Vmob}. The latter two are used in order to calculate the thermal emission probabilities. Thus, the only adtitional parameters at steady-state equilibrium are the capture cross-sections and the thermal velocities, whereas the incident flux Φ_0 and the photon energy $\hbar\omega$ art as a "free" parameter and the charge carrier densities (n and p) as "unknown" parameters. Knowing (n, p) for a specific case, it is possible to recalculate all other parameters, such as the occupation functions, the total conductivity $\sigma = e\{\mu_e n + \mu_h p\}$ and the total generation rate $G_{tot}(\hbar\omega)$.

In order to find the charge carrier densities (n and p), the two rate equations have to be zero under the charge conservation condition:

rate equations: $$\frac{\partial}{\partial t} n(p) = 0 \text{ and } \frac{\partial}{\partial t} p(n) = 0$$

charge conservation: $$Q_{tot}(E_F) = Q_{tot}(n, p)$$

The numerical approach to solve this system is quite simple. The unknown parameters are the charge carrier densities (n, p). When using the occupation functions at steady-state equilibrium, only one rate equation has to be solved, providing that the charge is conserved:

numerical approach: $$\frac{\partial}{\partial t} n(p) = 0 \quad \text{or} \quad \frac{\partial}{\partial t} p(n) = 0 \quad \text{with} \quad Q_0 = Q_{tot}(n, p)$$

As a numerical cross-check of a solution (n, p), the unused rate equation also has to be fulfilled.

3. Numerical analysis

The main goal of this chapter is to calculate CPM and PDS numerically. In a first step, the system in thermal equilibrium will be analysed, where a measured PDS spectrum will be deconvoluted within the framework of a new approach. Thus, the parameters of the DOS will be determined. In a second step the conductivity and the total generation rate will be calculated as a function of the incident photon flux and of the photon energy. This will allow one to calculate CPM and PDS in steady-state equilibrium. The main results of this chapter will be that a PDS spectrum in steady-state equilibrium is identical to the absorption spectrum at thermal equilibrium, whereas for CPM this is only the case if all capture cross sections are identical (a postulate which is probably far from being fulfilled). The generation rate is spectrally-dependent if not all capture cross sections are identical and then CPM does not necessarily detect the absolute absorption spectrum (i.e. the second CPM condition is, in general, not fulfilled).

3.1. The system in thermal equilibrium

The system of a-Si:H in thermal equilibrium is introduced and discussed in chapter 2. The corresponding definition equations for the following numerical analysis of this system in thermal equilibrium are shown in appendix B1 and B2. The numerical discretisation (HDS) used in this section is introduced in appendix C3.

3.1.1. The parameters of the numerical analysis

On the basis of the standard DOS introduced in section 2.1., of the transport concept introduced in section 2.2. and of the absorption introduced in section 2.3., the system in thermal equilibrium is here determined by the following parameters (**input**):

standard DOS: E_g^{opt}, $\bar{m}_e^*$, $\bar{m}_h^*$, E_C^0, E_V^0, N_{DB}^{tot}, $E_{DB}-E_V$, W_{DB}, U
transport properties: E_F-E_V, ε_c, ε_v, μ_e, μ_h, T
optical properties: C_0, R^2

Furthermore, if the charge neutrality condition of the dangling bonds is taken into account, the Fermi level E_F and the position of the defect N_{DB}^{tot} are related by $E_F = E_{DB} + U/2$ (see section 2.2.4. and appendix B3).

As numerical results, one gets the absorption $\alpha_{th}(\hbar\omega)$ at thermal equilibrium, the parameter z_0 of the Cody-plot, the conductivity, the effective DOS and the various charge densities (**output**):

absorption: $\alpha_{th}(\hbar\omega)$, $z_0 \equiv \sqrt{\alpha(\hbar\omega)/\hbar\omega}$
conductivity: σ, N_{Cmob}^{eff}, N_{Vmob}^{eff}
charge densities: Q_0, n, p, n_t, p_t, N_{DB}^{+}, N_{DB}^{-}

The following parameters appear here as numerical results (**output**), but they could alternatively be used as input parameters:

$$E_g^{mob},\ E_{Cmob}-E_F,\ E_{Cmob}-E_{DB},\ N_C^0,\ N_V^0,\ N_{Cmob},\ N_{Vmob}$$

3.1.2. The parameters presented in published literature

In order to determine the parameters of the system in thermal equilibrium, the author first analysed the values given in published literature. Tab.1 shows some values determined by different methods which are indicated.

Method		(inverse) x-ray photo emission	CPM deconvolution	photoelectric yield	PDS deconvolution
References	[Cody 84]	[Jackson 85]	[Vanecek 83]	[Ley 87]	[Wyrsch 92]
N_C^0 [$cm^{-3}eV^{-3/2}$]	-	$3.1\,10^{22}$ *	$6.7\,10^{21}$	-	$8.5\,10^{20}$
N_V^0 [$cm^{-3}eV^{-3/2}$]	-	$2.4\,10^{22}$ *	$6.7\,10^{21}$	$1.5\,10^{22}$ *	$8.5\,10^{20}$
$\breve{m}_e^* / m_e$	-	2.7	1	-	0.25
$\breve{m}_h^* / m_e$	-	2.3	1	1.6	0.25
E_g^{opt} [eV]	1.64	-	1.8	-	1.75
E_g^{mob} [eV]	1.67	2.0	-	-	-
R^2 [Å^2]	0.9	10	952 **	-	5164
N_{Cmob} [$cm^{-3}eV^{-1}$]	-	$4-8\,10^{21}$	-	-	$9.8\,10^{19}$
N_{Vmob} [$cm^{-3}eV^{-1}$]	-	$4-8\,10^{21}$	-	$2-3\,10^{21}$	$9.8\,10^{19}$

Tab.1: some basic references for the parameters of the DOS.
Notes: * deduced from graph (approximation)
** originally P^2= constant (recalculated, approximation)

The system in thermal equilibrium is determined by a full SET of parameters. The author distinguishes parameters which determine the band states / band tail states ("band parameters of the standard DOS"), parameters which describe the defect states ("defect parameters of the standard DOS"), parameters which are related to the transport ("transport parameters") and parameters which correspond to the optical properties ("optical parameters"). All these parameters are discussed next.

The band parameters of the standard DOS:

In section 2.1. the author suggested a description of the parabolic conduction and valence bands by some effective DOS masses ($\breve{m}_e^*,\ \breve{m}_h^*$) instead of the bending parameters ($N_C^0,\ N_V^0$) (see also appendix C1.1.). In tab.1 one notices a large variation in the values of these parameters (e.g. $\breve{m}_e^*$ = 0.25 - 2.7 m_e). The next section will indicate that these parameters are related to the values of the optical matrix element R^2. Further, tab.1 indicates that the values of the DOS at the mobility edges ($N_{Cmob},\ N_{Vmob}$) as well as the values of the optical bandgap E_g^{opt} also vary over a large range.

The slopes of the exponential tails (E_C^0 and E_V^0) are determined by two different experiments. The slope of the conduction band is approximately equal to kT, found by time-of-flight measurements (TOF) (see e.g. [Wyrsch 92]), whereas the slope of the valence band is e.g. determined by the deconvolution of CPM or PDS measurements as well as by TOF measurements (see e.g. [Wyrsch 92]).

The defect parameters of the standard DOS:

In this study, the defect peak of the DOS (dangling bonds) is given by its energy position E_{DB}, the total defect density N_{DB}^{tot}, the width W_{DB} of the assumed Gaussian distribution and the correlation energy U.

The dangling bonds in crystalline semiconductors are surface defects with a small volume (atomic radius 1Å). The dangling bonds in amorphous silicon may (to a great extent) be located at internal void surfaces ("Swiss cheese"). Electron Spin Resonance (ESR) measurements detect single-occupied spin densities. The g-factor of 2.055 has been identified as the g-factor of dangling bonds in amorphous silicon with an ESR dangling bond spin density N_S. In amorphous silicon without hydrogen, N_S is high ($10^{19} - 10^{20}cm^{-3}$) [Elliott 90]. In hydrogenated amorphous silicon (a-Si:H) N_S is much lower. In terms of the three dangling bond states (D^+, D^0, D^-) the ESR dangling bond spin density N_S corresponds to the density of single-occupied dangling bonds (D^0).

In the case of undoped a-Si:H it is an established practice to assume that the "deep defect absorption values" of a measured absorption spectrum is related to the measured ESR dangling bond spin density N_S. With the help of such a calibration the "deep defect absorption values" of any measured absorption spectrum is related to the total deep defect density N_{DB}^{tot} under the assumption that the total deep defect density N_{DB}^{tot} of an undoped a-Si:H layer is identical to the ESR dangling bond spin density N_S.

Different methods exist to determine the "deep defect absorption values" of a measured absorption spectrum. Here, the integrated excess absorption and the single-energy absorption are discussed (for details see appendix C2).

Jackson and Amer [82] introduced the integrated excess absorption $\overline{\alpha}_I$ and found:

$$N_{DB} = 7.9\,10^{15}cm^{-2}eV^{-1}\,\overline{\alpha}_I \qquad \text{(for PDS spectra)}$$

Wyrsch et al. [91] introduced the single-energy absorption α_W at a specific photon energy $\hbar\omega_W$ and found:

$$N_{DB} = 1.2 - 2.5\,10^{16}cm^{-2}\,\alpha_W(\hbar\omega_W = 1.2eV) \qquad \text{(for PDS spectra)}$$

Wyrsch et al. [91] used strongly degraded layers for the determination of this proportionality factor. Favre et al. [91] showed that the ESR dangling bond spin density N_S of annealed layers depends on thickness. Further, fig.1 - discussed later on - indicates that the ESR dangling bond spin density N_S of the dangling bond states as a function of the gas dopant ratio does not show its maximum for undoped a-Si:H, but for slightly "p-type" a-Si:H in the annealed state. Note that the absolute values of the ESR dangling bond spin densities N_S are uncertain within at least a factor of 10 [Favre 94/2].

Therefore, the author would like to point out that N_S is only a lower limit of the total defect density N_{DB}^{tot} depending on the correlation energy U (and the gas dopant ratio). If the correlation energy U is negative, the ESR dangling bond spin density N_S can be much lower than the total deep defect density N_{DB}^{tot}. Anderson [75], as well as Adler [76], studied negative correlation energy for amorphous materials. However, it is an established practice to assume a positive correlation energy U in the case of a-Si:H based on ESR measurements on doped samples shown in fig.1.

In general, the correlation energy U is defined as the difference of "the repulsive Coulomb interaction between the two spatially correlated electrons occupying the same defect orbital" and "the structural relaxation energy which can be gained by the defect due to the additional electron-phonon coupling in the doubly occupied state" [Stutzmann 85].

Dersch et al. [81] identified the maximum of the dangling bond peak in fig.1 as the total dangling bond density N_{DB}^{tot}. He assumed that this total dangling bond density was independent of the gas dopant ratio and found a positive correlation energy of U = 0.4eV. Stutzmann [87] correlated the "deep defect absorption value" of PDS spectra with the ESR dangling bond spin density N_S shown in fig.1 and found U = 0.2eV ± 0.1 eV.

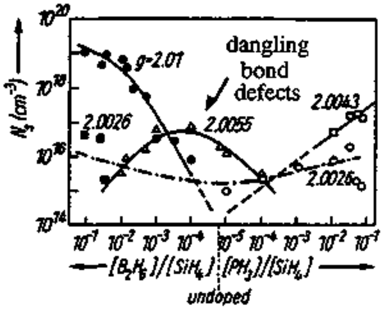

Fig.1: the measured ESR spin density N_S as a function of the gas dopant ratio in a-Si:H. [Dersch 81]

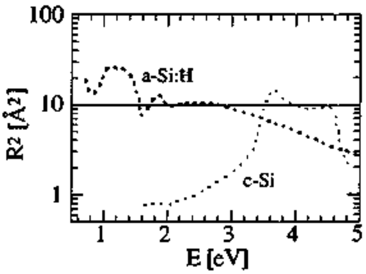

Fig.2: the optical matrix element R^2 as a function of the photon energy $\hbar\omega$ for a-Si:H and c-Si. [Jackson 85]

The transport parameters:

The value of the mobility bandgap E_g^{mob} is in the range of 1.8 - 2eV as estimated by Jackson et al. [85], Lee et al. [89] and Dawson et al. [92]. The ratio of the charge carrier mobilities (μ_e / μ_h) varies between 1 and 10 in published literature (see tab. 3). The Fermi-level E_F can be estimated by the measurement of the dark conductivity σ after annealing [Overhof 89] or by measuring the thermal activation energy [Overhof 89]. The threshold energies of the mobility gap (ε_c, ε_v) connect the optical bandgap (tab.1: E_g^{opt} = 1.64 - 1.8 eV) with the mobility gap E_g^{mob} (E_g^{mob} = 1.8 - 2eV). Their sum ($\varepsilon_c + \varepsilon_v$) can then lie between 0 and 0.36eV.

The optical parameters:

The absorption can be written as

$$\alpha(\hbar\omega) = C_0\, \hbar\omega\, R^2\, J(\hbar\omega) \qquad \text{with } C_0 \equiv \frac{(2\pi)^2}{n_0}\frac{e^2}{\hbar c_0}\frac{1}{3\rho_A}$$

Cody [84] showed that the refraction coefficient n_0 varies between 3.6 and 5 for $\hbar\omega$=0.5-2.5eV. As a matter of simplicity, the refraction coefficient n_0 is assumed to be constant here.

The atomic density ρ_A, here, is assumed to be identical to the atomic density of c-Si. In fact, the atomic density ρ_A of a-Si:H depends on the specific sample and can be smaller than in the case of c-Si, maybe due to some large voids ("Swiss cheese"). The author expects neither absorption nor transport within these voids. "Outside" these voids the distances between the atoms in a-Si:H and c-Si are identical (see e.g. [Street 91]). Therefore, the author chose the atomic density ρ_A of c-Si for a-Si:H.

The proportionality factor C_0 is then given as

$$C_0 \equiv 4.57\,10^{-41}\,\text{cm}^5\,\text{Å}^{-2} \qquad \text{with } \rho_A = 5\,10^{22}\,\text{cm}^{-3} \text{ and } n_0 = 4.2$$

Fig.2 shows the optical matrix element R^2 for a-Si:H and c-Si as a function of the photon energy $\hbar\omega$ published by Jackson et al. [85]. Unfortunately, the exact procedure of its deduction was not published. Fig.2 is the basic reference for an energy-independent optical matrix element in a-Si:H, but tab. 1 indicates that the absolute value of R^2 varies in published literature over more than three orders of magnitude (0.9 Å^2 and >5000 Å^2).

3.1.3. Deconvolution of a PDS spectrum

From the previous section one has to note that many values of the a-Si:H parameters at thermal equilibrium are not strictly fixed. In this section the author introduces a new procedure for the deconvolution of an absorption spectrum at thermal equilibrium. The goal of this procedure is not to present some "very best fits", but it is (i) to fulfil as many conditions (e.g. conditions which determine the thermal equilibrium) as possible at the same time and (ii) to find which values of the parameters at all can be fixed by a deconvolution approach and which not. In fact, in a numerical work one can come up easily with a situation where the system is overdetermined. This indeed seems to be the case here with the system in thermal equilibrium as is defined by 17 (input) parameters and by the equations of appendix B2 and some "very best fits" could screen an overdetermination.

For this new deconvolution approach, the author suggests that the measured and the calculated absorption spectrum as well as the measured and the calculated Cody-plot have to be identical at the same time. Further, the localised-to-localised transitions (transitions of type D, see section 2.3.2.) have to be dropped. The deconvolution approaches discussed in published literature do not neglect these transitions (see e.g. [Wyrsch 92]), but by neglecting them it will be possible to compare the absorption spectrum at thermal equilibrium with the absorption spectrum in steady-state equilibrium (discussed in section 3.2.). Note that it is an established procedure to drop these transitions for a system in steady-state equilibrium. Furthermore, for the new deconvolution approach the Fermi level E_F has to be fixed in such a way that the measured dark conductivity σ_d is identical to the calculated conductivity σ at thermal equilibrium. And finally, postulation of the charge neutrality of the dangling bonds (= charge neutrality of the system) is suggested (i.e. $E_F = E_{DB} + U/2$, see section 2.2.4.). This postulate remains weak from the experimental point of view (e.g. influence of interface / surface states; accumulation of charge carriers in the dangling bond states, see section 1.7.3.), but the numerical system discussed here does not take into account any kind of inhomogeneities. - Note that in section 3.1.4. some cases are also discussed where the charge neutrality of the dangling bonds is not fulfilled ("isolated" variation in the Fermi level E_F).

One can conclude all these conditions for a system in thermal equilibrium which are proposed to be fulfilled, as follows:

New deconvolution approach at thermal equilibrium:

- Deconvolution of the measured absorption spectrum $\alpha(\hbar\omega)$
- Deconvolution of the Cody-plot $z_0 \equiv \sqrt{\alpha(\hbar\omega) / \hbar\omega}$
- Suppression of localised-to-localised transitions (transitions of type D)
- Adaptation of the Fermi level E_F to the measured dark conductivity σ_d
- Taking the charge neutrality of the dangling bonds into account: $E_F = E_{DB} + U/2$

Wyrsch [92] discussed the deconvolution of PDS and CPM spectra at thermal equilibrium. In contrast, the author will calculate numerically the PDS and CPM spectra at steady-state equilibrium in section 3.2. For the new deconvolution approach at thermal equilibrium the author uses a PDS spectrum and not a CPM spectrum here because it can be expected that a PDS spectrum at thermal equilibrium is identical to a PDS spectrum in steady-state equilibrium. In fact, the PDS spectrum is experimentally not found to be influenced by the probe beam (= HeNe laser, see chapter 1) and it will be shown in section 3.2. that the pump beam can hardly influence the PDS spectrum. In contrast, it will be shown in section 3.2. that CPM is very sensitive to the values of the steady-state equilibrium parameters.

A PDS spectrum of an annealed film was arbitrarily chosen for this new deconvolution approach (sample D170293 introduced in section 1.4.4 and in appendix A2.4.: d=2.53µm, T_S=300K, $\sigma_d \approx 8\,10^{-10}\Omega^{-1}\mathrm{cm}^{-1}$).

Four input parameter SETs were selected for the new deconvolution approach, noted as SET1, SET2, SET3 and SET4 with different optical matrix elements $R^2 = 1\,\text{Å}^2$, $10\,\text{Å}^2$, $100\,\text{Å}^2$ and $1000\,\text{Å}^2$ (corresponding to the wide range of values used in published literature and shown in tab.1).

The values of the following 8 parameters were determined by this deconvolution (see tab.2): The total defect density N_{DB}^{tot}, the Fermi level position E_F, the defect position E_{DB}, the effective DOS masses $\tilde{m}_e^*$ and $\tilde{m}_h^*$, the threshold energies of the mobility gap (ε_c and ε_v) and the optical bandgap E_g^{opt}.

The following values were not varied for this deconvolution (see tab.2): the correlation energy U of the deep defects (dangling bonds) were chosen as 0.2eV [Stutzmann 87], the half width W_{DB} of the gaussian deep defect peak as 0.09eV (determined by Wyrsch's deconvolution approach [92]), the slopes of the exponential conduction band tail E_C^0 as 27meV, the proportionality factor C_0 between the absorption and the JDOS as $4.57\,10^{-41}\,\mathrm{cm}^5\,\text{Å}^{-2}$ (see section 3.1.1.), the temperature T as 300K (room temperature), the mobilities of the charge carriers as $\mu_e = 10\ \mathrm{cm}^2/(\mathrm{Vs})$ and $\mu_h = 1\ \mathrm{cm}^2/(\mathrm{Vs})$ (see chapter 2 and [Vaillant 86]).

The input and output parameters are shown in tab. 2. The occupation of the DOS, the absorption $\alpha_{th}(\hbar\omega)$ and the Cody plot $z_0(\hbar\omega)$ at thermal equilibrium are shown for SET 1-4 in fig.3. As can be seen in fig.3, all four SETs fit the experimental data in a reasonable way. **This means that the optical matrix element R^2 can not been determined by this deconvolution approach.**

In fig.3, the total absorption is drawn in bold lines, the partial absorptions as straight lines and the suppressed localised-to-localised transitions (transitions of type D) are shown as dashed lines. The partial absorptions are numbered as followed in fig.3 (see also appendix B2.4.):

(1): $V \leftrightarrow C$
(2): $V \leftrightarrow c$
(3): $V \leftrightarrow v$
(4): $C \leftrightarrow c$
(5): $C \leftrightarrow v$
(6): $V \leftrightarrow D^+$
(7): $V \leftrightarrow D^0$
(8): $C \leftrightarrow D^0$
(9): $C \leftrightarrow D^-$
(10): $(v \leftrightarrow c)$

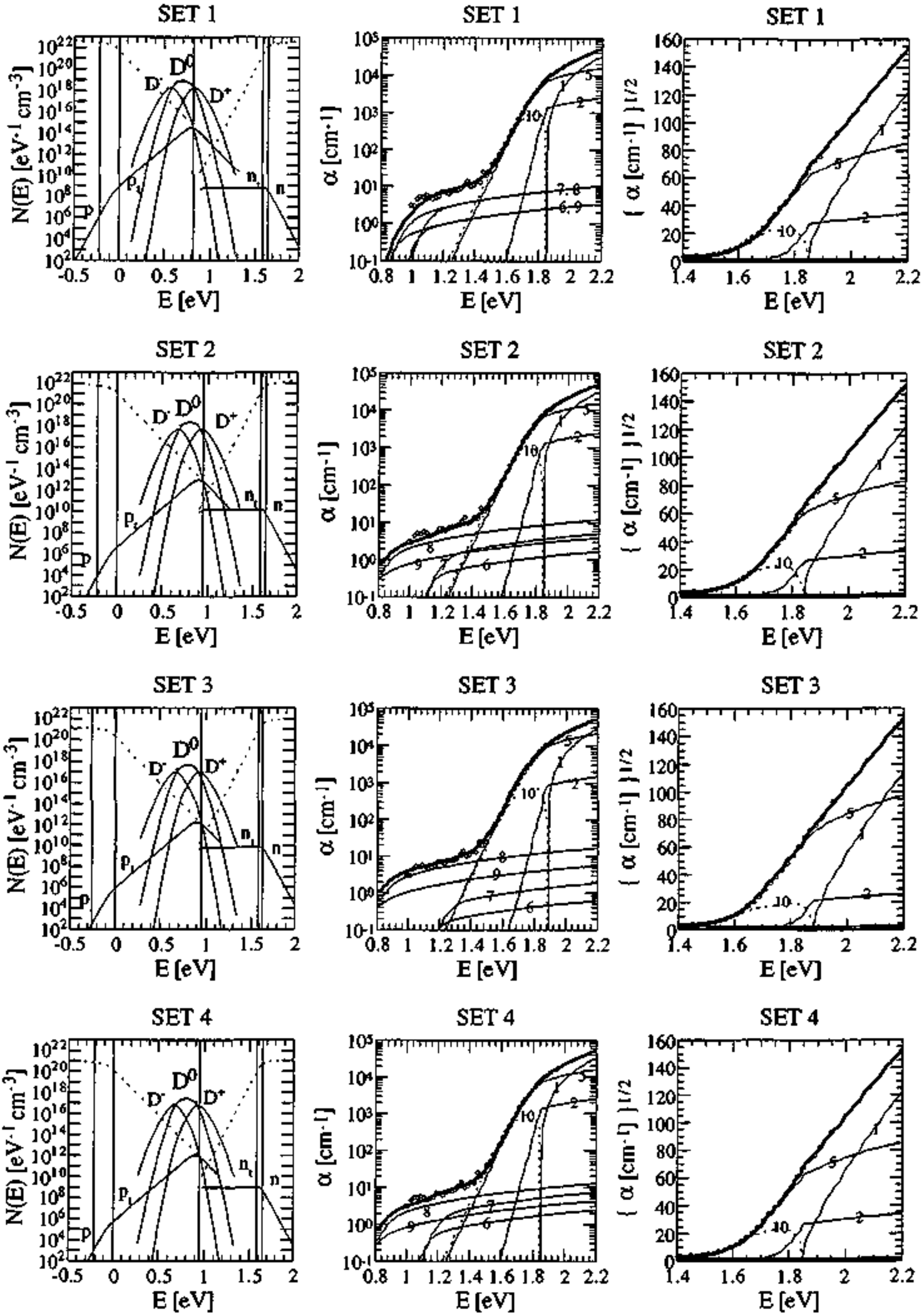

Fig.3: SET 1-4: occupation of the DOS, the absorption $\alpha_{th}(\hbar\omega)$ and the Cody plot $z_0(\hbar\omega)$ at thermal equilibrium. (Deconvolution of a PDS spectrum and of its Cody plot; sample D170293).

INPUT	**SET 1**	**SET 2**	**SET 3**	**SET 4**
R^2 [$\mathring{A}^2$]	**1**	**10**	**100**	**1000**
N_{DB}^{tot} [cm^{-3}]	$2\,10^{18}$	$5\,10^{17}$	$1.1\,10^{17}$	$6\,10^{16}$
$E_F - E_V$ [eV]	0.8	0.9	0.9	0.9
$E_{DB} - E_V$ [eV]	0.7	0.8	0.8	0.8
$\bar{m}_e^* / m_e$	4.25	2.5	1.85	0.5
$\breve{m}_h^* / m_e$	4.25	1.5	0.5	0.36
ε_c [eV]	0.05	0.05	0.03	0.05
ε_v [eV]	0.2	0.2	0.25	0.2
E_g^{opt} [eV]	1.6	1.59	1.6	1.6
U [eV]	<------------	0.2	------------>	------------>
W_{DB} [eV]	<------------	0.09	------------>	------------>
E_C^0 [meV]	<------------	27	------------>	------------>
E_V^0 [meV]	<------------	50	------------>	------------>
C_0 [$cm^{-5}\mathring{A}^{-2}$]	<------------	$4.57\,10^{-41}$	------------>	------------>
μ_e [$cm^2(Vs)^{-1}$]	<------------	10	------------>	------------>
μ_h [$cm^2(Vs)^{-1}$]	<------------	1	------------>	------------>
T [K]	<------------	300	------------>	------------>
OUTPUT	**SET 1**	**SET 2**	**SET 3**	**SET 4**
E_g^{mob} [eV]	1.85	1.84	1.88	1.85
$E_{Cmob} - E_F$ [eV]	0.85	0.74	0.73	0.75
$E_{Cmob} - E_{DB}$ [eV]	0.95	0.84	0.83	0.85
N_C^0 [$cm^{-3}eV^{-3/2}$]	$5.9\,10^{22}$	$2.7\,10^{22}$	$1.7\,10^{22}$	$2.4\,10^{21}$
N_V^0 [$cm^{-3}eV^{-3/2}$]	$5.9\,10^{22}$	$1.2\,10^{22}$	$2.4\,10^{21}$	$1.5\,10^{21}$
N_{Cmob} [$cm^{-3}eV^{-1}$]	$1.3\,10^{22}$	$6.0\,10^{21}$	$2.9\,10^{21}$	$5.4\,10^{20}$
N_{Vmob} [$cm^{-3}eV^{-1}$]	$2.6\,10^{22}$	$5.4\,10^{21}$	$1.5\,10^{21}$	$6.7\,10^{20}$
N_{Cmob}^{eff} [cm^{-3}]	$4.4\,10^{20}$	$2.0\,10^{20}$	$1.1\,10^{20}$	$1.8\,10^{19}$
N_{Vmob}^{eff} [cm^{-3}]	$7.6\,10^{20}$	$1.6\,10^{20}$	$2.9\,10^{19}$	$1.9\,10^{19}$
n [cm^{-3}]	$9.3\,10^{6}$	$2.5\,10^{8}$	$1.9\,10^{8}$	$1.5\,10^{7}$
p [cm^{-3}]	$6.3\,10^{4}$	$3.2\,10^{2}$	$9.2\,10^{0}$	$3.8\,10^{1}$
σ [$\Omega^{-1}cm^{-1}$]	$1.5\,10^{-11}$	$4\,10^{-10}$	$3\,10^{-10}$	$2.5\,10^{-11}$
Q_0 [cm^{-3}]	$+5.5\,10^{13}$	$+1.5\,10^{12}$	$+2.5\,10^{11}$	$+1.8\,10^{11}$

Tab.2: input and output parameters of the proposed deconvolution approach at thermal equilibrium. SET 1-4 have optical matrix elements R^2 that vary over three orders of magnitude different.

Discussion of the values of the four SETs (cf. tab. 2.):

One remarks that the lower the value of the optical matrix element R^2, the higher the total defect density N_{DB}^{tot} of the dangling bonds; however, there is no linear correlation between these two parameters (see discussion of fig.34) and, additionally, the effective DOS masses ($\breve{m}_e^*$, $\breve{m}_h^*$) interact: the lower the optical matrix element R^2, the higher the effective DOS masses ($\breve{m}_e^*$, $\breve{m}_h^*$).

The fact that the localised-to-localised transitions (transitions of type D) are neglected here leads to an asymmetry in the effective DOS masses ($\breve{m}_e^* \geq \breve{m}_h^*$) and/or an asymmetry in the threshold energies of the mobility gap ($\varepsilon_c << \varepsilon_v$). Due to the fact that the localised-to-localised transitions are neglected here, the partial absorption of localised valence band tail states to delocalised conduction band states (v -> C) is always much larger than the partial absorption of delocalised valence band states to localised conduction band tail states (V -> c). The absorption spectra, shown in fig.3, are dominated by transitions of type B and C (even above the mobility gap, here up to 2eV) which means that up to 2eV the total generation rate G_{tot} (see section 2.4.4. and section 2.4.5.) is not dominated by delocalised band-to-band transitions (transitions of type A) either. (The transition types A, B, C and D are introduced in section 2.3.2.)

The optical bandgap ($E_g^{opt} = 1.6\text{eV}$) as well as the mobility gap ($E_g^{mob} \approx 1.85\text{eV}$) have remained approximately constant for all these cases as were the threshold energies of the mobility gap ($\varepsilon_c \approx 0.05\text{eV}$, $\varepsilon_v \approx 0.2\text{eV}$). Therefore, the DOS at the mobility edges (N_{Cmob}, N_{Vmob}) basically increase with increasing effective DOS masses ($\breve{m}_e^*$, $\breve{m}_h^*$). The effective DOS at the mobility edges (N_{Cmob}^{eff}, N_{Vmob}^{eff}) increase with decreasing effective DOS masses ($\breve{m}_e^*$, $\breve{m}_h^*$). Further, they are determined by the threshold energies of the mobility gap (ε_c, ε_v) (c.f. appendix B4). Here, the ratio of the effective DOS at the mobility gap ($N_{Cmob}^{eff} / N_{Vmob}^{eff}$) was chosen to be about 1, and the ratio of the mobilities was chosen to be $\mu_e / \mu_h = 10$. However, it may be quite simple to select some effective DOS at the mobility gap with a ratio of $N_{Cmob}^{eff} / N_{Vmob}^{eff} = 10$ and some charge carrier mobilities with a ratio of $\mu_e / \mu_h = 1$. Both of these alternate cases result in the same conductivity at thermal equilibrium.

The conductivity at thermal equilibrium is determined by the effective DOS at the mobility edges (N_{Cmob}^{eff}, N_{Vmob}^{eff}) and the Fermi level position E_F. In SET1, $E_F - E_V$ [eV] was chosen as 0.8eV. In SET 2-4, $E_F - E_V$ [eV] was chosen as 0.9eV. Due to the charge neutrality condition of the dangling bonds ($E_{DB} = E_F - U/2$), this lead to a change in the defect position E_F with a resulting change in the absorption below 1.1eV. Whenever the charge neutrality condition of the dangling bonds was taken into account, the total charge Q_0 was still not exactly zero and was dominated by the charge in the valence band tail (see DOS in fig. 3 and discussion in section 2.2.4.).

The goal of this deconvolution was not to present some "very best fits" but to test the proposed deconvolution approach. Whenever the optical matrix elements R^2 vary over three orders of magnitude, one recognises that the partial absorptions in fig. 3 look quite similar for the four parameter SETs because of the suppressed localised-to-localised transitions.

For the following numerical analysis, SET2 has been chosen because the effective DOS masses ($\breve{m}_e^*$, $\breve{m}_h^*$) and the optical matrix element R^2 correspond in a reasonable way to the values of Jackson et al. [85] and of Ley et al. [87], shown in tab. 1.

Note that the deep defect absorption value of this PDS spectrum is given as $\alpha_{PDS}(1.2eV) \approx 8cm^{-1}$, which corresponds to a total defect density of $N_{DB}^{tot} \approx 1.6\,10^{17}cm^{-3}$ while using the calibration formula of Wyrsch et al. [91] (discussed in 3.1.1. and in appendix C2). This total defect density value could even be lower, if the PDS spectrum is influenced in the deep defect absorption range by interface / surface states. In contrast, the total defect density ($N_{DB}^{tot} = 5\,10^{17}cm^{-3}$) of SET2 is higher by a factor of 2-3 due to the small value of the optical matrix element of SET2 ($R^2 = 10\,\text{Å}^2$) assumed here.

3.1.4. Sensitivity analysis of the important parameters of the absorption spectrum

The plots shown in this section are based on the parameters of SET 2. The goal of this section will be to get an idea of the sensitivity of the different parameters on the absorption spectrum. It has to be pointed out that, basically, one parameter is varied while the other parameters are kept constant. This section is important to isolate the critical parameters controlling the absorption spectra.

The band parameters of the standard DOS (cf. fig.4):

The variation in the optical bandgap E_g^{opt} leads to a shift of the absorption spectrum on the horizontal axis. The variation of the optical matrix element R^2 leads to a change in the absorption spectrum in the vertical axis under the assumption used here that the optical matrix element is energy-independent and identical for transitions of types A, B and C.

The value of the effective DOS masses $\breve{m}_e^*$ and $\breve{m}_h^*$ can also influence the whole absorption spectrum. In the range of the band-to-band transitions, the absorption increases due to an increase in the effective DOS masses $\breve{m}^*$: similarly, the absorption increases due to an increase in the optical matrix element R^2. Therefore, a low optical matrix element R^2 is related to a high value of the effective DOS mass $\breve{m}^*$ for the same absorption spectrum.

The slope of the exponential conduction band tail E_C^0 influences the absorption spectrum only in the case of unrealistically high values. Otherwise, the absorption spectrum is quite insensitive to the slope E_C^0 of the exponential conduction band tail. In contrast, the absorption spectrum is strongly influenced by the slope of the exponential valence band tail E_V^0. One recognises that the absorption spectrum shows no discontinuity, due to the connection point introduced in chapter 2.

The valence band threshold energy ε_v of the mobility gap does not seriously influence the absorption spectrum. In contrast, the conduction band threshold energy ε_c of the mobility gap influences the absorption spectrum in a similar way to a change in the optical bandgap E_g^{opt}. The Cody-plots would also be influenced by the variation of the threshold energies.

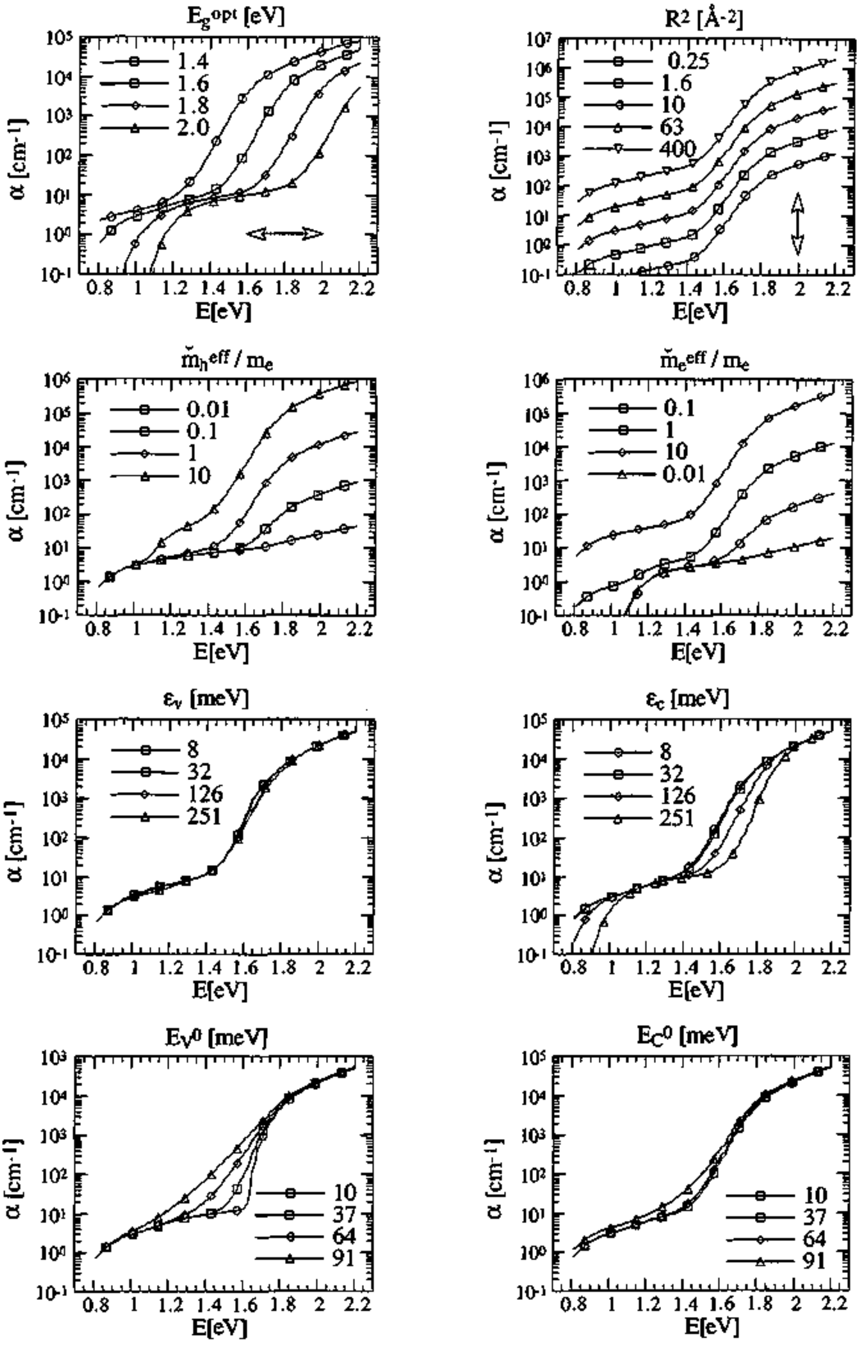

Fig.4: influence of the band parameters on the absorption $\alpha_{th}(\hbar\omega)$ at thermal equilibrium.

The defect parameters of the standard DOS (cf. fig.5):

The total deep defect density N_{DB}^{tot} is proportional to the absorption in the deep defect range. This relationship is used in the determination of N_{DB}^{tot} from the single-energy absorption α_W introduced by Wyrsch et al. [91] (see also appendix C2). The variation in the half width of the dangling bond peak W_{DB} leads to no change in the absorption spectrum, except if one takes very large values for it, so high that a part of the peak is outside the mobility gap and, thus, the numerical integration is incomplete (this is the case for W_{DB} = 1eV in fig.5). Therefore, the author would like to point out that the half-width of the dangling bond peak W_{DB} cannot be deduced from the deconvolution of an absorption spectrum.

An "isolated" variation of the correlation energy U violates the charge neutrality condition of the dangling bonds. Therefore, in a second plot, the correlation energy U and the deep defect energy position E_{DB} were both varied, while the Fermi level position E_F was kept fixed in such a way that the charge neutrality condition of the dangling bonds was fulfilled ($E_{DB} = E_F - U / 2$). An influence on the absorption spectrum can only be observed for photon energies below 1eV. Otherwise, the absorption spectra are very similar.

The "isolated" variation in the dangling bond position E_{DB}, with a fixed Fermi level position E_F, leads to a dramatic change in the absorption spectrum in the deep defect range (neglecting the charge neutrality of the dangling bonds). In a second plot, the dangling bond position E_{DB} and the Fermi level position E_F were varied, while the correlation energy U was kept fixed in such a way that the charge neutrality condition of the dangling bonds was fulfilled ($E_F = E_{DB} + U / 2$). An influence on the absorption spectrum can only be observed for photon energies below 1.2eV. Otherwise, the absorption spectra are very similar in the second plot.

The Fermi level position (cf. fig.5):

The "isolated" variation in the Fermi level position E_F is of fundamental interest. A priori, a variation in the Fermi level position violates the charge neutrality condition of the dangling bonds ($Q_0 = N_{DB}^{tot}$). If the Fermi level E_F is close to the mobility edges, the tail states are occupied and dominate the absorption spectrum in the deep defect range, as can be seen (transition 3: V ↔ v or transition 4:C ↔ c) (see also fig.27 and fig.28).

From this sensitivity analysis, the author concludes that the width of the defect peak W_{DB}, the defect level position E_{DB} and the correlation energy U cannot simply be determined by the deconvolution of a PDS spectrum. Further, the "isolated" variation in the Fermi level position E_F always leads to a violation of the charge neutrality condition of the dangling bonds. Note that the influence of all these parameters on the absorption spectrum $\alpha(\hbar\omega)$ at thermal equilibrium is expected to be similar at steady-state equilibrium. But in addition, the influence of the "steady-state parameters" (e.g. the capture cross sections) has to be analysed in the next sections.

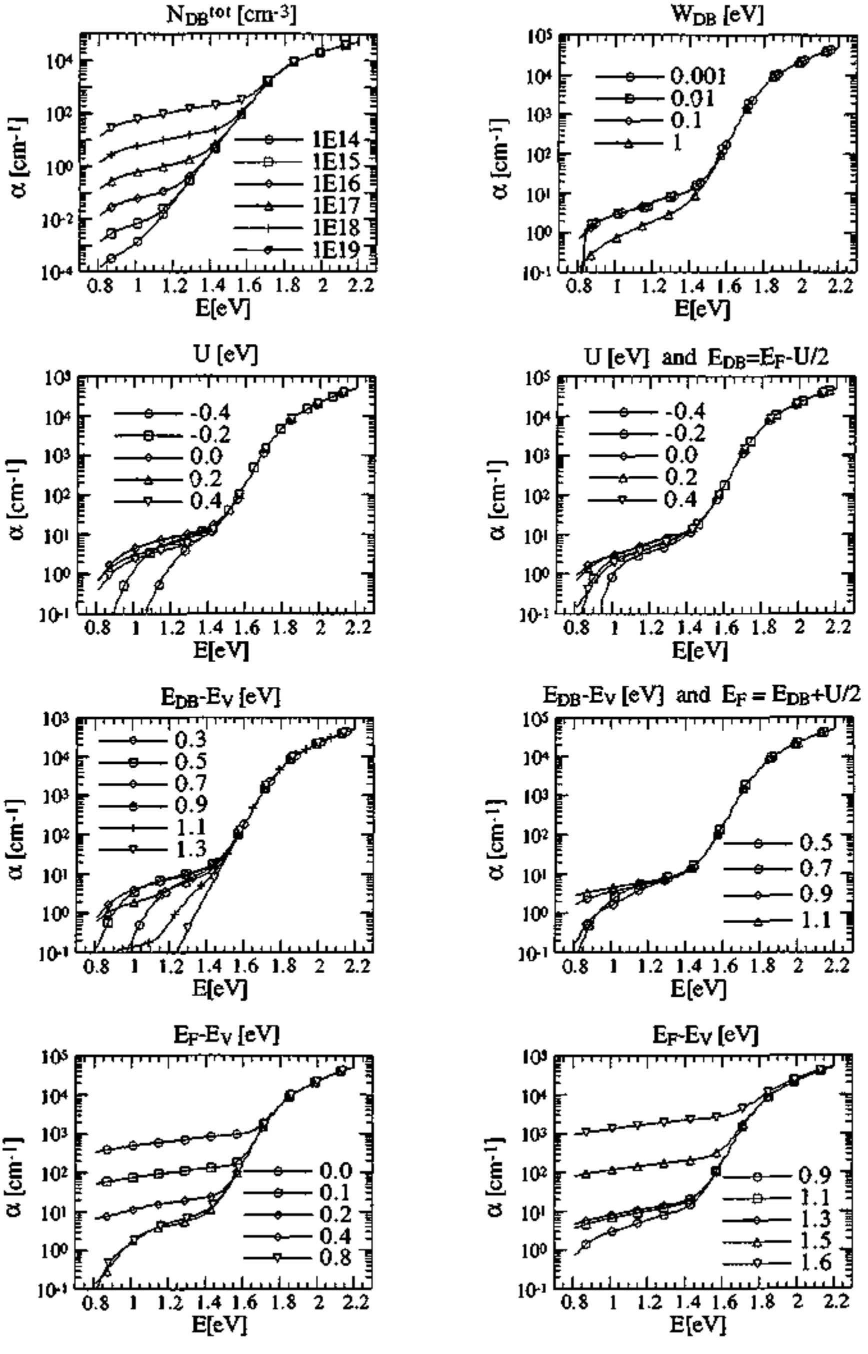

Fig.5: influence of the defect parameters and of the Fermi level E_F on the absorption $\alpha_{th}(\hbar\omega)$ at thermal equilibrium.

3.2. The system in steady-state equilibrium

In the previous section 3.1., the system of a-Si:H was studied in thermal equilibrium (no illumination). In this section, the system of a-Si:H is "illuminated by a pump beam" (cw-mode), which means that the system is in steady-state equilibrium. This will allow one to analyse the PDS and CPM techniques at steady-state equilibrium. To analyse these techniques at thermal equilibrium is - a priori - a simplification (corresponding to the deconvolution at thermal equilibrium). The steady-state equilibrium is computationally defined by solving the rate equations (see section 2.4.8.). Due to the long calculation times that would have been involved, it was not possible to execute a full deconvolution of a measured PDS or CPM spectrum at steady-state equilibrium. Nevertheless, the numerical calculations that have been performed in this section will open new understandings in reference to these two absorption measurement techniques.

The system of a-Si:H in steady-state equilibrium is introduced and discussed in chapter 2. The corresponding definition equations for the following numerical analysis of this system in steady-state equilibrium are shown in appendix B1 and B5. The numerical discretisation (LDS) used in this section is shown in appendix C3.

Note that the numerical system studied here is not limited to photon energies larger than the mobility gap ($\hbar\omega > E_g^{mob}$) which means that the photon energies can also be smaller than the mobility gap ($\hbar\omega < E_g^{mob}$). This will allow one to analyse CPM and PDS in steady-state equilibrium.

3.2.1. The parameters of the numerical analysis

On the basis of the standard DOS introduced in 2.1., of the transport concept introduced in 2.2. and of the steady state equilibrium concept introduced in 2.4., the system in steady-state equilibrium is determined by the following parameters (**input**):

standard DOS:	E_g^{opt}, $\breve{m}_e^*$, $\bar{m}_h^*$, E_C^0, E_V^0, N_{DB}^{tot}, E_{DB}, W_{DB}, U	
transport properties:	ε_c, ε_v, μ_e, μ_h, T, ν_n, ν_p	
	$Q_0(E_F)$, N_{Cmob}^{eff}, N_{Vmob}^{eff}	
cross sections:	σ_{nc}, σ_{pc},	(conduction band)
	σ_{nv}, σ_{pv},	(valence band)
	σ_n, σ_p, σ_{nU}, σ_{pU}	(defect with correlation energy)
optical properties:	C_0, R^2, Φ_0, $\hbar\omega$	

The system in steady-state equilibrium discussed here is determined by 31 parameters! In section 3.2.3., these input parameters will be reduced and in section 3.2.4., a strategy will be presented in order find some "reasonable" values. However, the remarks concerning the overdetermination of the system given in section 3.1.4. are still valid here.

As numerical results, one gets the total conductivity σ_{tot} and the total generation rate G_{tot} as a function of the incident photon flux Φ_0 and of the photon energy $\hbar\omega$ (**output**):

conductivity:	$\sigma_{tot}(\hbar\omega, \Phi_0)$
generation rate:	$G_{tot}(\hbar\omega, \Phi_0)$
charge densities:	$n, p, n_t, p_t, N_{DB}^+, N_{DB}^-$

The total conductivity $\sigma_{tot}(\hbar\omega, \Phi_0)$ will be used to analyse CPM (cw-mode). The total generation rate G_{tot} will be used to analyse PDS. The total charge of the system $Q_0(E_F)$ and the effective DOS (N_{Cmob}^{eff}, N_{Vmob}^{eff}) can be calculated from the system in thermal equilibrium.

3.2.2. The parameters presented in published literature

In order to determine the parameters of the system in steady-state equilibrium, the author first analysed the values given in published literature. Tab. 3 gives an overview of the parameters used for the modelling of the photo conductivity of a-Si:H. All these references used photon energies larger than the mobility gap ($\hbar\omega > E_g^{mob}$).

In general, the photo conductivity of a-Si:H is calculated while the effective DOS at the mobility edges (N_{Cmob}^{eff} and N_{Vmob}^{eff}), the band-to-band generation rates G_{bb} (only transitions of type A) and some recombination levels are taken into account. Vaillant and Jousse [86] calculated the photo conductivity for a four-level system: the exponential tail states were approximated by two levels and tail state recombinations were neglected; the dangling bond distribution was approximated by two further energy levels. Their numerical results are the standard reference which indicates that the dangling bond occupations do not differ significantly from the thermal equilibrium occupations for generation rates below $10^{16}cm^{-3}s^{-1}$. Later, Vaillant et al. [88] presented some analytical expressions for the case of exponential tail states in a-Si:H and thereby calculated the photo conductivity as a function of temperature.

In tab.3, one can note the uncertainty in the capture cross section values. Further, the values of the effective DOS, given in some references, differ from the analytical approach presented in appendix B4. All references in tab.3 show symmetrical bands. Some references used acceptor-like and donor-like deep defects with an infinite correlation energy. In these cases, the correlation energy U, shown in tab. 3, corresponds to the difference between the two ionisation energies (recalculated here). Some publications do not fulfil the charge neutrality condition of the dangling bonds ($E_d = E_F - U/2$) in thermal equilibrium, as indicated in tab.3.

Reference	[V86]	[V88]	[K91]	[M89]	[R92]	[K92]	[F94]
Type	layer	layer	layer	PIN	PIN	PIN	PIN
Charge neutrality	non	non	yes	-	-	-	-
E_g^{mob} [eV]	-	1.8	1.75	1.75	1.9	1.72	1.8
E_g^{opt} [eV]	1.8	-	-	-	1.72	-	-
$N_{Cmob}^{eff} = N_{Vmob}^{eff}$ [cm^{-3}]	10^{21}	-	$1.25\,10^{20}$	$1.5\,10^{20}$	$2\,10^{20}$	$2\,10^{21}$	$3\,10^{21}$
$N_{Cmob} = N_{Vmob}$ [cm^{-3}eV^{-1}]	-	10^{21}	$5\,10^{21}$	$2\,10^{21}$	-	$3\,10^{21}$	$3\,10^{21}$
E_C^0 [meV]	**	25-50	27	30	27	?	30
E_V^0 [meV]	**	65-80	50	50	50	45	45
N_{DB}^{max} [cm^{-3}]	$5\,10^{15}$	10^{14} - 10^{15}	10^{15} - 10^{17}	$5\,10^{15}$ - $5\,10^{16}$	$3\,10^{15}$	$6\,10^{15}$	10^{15}- 10^{16}
$E_{DB} - E_{Vmob}$ [eV]	0.9-1.1	0.85	0.92	0.75	≈0.66	0.93	0.8
U [eV]	0.4	0.4	0.26	0.4	0.5 *	0.22 *	0.3
W_{DB} [eV]	-	-	-	0.15	0.15	0.06A 0.1D	-
$E_F - E_{Vmob}$ [eV]	-	0.9	1.05	-	-	-	-
μ_e [cm^2(Vs)$^{-1}$]	10	10	10	10	20	10	10
μ_h [cm^2(Vs)$^{-1}$]	1	1	1	10	2	2	1
T [K]	300	variable	300	300	300	300	300
$v_n = v_p$ [cm s^{-1}]	10^7	10^7	10^7	10^7	10^7	10^7	10^7
σ_{DB}^0 [cm^2]	$3\,10^{-15}$	$3\,10^{-15}$	10^{-16}	10^{-16}	10^{-15}	10^{-16}	10^{-15}
$\sigma_{DB}^{+/-} / \sigma_{DB}^0$	5-50	50	10	100	10	100	10
σ_t^0 [cm^2]	-	10^{-15}	10^{-15}		10^{-15}	10^{-17}	10^{-15}
$\sigma_t^{+/-} / \sigma_t^0$	-	1	1		10	100	10
DOS discretisation	4		22	?	?	14	analyt.

Tab.3: parameters found in published literature for the numerical analysis of the a-Si:H photo conductivity in steady-state equilibrium in the case of undoped layers ("layers") and in the case of the i-layers of PIN solar cells ("PIN").

Note of tab.3: * deep defects without a finite correlation energy:
acceptor-like ("D") and donor-like ("A") defects;
** two tail levels, recombination suppressed

References of tab.3:

[V86] F.Vaillant and D.Jousse, Phys. Rev. B, 34 (1986) 4088
[V88] F.Vaillant, D.Jousse and J.-C.Bruyere, Phyl. Mag. B, 57 (1988) 649
[K91] J.Kocka, C.E.Nebel and C.D.Abel, Phil. Mag. B 63 (1991) 221
[M89] A.Mittagi, et.al., J.Appl.Phys. 66 (1989) 2667
[R92] F.A.Rubinelli, S.J.Fonash and J.K.Arch, PVSEC-6, New Delhi, India, February 1992
[K92] W.J. Kopetzy, thesis, Technische Universität, Munich, 1992
[F94] D.Fischer, thesis, University of Neuchâtel, 1994

Following are some remarks concerning the numerical analysis of sub-band-gap photo conductivity in a-Si:H ($\hbar\omega < E_g^{mob}$). Bube et al. [92] presented the first numerical calculations of CPM while applying Lucovsky's c-Si absorption model [65] to a-Si:H. They used very large capture cross sections (discussion see appendix C4) and neglected the thermal emission probabilities. Bube et al. [92] concluded that CPM only worked under some specific conditions (e.g. corresponding to the first CPM condition, see chapter 1). Platz et al. [93] presented some CPM calculations, based on a model with an acceptor-like and a donor-like deep defect peak without a finite correlation energy. In contrast to the conclusions of Bube et al. [92], Platz et al. [93] concluded that CPM is insensitive to the Fermi level position E_F as well as to the capture cross sections of the deep defects. Furthermore, they assumed identical mobilities and found that the majority charge carrier of the CPM current can change as a function of the photon energy $\hbar\omega$, without an influence on the CPM spectra. Mittiga et al. [90] analysed CPM on solar cells for a deep defect without a finite correlation energy. He concluded that CPM on solar cells detect the deep defect density only within a factor of 2, under the assumption that the recombination can be neglected.

Note that the system in steady-state equilibrium discussed here takes into account the thermal emission probabilities and the defect-to-band generation probabilities. A defect peak with a finite correlation energy was chosen for deep defects. It acts in a different way to an acceptor-like and a donor-like deep defect peak without a finite correlation energy (see chapter 2).

3.2.3. Reduction of the input parameters

The author introduced the following reduction of the parameters of the system in steady-state equilibrium. The thermal velocities of each charge carrier type were assumed to be equal and fixed, corresponding to the references of tab.3 (discussion see appendix C5):

thermal velocity: $v_{th} \equiv v_n = v_p = 10^7 \mathrm{cm\,s^{-1}}$

Continuing, the author followed the arguments of Vaillant and Jousse [86] and used only two capture cross section values for the dangling bonds σ^0 (neutral) and $\sigma^{+/-}$ (charged), instead of the four capture cross section values σ_n, σ_p, σ_{nU} and σ_{pU} used in chapter 2 (defect with a finite correlation energy).

neutral dangling bond states: $\sigma^0 \equiv \sigma_p = \sigma_{nU}$
charged dangling bond states: $\sigma^{+/-} \equiv \sigma_n = \sigma_{pU}$
ratio: $r_{DB} \equiv \sigma^{+/-} / \sigma^0$

Finally, the author assumed that capture cross sections of the localised band tail states are all identical, mainly with the argument that the physical origin of the exponential tail states is contradictory (see chapter 2):

localised band tail states: $\sigma_t \equiv \sigma_{nc} = \sigma_{pc} = \sigma_{nv} = \sigma_{pv}$

Note that the recombination by these localised band tail states is taken into account here, additionally to the recombination by the deep defects. Some remarks concerning the capture cross sections are given in appendix C4. In contrast to crystalline semiconductors, no physical approach exists to calculate the capture cross sections in amorphous semiconductors.

Additionally to the parameters determining the system in thermal equilibrium (see section 3.1.1.), the system in steady-state equilibrium is determined by the following 5, additional parameters: the capture cross sections of the dangling bonds (σ^0 and $\sigma^{+/-}$), the capture cross section of the localised band tail states σ_t and the properties of the pump beam (incident photon flux Φ_0 and photon energy $\hbar\omega$).

From the analytical analysis given in chapter 2, one can expect that the system in steady-state equilibrium is determined basically by the following three important ratios:

$$r_{DB} \equiv \sigma^{+/-} / \sigma^0 \qquad r^t_{DB} \equiv \sigma_t / \sigma^0 \qquad \theta_{DB} \equiv R^2 / \sigma^0$$

r_{DB} corresponds to the ratio of the charged and the neutral dangling bond capture cross section, r^t_{DB} to the capture cross section ratio of the localised band tail states and the neutral dangling bond states and θ_{DB} to the ratio of the optical matrix element and the neutral dangling bond capture cross section. The latter was already introduced in a more general way in chapter 2.

3.2.4. Parameters for the numerical calculation at steady-state equilibrium

The author selected SET2 (of tab. 2) from the deconvolution approach at thermal equilibrium (see section 3.1.3.) as the set of fixed parameters for a further study. For the calculation of the steady state equilibrium, two cases of the important ratios (r_{DB}, r^t_{DB}, θ_{DB}) were selected on the one hand, on the other, two different values of the total deep defect density N^{tot}_{DB} ($5\,10^{15}$ cm^{-3}, $5\,10^{17}$ cm^{-3}) were chosen. These two values correspond approximately to those of an annealed and of a light-soaked sample, respectively. The Fermi level position E_F was not changed between these sets. This lead to SET a, SET b, SET c and SET d, as shown in tab.4.

Parameters:	SET a	SET b	SET c	SET d
σ^0 [cm^2]	10^{-15}	10^{-15}	10^{-16}	10^{-16}
$\sigma^{+/-}$ [cm^2]	10^{-15}	10^{-15}	10^{-14}	10^{-14}
σ_t [cm^2]	10^{-15}	10^{-15}	10^{-15}	10^{-15}
N^{tot}_{DB} [cm^{-3}]	$5\,10^{17}$	$5\,10^{15}$	$5\,10^{17}$	$5\,10^{15}$
$r_{DB} \equiv \sigma^{+/-} / \sigma^0$	1	1	100	100
$r^t_{DB} \equiv \sigma_t / \sigma^0$	1	1	10	10
$\theta_{DB} \equiv R^2 / \sigma^0$	1	1	10	10

Tab.4: parameters in order to calculate the steady-state equilibrium (input).

For SETs 2a&b, all capture cross section were chosen to be identical to the optical matrix element R^2, which means that the corresponding ratios are all equal to one (cf. tab.3):

$$\text{SETs 2a\&b:} \qquad r_{DB} = r'_{DB} = \theta_{DB} = 1$$

For SETs 2c&d, the capture cross section of the charged dangling honds were increased by a factor 10 and the capture cross section of the neutral dangling bonds were decreased by a factor 10. This lead to a ratio r_{DB} of 100 between the charged and the uncharged dangling bond capture cross sections (cf. tab.3):

SETs 2c&d: dangling bonds: $\sigma^{+/-} = 10^{-14}\ \mathrm{cm}^2$ (charged)
$\sigma^0 = 10^{-16}\ \mathrm{cm}^2$ (neutral)
else: $\sigma_t = R^2 = 10\ \text{Å}^2 = 10^{-15}\ \mathrm{cm}^2$

For SETs 2a&c, the total deep defect density N_{DB}^{tot} is high ($5\,10^{17}\ \mathrm{cm}^{-3}$) and for SETs 2b&d, the total deep defect density N_{DB}^{tot} is low ($5\,10^{15}\ \mathrm{cm}^{-3}$).

Note: Whereas the deconvolution in thermal equilibrium (presented in section 3.1.3.) was calculated with the discretisation set HDS, the following results in steady-state equilibrium were calculated with the discretisation set LDS (see appendix C3). Therefore, the optical bandgap of SET2 was changed from $E_g^{opt} = 1.59\mathrm{eV}$ (HDS) to 1.6eV (LDS). Note further that all numerical results for the PDS analysis (based on SETs 2a-d) are shown in appendix C7, whereas all numerical results for the CPM analysis (based on SETs 2a-d) are shown in appendix C8; but only some of them will be used for the discussion in the following two sections.

3.2.5. Numerical analysis of PDS spectra at steady-state equilibrium

The motivation to analyse PDS in steady-state equilibrium is to check if the occupation function changes under the illumination of the spectrally dependent pump beam in such a way that the PDS absorption $\alpha_{PDS}(\hbar\omega)$ does not correspond to the absorption $\alpha_{th}(\hbar\omega)$ at thermal equilibrium. In principle, this could indeed be a possible reason for the large differences between CPM and PDS experimentally observed in the deep defect absorption range (As mentioned in section 1.7.3d, the test turns out to be negative. The reason must be elsewhere).

The PDS signal is proportional to the total generation rate $G_{tot}(\hbar\omega)$ and the PDS absorption $\alpha_{PDS}(\hbar\omega)$ is then given as follows (under the uniform absorption condition, numerically studied here: $\alpha\, d \ll 1$):

$$\alpha_{PDS}(\hbar\omega) = \frac{G_{tot}(\hbar\omega)}{\Phi_0} \qquad \text{with } \Phi_0 \approx \text{constant}$$

For the numerical analysis of PDS, the incident photon flux Φ_0 is assumed to be constant with a value of $\Phi_0 = 5\,10^{15}\mathrm{cm}^{-2}\mathrm{s}^{-1}$. Fig.6 shows the total generation rate $G_{tot}(\hbar\omega)$ at steady-state equilibrium for the four parameter SETs of tab.4. No differences for different capture cross sections are observed. Fig.7 shows the absorption $\alpha(\hbar\omega)$, calculated either as the absorption $\alpha_{th}(\hbar\omega)$ at thermal equilibrium (corresponding to the deconvolution approach) or as the PDS absorption $\alpha_{PDS}(\hbar\omega)$ at steady-state equilibrium (corresponding to fig.6). No differences of the spectra between the system in thermal equilibrium and the system in steady-state equilibrium are observed.

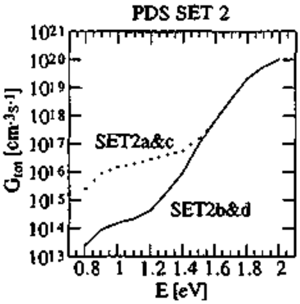

Fig.6: the total generation rate $G_{tot}(\hbar\omega)$ with a constant incident photon flux Φ_0 of $5\,10^{15}cm^{-2}s^{-1}$ (system in steady-state equilibrium).

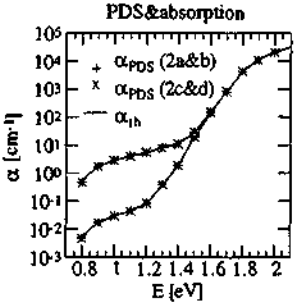

Fig.7: the PDS spectra $\alpha_{PDS}(\hbar\omega)$ at steady-state equilibrium (SETs 2a-d) and the absorption $\alpha_{th}(\hbar\omega)$ at thermal equilibrium (SET 2).

From figures 6 and 7, one may conclude that PDS is not sensitive to the capture cross sections, that the occupation functions in steady-state equilibrium (i.e. during the PDS measurement) are identical to the occupation functions in thermal equilibrium, and that PDS can be deconvoluted by the thermal equilibrium approach.

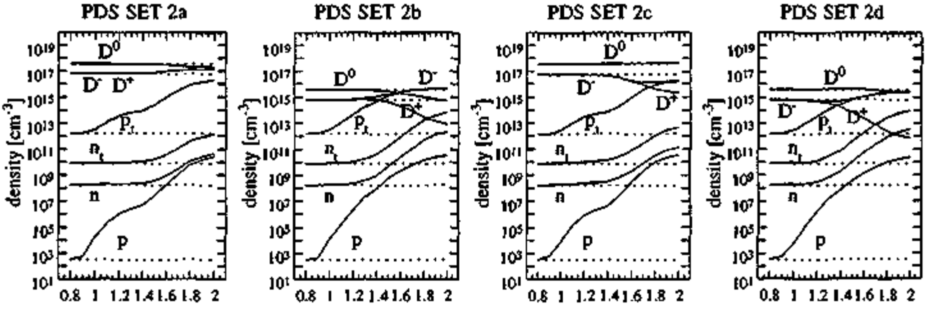

Fig.8: numerical analysis of PDS: densities (n, p, n_t, p_t, N_{DB}^+, N_{DB}^0, N_{DB}^-) as a function of the photon energy $\hbar\omega$. Straight lines = system in steady-state equilibrium (SETs 2a-d), dashed lines = system in thermal equilibrium (SET 2).

Fig.8 shows the densities (n, p, n_t, p_t, N_{DB}^+, N_{DB}^0, N_{DB}^-) as a function of the photon energy $\hbar\omega$, corresponding to the four parameter sets (SETs 2a-d) and corresponding to the numerical results of fig.6 and fig.7. As one can note, the "occupation" of the three dangling bond states (N_{DB}^{+}, N_{DB}^{0}, N_{DB}^{-}) is almost identical to the thermal equilibrium "occupation" for photon energies $\hbar\omega < 1.5\text{eV}$. Therefore, this numerical analysis confirms (at least for this numerical case) that **PDS measures the absorption spectrum correctly**, under typical PDS measurement conditions ($\Phi_0 = 5\,10^{15}\text{cm}^{-2}\text{s}^{-1}$), provided one neglects all effects of inhomogeneities (such as inhomogeneous illumination, inhomogeneous defect distribution or surface / interface states). Fig.9 indicates for the parameter SET 2c (system in steady-state equilibrium) that the incident photon flux Φ_0 (= pump beam intensity) influences the PDS spectrum only for unrealistically high values ($\Phi_0 > 5\,10^{24}\text{cm}^{-2}\text{s}^{-1}$).

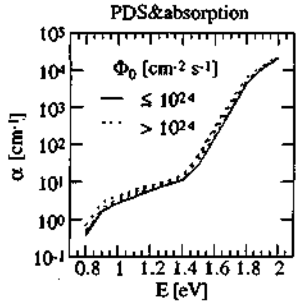

Fig.9: PDS spectra $\alpha_{PDS}(\hbar\omega)$ calculated with different incident photon fluxes Φ_0 (System in steady-state equilibrium: parameter SET 2c).

From this section, one can conclude that the PDS spectrum $\alpha_{PDS}(\hbar\omega)$ at steady-state equilibrium is identical to the absorption spectrum $\alpha_{th}(\hbar\omega)$ at thermal equilibrium. There is no indication that the different defect-to-band generation mechanisms (as discussed in section 2.4.6. and in section 1.7.3d) influence the PDS spectrum $\alpha_{PDS}(\hbar\omega)$ in such a way that it could not be deconvoluted by the approach proposed in section 3.1.3.

3.2.6. Numerical analysis of CPM spectra at steady-state equilibrium

The motivation for this section is to check if a CPM spectrum $\alpha_{CPM}(\hbar\omega)$ corresponds to the absorption spectrum $\alpha_{th}(\hbar\omega)$ at thermal equilibrium. Further, one would like to know the dominating parameters which determine the CPM conductivity σ_{CPM} as a function of the photon energy $\hbar\omega$ and the incident photon flux $\Phi_0(\hbar\omega)$. Concerning the CPM conditions introduced in chapter 1, the main interest concerns the CPM "working point" which has to be spectrally-independent (second CPM condition).

The relative CPM spectrum $\alpha_{CPM}(\hbar\omega)$ is inversely-proportional to the incident photon flux $\Phi_0(\hbar\omega)$ if the CPM conductivity σ_{CPM} is kept constant [Vanecek 81]:

$$\alpha_{CPM}(\hbar\omega) \propto \frac{1}{\Phi_0(\hbar\omega)} \qquad \text{with } \sigma_{CPM} = c_{CPM}\,\sigma_d = \text{constant}$$

The CPM factor c_{CPM} corresponds to the ratio of the CPM conductivity σ_{CPM} at steady-state equilibrium and the (dark) conductivity σ_d at thermal equilibrium. For the numerical analysis of CPM in this section, the CPM factor c_{CPM} has been chosen as 5 (similar to the experiments used; see chapter 1). Further, the CPM conductivity σ_{CPM} is kept numerically constant with an accuracy of 1% (similar to experiments, see chapter 1): for each photon energy $\hbar\omega$, the total conductivity $\sigma_{tot}(\hbar\omega, \Phi_0)$ was numerically recalculated while changing the incident photon flux Φ_0 until $\sigma_{tot}(\hbar\omega, \Phi_0) = \sigma_{CPM}$.

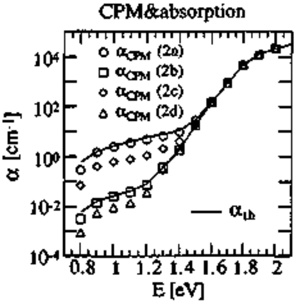

Fig.10: CPM spectra $\alpha_{CPM}(\hbar\omega)$ at steady-state equilibrium (SETs 2a-d) and absorption spectra $\alpha_{th}(\hbar\omega)$ at thermal equilibrium (SET 2): the CPM spectra are calibrated in the band absorption range with $\alpha_{th}(\hbar\omega)$.

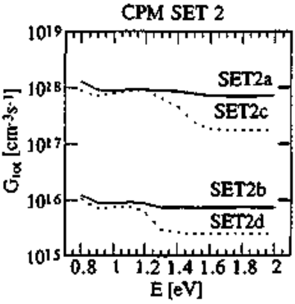

Fig.11: the total generation rate $G_{tot}(\hbar\omega)$ (corresponding to the CPM "working point") for the CPM spectra $\alpha_{CPM}(\hbar\omega)$ shown in fig.10 .

Fig.10 shows the CPM spectra $\alpha_{CPM}(\hbar\omega)$ at steady-state equilibrium for the four parameter SETs of tab.4 (CPM conductivity σ_{CPM} of $1.4\,10^{-9}(\Omega\mathrm{cm})^{-1} = 5\ \sigma_d$, corresponding to sample D170293). The CPM spectra $\alpha_{CPM}(\hbar\omega)$ were calibrated in the band absorption range with the (absolute) absorption spectra $\alpha_{th}(\hbar\omega)$ at thermal equilibrium, which are also shown in fig.10. One can see that the CPM spectrum $\alpha_{CPM}(\hbar\omega)$ is approximately **identical** to the absorption spectrum $\alpha_{th}(\hbar\omega)$ at thermal equilibrium in the case of identical capture cross section ratios ($r_{DB} = r^t_{DB} = \theta_{DB} = 1$, SET2a&b), whereas for different capture cross section ratios ($r_{DB} \neq r^t_{DB} \neq \theta_{DB}$, SET2c&d) this is not the case: for a high deep defect density (SET2c), the CPM deep defect absorption value $\alpha_{CPM}(1.2\mathrm{eV})$ is **underestimated** by a factor of 4.4, whereas for a low deep defect density (SET2d), the CPM deep defect absorption value $\alpha_{CPM}(1.2\mathrm{eV})$ is **underestimated** by a factor 2. Further, the CPM deep defect absorption value $\alpha_{CPM}(0.8\mathrm{eV})$ is **underestimated in** all four cases.

Independent of the total deep defect density N^{tot}_{DB}, the CPM spectrum $\alpha_{CPM}(\hbar\omega)$ is not equal to the absorption spectrum $\alpha_{th}(\hbar\omega)$ at thermal equilibrium if not all capture cross sections are identical (SET 2c&d). Furthermore, the total generation rate $G_{tot}(\hbar\omega)$ - shown in fig.11 - is then spectrally-dependent (the second CPM condition is not fulfilled, the CPM "working point" is spectrally-dependent, cf. chapter 1). Finally, the total generation rate $G_{tot}(\hbar\omega)$ (cf. fig.11) is spectrally-dependent - independent of the capture cross sections - in the very low photon energy range (e.g. $\hbar\omega \leq E_g^{mob}/2$).

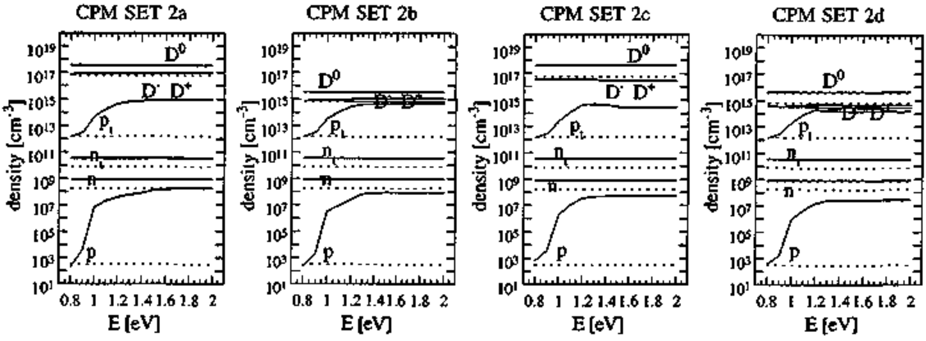

Fig.12: Numerical analysis of CPM: densities (n, p, n_t, p_t, N_{DB}^+, N_{DB}^0, N_{DB}^-) as a function of the photon energy $\hbar\omega$. Straight lines = system in steady-state equilibrium (SETs 2a-d), dashed lines = system in thermal equilibrium (SET 2).

As one can see in fig.12, some of the densities (n, p, n_t, p_t, N_{DB}^+, N_{DB}^0, N_{DB}^-) are different from the thermal equilibrium densities. The density n of the majority charge carriers is constant over the whole spectra, whereas the density p of the minority charge carriers varies for all four sets in the same manner. The carrier density N_{DB}^0 of the neutral dangling bonds is also constant over the whole spectra. This means that the CPM pump beam cannot change the "occupation" of the dangling bond states in such a way that the absorption spectrum would change. For SETs 2b&d (lower defect densities) in the range of the tail absorption, the density p_t of the localised holes is identical to the density N_{DB}^- of the negatively charged dangling bonds.

The partial rates (recombination R_{ij}, generation G_{ij} and thermal emission T_{ij}) - defined in appendix B3.4. and shown in fig.13 - are rather confusing. However, one can see that the partial generation rates G_{ij}, which dominate the total generation rate G_{tot}, are always smaller than the corresponding recombination R_{ij} and the thermal emission rates T_{ij}: this means that these parameter sets used here seem to operate in region IV introduced in section 2.4.6. (for only one defect level); note here that each rate corresponds to an integral over the DOS. Concerning the underestimation of CPM in the case of different capture cross sections (SETs 2c&d), one is left with the observation that the total generation rate $G_{tot}(\hbar\omega)$ is spectrally-dependent (see fig.11), but its origin could not be deduced from these plots.

The occupation functions and the occupation of the DOS (shown in appendix C8) are very difficult to analyse and discuss. But they do not provide any indication of the underestimation of CPM in the case of different capture cross sections (SETs 2c&d). - A simple, possible interpretation of the numerical results (especially of the underestimation of CPM) will be given in section 3.3.

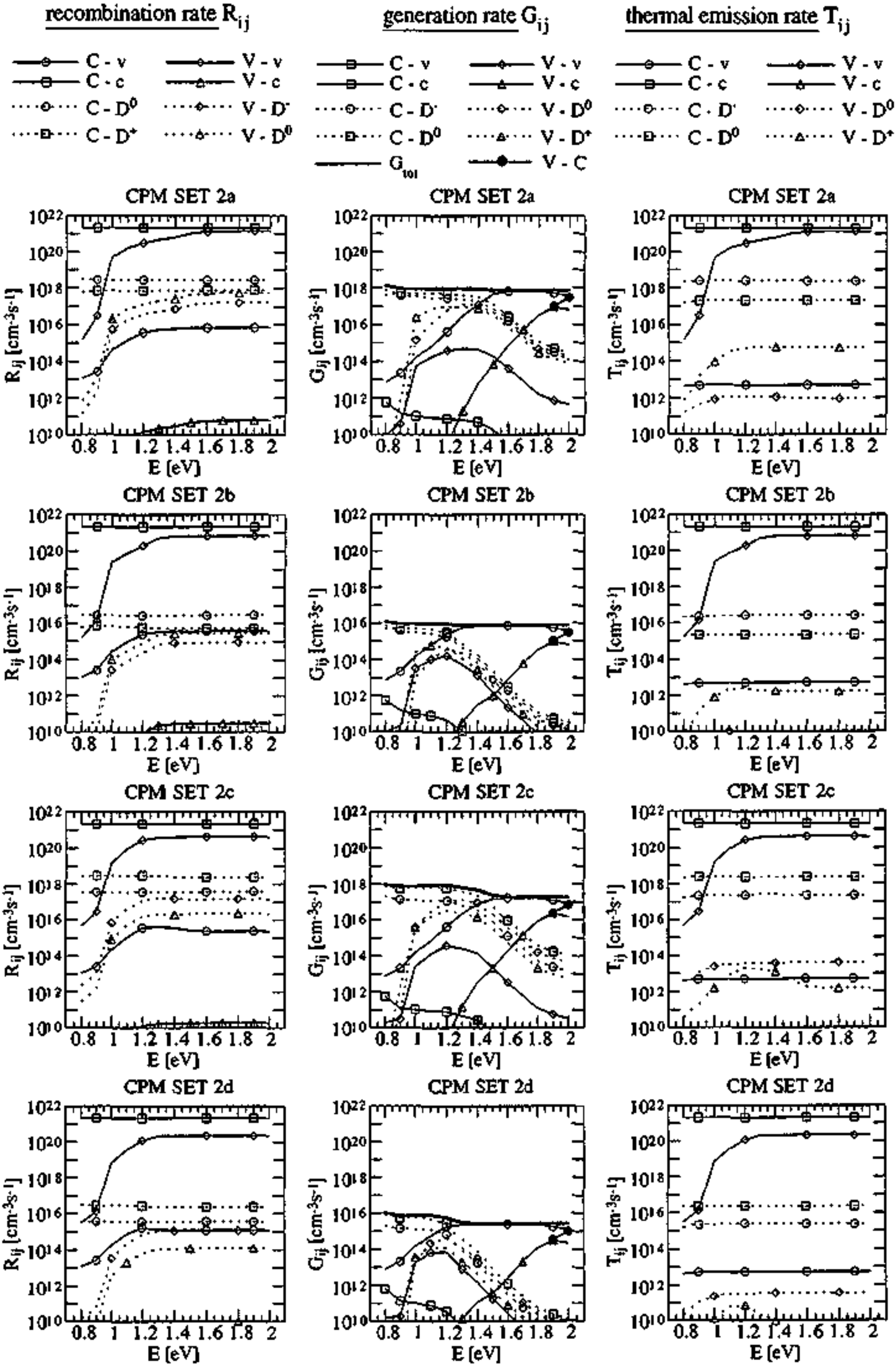

Fig.13: numerical analysis of CPM: partial rates (bold = total generation rate G_{tot}).

From this section, one can conclude, that CPM spectra depend on the capture cross sections and that CPM spectra do not generally correspond to the absorption spectra, even in the case of identical capture cross sections for all states, in the very low photon energy range (e.g. $\hbar\omega \leq E_g^{mob}/2$). But, one can note that the CPM pump beam cannot change the "occupation" of the dangling bond states in such a way that the absorption spectrum would change (cf. fig.12).

3.2.7. Sensitivity analysis of the important parameters of CPM and PDS

Whereas in section 3.1.4., the sensitivity analysis of the absorption $\alpha_{th}(\hbar\omega)$ at thermal equilibrium was presented and discussed, the same sensitivity analysis of the CPM absorption $\alpha_{CPM}(\hbar\omega)$ at steady-state equilibrium and of the PDS absorption $\alpha_{PDS}(\hbar\omega)$ at steady-state equilibrium will be presented here. The remarks (given in section 3.1.4.) concerning the variation of one parameter at a time are still valid here. Besides the variation of the parameters of the absorption $\alpha_{th}(\hbar\omega)$ at thermal equilibrium in section 3.1.4., the parameters which determine the steady-state equilibrium are varied here (capture cross sections: σ_t, σ^0, $\sigma^{+/-}$, v_{th}; optical properties: Φ_0, $\hbar\omega$; see section 2.3.2.). Whereas in section 3.1.4., the absorption $\alpha_{th}(\hbar\omega)$ in thermal equilibrium was presented on an absolute scale, here, the spectra $\alpha_{th}(\hbar\omega)$, $\alpha_{CPM}(\hbar\omega)$ and $\alpha_{PDS}(\hbar\omega)$ are calibrated at $\alpha(\hbar\omega = 2\text{eV}) = 12'544\text{cm}^{-1}$. This allows one to compare these relative spectra in a simple way. For this numerical analysis, the input parameters of **SET2c** (see tab.2 in section 3.1.3. and tab.4 in section 3.2.4.) and the discretisation set LDS (see appendix C3) have been chosen. In this section, only some main aspects will be presented and discussed. The details and the complete, numerical results (plots) are given in appendix C6, whereas here only the numerical results of the interesting cases will be discussed.

As a general numerical result, one can note that, for all cases of this sensitivity analysis, the PDS spectra $\alpha_{PDS}(\hbar\omega)$ are identical to the absorption spectra $\alpha_{th}(\hbar\omega)$ at thermal equilibrium. In contrast, CPM spectra are sensitive to the capture cross sections and to a change in the type of majority charge carrier. For the other variation of the parameters, the CPM absorption $\alpha_{CPM}(\hbar\omega)$ follows the trends of the absorption $\alpha_{th}(\hbar\omega)$ in thermal equilibrium (details see appendix C6).

Note: *As far as this numerical sensitivity analysis of the important parameters of CPM and PDS is concerned, the author has to point out that **these numerical results - as any numerical results - are, in principle, strictly related to the parameter chosen** (here SET 2c) **and to the numerical system discussed here**. However, further analysis will indicate that the observed "CPM effects" can also be expected in other parameter sets.*

Numerical variation of the capture cross sections (parameter SET 2c):

In fig.14, the deep defect absorption value $\alpha(1.2\text{eV})$ is shown as a function of an assumed "universal" capture cross section $\sigma_{all} \equiv \sigma_t = \sigma^0 = \sigma^{+/-}$. One can see that CPM and PDS are not influenced by this parameter σ_{all}. This means that the ratio $\theta_{DB} \equiv R^2/\sigma^0$ between the optical matrix element R^2 and the capture cross section σ^0 does not influence the absorption spectra, as would be expected from the analysis of the defect-to-band generation mechanism (discussed in section 2.4.6.). Further, this means that the absolute value of the capture cross section does not influence the relative CPM spectra.

In fig.15, the deep defect absorption value $\alpha(1.2eV)$ is shown as a function of the localised band tail states capture cross section σ_t. One can see that the CPM spectrum changes if this capture cross section σ_t is larger than the largest capture cross section of the dangling bonds. Fig.16 shows such CPM spectra, which could not be observed experimentally. In terms of $r_{DB} \equiv \sigma^{+/-} / \sigma^0$ and $r^t_{DB} \equiv \sigma_t / \sigma^0$, this means that the ration r^t_{DB} / r_{DB} has to be smaller than one.

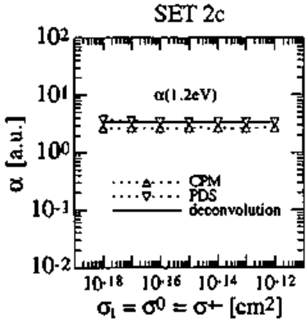

Fig.14: deep defect absorption value $\alpha(1.2eV)$ as a function of the uniform capture cross section σ_{all}.

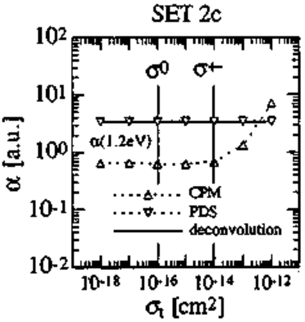

Fig.15: deep defect absorption value $\alpha(1.2eV)$ as a function of the localised band tail state capture cross section σ_t.

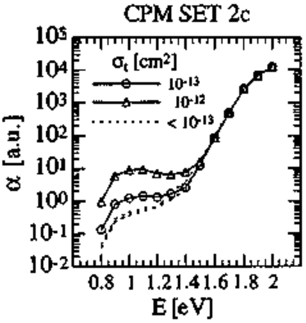

Fig.16: CPM spectra $\alpha_{CPM}(\hbar\omega)$ for different localised band tail state capture cross sections σ_t.

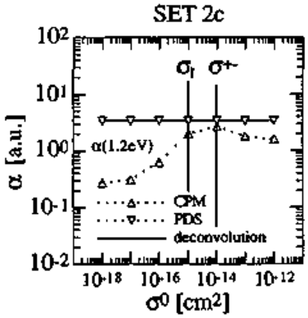

Fig.17: deep defect absorption value $\alpha(1.2eV)$ as a function of the neutral DB capture cross section σ^0.

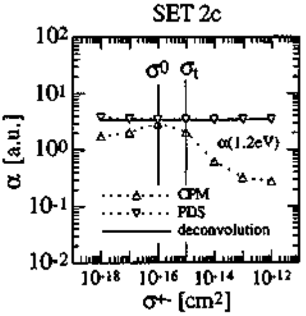

Fig.18: deep defect absorption value $\alpha(1.2eV)$ as a function of the charged DB capture cross section $\sigma^{+/-}$.

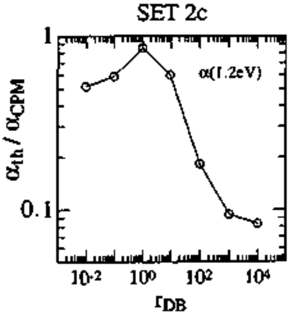

Fig.19: deep defect absorption value ratio $\alpha_{th}(1.2eV)/\alpha_{CPM}(1.2eV)$ as a function of the ratio $r_{DB} \equiv \sigma^{+/-} / \sigma^0$.

In fig.17, the deep defect absorption value $\alpha(1.2\text{eV})$ is shown as a function of the <u>neutral DB capture cross section</u> σ^0. In fig.18, deep defect absorption value $\alpha(1.2\text{eV})$ is shown as a function of the <u>charged DB capture cross section</u> $\sigma^{+/-}$. Fig.19 combines the results of fig.17 and fig.18: deep defect absorption value ratio $\alpha_{th}(1.2\text{eV})/\alpha_{CPM}(1.2\text{eV})$ is shown as a function of the DB capture cross section ratio $r_{DB} \equiv \sigma^{+/-} / \sigma^0$. One can see that the CPM deep defect absorption can indeed be **underestimated** if the capture cross section ratio $r_{DB} \equiv \sigma^{+/-} / \sigma^0$ differs from 1.

Numerical variation of the mobilities (parameter SET 2c):

The CPM current σ_{CPM} is given as $\sigma = e\{\mu_e n + \mu_h p\}$. The sensitivity of the mobilities will be discussed here. In fig.20, the CPM deep defect absorption values $\alpha_{CPM}(1.2\text{eV})$ and $\alpha_{CPM}(1.0\text{eV})$ are shown as a function of the electron mobility μ_e. Fig.21 shows the corresponding CPM spectra $\alpha_{CPM}(\hbar\omega)$ under the variation of the mobility ratio μ_e / μ_h. One can see that the spectra remains identical as long as the mobility ratio μ_e / μ_h is larger than 1 or equal to 1. Otherwise, the CPM spectra below $\hbar\omega = 1.2\text{eV}$ are strongly **underestimated.** Fig.22 shows the charge carrier densities n and p for the specific case of $\mu_h = 100\,\mu_e$ (mobility ratio $\mu_e / \mu_h = 0.01$). One can see that in the case of underestimation (i.e. $\hbar\omega < 1.2\text{eV}$), the CPM conductivity $\sigma_{CPM} = e(\mu_e\, n + \mu_h\, p)$ is constant, but **both charge carrier densities are spectrally-dependent**: $n(\hbar\omega)$ **and** $p(\hbar\omega)$. This means that the <u>third CPM measurement condition is not fulfilled here</u>. Similar effects can also be observed for p-type material in the case of $\mu_e / \mu_h > 1$ (see in the following the numerical variation of the Fermi level E_F).

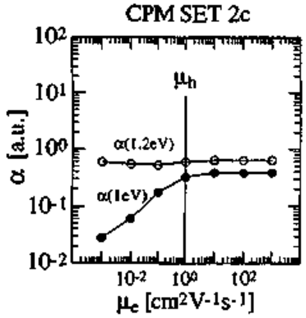

Fig.20: CPM deep defect absorption values $\alpha(1.2\text{eV})$ and $\alpha(1.0\text{eV})$ as a function of the electron mobility μ_e.

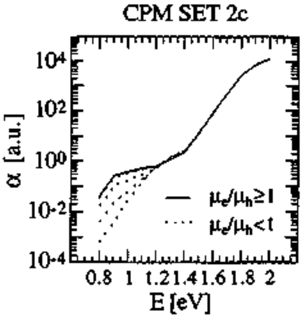

Fig.21: CPM spectra $\alpha_{CPM}(\hbar\omega)$ for different mobility ratio μ_e / μ_h.

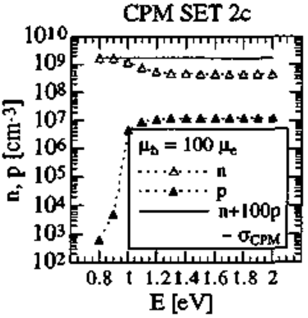

Fig.22: charge carrier densities n and p for the specific case of $\mu_h = 100\,\mu_e$ (mobility ratio μ_e / μ_h = 0.01).

Numerical variation of the CPM conductivity (parameter SET 2c):

The CPM current σ_{CPM} is given as $\sigma = e\{\mu_e n + \mu_h p\}$ with $\sigma_{CPM} = c_{CPM}\,\sigma_d$. Here, the sensitivity on the CPM conductivity σ_{CPM} and the CPM factor c_{CPM} is discussed. In fig.23, the CPM deep defect absorption values $\alpha_{CPM}(1.2eV)$ and $\alpha_{CPM}(1.0eV)$ are shown as a function of the CPM factor c_{CPM}. For very low CPM factors c_{CPM}, the CPM deep defect absorption values increase. This behaviour is related to a spectrally dependent CPM "working point" in the <u>cw-mode</u> (discussion in the next section 3.2.8., see fig.30).

Numerical variation of the deep defect density (parameter SET 2c):

The main interest of CPM is to identify the deep defect absorption value with the total deep defect density N_{DB}^{tot} (see section 3.1.2. and appendix C2). Fig.24 shows the CPM and PDS spectra at steady-state equilibrium, while the total deep defect density N_{DB}^{tot} is varied. In fig.25, the corresponding deep defect absorption value $\alpha(1.2eV)$ is shown as a function of the total deep defect density N_{DB}^{tot}. From these two figures, one can conclude that the **underestimation** of the CPM deep defect absorption values **is constant during the variation of the total deep defect density** N_{DB}^{tot}, as long as other parameters (as the capture cross sections or the Fermi level position E_F) do not change at the same time! Further, fig.25 indicates that the CPM deep defect absorption value $\alpha_{CPM}(1.2eV)$ is proportional to the total deep defect density N_{DB}^{tot} for reasonably high values of N_{DB}^{tot} (Note that the values of N_{DB}^{tot} in fig.24 and fig.25 are related to the value of the optical matrix element R^2, see section 3.1.3.). The lower limit of this proportionality depends on the value of the exponential Urbach tail slop (here 50meV).

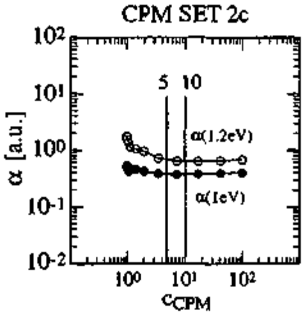

Fig.23: CPM deep defect absorption value $\alpha(1.2eV)$ and $\alpha(1.0eV)$ as a function of the CPM factor c_{CPM}.

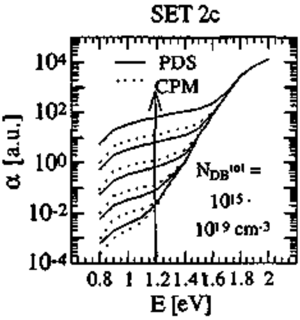

Fig.24: CPM and PDS spectra $\alpha(\hbar\omega)$ for different total deep defect densities N_{DB}^{tot}.

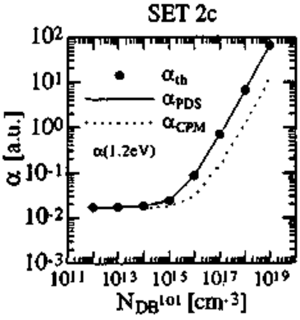

Fig.25: deep defect absorption value $\alpha(1.2eV)$ as a function of the total deep defect density N_{DB}^{tot}.

Numerical variation of the Fermi level position (parameter SET 2c):

The Fermi level position was varied in the range of $E_F - E_V = 0.7$ - 1.1eV, whereas all other parameters did not change. Therefore, the charge neutrality of the dangling bonds was fulfilled for $E_F - E_V = 0.9$eV only (c.f. section 2.2.4. and 1.7.3d). Fig.26 shows the numerically calculated CPM spectra for SETs 2a-d. Fig.27 shows the CPM deep defect absorption value $\alpha_{CPM}(1.2eV)$ deduced from fig.26 and the deep defect absorption value $\alpha_{th}(1.2eV)$ at thermal equilibrium. Further, fig.28 shows the ratio $\alpha_{th}(1.2eV)$ / $\alpha_{CPM}(1.2eV)$ as a function of $E_F - E_V$. Note that $E_F - E_V + \varepsilon_v = E_F - E_{Vmob}$ and $\varepsilon_v = 0.2$eV here.

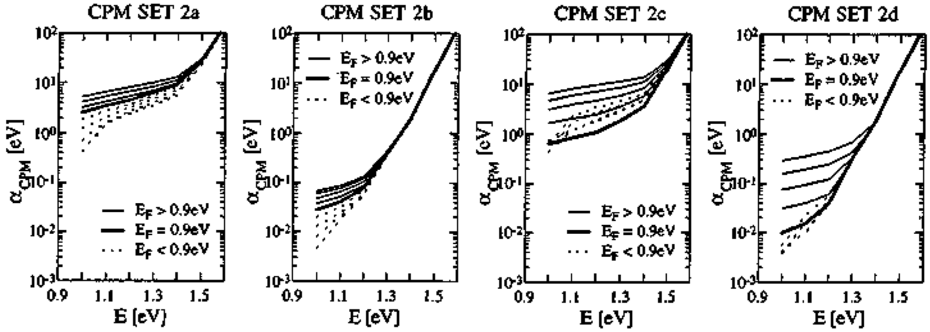

Fig.26: CPM spectra $\alpha_{CPM}(\hbar\omega)$ for different Fermi level positions $E_F - E_V$ (SETs 2a-d).

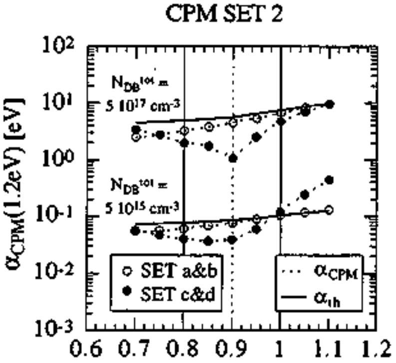

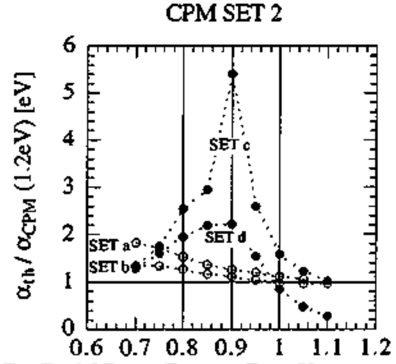

Fig.27: CPM deep defect absorption value $\alpha_{CPM}(1.2eV)$ deduced from fig.26 and deep defect absorption value $\alpha_{th}(1.2eV)$ at thermal equilibrium (SETs 2a-d).

Fig.28: ratio $\alpha_{th}(1.2eV)$ / $\alpha_{CPM}(1.2eV)$ deduced from fig.27 as a function of $E_F - E_V$ (SETs 2a-d).

For the case of different capture cross sections (SETs 2c&d), one recognises a large discrepancy between the CPM spectra $\alpha_{CPM}(\hbar\omega)$ and the absorption spectra $\alpha_{th}(\hbar\omega)$ at thermal equilibrium, because the second CPM condition is not fulfilled. For the case of identical capture cross sections (SETs 2a&b), one recognises a slight discrepancy between the CPM spectra $\alpha_{CPM}(\hbar\omega)$ and the absorption spectra $\alpha_{th}(\hbar\omega)$ at thermal equilibrium if the Fermi level moves to the valence band edge because then, the third CPM condition is not fulfilled (**both charge carrier densities are spectrally-dependent**: $n(\hbar\omega)$ and $p(\hbar\omega)$).

3.2.8. Numerical analysis of the conductivity at steady-state equilibrium

It is evident that understanding CPM means understanding the conductivity σ of a-Si:H as a function of the photon energy $\hbar\omega$ and of the incident photon flux Φ_0 - and vice versa.

This section consists of two parts. First, the conductivity σ of SETs 2a-d will be analysed (these parameter sets were used for the calculation of CPM and PDS in the previous sections). Second, the conductivity σ of SETs 1-4 a-d will be analysed in order to study the potential influence of the value of the optical matrix element R^2 (these 16 parameter sets consist of SETs 1-4 of tab.2 at thermal equilibrium in combination with SETs a-d of tab.4 at steady-state equilibrium).

As numerical results of the system in steady-state equilibrium, one gets the total conductivity σ_{tot} and the total generation rate G_{tot} as a function of the incident photon flux Φ_0 and of the photon energy $\hbar\omega$ (see section 3.2.1.). On the one hand, one can express $\sigma_{tot}(\Phi_0)$, on the other hand, one can express $\sigma_{tot}(G_{tot})$ while using $G_{tot}(\Phi_0)$.

Conductivity σ based on SETs 2 a-d:

Fig.29 shows the total generation rate $G_{tot}(\Phi_0)$ as a function of the incident photon flux Φ_0 for different photon energies $\hbar\omega$ and the corresponding PDS spectrum at a specific incident photon flux. From this figure, one can conclude that the total generation rate G_{tot} is proportional to the incident photon flux Φ_0, independent of the photon energy $\hbar\omega$ and independent of the total defect density N_{DB}^{tot}:

$$\boxed{G_{tot} \propto \Phi_0} \qquad \text{for any } \hbar\omega \text{ and for any } N_{DB}^{tot}$$

One can conclude from fig.29 that PDS shows identical spectra for different incident photon fluxes Φ_0. In fact, different PDS spectra could only be found for unrealistically high values of Φ_0 ($\Phi_0 > 5\,10^{24}\,cm^{-2}s^{-1}$), as shown in fig.9.

Fig.30 shows the total conductivity $\sigma_{tot}(\Phi_0)$ as a function of the incident photon flux Φ_0 for different photon energies $\hbar\omega$ and the corresponding CPM spectra of two specific CPM conductivities σ_{CPM}. This figure indicates that a very low CPM current can lead to a different absorption spectra, as also observed in fig.23 (variation of the CPM conductivity σ_{CPM}, also parameter SET 2c). The origin of this behaviour is found in fig.31, but it seems to be strictly related to the cw-mode. Note that for high CPM conductivities σ_{CPM}, the same CPM spectra can always be expected, which means that the pump beam does not change the occupation in such a way that the absorption spectrum changes (as in the case of PDS).

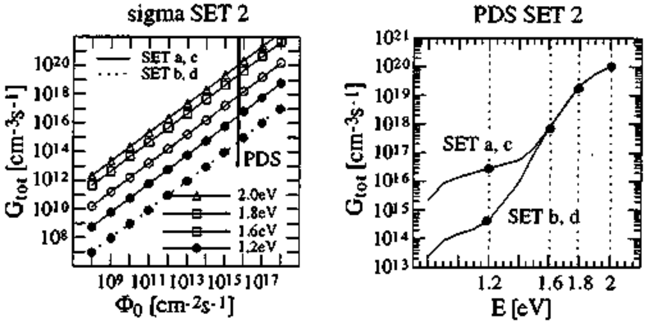

Fig.29: the total generation rate $G_{tot}(\Phi_0)$ as a function of the incident photon flux Φ_0 for different photon energies $\hbar\omega$ and the corresponding PDS spectrum at $\Phi_0 = 5\,10^{15}\mathrm{cm}^{-2}\mathrm{s}^{-1}$.

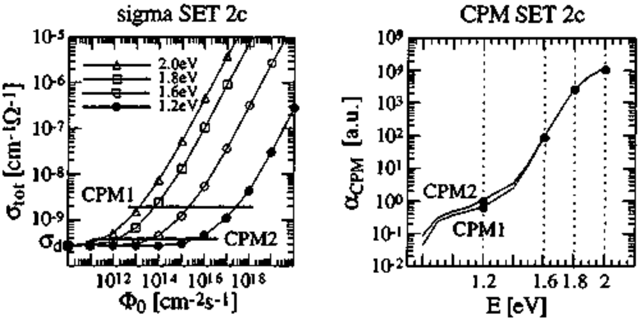

Fig.30: the total conductivity $\sigma_{tot}(\Phi_0)$ as a function of the incident photon flux Φ_0 for different photon energies $\hbar\omega$ and the corresponding CPM spectra with two different CPM factors: c_{CPM} = 5 (CPM1) and c_{CPM} = 1.4 (CPM2).

Fig.31 combines the information contained in fig.29 and fig.30. It shows total conductivity $\sigma_{tot}(G_{tot})$ as a function of the total generation rate G_{tot} for different photon energies $\hbar\omega$ (SETs 2a&d). One can see that SET2a (with identical capture cross sections) shows no spectrally dependent CPM "working point", whereas SET2c (with different capture cross sections) shows a spectrally dependent CPM "working point" for low photon energies $\hbar\omega$. From these figures, one can conclude that the relation $\sigma_{tot}(G_{tot})$ is controlled by the capture cross sections - for any photon energy $\hbar\omega$ and for any total generation rate G_{tot}.

In fig.32, the power law exponent $\gamma^*(G_{tot})$ as a function of the total generation rate G_{tot} for different photon energies $\hbar\omega$ is shown (SETs 2a&c). Fig.32 corresponds to the first CPM measurement condition and fig.31 to the second CPM measurement condition. For parameter SET

2a, both conditions are fulfilled, for parameter SET 2c neither of them are fulfilled. However, from the experimental point of view (in contrast to the numerical calculations), it can be difficult - for a specific case - to decide if these CPM measurement conditions are fulfilled or not, because only $\sigma_{tot}(\Phi_0)$ and $\gamma^*(\Phi_0)$ can be measured, but not $\sigma_{tot}(G_{tot})$ and $\gamma^*(G_{tot})$.

In the appendix C9, the full results of the conductivity $\sigma_{tot}(\Phi_0)$ are presented for $\hbar\omega$ = 1.9eV (SET 2a-d).

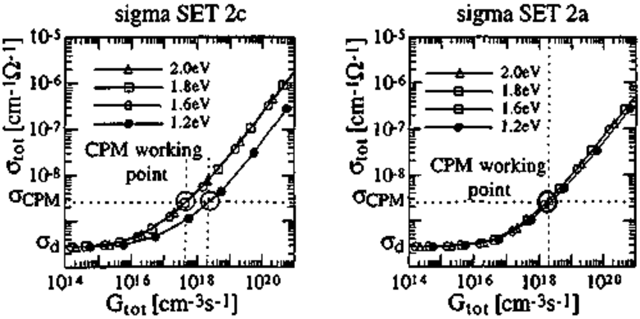

Fig.31: the total conductivity $\sigma_{tot}(G_{tot})$ as a function of the total generation rate G_{tot} for different photon energies $\hbar\omega$, once for a spectrally dependent CPM "working point" (SET 2c, different capture cross sections) and once for a spectrally independent CPM "working point" (SET 2a, identical capture cross sections).

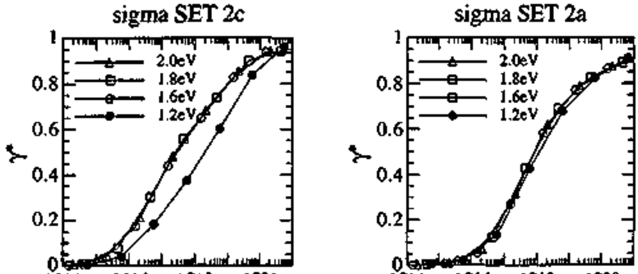

Fig.32: the power law exponent $\gamma^*(G_{tot})$ as a function of the total generation rate G_{tot} for different photon energies $\hbar\omega$, once for SET 2c (different capture cross sections) and once for SET 2a (identical capture cross sections).

Conductivity σ based on SETs 1-4 a-d:

Until here, the analysis of CPM, PDS and the conductivity at steady-state equilibrium were based on SET 2 with an optical matrix element of $R^2 = 10Å^2$. In order to check whether the previous results for CPM and PDS are different for other optical matrix elements, it is useful to analyse $G_{tot}(\Phi_0)$ and $\sigma(G_{tot})$ for SETs 1-4.

The parameters of SETs 1-4 at thermal equilibrium, which are given in tab.2, all showed the same absorption spectrum at thermal equilibrium. For the following analysis, the parameters of the capture cross sections have been chosen to be identical as those analysed in the previous sections (shown in tab.4 SETs a-d). The combination of tab.2 and tab.4 leads to 16 parameter sets (SETs 1-4 a-d), which are analysed hereafter. Tab.5 shows the optical matrix elements R^2 and the total deep defect density N_{DB}^{tot} of these 16 parameter sets. Concerning the total deep defect densities N_{DB}^{tot}, they are 100 times lower in SETs b&d than in SET a&c.

Parameters:	$R^2[\text{Å}^2]$	$N_{DB}^{tot}\,[cm^{-3}]$
SET 1a&c	1	$2\,10^{18}$
SET 1c&d	1	$2\,10^{16}$
SET 2a&c	10	$5\,10^{17}$
SET 2c&d	10	$5\,10^{15}$
SET 3a&c	100	$1.1\,10^{17}$
SET 3c&d	100	$1.1\,10^{15}$
SET 4a&c	1000	$6\,10^{16}$
SET 4c&d	1000	$6\,10^{14}$

Tab.5: optical matrix element and total deep defect density N_{DB}^{tot} (input parameters).

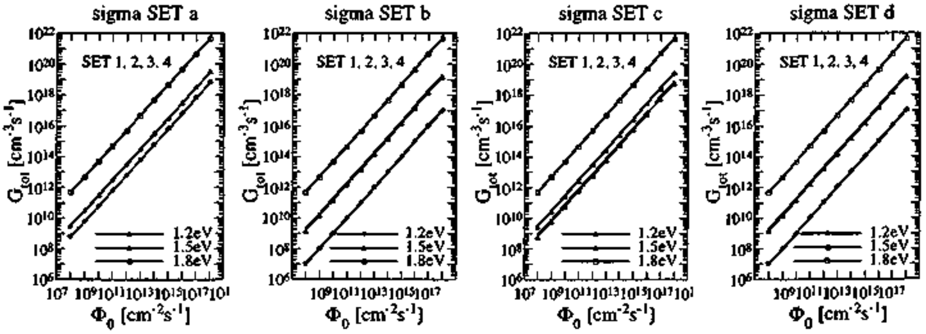

Fig.33: the total generation rate $G_{tot}(\Phi_0)$ as a function of the incident photon flux Φ_0 for different photon energies $\hbar\omega$(SETs 1-4 a-d).

Fig.33 shows for all these parameter SETs, the total generation rate $G_{tot}(\Phi_0)$ as a function of the incident photon flux Φ_0 for different photon energies $\hbar\omega$. One can find - independent of the parameter sets - the proportionality between the total generation rate G_{tot} and the incident photon flux Φ_0:

$$\boxed{G_{tot} \propto \Phi_0} \qquad \text{for any } \hbar\omega \text{ and for any } N_{DB}^{tot}$$

This means that the absorption α_{th} at thermal equilibrium is equal to the PDS absorption α_{PDS} at steady-state equilibrium - independent of the optical matrix element R^2. Further, fig.33 indicates that no dependency on the different capture cross sections can be observed (SET b = d and SET a=c).

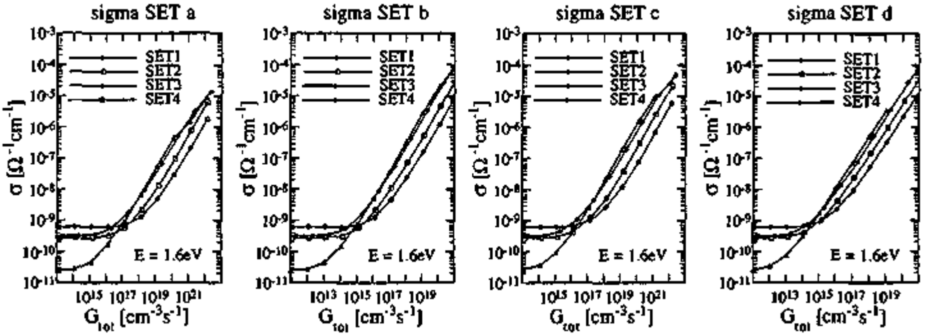

Fig.34: SETs 1-4 a-d: the total conductivity $\sigma_{tot}(G_{tot})$ as a function of the total generation rate G_{tot} for a specific photon energies of $\hbar\omega$ = 1.6eV (different scales!).

For all these parameter SETs, fig.34 shows the total conductivity $\sigma_{tot}(\Phi_0)$ as a function of the incident photon flux Φ_0 for a specific, arbitrarily chosen photon energy of $\hbar\omega$ = 1.6eV. In appendix C10, the numerical results of the total conductivities $\sigma_{tot}(\Phi_0)$ and $\sigma_{tot}(G_{tot})$ as well as the corresponding power law factors $\gamma^*(\Phi_0)$ and $\gamma^*(G_{tot})$ are presented for SETs 1-4 a-d at different photon energies $\hbar\omega$. In fig.34, one can see that the relative, total conductivity $\sigma_{tot}(G_{tot})$ is quite insensitive to the parameter SETs a-d for a given photon energy $\hbar\omega$.

Fig.35 indicates that the total generation rate $G_{tot}(\hbar\omega)$ at a constant (CPM) conductivity σ_{CPM} (>> σ_d) is approximately proportional to the total deep defect density N_{DB}^{tot} for a specific photon energy of $\hbar\omega$ = 1.6eV (extraction from fig.34). This proportionality can be found in approximation for all photon energies studied here (see appendix C8) and it corresponds to the results of chapter 2:

Approximation: $$\boxed{G_{tot} \propto N_{DB}^{tot}} \qquad \text{for any } \hbar\omega \text{ and for any } N_{DB}^{tot}$$

But the absolute relation between the total generation rate $G_{tot}(\hbar\omega)$ and the total deep defect density N_{DB}^{tot}, which determines the CPM spectra and the CPM "working point", additionally depends on the transport parameters. In the case of different capture cross sections (SETs c&d), the CPM "working point" is spectrally-dependent for SETs 1-4 (see appendix C8). In the case of identical capture cross sections (SETs a&b), the CPM "working point" is not spectrally-dependent and, then, the CPM spectra correspond to the absorption spectra for SETs 1-4 (see appendix C8). This indicates that it was reasonable to analyse only SETs 2a-d in the previous sections and that the optical matrix element R^2 does not influence the CPM analysis of the previous sections.

As far as the optical matrix element R^2 is concerned, fig.36 shows the total defect density N_{DB}^{tot} as a function of the optical matrix element R^2, as determined by deconvolution at thermal equilibrium. One finds that the deduced total defect density N_{DB}^{tot} is approximately inversely-proportional to the square root of the optical matrix element R^2 in the case of the deconvolution approach combined with the DOS model which is used here:

Approximation: $\boxed{N_{DB}^{tot} \propto \frac{1}{\sqrt{R^2}} \propto \frac{1}{|R|}}$ for a fixed Fermi level E_F

This relation seems to be related to the parabolic DOS bands, but will not be further discussed.

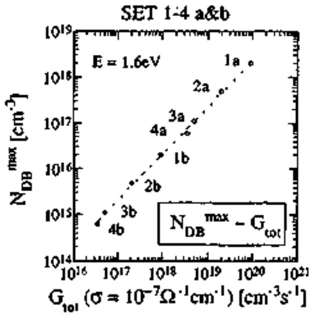

Fig.35: the total deep defect density N_{DB}^{tot} as a function of the total generation rate $G_{tot}(\hbar\omega)$ (SETs 1-4 a&b) at a fix conductivity at steady-state equilibrium.

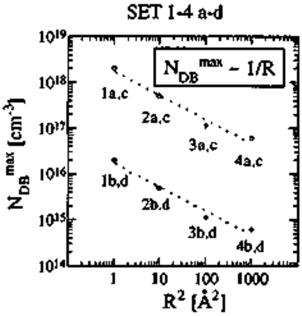

Fig.36: the total deep defect density N_{DB}^{tot} as a function of the optical matrix elements R^2 (SETs 1-4 a-d) at thermal equilibrium (found by the numerical deconvolution in section 3.1.3.).

3.3. Main generation-recombination mechanism of CPM

The main purpose of this section is to find the origin of the "CPM effects" observed in the previous section for the numerical analysis of CPM (especially the capture cross section ratio dependency) in a qualitative manner.

In the previous section (section 3.2.), it has been numerically found (for the case of a homogeneous material without dopant atoms) that the absorption spectrum at thermal equilibrium is equal to the absorption spectrum at steady-state equilibrium, but that the CPM spectra do not always correspond to these absorption spectra, whereas PDS spectra do (c.f. situation (1) and situation (2) in section 1.7.3d).

In this section, the author qualitatively discusses the main generation-recombination mechanisms which are present in CPM (and also in PDS) and which determine CPM conductivity. These generation-recombination mechanisms define the relation between the CPM conductivity and the CPM generation rate (called CPM "working point"). One can expect that **a change in the main generation-recombination mechanism can lead to a change of the CPM "working point"** but a spectrally dependent CPM "working point" means that a CPM spectrum does not correspond to the absorption spectrum (c.f. section 1.2.).

For the following discussion different elements need to be introduced first:

System of one or two defect levels:

In chapter 2, the simple system of one defect level (at the energy position E_d with the defect density N_d) was analytically analysed and discussed. This situation is schematically shown in fig.37 (and called situation A); the generation and recombination mechanisms are schematically indicated by "G" and "R". The defect-to-band generation mechanism G_n is shown in fig.37, but the following discussion is also valid for the defect-to-band generation mechanisms G_p or G_{np} (these defect-to-band generation mechanisms were introduced in section 2.4.6.). Effects on the correlation energy are neglected for the following discussion.

Next, the author introduces a system of two defect levels (one defect level at the energy positions E_{d1} with the defect density N_{d1} and one defect level at the energy positions E_{d2} with the defect density N_{d2}). This situation is schematically shown in fig.38 (and called situation B); the generation and recombination mechanisms are schematically indicated by "G" and "R". The defect-to-band generation mechanism G_n is shown in fig.38, but the following discussion is also valid for the defect-to-band generation mechanisms G_p or G_{np}.

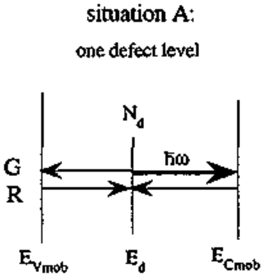
situation A:
one defect level

Fig.37: situation A: system of one defect level.

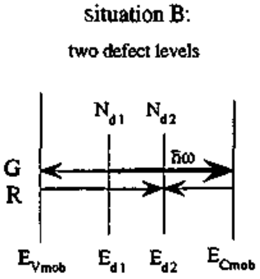
situation B:
two defect levels

Fig.38: situation B: system of two defect levels.

In situation A, generation and recombination take place at the same defect level (E_d, N_d). In situation B, generation takes place at the one energy level (E_{d1}, N_{d1}) and recombination takes place at the other energy level (E_{d2}, N_{d2}).

Different defect types:

Before the discussion can start, one has to distinguish further between different defect types. Here, a defect type is assumed to be characterised by its capture cross sections (furthermore, one could characterise a defect type by the possible occupation states, e.g. non-occupied or occupied by one electron = donor-like defect type). For situation B, this means that one energy level (E_{d1}, N_{d1}) can corresponds to one defect type X and the other energy level (E_{d2}, N_{d2}) to another defect type Y. Alternatively, both energy levels of situation B can correspond to the same defect type X or Y. The situations A and B are then characterised as follows:

situation A:	system of one defect level:	E_d, N_d
	* one defect type:	X or Y
situation B:	system of two defect levels:	E_{d1}, N_{d1}, E_{d2}, N_{d2}
	* one defect type:	X or Y
	* two defect types:	X and Y

Simplified DOS:

The numerical analysis in chapter 3 was based on the (complete) standard DOS of a-Si:H (introduced in section 2.1.). This standard DOS is reduced schematically for the following discussion. The simplified DOS consists only of a localised band tail state distribution $N_t(E)$ (exponential valence tail states) and of the deep defect state distribution $N_d(E)$ with its maximum value N_d^{max}. Fig.39 shows this simplified DOS, where the defects are energy-distributed (in contrast to situations A and B). It can be assumed that $N_t(E)$ and $N_d(E)$ each correspond to a different defect type (i.e. each with different capture cross sections) as shown in fig.40.

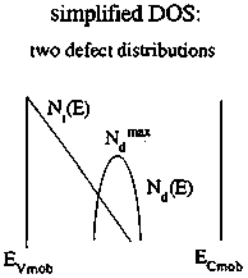

Fig.39: simplified DOS: energy-dependent defect distribution $N_t(E)$ and $N_d(E)$.

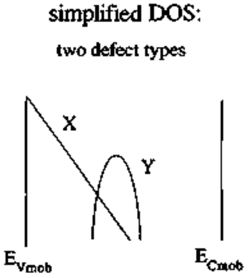

Fig.40: simplified DOS: two defect types X and Y.

3.3.1. Possible generation-recombination mechanism

With the help of the introduced elements (system of one or two defect levels, defect types, simplified DOS) it is assumed to be possible to describe the main generation-recombination mechanism which determine the CPM conductivity at a specific photon energy. The idea is that the simplified DOS (or more general even the (complete) standard DOS) can be schematically reduced to a situation A or a situation B for a given set of parameters. Fig.41 to fig.46 illustrates some possible generation-recombination mechanisms. They are summarised in the following overview 1:

situation A_1:	system of one defect level: G and R at E_d, N_d^{max}	one defect type: Y	photon energy: $\hbar\omega \geq E_{Cmob} - E_d$ $\hbar\omega > E_g^{mob}/2$
situation A_2:	system of one defect level: G and R at E_d, $N_t(E_d)$	one defect type: X	photon energy: $\hbar\omega = E_{Cmob} - E_d$
situation A_3:	system of one defect level: G and R at E_d, $N_d(E_d)$	one defect type: X	photon energy: $\hbar\omega = E_{Cmob} - E_d$ $\hbar\omega < E_g/2$
situation B_1:	system of two defect levels: G at E_{d1}, $N_t(E_{d1})$ R at E_{d2}, N_d^{max}	two defect types: X Y	photon energy: $\hbar\omega = E_{Cmob} - E_{d1}$ $E_{d2} > E_{d1}$
situation B_2:	system of two defect levels: G at E_{d1}, $N_d(E_{d1})$ R at E_{d2}, N_d^{max}	one defect type: X Y	photon energy: $\hbar\omega = E_{Cmob} - E_{d1}$ $E_{d1} > E_{d2}$, $\hbar\omega > E_g^{mob}/2$

Overview 1: possible generation-recombination mechanism

Note that the defect-to-band generation mechanisms G_n, G_p and G_{ap} have to fulfil the conditions $\hbar\omega \geq E_{Cmob} - E_d$ and $\hbar\omega \geq E_d - E_{Vmob}$ by definition (see section 2.4.6.). In situation A_3, these conditions are not fulfilled (i.e. $\hbar\omega < E_g/2$) leading to a complex occupation function in the numerical analysis of CPM (c.f. fig. 44 as example) and to a discrepancy between the absorption values at thermal equilibrium $\alpha_{th}(\hbar\omega < E_g/2)$ and the CPM deep defect absorption values $\alpha_{CPM}(\hbar\omega < E_g/2)$ for all parameter sets studied here. However, this absorption range is not of central interest and will not be discussed any further.

Also note that the defect-to-band generation mechanism G_n (transitions of type C) is taken into account in overview 1 only. Other generation-recombination mechanisms (other than shown in overview 1) are also possible, e.g. based on defect-to-band generation mechanism G_p (transitions of type B), but lead to no major changes concerning the discussion.

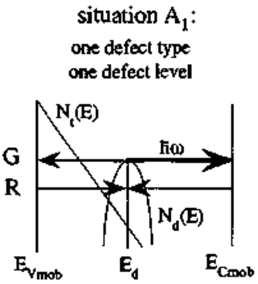

Fig.41: situation A_1.

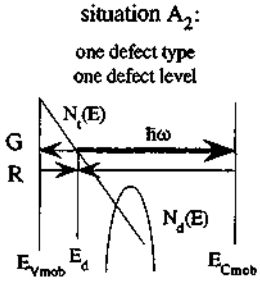

Fig.42: situation A_2.

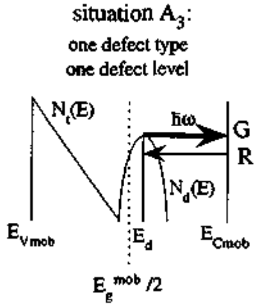

Fig.43: situation A_3.

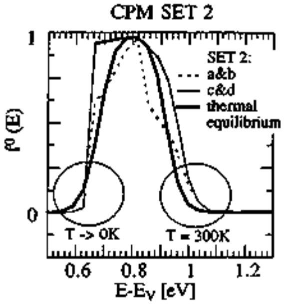

Fig.44: occupation functions $f^0(E)$ of the neutral dangling bonds for $\hbar\omega$ = 0.8eV (numerical CPM analysis SET 2a-d).

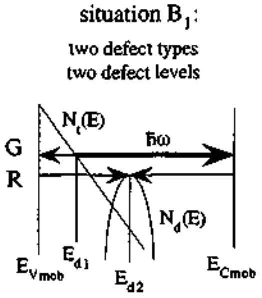

Fig.45: situation B_1.

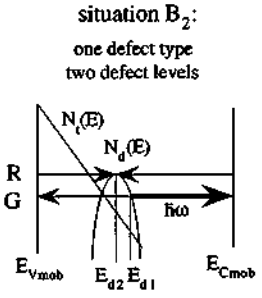

Fig.46: situation B_2.

Why are the CPM spectra capture cross section dependent?

The main point is the following: the electron-hole pair generation mechanisms "G" is related to the thermal emission rate which itself depends on capture cross sections. Furthermore, the recombination mechanisms "R" is related to capture cross sections. All these capture cross sections are related to a specific defect type. Therefore, all possible generation-recombination mechanisms (as e.g. shown in overview 1) are determined by a <u>set of capture cross sections</u>. If the generation-recombination mechanisms are spectrally-dependent (as expected) and - at the same time - they are related to a change of the set of capture cross sections, the CPM "working point" will be spectrally-dependent. Therefore, a change from situation A_1 to situation B_1 leads to a change in the CPM "working point" (change of the defect types involved), but a change from situation A_1 to situation B_2 does not (no change of the defect types involved).

One can say in a more general way that if the defect types which determine the main generation-recombination mechanism change as a function of the photon energy, the CPM "working point" will be spectrally-dependent, and a spectrally dependent CPM "working point" leads to distorted CPM spectra.

This qualitative estimation is, in fact, observed in the numerical analysis of the CPM spectra at steady-state equilibrium (c.f. fig.10 and fig.11). Identical capture cross sections for all localised states within the mobility gap (= one defect type) lead to a spectrally independent CPM "working point" (SET a&b), but different capture cross sections for the localised states within the mobility gap (= several defect types) lead to a spectrally dependent CPM "working point" (SET c&d).

For a qualitative discussion, it seems to be reasonable to reduce the complete standard DOS by a **system of one or <u>two</u> defect levels**, where in the case of two defect levels **either one or two defect types** are involved. But this reduction seems **not** to be valid for a quantitative (numerical) analysis. In fact, the defect-to-band generation mechanism G_{np} **could not be found** numerically in the case of the standard DOS by varying the optical matrix element R^2 as would be expected from the analytical analysis of the different defect-to-band generation mechanism (G_n, G_p or G_{np}) in section 2.4.6.

Note that so far CPM has been understood as a system of one defect level (see [Vanecek 81], [Mittiga 90] and chapter 2) but motivated by the qualitative discussion of the numerical analysis of CPM spectra at steady-state equilibrium, the author points out that CPM should be understood as a system of (at least) two defect levels which strongly depends on the defect types.

4. Conclusions

4.1. Conclusions of chapter 1

* *CPM Measurements* *

The Constant Photocurrent Method (CPM) is one of the most commonly used measurement techniques employed to determine the sub-band-gap absorption spectrum of amorphous hydrogenated silicon (a-Si:H). The theory behind CPM was originally developed on the basis of assuming "n-type" a-Si:H material. However, CPM is most often used to characterise undoped material (which means not doped with PH_3 or B_2H_6) and sometimes also for "p-type" material. Therefore, it is of basic interest to know in which cases CPM succeeds in detecting the absorption spectrum of a-Si:H correctly.

In chapter 1, three conditions, which have to be fulfilled in order to ensure the correct operation of the CPM measurement, were introduced and discussed; also introduced was the concept of a CPM "working point" (see section 1.2.). From the *theoretical* point of view, it is shown that CPM detects the absorption spectrum of a-Si:H only if these "three CPM measurement conditions" are all fulfilled. From the *experimental* point of view, the author found that there are indeed practical cases where these conditions are not fulfilled.

The experimental results obtained on several series of different doped samples can be commented as follows (see section 1.4.): CPM spectra of light-soaked, undoped layers are identical to PDS spectra (within a factor of 2 in the deep defect absorption range). In the case of annealed layers, the situation is as follows: For undoped layers, the sensitivity of the PDS technique in the deep defect absorption range is limited by surface-states, and a comparison with CPM spectra becomes difficult. It would seem, however, that the CPM results for the undoped layers studied here are quite reasonable. In the case of annealed, slightly doped layers, it is found that "n-type" samples show identical CPM and PDS spectra, whereas "p-type" samples show different CPM and PDS spectra: the CPM deep defect absorption values are found to be larger than the PDS deep defect absorption values for these "p-type" samples. In this specific case, the CPM measurement conditions are indeed not fulfilled. **Therefore, special care has to be taken while measuring CPM spectra on annealed, slightly "p-type" layers.** This is, to the author's best knowledge, the first systematic indication of such a failure of the CPM technique for a-Si:H samples. For all other samples investigated here, no experimental indications could be found that the CPM technique does not correctly detect the absorption spectrum of amorphous hydrogenated silicon.

However, the very low values of sub-bandgap absorption (measured by CPM) - as found here - for "compensated" material (which are "midgap" samples being, in this case, very slightly doped with B_2H_6) are troublesome. CPM measurements on annealed, "compensated" samples could suffer from the same basic problems as observed for the slightly "p-type" samples (first CPM measurement condition not fulfilled). But the second or third CPM measurement conditions (spectrally-dependent generation mechanism or spectrally-dependent charge carrier types, respectively) may as well not be fulfilled. Therefore, this particular type of "midgap" samples should be further investigated in future work.

In general, CPM spectra are measured on thin layers, which are contacted by a coplanar electrode configuration (standard CPM spectra). However, as demonstrated here, it is additionally possible to measure CPM on devices. In chapter 1, CPM spectra of sandwich-contacted or coplanar-contacted PIN diodes (see section 1.5. and 1.6.) and CPM spectra of coplanar-contacted, "partial" diodes (see section 1.7.) are presented. The motivation for performing CPM measurements on PIN diodes had originally been to check if CPM can be used as a simple tool for the characterisation of its "intrinsic" layer. The motivation for performing CPM measurements on "partial" diodes was to study the influence of surface effects. Due to the complexity of the problem, these CPM results on devices are, however, analysed and discussed here in a qualitative way only.

4.2. Conclusions of chapter 2

* *Analytical studies and definitions for numerical calculations* *

Analytical studies as well as definitions forming the basis for the numerical calculations of chapter 3 have been presented in chapter 2. These studies and definitions are based on the standard model for a-Si:H. This model consists of the well-established standard density of state (DOS) profile (parabolic bands, exponential tail states and a distribution of defects with a positive, finite correlation energy) and of the standard transport model (two mobility edges in the range of the parabolic bands).

Concerning the standard DOS, several new, unconventional aspects have been introduced and discussed here (see section 2.1.): The parabolic bands are described by effective DOS masses; the parabolic bands and the exponential tail states are connected in a new manner; the mobility edge - as element of the standard transport concept - is defined independently with respect to the DOS profile.

Concerning the statistics of a defect with a finite correlation energy, the author found that the charge neutrality condition leads - in the case of dangling bond defects (where $N_{DB}^{+} = N_{DB}^{-}$ is assumed) - to a temperature-independent Fermi level at thermal equilibrium (see section 2.2.). For the case of steady-state equilibrium, "recombination levels" were introduced and discussed for the specific statistics of a defect with a finite correlation energy (see section 2.4.).

Concerning the transition behaviour of a defect with a finite correlation energy, the author showed that the one-peak picture and the two-peak picture are equivalent, but that certain transitions have been underestimated in the published literature, so far, by a factor of two (see section 2.3.). Furthermore, one can conclude that a defect with a finite correlation energy (e.g. dangling bonds) cannot simply be replaced by the combination of a donor-like defect *and* an acceptor-like defect.

The understanding of the Constant Photocurrent Method (CPM) is generally based on the sub-band-gap statistics at steady-state equilibrium. The localised-to-localised transitions were neglected here in order to describe the generation and recombination mechanisms analytically. For the case of a defect without a finite correlation energy, the results were discussed in terms of certain "generation levels" that have been newly introduced here.

For the case of a defect with a finite correlation energy (e.g. dangling bonds), the analytical results remain complex. Therefore, the system at steady-state equilibrium is analysed numerically in chapter 3. Whereas in chapter 2 only one defect type was taken into account, the numerical analysis in chapter 3 showes that the presence of several types of defects (e.g. dangling bonds and tail states; each with different capture cross sections) can lead - by itself - to a discrepancy between CPM and PDS spectra: In the specific cases studied here, the CPM measurement conditions (as introduced in section 1.2.) are, then, not any longer fulfilled.

4.3. Conclusions of chapter 3

* *Numerical analysis* *

The author has to conclude that in the *numerical* analysis CPM spectra show a strong sensitivity to the value of the transport parameters ratios (e.g. to the ratios of the capture cross sections) and that, depending on the DOS parameters, different generation-recombination mechanisms determine the CPM spectra.

The numerical system studied here can explain the experimental conductivity measurements { $\sigma_{tot}(G)$ and $\gamma^*(G)$} of layers in the light-soaked state (c.f. fig.14b in chapter 1) and of "partial diodes" in the annealed state (c.f. fig.A6-3 in appendix A6), in a qualitative way, at least. This indicates that the simple standard DOS model in combination with a mobility gap is a reasonable approach to explain these measurements at room temperature.

But the numerical system studied here can not explain the experimental conductivity measurements { $\sigma_{tot}(G)$ and $\gamma^*(G)$} of the layers studied here in the annealed state (c.f. fig.A2-5 in appendix A2). This means that the behaviour of a-Si:H layers in the annealed state (at least at low illumination levels) is more complex than in the light-soaked state.

Especially, the electronic states of the dopant atoms could be of importance for the description of the total conductivity in the annealed state. Now, the numerical system used here does not contain the electronic states of the dopant atoms. Such electronic states could be a possible reason why the very specific situation of supra-linear power law factors ($\gamma^* > 1$) - as measured on slightly "p-type" samples - could not be reproduced by the present numerical analysis. One could imagine also other reasons why the present, numerical analysis fails to reproduce the experimental results for the annealed layers studied here: In these samples other transport mechanism (such as hopping) or other recombination paths (not considered in the present numerical model) could be of importance.

On the other hand, the ballistic recombination model used here seems to be quite reasonable as a simple description of transport at room temperature. But, as mentioned, the evolution of transport and conductivity models in a-Si:H is still in progress.

The author would like to close the present study by repeating the statement that CPM detects the absorption spectrum of a-Si:H only if the "three CPM measurement conditions" (as introduced in this thesis) are all fulfilled. Whereas the first condition can be checked by experiment, the second and third condition must be checked by a numerical or analytical analysis based on a **specific** a-Si:H model. The author showed that, in fact, these CPM conditions are in some specific cases - in the experiments as well as in the numerical analysis - not fulfilled.

* * *

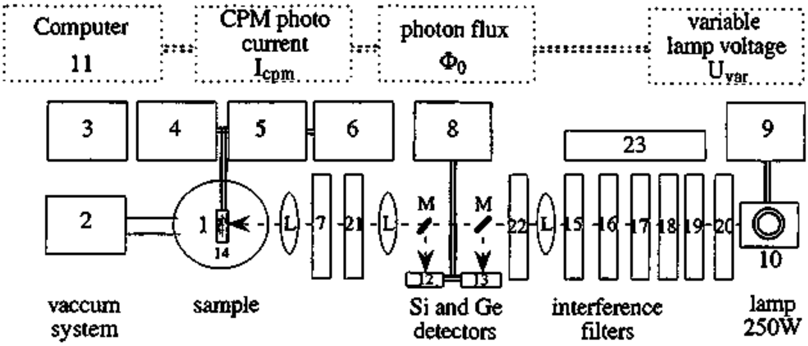

1 sample	
2 vacuum system ($p = 10^{-5}$ mbar):	Mechanical Forepump Alcatel 2004A Turbo Pump Balzers
3 temperature controller (T = 0 - 250°C):	Eurotherm 822 for a Pt 100 element
4 electrometer (I = 0.1fA - 20mA):	Keithley 617 Programmable Electrometer
(U = 0 - 100V)	
5 current amplifier ($10^3 - 10^{11}$ V/A):	Keithley 428 Current Amplifier
($10^4 - 10^9$ V/A):	Princeton Applied Research EG&G 181
6 lock-in amplifier (U = 1nV - 500mV):	Standford Research SR 530 Lock-in Amplifier
7 chopper unit (ν = 0 - 4kHz):	Standford Research SR 540 Chopper Controller
8 picoamper meter (I = 0.1pA - 2mA):	Keithley 485 Autoranging Picoammeter
9 variable power supply (0 - 30V, 0 - 10A):	Delta Electronika EK 030-10 power supply
10 halogen lamp 250W / 12V:	Oriel 66056 lamp system
11 computer controller and regulator:	Olivetti PC M24 PC LabCard PCL-711S
12 Si diode	Si diode S2386-8K (33 mm^2) 400 - 1100nm used for $\hbar\omega$ = 1.24 - 2.43eV
13 Ge diode	Hamamatsu Ge diode B1919-01 (20 mm^2) used for $\hbar\omega$ = 0.83 - 1.18eV
14 pyro detector	High Performance Pyroelectric IR detector ELTEC 404VM used for the calibration of the Si- and Ge-diodes
15 band pass filter RG850	used for $\hbar\omega$ = 0.83 - 1.42eV
16 band pass filter RG695	used for $\hbar\omega$ = 0.83 - 1.65eV
17 grey filter 1/100	used for $\hbar\omega$ = 1.70 - 2.43eV
18 filter wheel I ($\hbar\omega$ = 1.49 - 2.43eV)	interference filters 510 - 830nm
19 filter wheel II ($\hbar\omega$ = 0.83 - 1.43eV)	interference filters 840 - 1500nm
20 band pass filter GG420	fix
21 grey filter 1/10'000	used for measurements of $\sigma_{tot}(G)$
22 shutter	used during the change of the interference filters
23 filter cooling unit	ventilator
M small mirrors	aluminium metalisation
L various lenses	

Fig.A1-1: CPM measuring set-up.

APPENDIX

Appendix A (corresponding to chapter 1)

A1. The measurement set-up

The measurement set-up consists of the following elements (The numbers in "{}"-brackets correspond to the notation of fig.A1-1). The sample {1} is located within the vacuum chamber {2}. The temperature of the sample is controlled by a temperature controller {3}. The voltage applied to the sample comes from the electrometer (4). The dark current and the total current of the sample can be measured by the same electrometer {4} (cw-mode). The photo current can be measured with a lock-in amplifier {6} in combination with a current-voltage preamplifier {5} and a chopper unit {7} (lm-mode). The sample is illuminated by a halogen lamp {10}. The intensity of this lamp can be regulated with a variable lamp power supply {9}. The light intensity, with which the sample is illuminated, is measured with a Si-diode or a Ge-diode, depending on the photon energy. These two diodes are calibrated by a calibrated pyrodetector {14}, which, in this case, is located at the position of the sample in the vacuum chamber. In this set-up, the monochromatic light is obtained by a number of interference filters which are located on two filter wheels {15, 16}. In comparison to a monochromator, the advantage of these interference filters is that the maximum light intensity is higher, but the disadvantage is that only a limited spectral resolution (here: 30 interference filters) is available. Other elements of this set-up are band pass filters {17, 18, 19}, grey filters {20, 21}, a shutter {22}, a filter cooling unit {23}, lenses {L} and mirrors {M}. The basic measurement units as well as the filters of this set-up are controlled by a computer {11}. Therefore, the measurements are performed automatically.

A1.1. Measuring CPM on layers in the cw-mode

In order to measure CPM spectra on layers in the cw-mode, the following points are important. Before and after the detection of the CPM spectra, the dark conductivity must be measured. A change in these two dark conductivities can be an indication that the Fermi level position changed during the measurement and that, therefore, the CPM spectra can be distorted [Finger 90]. The author used a stabilisation time of 10min before measuring dark conductivity. In order to measure dark conductivity, a vacuum chamber is required for low conducting samples in order to exclude surface effects (e.g. due to humidity). In order to measure the sample in the initial state (annealed state), the sample can be annealed as a first step, and the CPM spectrum can be measured in the same system as a second step. The CPM current measured in the cw-mode (e.g. by an electrometer) has to be larger than the dark current ($I_{CPM} > I_{dark}$). In order to fulfil this condition on high conducting samples (e.g. strongly doped), the incident light intensity (for low photon energies) must be large. Therefore, interference filters are ideal for the cw-mode (higher light intensity than with a monochromator). The regulation in the cw-mode is also very fast. The electrometer used here delivers a measured value every 0.3s and the CPM spectrum can be measured within 30min.

A1.2. Measuring CPM on layers in the lm-mode

Measuring CPM in the lm-mode requires a lock-in amplifier which detects the photo current. The dark current need not be measured either before or after detecting the CPM spectrum as in the cw-mode. The CPM photo current can be lower than the dark current ($I_{CPM} < I_{dark}$). Therefore, no interference filters (high light intensity) are necessary as in the cw-mode. Whether a photo current measured in the lm-mode can be influenced by surface humidity and that, therefore, a vacuum chamber is to be recommended, is unknown to the author. However, it is certain that the photo current has to be measured without any unwanted bias light (room light) because it could influence the occupation of the deep defects.

In the case of undoped a-Si:H, three seconds are a typical integration time of the lock-in amplifier (for low photon energies). This means that every 10 seconds a measured value is available. In comparison to the cw-mode, this leads to very long regulation times. In the lm-mode, a monochromator should be better than some interference filters. In the case of interference filters, the sample is not illuminated during the change of the filters (this would lead to a change in the occupation each time). In the case of a monchromator, the photon energy can be changed smoothly and the regulation time is, therefore, faster. In the case of the lm-mode, manual regulations with a monochromator require up to half a day. For the computer controlled set-up used here, a CPM measurement in the lm-mode takes several hours. If a bias-light is present, CPM spectra can be measured in a much faster way due to the quicker response time.

A1.3. Measuring CPM on solar cells

Solar cells are not generally characterised in vacuum chamber systems and it is rather a luxury to measure them in a vacuum chamber, as done here. CPM spectra of solar cells can be measured in the cw-mode or in the lm-mode. The response time of solar cells is so quick that CPM spectra can be measured even in the lm-mode in a very short time.

A1.4. Regulation of the constant photo current

Many different methods were tried by the author in order to reduce the regulation time of the CPM measurements. It turned out that the regulation of the voltage of the halogen lamp is a disadvantage, because the voltage intensity characteristic of the lamp is not linear and because, gradually, the lamp changes the intensity at a given voltage due to the temperature changes of the lamp filament. Also, the lamp has a temperature-dependent "on/off" voltage-offset, including an hysteresis behaviour. A reasonable advantage would be to have an intensity-stabilised lamp where the intensity can be regulated in a linear way. Another approach was seen in other laboratories, where the light intensity was regulated with the help of some linearly graded grey filters. Whether the sample is still homogeneously illuminated in this way is questionable. However, the author has found a simple software procedure, which can be used independently of the response time of the sample.

As a stabilisation criterion of the CPM current, the author averaged out the last measured points (e.g. 10) and compared this value with the required value. If the relative difference between these values was below, e.g. 2%, the regulation was stopped for a certain stabilisation time (e.g. 1s). If after this stabilisation time the measured value was still constant within the required range, the next photon energy was chosen. From Vanecek [91/1], the author has learnt to keep the photo current of the first photon energy (while starting in the low photon energy range) constant over several minutes (e.g. 10 minutes) in order to stabilise the system. Cross checks of some CPM spectra measured with Vanecek's set-up ([Vanacek 91/1] and [Mettler 93/1]) showed that both systems measure identical CPM spectra (see fig.A1-2).

Fig.A1-2: CPM spectrum $\alpha_{CPM}(\hbar\omega)$ for a "p-type" sample as measured in the cw-mode by the set-up described in fig.A1-1 and as additionally measured in the lm-mode by Vanecek's set-up [Mettler 93/1]. (sample C270991)

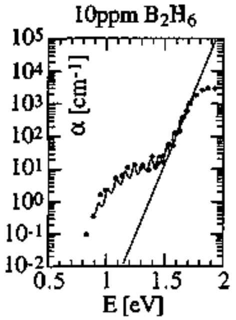

A2. Details on the dopant dependency of PDS and CPM

A2.1. First series*

Sauvain et al. [93] analysed the properties of some slightly doped and undoped a-Si:H layers deposited on a glass substrate (Corning 7059) at 220°C with the VHF-CD technique in a single chamber deposition system usually used for the development of solar cells. Doping was achieved by mixing the dopant gases in hydrogen (500ppm diborane (B_2H_6) in H_2 for "p-type" samples and 1000ppm phosphine (PH_3) in H_2 for "n-type" samples). This mixture was used with pure silane for the layer deposition. The gas dopant ratio of the boron-doped layers varied between $C(B_2H_6 / SiH_4)$ = 0.2 and 10 ppm; for the phosphorus-doped layers, it varied from $C(PH_3 / SiH_4)$ = 0.1 ppm to 1 ppm. The layers had a thickness ranging between 1.7 µm and 2.5 µm. After deposition, all these layers were annealed at 200°C for 1h. Fig.A2-4 shows the corresponding dark conductivities after annealing. Fig.A2-1 shows the results of these CPM and PDS measurements for an "n-type", two "p-types" and an undoped sample. One recognises that the "p-type" samples show a higher deep defect absorption range measured with CPM than measured with PDS. So far, this behaviour had not been observed and led to some basic questions concerning the reliability of these absorption measurement techniques [Sauvain 93].

---

* samples: C270991, C211091, C181091, C071091, C141091, C021091, C241091, C031291, C251091, C041291

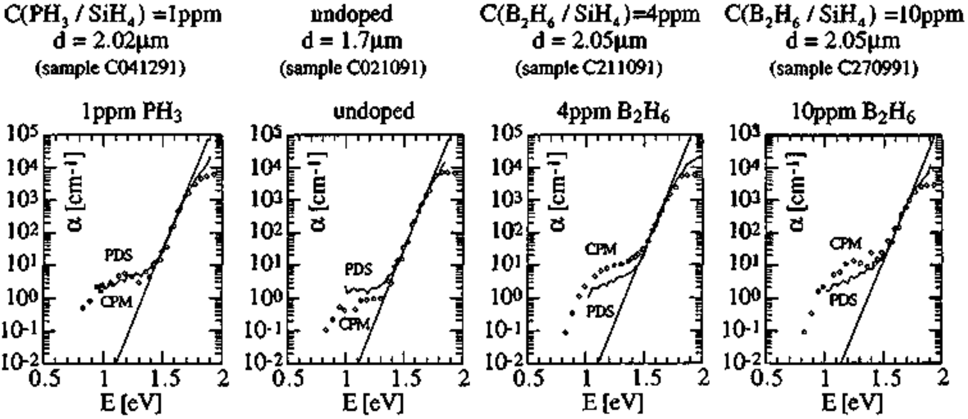

Fig.A2-1: CPM and PDS spectra $\alpha(\hbar\omega)$ of some slightly doped a-Si:H samples. [Sauvain 93]

Fig.A2-2 shows the CPM and PDS absorption values of the ten analysed layers in the annealed state at a photon energy of 1.2eV as a function of the gas dopant ratio. The PDS absorption values vary between 1 - 5 cm^{-1}, whereas the CPM absorption values vary between 0.3 - 20 cm^{-1}. Fig.A2-3 shows the ratios of the CPM and the PDS absorption values as a function of the gas dopant ratio. This ratio is 1 for "n-type" samples, about 4 for "p-type" samples and about 1/2 for very low doped and undoped samples. The factor of 1/2 is supported by arguments of Wyrsch et al. [91], based on the different transition behaviours of CPM and PDS.

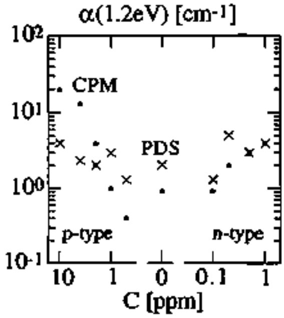

Fig.A2-2: PDS (dotes) and CPM (crosses) deep defect absorption values α(1.2eV) as a function of the gas dopant ratio C. [Sauvain 93]

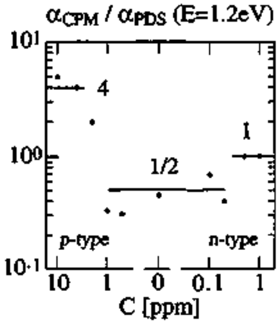

Fig.A2-3: ratio of the PDS and the CPM deep defect absorption values α(1.2eV) as a function of the gas dopant ratio C. [Sauvain 93]

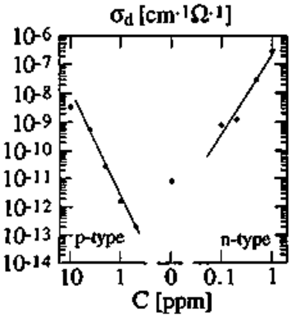

Fig.A2-4: dark conductivity σ_d (after annealing) as a function of the gas dopant ratio C. [Sauvain 93]

The author checked whether the CPM set-up worked in a proper way for "p-type" samples, where this unexpected deep defect absorption behaviour was observed. Fig.A1-2 shows the CPM spectrum for a "p-type" sample as measured in the cw-mode by the set-up described in fig.A1-1 and as additionally measured in the lm-mode by the set-up of Vanecek [Mettler 93/1]. No principle differences between these two measurements could be observed. Furthermore, effects of contacts (Al or Cr contacts, see fig.8b of chapter 1) or effects of the CPM regulation time (1min to 60min for each photon energy) were not observed for these "p-type" samples.

A2.2. Second series*

* samples: C140193, C220293/1&2, C230293/1&2, C240293, C180393/1&2, C190393/1, C230393, C070493/1&2

In order to prove the reproducibility and in order to check if this behaviour can also be observed for higher doped "p-type" samples, a second series of doped samples were deposited in the same way as for the first series. These layers have thicknesses ranging between 2.2 µm and 4.1 µm for series 2, whereas in the first series, the thicknesses were between 1.7 µm and 2.5 µm. The results are presented in fig.11 of chapter 1.

A2.3. Spectrally dependent conductivity measurements*

* samples: C211091, C021091, C041291

The main motive in carrying out the conductivity measurements $\sigma_{tot}(G)$ and $\gamma^*(G)$ was the slightly "p-type" samples, where the deep defect absorption range measured by CPM was higher than measured by PDS.

The total conductivity was measured with the electrometer (cw-mode) in the CPM set-up under vacuum by illuminating the sample with monochromatic light in the following order: $\hbar\omega = 1.24\text{eV}$, 1.53eV and 1.82eV with the maximum intensity of $I_0 \approx 4\ \text{mWcm}^{-2}$. The photon energy 1.82eV corresponds to band transitions, 1.53eV to tail-band transitions and 1.24eV to deep defect transitions for the case of a-Si:H (see chapter 2). It was observed that the total conductivity (cw-mode), as a function of the light intensity, depends strongly on the measurement speed, especially in the low intensity range, due to some relaxation processes. The spectral conductivity was automatically measured at about 100 different light intensities for each photon energy with a stabilisation time of 60s for each intensity. This stabilisation time is also typical for CPM measurements in the cw-mode. The generation rate scale was calculated by the following equation taking into account a reflectivity of R=0.3 and a photon energy of $\hbar\omega = 1.82\text{eV}$:

$$G = d^{-1}[1 - \exp(-\alpha d)]\,\Phi_0$$

The values of the power law exponent γ^* were calculated as the slope between two measured points of $\sigma_{tot}(G)$ in the double logarithmic scale.

Fig.A2-5 shows the total conductivity as a function of the generation rate for three different photon energies.

The top plot corresponds to the annealed, "n-type" sample. One recognises a large peak of factor $\gamma^*(G)$ at $G = 10^{16}\,cm^{-3}s^{-1}$. The factor $\gamma^*(G)$ drops below 0.5 for higher generation rates, which cannot be explained by a standard recombination mechanism. Degradation (= increase of the total defect density) during the measurement of $\sigma_{tot}(G)$ is almost excluded because no change of the CPM spectrum was observed after this measurement. A possible explanation for this drop may be a change of the Fermi level due to relaxation processes (changes in the occupation). One can conclude that factor γ^* may not just describe the recombination behaviour at higher generation rates. However, the power law exponent $\gamma^*(G)$ is very similar for all three photon energies.

The middle plot corresponds to the annealed, undoped sample, where the power law factor $\gamma^*(G)$ is constant at a value of about 0.8 for all three photon energies.

The bottom plot corresponds to the annealed, "p-type" sample. The conductivity seems to depend on the photon energy. Moreover, one can observe for each photon energy a different power law dependency. The factor γ^* shows a supralinear behaviour ($\gamma^* > 1$). This was interpreted by Rose [63] as the presence of sensitising states, located for a-Si:H between the dangling bond peaks and the valence band edge [Gu 86].

It has to be mentioned that the generation rate scale in these plots was calibrated for a photon energy of 1.82eV. For the two other photon energies, the curves were simply shifted along the generation rate scale, in such a way that they matched the calibrated curves. For the "p-type" sample, the photon energies are matched in the range of $G = 2\,10^{17}\,s^{-1}cm^{-3}$.

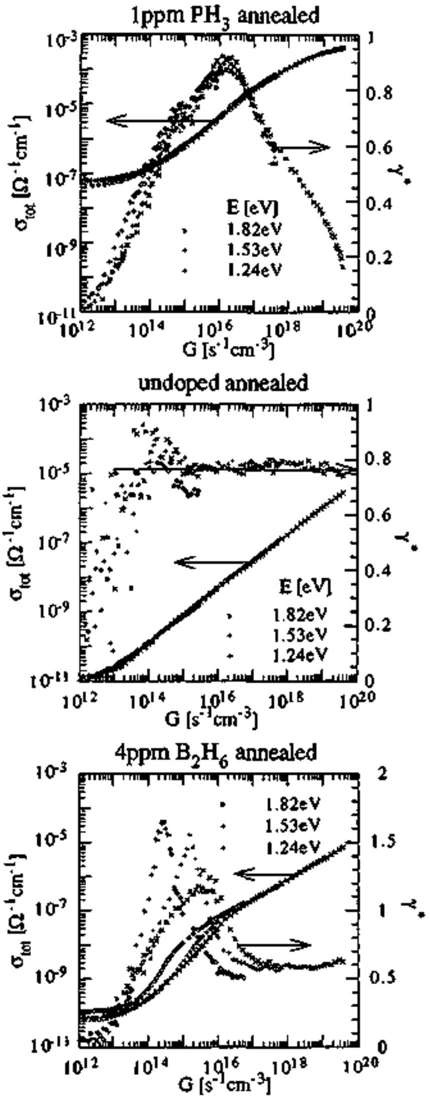

Fig.A2-5: conductivity σ_{tot} and factor γ^* as a function of generation rate G [Mettler 93/2]:

top: "n-type", annealed sample

middle: undoped, annealed sample

bottom: "p-type", annealed sample

With the help of these conductivity measurements $\sigma_{tot}(G)$ and $\gamma^*(G)$ measurements, it is possible to decide whether the first and second CPM conditions are fulfilled.

The first CPM condition ("spectrally independent power law factor γ^*") is fulfilled for the "n-type" and the undoped sample, whereas for the "p-type" sample, it is not fulfilled in the annealed state.

The proof of the second CPM condition (CPM "working point" spectrally independent) is rather critical because one should know the exact absorption values for each photon energy in order to calibrate these curves in the proper way. With the calibration presented here, one can note that the second CPM condition is fulfilled for the "n-type" and the undoped sample, whereas for the "p-type" sample, it is not.

A2.4. Degradation studies*

* samples: C270991, C211091, C021091, C041291

The samples were degraded in a new degradation system by a high pressure sodium lamp as developed by Goetz [93]. The samples were illuminated from both sides by a light intensity of $I_0 = 500\text{mWcm}^{-2}$. The corresponding photo conductivity (cw-mode) was measured during light-soaking at 55-60°C. The CPM spectra of these samples were measured several times after light-soaking, with intervals of several hours between these measurements: no changes in the CPM spectra could be observed as a function of time after light-soaking. Fig.A2-6 shows the CPM spectra of these four samples in the annealed and in the light-soaked state.

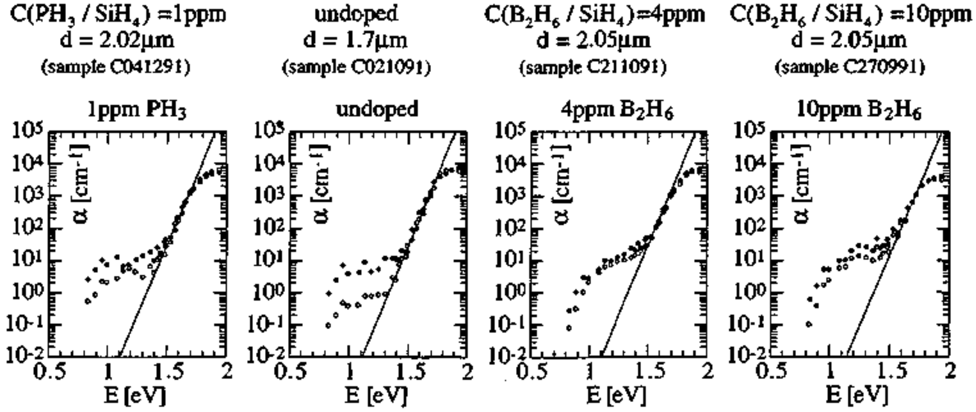

Fig.A2-6: CPM spectra $\alpha_{CPM}(\hbar\omega)$ of some slightly doped a-Si:H samples in the annealed state (circles), corresponding to fig.A2-1, and in the light-soaked state (dots).

A3. Details on the substrate temperature dependency of PDS and CPM

Kroll et al. [93] published the properties of some a-Si:H layers deposited at different temperatures with the VHF-CD technique in a new UHV-vacuum deposition system. The hydrogen content of these samples varies in the range of 6-12% linearly with the substrate deposition temperature (200°C - 400°C) but the sample properties are not related to these different hydrogen contents, as concluded by Kroll et al. [93]. The PDS absorption spectrum was measured by Kroll et al. [93] in the annealed and the light-soaked state. The samples were degraded in the system described in appendix A2.4.

The author additionally had the possibility of measuring the CPM spectra of those samples. CPM was measured in the cw-mode and fig.A3-1 to fig.A3-4 shows the results.

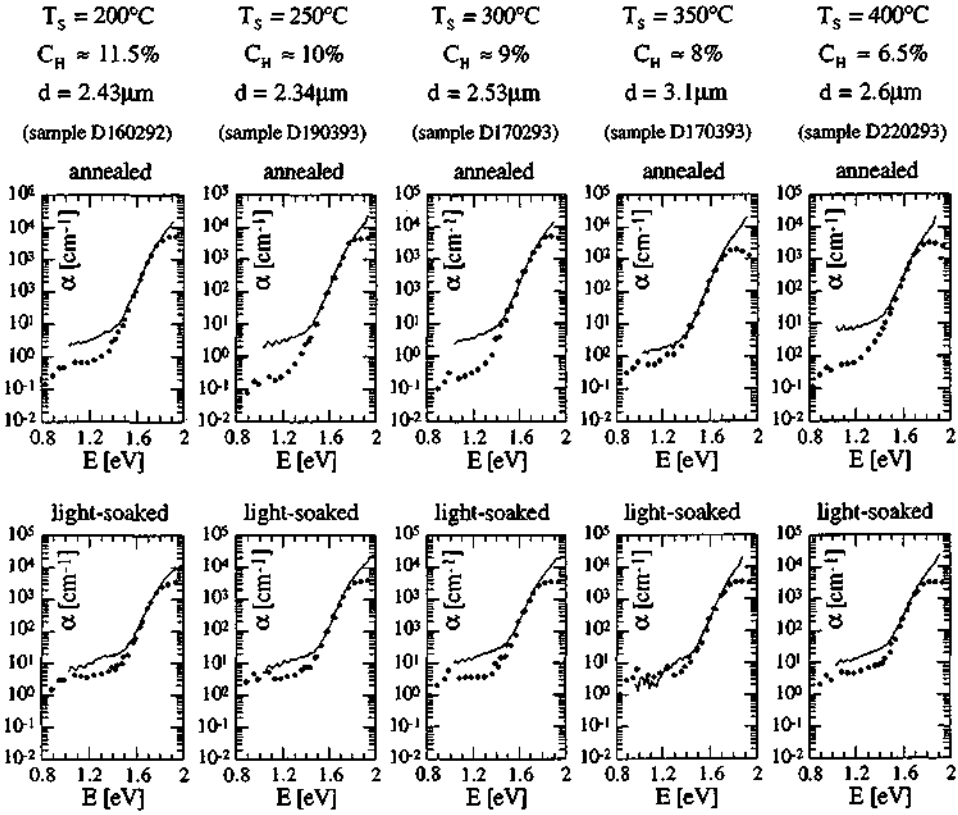

Fig.A3-1: CPM spectra $\alpha_{CPM}(\hbar\omega)$ (full dots) and PDS spectra $\alpha_{PDS}(\hbar\omega)$ (straight lines) of five samples deposited at different substrate deposition temperatures T_S (200°C - 400°C). The upper spectra correspond to the annealed state and the lower spectra correspond to the light soaked states.

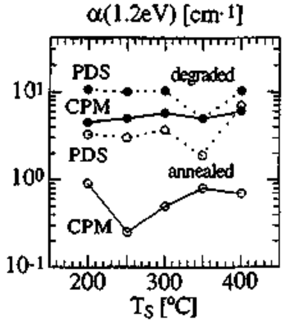

Fig.A3-2: PDS (dashed) and CPM (strait) deep defect absorption values α(1.2eV) in the annealed (circles) and in the light-soaked (dots) state.

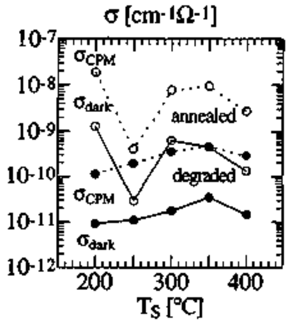

Fig.A3-3: CPM conductivity σ_{CPM} (dashed) and dark conductivity σ_d (strait) in the annealed (circles) and the light-soaked (dotes) state.

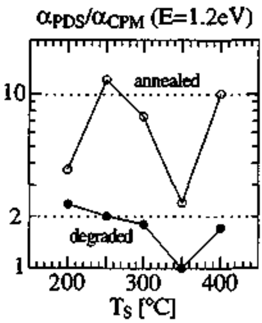

Fig.A3-4: ratio of the PDS and CPM deep defect absorption values α(1.2eV) in the annealed (circles) and in the light-soaked (dotes) state.

A4. Details on the measurement temperature dependency analysed by CPM

Undoped, "n-type" and "p-type" sample were selected for these measurements. As a first step, these samples were annealed after which the temperature was continually increased. Before the CPM spectra were measured, the temperature was stabilised for at least one hour. Up to about 100°C, CPM spectra were measured in the cw-mode ($I_{CPM} > I_{dark}$). Above about 100°C, CPM spectra could only be measured in the lm-mode due to the increase of dark current ($I_{CPM} < I_{dark}$). Fig.A4-1 to fig.A4-3 show the results.

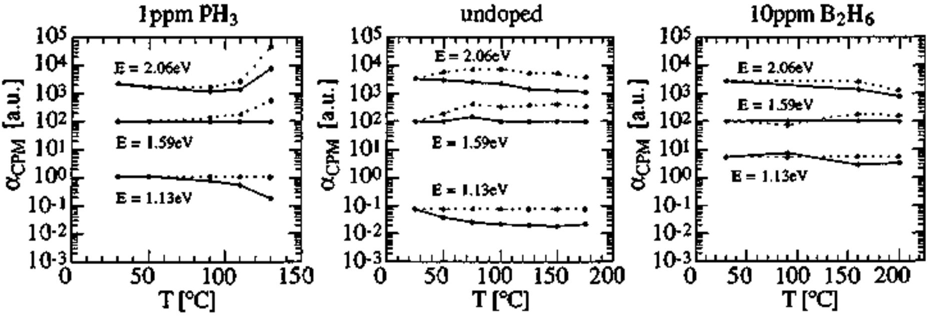

Fig.A4-1: CPM deep defect absorption values α_{CPM} as a function of measurement temperature T at $\hbar\omega$ = 1.13eV, 1.59eV and 2.06eV: the strait lines correspond to the relative "calibration" in the Urbach tail ($\alpha_{CPM}(1.59eV) = 100\ cm^{-1}$) (c.f. fig.A4-2) and the dashed lines to the relative "calibration" in the deep defect absorption range ($\alpha_{CPM}(1.13eV) = 0.075\ cm^{-1}$) (c.f. fig.A4-3).

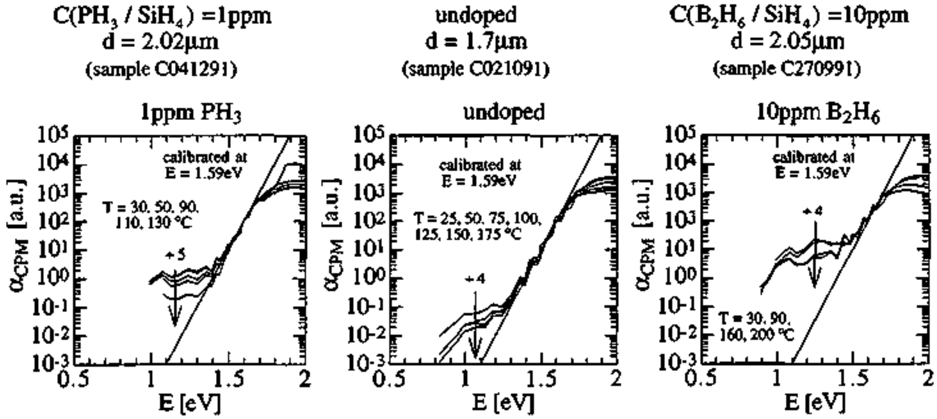

Fig.A4-2: CPM spectra $\alpha_{CPM}(\hbar\omega)$ of some slightly doped and undoped a-Si:H samples measured at different temperatures (relative "calibration" in the Urbach tail ($\alpha_{CPM}(1.59eV) = 100\ cm^{-1}$)).

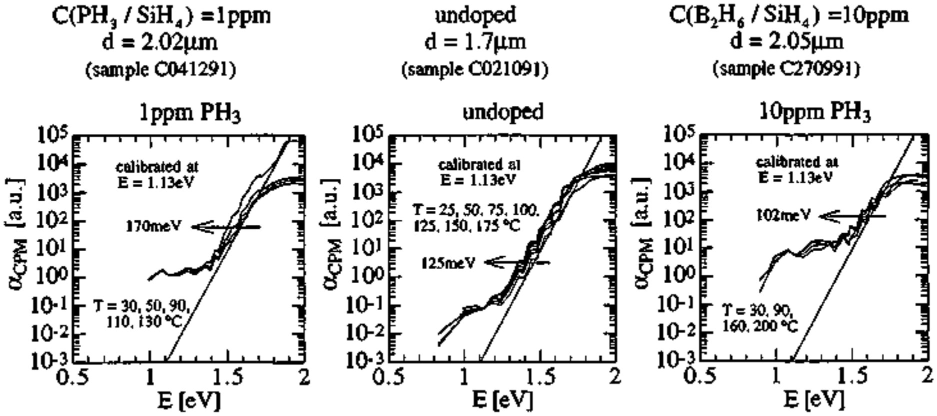

Fig.A4-3: CPM spectra $\alpha_{CPM}(\hbar\omega)$ of some slightly doped and undoped a-Si:H samples measured at different temperatures (relative "calibration" in the deep defect absorption range ($\alpha_{CPM}(1.13eV) = 0.075\ cm^{-1}$)).

A5. Details on the PIN diodes analysed by CPM

All samples are in the annealed state, all relative CPM spectra are "calibrated" within the Urbach tail range ($\alpha_{CPM}(1.59\text{eV}) = 100\ \text{cm}^{-1}$). The sandwich contacted PIN diodes have a TiAg metalisation surface of 2.5mm x2.5mm. The thin PIN diodes with a buffer layer have an efficiency of about 7%.

A5.1. CPM measurements on a thin PIN diode with a buffer-layer (sample C220590)

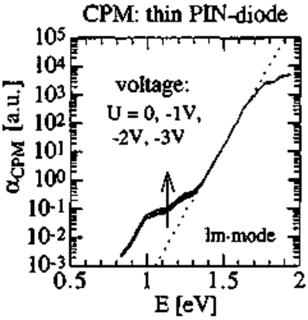

Fig.A5-1: a reverse voltage.

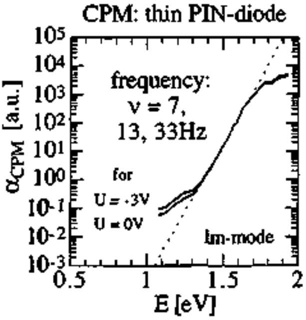

Fig.A5-1b: chopper frequency.

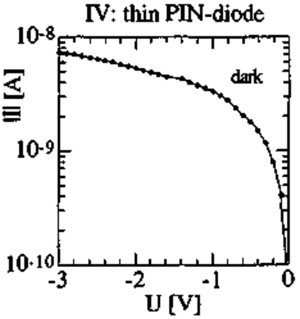

Fig.A5-1c: I-V characteristics.

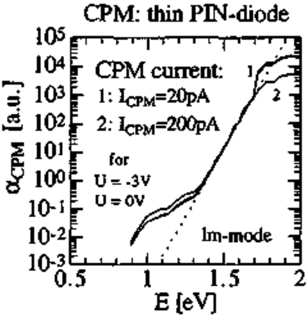

Fig.A5-1d: CPM current.

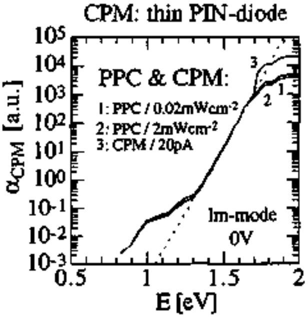

Fig.A5-1e: PPC spectra.

A5.2. CPM measurements on a thin PIN diode with a buffer-layer (sample C220690)

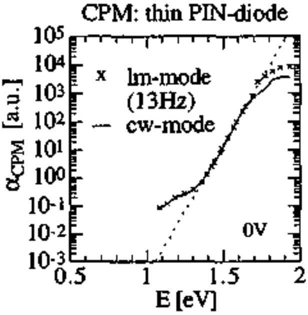

Fig.A5-2a: lm- and cw-mode.

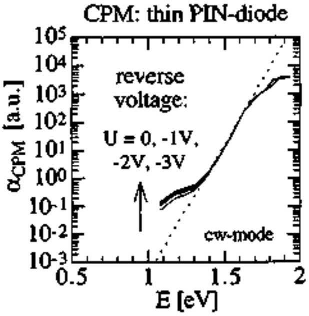

Fig.A5-2b: reverse voltage.

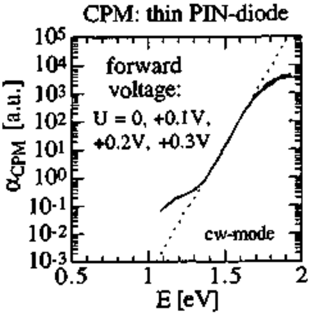

Fig.A5-2c: forward voltage.

A5.3. CPM measurements on thin PIN diodes (different samples)

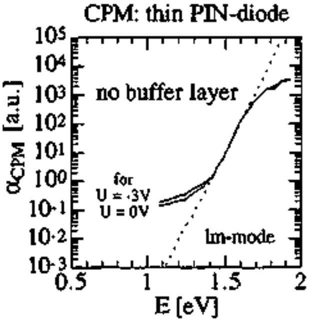

Fig.A5-3a: no buffer layer. (sample C060891)

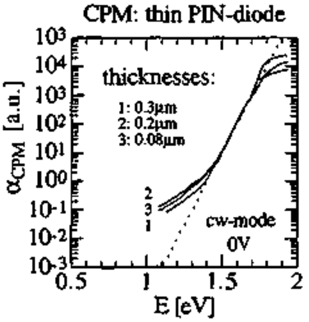

Fig.A5-3b: very thin samples with a buffer-layer. (samples C191190, C270491, C250191)

A5.4. CPM measurements on a thick PIN diode (sample B080692)

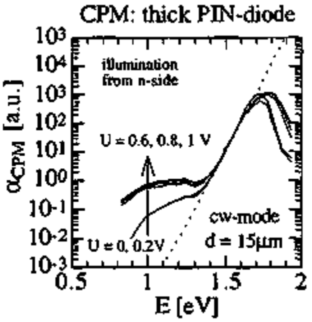

Fig.A5-4a: forward voltage.

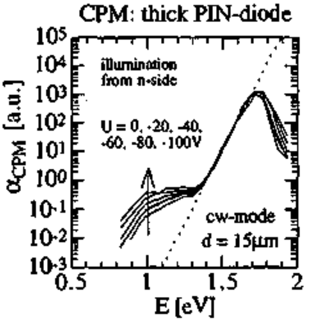

Fig.A5-4b: reverse voltages.

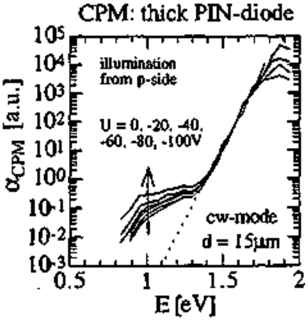

Fig.A5-4c: reverse voltages.

A5.5. Comparison to published literature

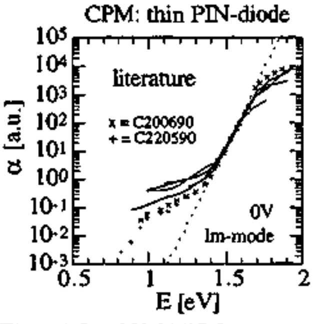

Fig.A5-5a: CPM&PPC spectra as "calibrated" at 1.6eV. (Ref: Fig.1 in [Hegedus 88], Fig.2 in [Dalal 90], Fig.5 in [Mittiga 90], Fig.4 in [Rübel 89])

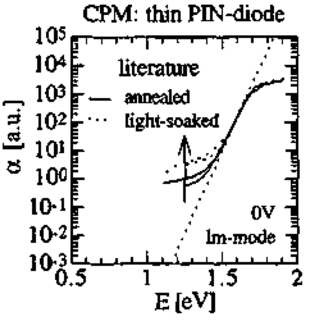

Fig.A5-5b: CPM&PPC spectra as "calibrated" at 1.6eV. (Ref: Fig.2 in [Hegedus 88], Fig.2 in [Dalal 90])

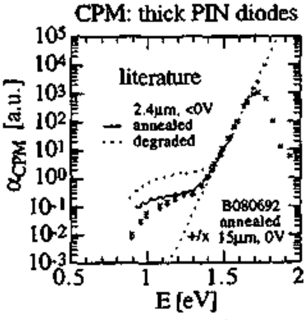

Fig.A5-5c: CPM&PPC spectra as "calibrated" at 1.6eV. (Ref: Fig.2 in [Kocka 88])

A6. Details on the"partial" diodes analysed by CPM *

* samples: C180692, C160692, C170692, C150692

As "new" configurations, some parts of a thin PIN diode were studied by CPM. An i-layer, followed by a heavily doped n-layer and an i-layer, followed by a heavily doped p-layer, were deposited on a glass substrate. Both configurations were contacted in the coplanar configuration (0.5 x 8mm); the n-layer (thickness 150-200Å) with TiAg (1500Å), the p-layer (thickness 100-150Å) with Al (1500Å). These two layers correspond to the doped layers used for thin PIN diodes.

The CPM spectra of a sample with a thick and a thin i-layer were measured in the "front" and "back" illumination modes (fig.A6-1). No differences in the deep defect absorption range could be observed. The CPM spectra were calibrated with transmission measurements, which showed a slight difference between the samples with a thick and thin i-layer. The CPM measurement conditions were also tested: the spectrally independent conductivity measurements $\sigma_{tot}(G)$ of the annealed samples show a similar behaviour as a degraded layer (c.f. fig.A6-3)! Further, the activation energy of these samples corresponds to the activation energy of some doped layers (fig.A6-2), but the dark current after annealing is unstable and decreases.

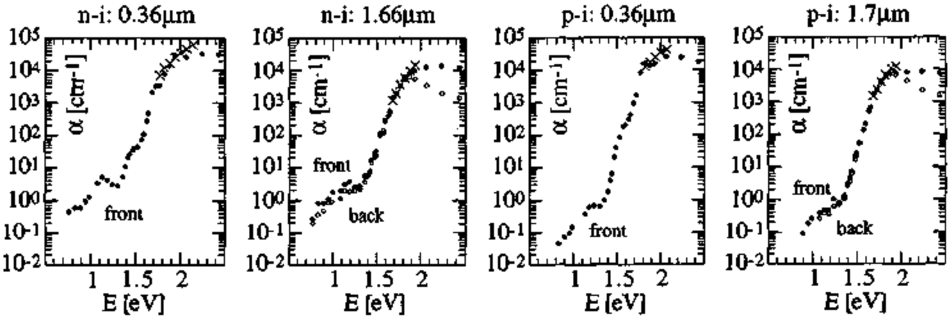

Fig.A6-1: Coplanar CPM spectra $\alpha_{CPM}(\hbar\omega)$ of the "n-i" and "p-i" configurations with different thicknesses of the i-layers, calibrated by transmission measurements as indicated by "x".

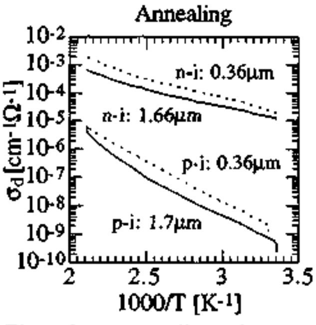

Fig.A6-2: annealing characteristics of the "n-i" and "p-i" configurations (see text).

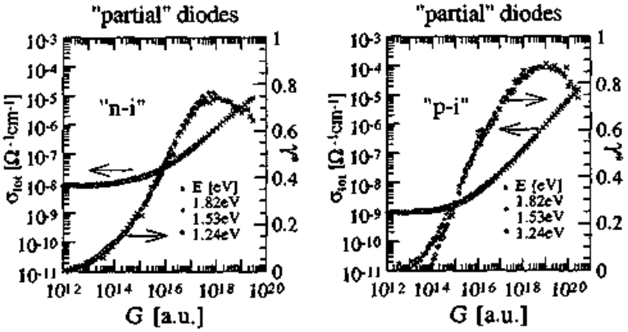

Fig.A6-3: conductivity characteristic $\sigma_{tot}(G)$ and $\gamma^{*}(G)$ for the "n-i" and "p-i" configurations (d≈1.7μm), measured at $\hbar\omega$ = 1.24, 1.53, 1.82eV.

Appendix B (corresponding to chapter 2)

B1. The standard DOS model used for the numerical analysis:

B1.1. The conduction band and the valence band:

DOS of the conduction band: $N_{CB/CBT}(E) = N_{CB}(E)$ for $E \geq E_C^{tail}$

$N_{CB/CBT}(E) = N_{CBT}(E)$ for $E < E_C^{tail}$

DOS of the valence band: $N_{VB/VBT}(E) = N_{VB}(E)$ for $E \leq E_V^{tail}$

$N_{VB/VBT}(E) = N_{VBT}(E)$ for $E > E_V^{tail}$

with the parabolic conduction band CB and the parabolic valence band VB:

DOS of the CB: $N_{CB}(E) = N_C^0\,(E - E_C)^{1/2}$ with $N_C^0 \equiv \dfrac{1}{2\pi^2}\left(\dfrac{2\breve{m}_e^*}{\hbar^2}\right)^{3/2}$

DOS of the VB: $N_{VB}(E) = N_V^0\,(E_V - E)^{1/2}$ with $N_V^0 \equiv \dfrac{1}{2\pi^2}\left(\dfrac{2\breve{m}_h^*}{\hbar^2}\right)^{3/2}$

with the exponential conduction band tail CBT and the exponential valence band tail VBT:

DOS of the CBT: $N_{CBT}(E) = N_C^0\left\{\sqrt{\dfrac{E_C^0}{2}}\exp\left(-\dfrac{1}{2}\right)\right\}\exp\left[-\dfrac{E_C - E}{E_C^0}\right]$

DOS of the VBT: $N_{VBT}(E) = N_V^0\left\{\sqrt{\dfrac{E_V^0}{2}}\exp\left(-\dfrac{1}{2}\right)\right\}\exp\left[-\dfrac{E - E_V}{E_V^0}\right]$

with the connection point (E_C^{tail}, N_C^{tail}) of the conduction band,
and with the connection point (E_V^{tail}, N_V^{tail}) of the valence band:

connection point CB/CBT: $E_C^{tail} = E_C + \dfrac{E_C^0}{2}$ $N_C^{tail} = N_C^0\sqrt{\dfrac{E_C^0}{2}}$

connection point VB/VBT: $E_V^{tail} = E_V - \dfrac{E_V^0}{2}$ $N_V^{tail} = N_V^0\sqrt{\dfrac{E_V^0}{2}}$

The (optical) band gap E_g^{opt}: $E_g^{opt} \equiv E_C - E_V$

B1.2. The Gaussian shaped dangling bond peak:

DOS of the DB: $N_{DB}(E) = \dfrac{N_{DB}^{tot}}{\sqrt{2\pi W_{DB}^2}}\exp\left[-\dfrac{(E - E_{DB})^2}{2W_{DB}^2}\right]$

B2. The system in thermal equilibrium used for the numerical analysis:

B2.1. The concept of the mobility gap and of localised / delocalised DOS:

the mobility gap:
$$E_g^{mob} \equiv E_{Cmob} - E_{Vmob} = E_g^{opt} + \varepsilon_c + \varepsilon_v$$

with the mobility edges of the conduction band and of the valence bands:

$$E_{Cmob} \equiv E_C + \varepsilon_c \qquad E_{Vmob} \equiv E_V - \varepsilon_v$$

with the charge carrier mobilities:
$$\mu_e > 0 \quad \text{for } E \geq E_{Cmob} \qquad \mu_h > 0 \quad \text{for } E \leq E_{Vmob}$$
$$\mu_e = 0 \quad \text{for } E < E_{Cmob} \qquad \mu_h = 0 \quad \text{for } E > E_{Vmob}$$

ε_c: threshold energy of the mobility edge of the conduction band

ε_v: threshold energy of the mobility edge of the valence band

with the localised / delocalised DOS:

delocalised CB/CBT: $N_C(E) = N_{CB/CBT}(E)$ for $E > E_{Cmob}$ else 0
localised CB/CBT: $N_c(E) = N_{CB/CBT}(E)$ for $E \leq E_{Cmob}$ else 0
delocalised VB/VBT: $N_V(E) = N_{VB/VBT}(E)$ for $E < E_{Vmob}$ else 0
localised VB/VBT: $N_v(E) = N_{VB/VBT}(E)$ for $E \geq E_{Vmob}$ else 0

with the DOS at the mobility edges:
$$N_{Cmob} \equiv N_c(E_{Cmob})$$
$$N_{Vmob} \equiv N_v(E_{Vmob})$$

B2.2. The conductivity:

$$\sigma = e\{\mu_e n + \mu_h p\}$$

with the charge carrier densities:
$$n = \int_{E_{Cmob}}^{\infty} f(E)\, N_C(E)\, dE$$
$$p = \int_{-\infty}^{E_{Vmob}} \{1 - f(E)\}\, N_V(E)\, dE$$

with the Fermi function:
$$f(E) = \frac{1}{1 + e^{-\beta(E-E_F)}} \qquad \text{with } \beta \equiv (kT)^{-1}$$

B2.3. The total charge density:

$$Q_{tot}(E_F) = Q^+ - Q^-$$
$$Q^+ = p + p_t + N_{DB}^+$$
$$Q^- = n + n_t + N_{DB}^-$$

with the localised band charge:
$$n_t = \int_{E_{Vmob}}^{E_{Cmob}} f(E)\, N_c(E)\, dE \quad p_t = \int_{E_{Vmob}}^{E_{Cmob}} \{1 - f(E)\}\, N_v(E)\, dE$$

with the charge of the DB: $N_{DB}^{-} = \int_{E_{Vmob}}^{E_{Cmob}} f^{-}(E)\, N_{DB}(E)\, dE \qquad N_{DB}^{+} = \int_{E_{Vmob}}^{E_{Cmob}} f^{+}(E)\, N_{DB}(E)\, dE$

with the DB occupation functions: $f^{+}(E) = \frac{1}{1 + 2\, e^{-\beta(E-E_F)} + e^{-\beta(2E-2E_F+U)}} \equiv z^{-1}$

$f^{0}(E) = z^{-1} 2\, e^{-\beta(E-E_F)}$ with $\beta \equiv (kT)^{-1}$

$f^{-}(E) = z^{-1} e^{-\beta(2E-2E_F+U)}$

B2.4. The absorption:

$$\alpha(\hbar\omega) = C_0\, \hbar\omega\, R^2\, J(\hbar\omega)$$

with a "constant" C_0: $C_0 \equiv \frac{(2\pi)^2}{n_0} \frac{e^2}{\hbar c_0} \frac{1}{3\rho_A}$

and with the joint density: $J(\hbar\omega) = \sum_{ij \neq vc} J^{ij}(\hbar\omega)$

with the partial joint densities $J^{ij}(\hbar\omega)$:

(1) $V \leftrightarrow C$: $J^{VC}(\hbar\omega) = \int_{E_{Cmob}-\hbar\omega}^{E_{Vmob}} dE\, N_V(E)\, N_C(E+\hbar\omega)$

(2) $V \leftrightarrow c$: $J^{Vc}(\hbar\omega) = \int_{E_{Vmob}}^{E_{Cmob}} dE\, N_c(E)\, (1-f(E))\, N_V(E-\hbar\omega)$

(3) $V \leftrightarrow v$: $J^{Vv}(\hbar\omega) = \int_{E_{Vmob}}^{E_{Cmob}} dE\, N_v(E)\, (1-f(E))\, N_V(E-\hbar\omega)$

(4) $C \leftrightarrow c$: $J^{Cc}(\hbar\omega) = \int_{E_{Vmob}}^{E_{Cmob}} dE\, N_c(E)\, f(E)\, N_C(E+\hbar\omega)$

(5) $C \leftrightarrow v$: $J^{Cv}(\hbar\omega) = \int_{E_{Vmob}}^{E_{Cmob}} dE\, N_v(E)\, f(E)\, N_C(E+\hbar\omega)$

(6) $V \leftrightarrow D^{+}$: $J^{V+}(\hbar\omega) = 2 \int_{E_{Vmob}}^{E_{Cmob}} dE\, N_{DB}(E)\, f^{+}(E)\, N_V(E-\hbar\omega)$

(7) $V \leftrightarrow D^{0}$: $J^{V0}(\hbar\omega) = \int_{E_{Vmob}}^{E_{Cmob}} dE\, N_{DB}(E)\, f^{0}(E)\, N_V(E-\hbar\omega+U)$

(8) $C \leftrightarrow D^{0}$: $J^{C0}(\hbar\omega) = \int_{E_{Vmob}}^{E_{Cmob}} dE\, N_{DB}(E)\, f^{0}(E)\, N_C(E+\hbar\omega)$

(9) $C \leftrightarrow D^{-}$: $J^{C-}(\hbar\omega) = 2 \int_{E_{Vmob}}^{E_{Cmob}} dE\, N_{DB}(E)\, f^{-}(E)\, N_C(E+\hbar\omega+U)$

(10) $(v \leftrightarrow c)$: $J^{vc}(\hbar\omega) = \int_{E_{Cmob}}^{E_{Vmob}} dE\, N_v(E)\, f(E)\, N_c(E+\hbar\omega)\, (1-f(E+\hbar\omega))$

B3. The system in steady state equilibrium used for the numerical analysis:

B3.1. The conductivity: $\sigma = e\{\mu_e n + \mu_h p\}$

B3.2. The total charge density: $Q_{tot}(n,p) = Q^+ - Q^-$

$$Q^+ = p + p_t + N_{DB}^+$$

$$Q^- = n + n_t + N_{DB}^-$$

with the localised charge in the bands:

$$n_t = \int_{E_{Vmob}}^{E_{Cmob}} f_c(E)\, N_c(E)\, dE$$

$$p_t = \int_{E_{Vmob}}^{E_{Cmob}} \{1 - f_v(E)\}\, N_v(E)\, dE$$

with the occupation functions:

$$f_i(E) = \frac{1}{1+K_i};\ \ K_i \equiv \frac{\tilde{p}_i + e_{ni}^{th} + e_{ni}^{ph}}{\tilde{n}_i + e_{pi}^{th} + e_{pi}^{ph}};\ \ i = c, v$$

with the charge in the DB:

$$N_{DB}^- = \int_{E_{Vmob}}^{E_{Cmob}} f^-(E)\, N_{DB}(E)\, dE$$

$$N_{DB}^+ = \int_{E_{Vmob}}^{E_{Cmob}} f^+(E)\, N_{DB}(E)\, dE$$

with DB occupation functions:

$$f^+(E) = \frac{1}{1 + K^{-1}\left(1 + K_U^{-1}\right)}$$

$$f^0(E) = K^{-1}\, f^+(E) \qquad K \equiv \frac{\tilde{p} + e_n^{th} + e_n^{ph}}{\tilde{n} + e_p^{th} + e_p^{ph}}$$

$$f^-(E) = K^{-1}\, K_U^{-1}\, f^+(E) \quad K_U \equiv \frac{\tilde{p}_U + e_{nU}^{th} + e_{nU}^{ph}}{\tilde{n}_U + e_{pU}^{th} + e_{pU}^{ph}}$$

B3.3. The rate equations:

Rate equation of the CB: $\frac{\partial}{\partial t} n = 0 = G_{VC}(\hbar\omega) + \sum_j \left\{G_{Cj}(\hbar\omega) + T_{Cj} - R_{Cj}\right\}$

Rate equation of the VB: $\frac{\partial}{\partial t} p = 0 = G_{VC}(\hbar\omega) + \sum_j \left\{G_{Vj}(\hbar\omega) + T_{Vj} - R_{Vj}\right\}$

Total generation rate: $G_{tot}(\hbar\omega) = G_{VC}(\hbar\omega) + \sum_j \left\{G_{Cj}(\hbar\omega) + G_{Vj}(\hbar\omega)\right\}$

with $j = v, c, +, 0, -$

B3.4. The partial rates:

Transition:	the partial generation rates G: (Z = "G" and index *i* = "ph") the partial, thermal emission rates T: (Z = "T" and index i = "th")	the partial recombination rates R:
(1) V ↔ C:	$G_{VC} = \int_{E_{Cmob}-\hbar\omega}^{E_{Vmob}} e_{bb}^{ph} N_V(E)\,dE$	neglected
(2) V ↔ c:	$Z_{Vc} = \int_{E_{Vmob}}^{E_{Cmob}} e_{pc}^{i} N_c(E)\left(1-f_c(E)\right)dE$	$R_{Vc} = \int_{E_{Vmob}}^{E_{Cmob}} \tilde{p}_c N_c(E)\, f_c(E)\,dE$
(3) V ↔ v:	$Z_{Vv} = \int_{E_{Vmob}}^{E_{Cmob}} e_{pv}^{i} N_v(E)\left(1-f_v(E)\right)dE$	$R_{Vv} = \int_{E_{Vmob}}^{E_{Cmob}} \tilde{p}_v N_v(E)\, f_v(E)\,dE$
(4) C ↔ c:	$Z_{Cc} = \int_{E_{Vmob}}^{E_{Cmob}} e_{nc}^{i} N_c(E)\, f_c(E)\,dE$	$R_{Cc} = \int_{E_{Vmob}}^{E_{Cmob}} \tilde{n}_c N_c(E)\left(1-f_c(E)\right)dE$
(5) C ↔ v:	$Z_{Cv} = \int_{E_{Vmob}}^{E_{Cmob}} e_{nv}^{i} N_v(E)\, f_v(E)\,dE$	$R_{Cv} = \int_{E_{Vmob}}^{E_{Cmob}} \tilde{n}_v N_v(E)\left(1-f_v(E)\right)dE$
(6) V ↔ D$^+$:	$Z_{V+} = \int_{E_{Vmob}}^{E_{Cmob}} e_{p}^{i} N_{DB}(E)\, f^{+}(E)\,dE$	$R_{V-}^{th} = \int_{E_{Vmob}}^{E_{Cmob}} \tilde{p}_U N_{DB}(E)\, f^{-}(E)\,dE$
(7) V ↔ D^0:	$Z_{V0} = \int_{E_{Vmob}}^{E_{Cmob}} e_{pU}^{i} N_{DB}(E)\, f^{0}(E)\ dE$	$R_{V0} = \int_{E_{Vmob}}^{E_{Cmob}} \tilde{p}\, N_{DB}(E)\, f^{0}(E)\ dE$
(8) C ↔ D^0:	$Z_{C0} = \int_{E_{Vmob}}^{E_{Cmob}} e_{n}^{i} N_{DB}(E)\, f^{0}(E)\ dE$	$R_{C0} = \int_{E_{Vmob}}^{E_{Cmob}} \tilde{n}_U N_{DB}(E)\, f^{0}(E)\ dE$
(9) C ↔ D$^-$:	$Z_{C-} = \int_{E_{Vmob}}^{E_{Cmob}} e_{nU}^{i} N_{DB}(E)\, f^{-}(E)\ dE$	$R_{C+} = \int_{E_{Vmob}}^{E_{Cmob}} \tilde{n}\, N_{DB}(E)\, f^{+}(E)\ dE$
(10) v ↔ c:	suppressed	suppressed

Note: T_{VC} is also neglected

B3.5. The probabilities:

transition:	the thermal emission probabilities:	the capture probabilities:	the generation probabilities:
(1) $V \leftrightarrow C$:	neglected	neglected	$e_{bb}^{ph} = K_0\, N_C(E + \hbar\omega)$
(2) $V \leftrightarrow c$:	$e_{pc}^{th} = \sigma_{pc}\, N_V^*(E)$	$\bar{p}_c = v_p\, \sigma_{pc}\, p$	$e_{pc}^{ph} = K_0\, N_V(E - \hbar\omega)$
(3) $V \leftrightarrow v$:	$e_{pv}^{th} = \sigma_{pv}\, N_V^*(E)$	$\bar{p}_v = v_p\, \sigma_{pv}\, p$	$e_{pv}^{ph} = K_0\, N_V(E - \hbar\omega)$
(4) $C \leftrightarrow c$:	$e_{nc}^{th} = \sigma_{nc}\, N_C^*(E)$	$\bar{n}_c = v_n\, \sigma_{nc}\, n$	$e_{nc}^{ph} = K_0\, N_C(E + \hbar\omega)$
(5) $C \leftrightarrow v$:	$e_{nv}^{th} = \sigma_{nv}\, N_C^*(E)$	$\bar{n}_v = v_n\, \sigma_{nv}\, n$	$e_{nv}^{ph} = K_0\, N_C(E + \hbar\omega)$
(6) $V \leftrightarrow D^+$:	$e_p^{th} = 2\, \sigma_p\, N_V^*(E)$	$\tilde{p} = v_p\, \sigma_p\, p$	$e_p^{ph} = 2\, K_0\, N_V(E - \hbar\omega)$
(7) $V \leftrightarrow D^0$:	$e_{pU}^{th} = \frac{1}{2}\, \sigma_{pU}\, N_V^*(E + U)$	$\bar{p}_U = v_p\, \sigma_{pU}\, p$	$e_{pU}^{ph} = K_0\, N_V(E + U - \hbar\omega)$
(8) $C \leftrightarrow D^0$:	$e_n^{th} = \frac{1}{2}\, \sigma_n\, N_C^*(E)$	$\tilde{n} = v_n\, \sigma_n\, n$	$e_n^{ph} = K_0\, N_C(E + \hbar\omega)$
(9) $C \leftrightarrow D^-$:	$e_{nU}^{th} = 2\, \sigma_{nU}\, N_C^*(E + U)$	$\tilde{n}_U = v_n\, \sigma_{nU}\, n$	$e_{nU}^{ph} = 2\, K_0\, N_C(E + \hbar\omega + U)$
(10) $v \leftrightarrow c$:	suppressed	suppressed	suppressed

with $K_0 = C_0\, \hbar\omega\, R^2\, \Phi_0$,

$$N_C^*(E) \equiv v_n\, N_C^{eff} \exp[-\beta(E_C - E)],$$

$$N_V^*(E) \equiv v_p\, N_V^{eff} \exp[-\beta(E - E_V)].$$

Note: The following picture shows the notation of the capture cross sections of a defect with a finite correlation energy U (dangling bonds) as used here and - in brackets - the notation of those used in published literature for the specific case of dangling bonds (see e.g. [Hubin 94]):

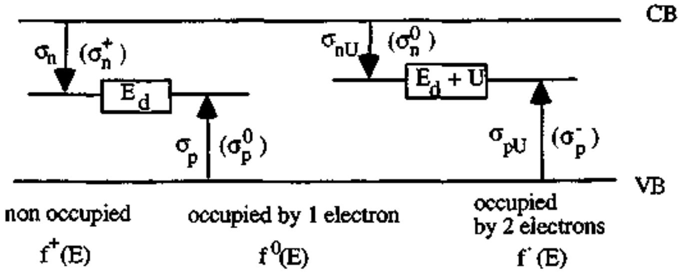

B4. The effective DOS for the case of parabolic bands

If the exponential tail states are localised and if the Fermi level E_F is within the optical band gap, the effective DOS can be analytically calculated for the case of parabolic bands.

the charge carrier densities: $n = N^{eff}_{Cmob} \exp[-\beta(E_{Cmob} - E_F)]$ $p = N^{eff}_{Vmob} \exp[-\beta(E_F - E_{Vmob})]$

If $E_{Cmob} \geq E_C^{tail}$ or $\varepsilon_c \geq \frac{E_C^0}{2}$ or $\chi_c \geq \frac{E_C^0}{2kT}$ with $\chi_c \equiv \beta\,\varepsilon_c = \varepsilon_c / (kT)$

$E_{Vmob} \leq E_V^{tail}$ or $\varepsilon_v \geq \frac{E_V^0}{2}$ or $\chi_v \geq \frac{E_V^0}{2kT}$ with $\chi_v \equiv \beta\,\varepsilon_v = \varepsilon_v / (kT)$

then the DOS at the mobility edges: $N_{Cmob} = N_C^0 \sqrt{\varepsilon_c}$ (units $[eV^{-1}cm^{-3}]$)

$N_{Vmob} = N_V^0 \sqrt{\varepsilon_v}$

then the effective DOS at the mobility edges: $N^{eff}_{Cmob} = \frac{N_{Cmob}}{\beta}\hat{f}(\chi_c)$ (units $[cm^{-3}]$)

$N^{eff}_{Vmob} = \frac{N_{Vmob}}{\beta}\hat{f}(\chi_v)$

or $N_i^{eff}[cm^{-3}] = 4\pi(\frac{2\,\tilde{m}_j^*}{h^2})^{3/2}\, kT\,\sqrt{\varepsilon_k}\,\hat{f}(\chi_k)$ with i = Cmob, Vmob; k = c, v; j = e, h

with the correction function:

$$\hat{f}(\chi) \equiv \chi^{-1/2} e^{\chi} \int_{\chi}^{\infty} x^{1/2}\, e^{-x}\, dx$$

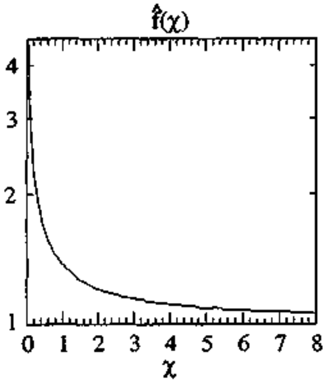

Fig.B4-1: the correction function $\hat{f}(\chi)$ as a function of the dimensionless parameter $\chi \equiv \beta\,\varepsilon = \varepsilon / (kT)$.

B5. The charge neutrality of the dangling bond defects at thermal equilibrium

The following table specifies the three states of a defect with a finite correlation energy (dangling bonds):

state i	0	1	2
energy of state i	0	E_d	$2E_d+U$
number of electrons in state i	0	1	2
energy per electron and per state i	0	E_d	$E_d+U/2$
charge of the electrons in state i	0	-1e	-2e
charge of the DB atom in state i	+1e	0	-1e
degeneracy of state i	1	2	1

The electron occupation function $f_e(E)$ varies between 0 and 2, is independent of the charge of the atoms and is given as ([Ashcroft 87], [Adler 76])

$$f_e(E) \equiv f^0(E) + 2f^-(E) = \frac{2\,e^{-\beta(E-E_F)} + 2e^{-\beta(2E-2E_F+U)}}{1+2\,e^{-\beta(E-E_F)} + e^{-\beta(2E-2E_F+U)}}$$

In contrast to f_e, the author introduces the charge occupation function f_{ch} which depends on the charge of the atom. In the case of dangling bonds, the DB charge occupation function $f_{ch}(E)$ varies between +1 and -1 and is defined as

$$f_{ch}(E) \equiv f^+(E) - f^-(E) = \frac{1-e^{-\beta(2E-2E_F+U)}}{1+2\,e^{-\beta(E-E_F)} + e^{-\beta(2E-2E_F+U)}}$$

The charge neutrality of the dangling bond defects leads to a temperature-independent Fermi level E_F, which is pinned.

$$f_{ch}(E_d) = 0 \quad \Leftrightarrow \quad f^+ = f^- \quad \Leftrightarrow \quad E_F = E_d + \frac{U}{2}$$

The DB occupation functions under this charge neutrality condition are independent of the Fermi level E_F and of the defect position E_d:

$$f^+\left(E = E_F - \frac{U}{2}\right) = \frac{1}{2}\frac{1}{1+e^{\beta U/2}} \qquad f^0\left(E = E_F - \frac{U}{2}\right) = \frac{1}{1+e^{-\beta U/2}} \qquad f^-\left(E = E_F - \frac{U}{2}\right) = \frac{1}{2}\frac{1}{1+e^{\beta U/2}}$$

If the correlation energy U is positive with $U \gg 2kT$, all dangling bond defects are in the neutral state ($f^+ = 0$, $f^0 = 1$, $f^- = 0$).

Fig.B5-1 to fig.B5-4 show the electron occupation function f_e, DB charge occupation function f_{ch}, the charge neutrality condition of the dangling bond defects and the total charge $Q_{tot}(E_F)$ of the standard DOS (see appendix B2.3.).

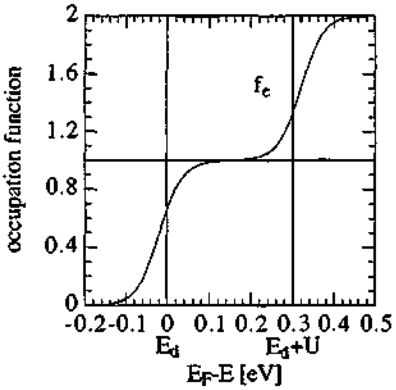

Fig.B5-1: electron occupation function $f_e(E)$ as a function of the Fermi level position E_F for T=300K and U=0.3eV.

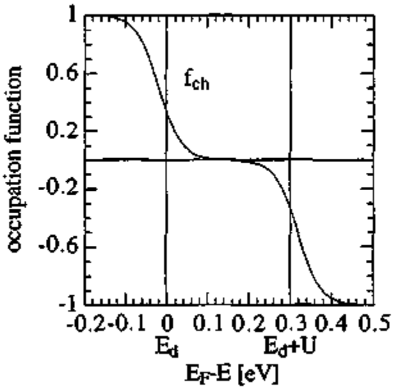

Fig.B5-2: charge occupation function $f_{ch}(E)$ as a function of the Fermi level position E_F for T=300K and U=0.3eV.

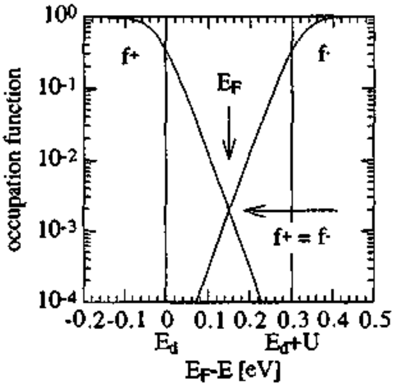

Fig.B5-3: two parts of the charge occupation function $f_{ch}(E)$ at T=300K and U=0.3eV as a function of the Fermi level position E_F.

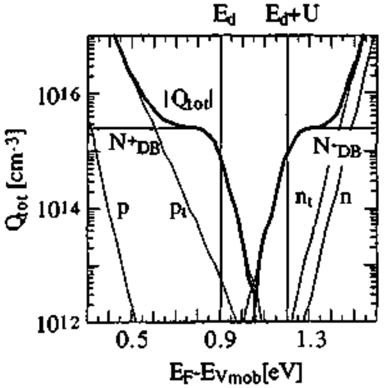

Fig.B5-4: total charge density $|Q_{tot}|$ of the standard DOS as a function of the Fermi level position E_F.

Used values: T=300K, $N_{DB}^{max} = 3\,10^{15}$cm^{-3}, E_{DB}=0.9eV, U=0.3eV and $2\,W_{DB}$=0.18eV.

B6. Numerical estimation of the "generation" levels for a-Si:H

The "generation" levels E_{Gn} and E_{Gp} of a defect without a finite correlation energy at steady state equilibrium are given as:

$$e_n^{th} = e_n^{ph} \quad \rightarrow \quad E_{Gn} = E_{Cmob} + kT \ln\left(Z_n \frac{N_C(E_d + \hbar\omega)}{N^{eff}_{Cmob}} \right) \qquad Z_n \equiv \theta_n \frac{C_0\, \hbar\omega}{v_n} \Phi_0 \qquad \theta_n = \frac{R^2}{\sigma_n}$$

$$e_p^{th} = e_p^{ph} \quad \rightarrow \quad E_{Gp} = E_{Vmob} - kT \ln\left(Z_p \frac{N_V(E_d - \hbar\omega)}{N^{eff}_{Vmob}} \right) \qquad Z_p \equiv \theta_p \frac{C_0\, \hbar\omega}{v_p} \Phi_0 \qquad \theta_p = \frac{R^2}{\sigma_p}$$

The figure below shows some possible "generation" levels E_{Gn} and E_{Gp} for the case of a-Si:H based on the following equations. Z_n and Z_p are calculated by:

$$Z_i \approx 2\, \theta_i\, I_0[\mathrm{mWcm^{-2}}] \qquad \text{with } \theta_i = \frac{R^2\,[\mathrm{\AA^2}]}{\sigma_i\,[\mathrm{cm^2}]} \quad \text{for } i=n,p.$$

$$v_n = v_p = 10^7\,\mathrm{cm\,s^{-1}},\ C_0 = 4.57\,10^{-41}\,\mathrm{cm^5\AA^{-2}} \text{ and } R_0 = 0.3$$

The ratio of the band DOS and the effective DOS are approximated by $(kT)^{-1}$ (see appendix B4). At room temperature, the "generation" levels E_{Gn} and E_{Gp} are given as

$$E_{Gn} = E_{Cmob} - 0.88 + 0.027\ \ln(\theta_n\, I_0[\mathrm{mWcm^{-2}}])$$

$$E_{Gp} = E_{Vmob} + 0.88 - 0.027\ \ln(\theta_p\, I_0[\mathrm{mWcm^{-2}}])$$

In fig.B6-1, the mobility gap is 1.8eV and the light intensity range I_0^{cpm} of CPM is indicated. The region II of the defect-to-band generation mechanism G_{np} is patterned for the case of $\theta_n = \theta_p = 1'000$. The ratios θ_n and θ_p need not be identical.

Mittiga et al. [90] argued that the deep defect absorption range is controlled by the generation mechanism G_{np}: they used $\theta_i = 40$ as well as $\theta_i = 4'000$ for the neutral dangling bond states in the simulation of CPM on solar cells.

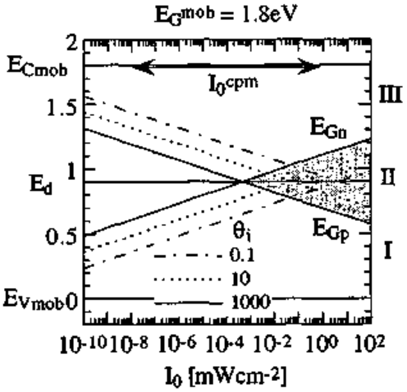

Fig.B6-1: the "generation" levels E_{Gn} and E_{Gp} as a function of the light intensity I_0 for three different θ_i.

Appendix C (corresponding to chapter 3)

C1. Units

C1.1. The bending parameter and the effective masses of the parabolic bands:

$$N_i^0[\mathrm{cm^{-3}eV^{-3/2}}]=\frac{1}{2\pi^2}\left(\frac{2\breve{m}_j^*}{\hbar^2}\right)^{3/2}=6.77\,10^{21}\left(\frac{\breve{m}_j^*}{m_e}\right)^{3/2} \qquad \text{with } i=C, V \text{ and } j=e, h$$

$$\frac{\breve{m}_j^*}{m_e}=2.79\,10^{-15}\left(N_i^0[\mathrm{cm^{-3}eV^{-3/2}}]\right)^{2/3} \qquad \text{with } i=C, V \text{ and } j=e, h$$

C1.2. The conductivity:

$$\sigma[\Omega^{-1}\mathrm{cm^{-1}}]=1.62\,10^{-19}\left\{\mu_e[\mathrm{cm^2V^{-1}s^{-1}}]\,n[\mathrm{cm^{-3}}]+\mu_h[\mathrm{cm^2V^{-1}s^{-1}}]\,p[\mathrm{cm^{-3}}]\right\}$$

$$\sigma_{tot}[(\Omega\mathrm{cm})^{-1}]=k_L\,\frac{I[A]}{d[\mu m]\,V[V]} \text{ with } k_L\equiv 10^4\,\frac{\text{W (coplanar contact width)}}{\text{L (coplanar contact length)}}(=625 \text{ here})$$

$$\sigma(T)\,[(\Omega\,\mathrm{cm})^{-1}]=\sigma_0\,[(\Omega\,\mathrm{cm})^{-1}]\exp\left\{11'609\,\frac{E\,[eV]}{T\,[K]}\right\}$$

C1.3. The effective DOS at the mobility edges:

$$N_j^{eff}[\mathrm{cm^{-3}}]=6.77\,10^{21}\,kT[eV]\,\sqrt{\varepsilon_k[eV]}\left(\frac{\breve{m}_j^*}{m_e}\right)^{3/2}\hat{f}(\chi_k)$$

with i = Cmob, Vmob, k = c, v and j = e, h

C1.4. The absorption:

$$\alpha(\hbar\omega)[\mathrm{cm^{-1}}]=C_0[\mathrm{cm^5Å^{-2}}]\,\hbar\omega[eV]\,R^2[Å^2]\sum_j J_j(\hbar\omega)[\mathrm{eV^{-1}cm^{-6}}]$$

$$C_0[\mathrm{cm^5Å^{-2}}]=9.605\,10^{-18}\,\frac{1}{n_0}\frac{1}{\rho_A[\mathrm{cm^{-3}}]}$$

C1.5. The photon flux:

$$\Phi_0\left[\#\mathrm{s^{-1}cm^{-2}}\right]=(1-R_0)\,\frac{10^{-3}}{e\,\hbar\omega}\,I_0=(1-R_0)\,6.24\,10^{15}\,\frac{I_0\left[\mathrm{mWcm^{-2}}\right]}{\hbar\omega[eV]}.$$

C1.6. The factor of the generation probability:

$$K_0[\mathrm{cm^3eVs^{-1}}]=C_0[\mathrm{cm^5Å^{-2}}]\,\hbar\omega[eV]\,R^2[Å^2]\,\Phi_0[\mathrm{cm^{-2}s^{-1}}]$$

$$K_0[\mathrm{cm^3eVs^{-1}}]=(1-R_0)\,6.24\,10^{15}\,C_0[\mathrm{cm^5Å^{-2}}]\,R^2[Å^2]\,I_0[\mathrm{mWcm^{-2}}]$$

C1.7. The energy:

$$E[\mathrm{eV}] = \hbar\omega[\mathrm{eV}] = \frac{h\,c_0}{\lambda} = \frac{1.24}{\lambda[\mu\mathrm{m}]} \qquad\qquad E[\mathrm{eV}] = \frac{k}{e}\,T[\mathrm{K}] = \frac{T[\mathrm{K}]}{11'609}$$

C2. The deep defect absorption and the ESR spin density

In the case of undoped a-Si:H, it is an established practice to identify the deep defect absorption range by the ESR dangling bond spin density N_S:

integrated excess absorption $\overline{\alpha}_I$: $N_S = 7.9\,10^{15}\mathrm{cm}^{-2}\mathrm{eV}^{-1}\,\overline{\alpha}_I$ [Jackson 82]

single-energy absorption α_W: $N_S = 1.2 - 2.5\,10^{16}\mathrm{cm}^{-2}\,\alpha_W(\hbar\omega_W = 1.2\mathrm{eV})$ [Wyrsch 91]
(at a specific photon energy $\hbar\omega_W$)

The "integrated excess absorption" deep defect determination is well established [Jackson 82]. The exponential Urbach tail is subtracted from the absorption spectrum (see fig.C2-1), and the resulting spectrum is integrated and noted as $\overline{\alpha}_I$. The corresponding area $\overline{\alpha}_I$ is marked in the figure below and is assumed to be proportional to the ESR dangling bond spin density N_S. This method produces some misleading situations if the standard DOS of chapter 2.1. is used: for the same deep defect density N_{DB}^{tot}, an increase in the Urbach tail slope leads to a reduction of $\overline{\alpha}_I$. Furthermore, the figure below indicates that the deep defect transitions are present for any photon energy larger than the deep defect ionisation energies.

Wyrsch et al. [91] proposed the "single-energy absorption" deep defect determination. For a specific photon energy $\hbar\omega_W$ in the deep defect range (e.g. $\hbar\omega_W$=1.2eV in fig.C2-1), the absorption coefficient α_W is assumed to be proportional to the ESR dangling bond spin density N_S. In this case, an increase in the total deep defect density N_{DB}^{tot} leads to an increase in the absorption coefficient α_W.

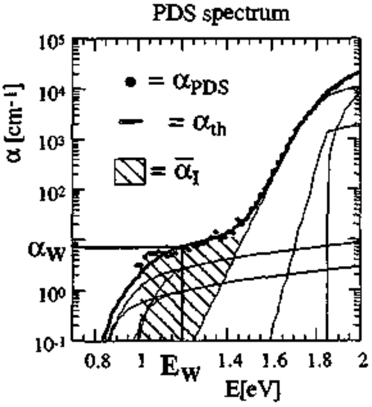

Fig.C2-1: the measured PDS spectrum $\alpha_{PDS}(\hbar\omega)$, the integrated excess absorption $\overline{\alpha}_I$ and the single-energy absorption α_W at a specific photon energy $\hbar\omega_W$ = 1.2eV.

C3. Numerical discretisation

The parameters of the discretisation are: Y_1, Y_2, E_Y, N_{min}. The DOS is split into 4 parts, each of which is discretisised by Y_1 energy levels, as shown in fig.C3-1. The lowest energy value of the delocalised band states DOS is here $E_{V_{mob}} - E_Y = 0.5\text{eV}$. The lowest value of the DOS is here $N_{min} = 10^{10}\text{cm}^{-3}\text{eV}^{-1}$. The output functions are discretisised by Y_2 values, as shown in fig.C3-2.

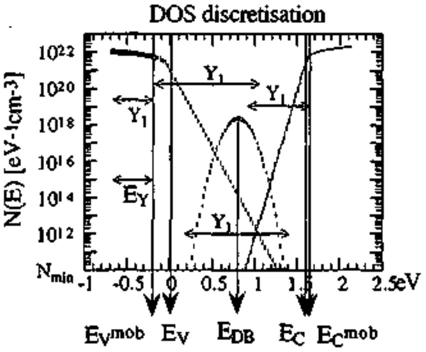

Fig.C3-1: Discretisation of the energy scale of DOS.

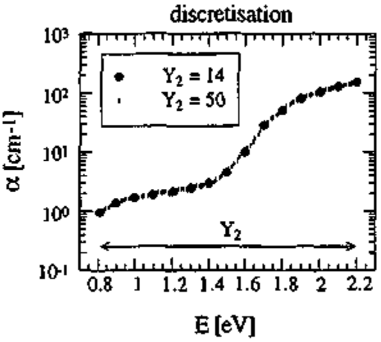

Fig.C3-2: Discretisation of the output function with LDS and HDS.

Two different discretisation sets are used here (LDS and HDS):

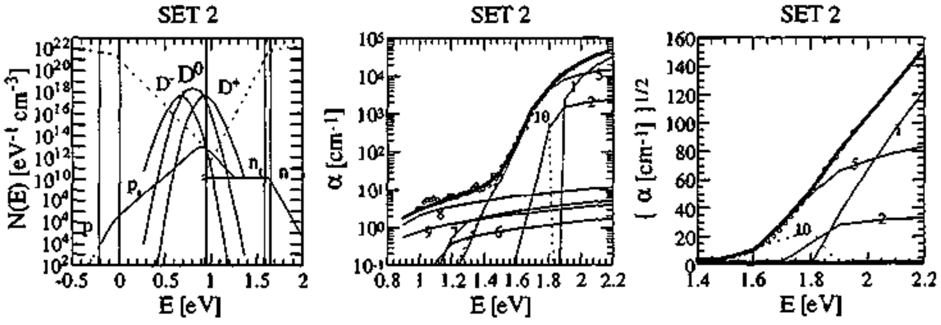

Low discretisation set LDS: Y1 = 50 and Y2 = 10

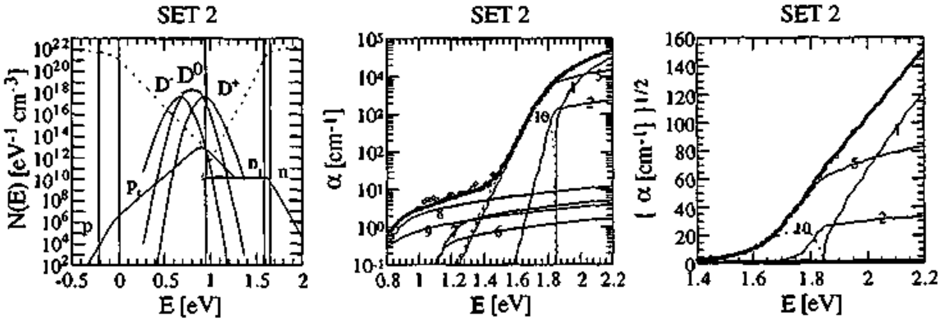

High discretisation set HDS: Y1 = 200 and Y2 = 50

C4. The capture cross sections

The input parameters at steady state equilibrium are reduced in the following way in section 3.2.3.:

localised band tail states: $\sigma_t \equiv \sigma_{nc} = \sigma_{pc} = \sigma_{nv} = \sigma_{pv}$
neutral dangling bond states: $\sigma^0 \equiv \sigma_p = \sigma_{nU}$
charged dangling bond states: $\sigma^{+/-} \equiv \sigma_n = \sigma_{pU}$

On the one hand, it is a strong oversimplification to describe all localised band tail states with the help of only one capture cross section σ_t, on the other hand, the physical origin of the exponential tail states is still so contradictory that this approach remains reasonable; it is unknown whether the localised tail states in a-Si:H may be described by donor-like or by acceptor-like defects which each ask for different capture cross sections for the charged and uncharged states. Some authors have distinguished between charged and uncharged capture cross sections for exponential tail states, as shown in tab.3 of section 3.2.2. However, no approach describes the exponential tail states by states with a finite correlation energy, as postulated by the ESR measurements shown in fig.3 of section 3.1.2.

From the physical point of view, it is also an oversimplification to reduce the number of the capture cross sections of the deep defect with a finit correlation energy (dangling bonds). In fact, there is no physical indication that the capture cross section of non-occupied atomic cores (D^+) is identical to the capture cross section of a defect atom with two localised electrons (D^-).

The standard value for the capture cross section of the neutral dangling bond states in a-Si:H is calculated from life time measurements. Under the strong assumption that no tail state recombination takes place, one finds values in the order of $\sigma^0 = 10^{-16}\,\mathrm{cm}^2 = 1\,\text{Å}^2$ [Pipoz 93].

As far as the <u>capture cross section ratio</u> $r_{DB} \equiv \sigma^{+/-} / \sigma^0$ <u>of the charged to uncharged dangling bond states</u> is concerned, it is an established practice to use values equal or larger than 1 (see tab.3 in section 3.2.2.). This may be based on the calculations of charged capture cross sections in c-Si: the ionised-atom scattering theory of crystalline semiconductors (see e.g. [Kireev 75]) seems to be valid to the author also for ionised atoms in amorphous semiconductors and gives capture cross sections in the range of $\sigma_{ion} = 10^{-13} - 10^{-12}\,\mathrm{cm}^2$ for <u>ionised defect densities</u> of $N_{ion} < 10^{19}\,\mathrm{cm}^{-3}$. Such high values for charged deep defect capture cross sections in a-Si:H were only used by Bube et al. [92]. The ionised-atom scattering theory of crystalline semiconductors leads to lower capture cross sections in the case of higher ionised defect densities, as observed in heavy doped c-Si and usually discussed in the standard textbooks on semiconductors: ionised atom densities of $N_{ion} = 10^{20} - 5\,10^{20}\,\mathrm{cm}^{-3}$ lead to $\sigma_{ion} = 10^{-14} - 10^{-15}\,\mathrm{cm}^2$. In a-Si:H, these are the typical values for the capture cross sections of charged states: the ratio r_{DB} of charged to uncharged capture cross sections varies between 1 - 100 in the case of a-Si:H (see tab.3 in section 3.2.2.).

C5. The thermal velocity

In order to calculate the steady-state equilibrium, one has to know the thermal velocity of the delocalised charge carriers. The average energy of a classical gas is well known:

$$\langle E\rangle = \frac{m}{2}\langle v\rangle^2 = \frac{m}{2} v_{th}^2 = \frac{3}{2} kT$$

For a non-degenerated, crystalline semiconductor, the thermal velocity of the electrons and holes is the velocity of the electrons in the conduction band and the velocity of the holes in the valence band at thermal equilibrium (see e.g. [Smith 78]):

$$v_{th}[\mathrm{cm\,s^{-1}}] = \left(\frac{3\,kT}{\tilde{m}^*}\right)^{1/2} = 6.743\,10^5 \left(\frac{T\,[K]}{\tilde{m}^* / m_e}\right)^{1/2}$$

This thermal velocity v_{th} depends on the effective conductivity mass $\tilde{m}^*$, which is different from the effective DOS mass $\breve{m}^*$ introduced in chapter 2. At room temperature T, one finds the following value, using the electron rest mass m_e as the effective conductivity mass:

$$v_{th} = 1.168\,10^7 \mathrm{cm\,s^{-1}} \quad \text{for T=300K and } \tilde{m}^* / m_e = 1$$

For amorphous semiconductors, no reasonable theory exists which allows one to calculate the thermal velocity v_{th} of the charge carriers. Instead, many authors use the value of the classical gas theory (see tab. 1 in 3.2.2.). The author also uses this value for both carrier types for the sake of simplicity:

$$v_{th} = v_n = v_p = 10^7 \mathrm{cm\,s^{-1}} \qquad \text{for T=300K}$$

C6. Numerical sensitivity analysis of CPM and PDS

For this numerical analysis, the input parameter **SET2c** (see tab in 3.1.3. and tab.4 in 3.2.4.) and the discretisation set LDS (see appendix C3) were chosen. For the numerical analysis of PDS, the incident photon flux Φ_0 is assumed to be constant with a value of $\Phi_0 = 5\,10^{15}\mathrm{cm^{-2}s^{-1}}$. For the numerical analysis of CPM, the CPM factor c_{CPM} is chosen as 10 here. Further, the CPM conductivity σ_{CPM} is regulated with an accuracy of 1%. All spectra ($\alpha_{th}(\hbar\omega)$, $\alpha_{CPM}(\hbar\omega)$ and $\alpha_{PDS}(\hbar\omega)$) are calibrated at $\alpha(\hbar\omega = 2\mathrm{eV}) = 12'544\mathrm{cm^{-1}}$. Therefore, **all spectra are relative**. The spectra are presented in three columns (except on the last page of this sensitivity analysis):

left column: $\boxed{\text{"Deconvolution"}}$ = **absorption** $\alpha_{th}(\hbar\omega)$ at thermal equilibrium

middle column: $\boxed{\text{"}\Phi_0 = \text{const"}}$ = **PDS spectrum** $\alpha_{PDS}(\hbar\omega)$ at steady state equilibrium

right column: $\boxed{\text{"}\sigma_{CPM} = \text{const"}}$ = **CPM spectrum** $\alpha_{CPM}(\hbar\omega)$ at steady state equilibrium

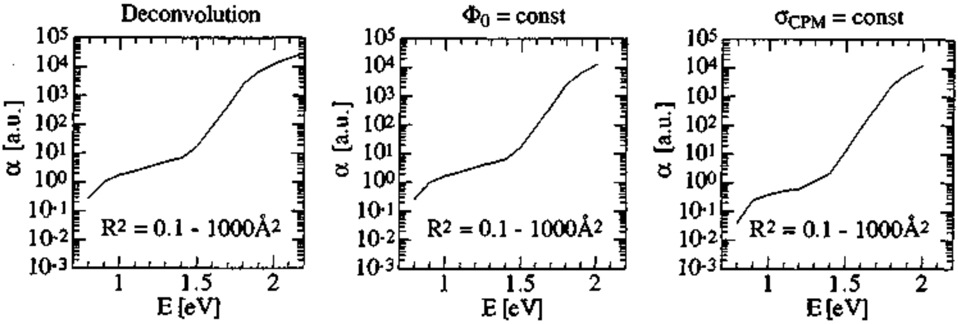

Variation of the **optical matrix element** R^2.

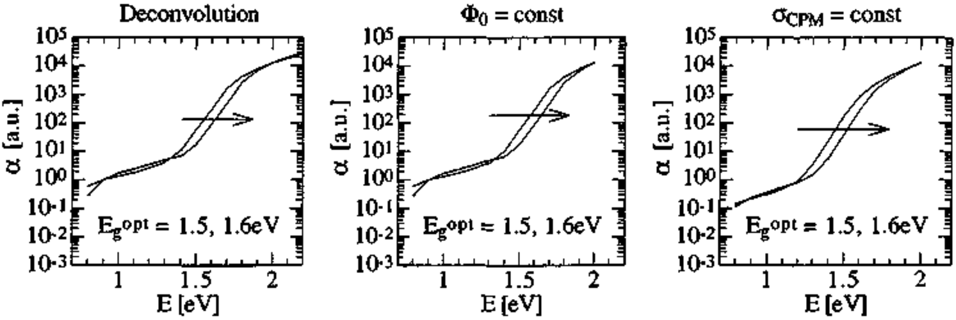

Variation of the **optical bandgap** E_g^{opt}.

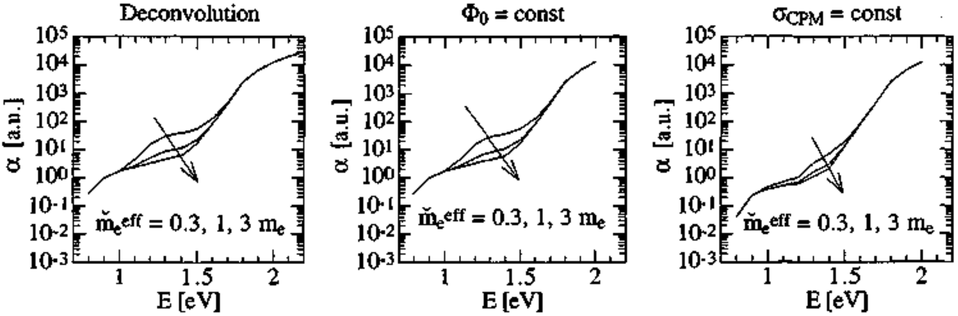

Variation of the **effective DOS mass** $\breve{m}_e^*$ **for electrons** in the conduction band.

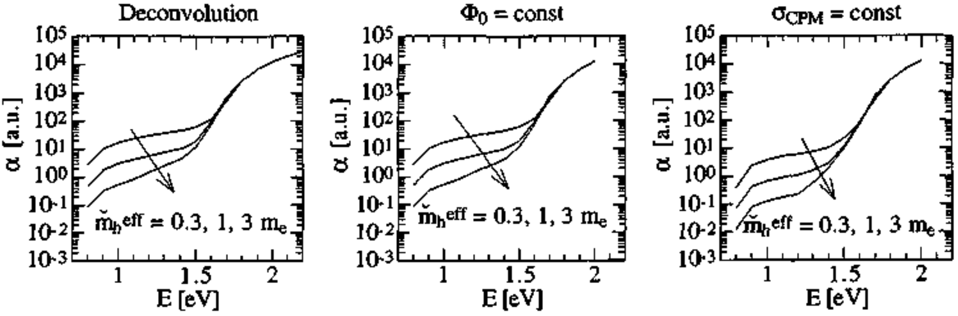

Variation of the **effective DOS mass** $\breve{m}_h^*$ **for holes** in the valence band.

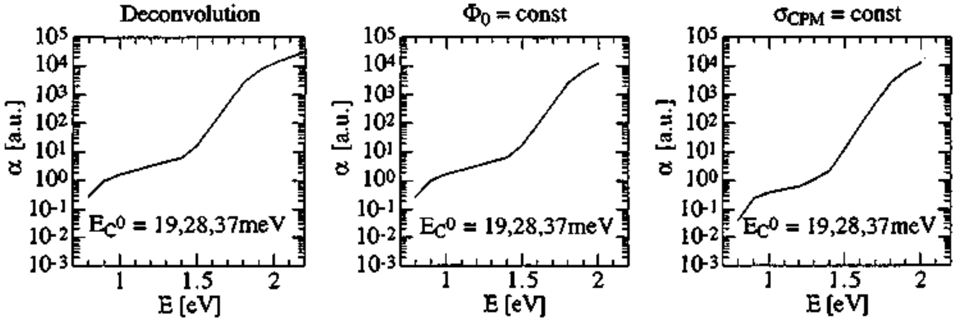
Deconvolution

Φ_0 = const

σ_{CPM} = const

Variation of the characteristic tail slope E_C^0 **of the exponential conduction band tail.**

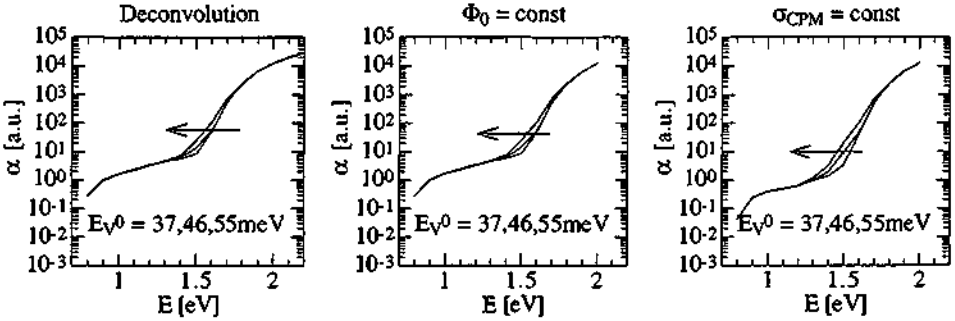
Deconvolution

Φ_0 = const

σ_{CPM} = const

Variation of the characteristic tail slope E_V^0 **of the exponential valence band tail.**

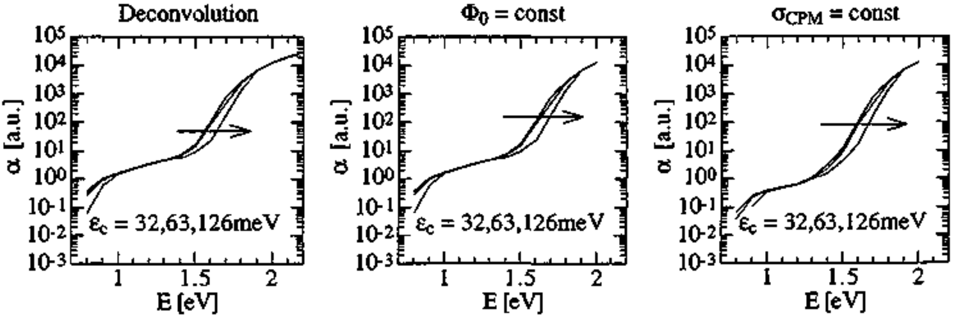
Deconvolution

Φ_0 = const

σ_{CPM} = const

Variation of the **threshold energy ε_c of the mobility edge of the conduction band.**

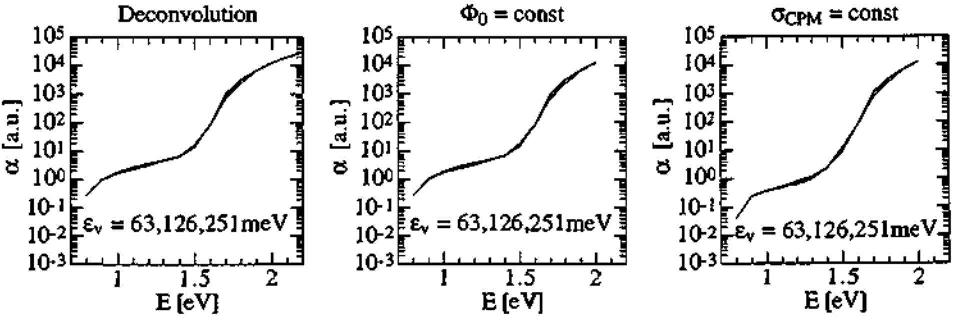
Deconvolution

Φ_0 = const

σ_{CPM} = const

Variation of the **threshold energy ε_v of the mobility edge of the valence band.**

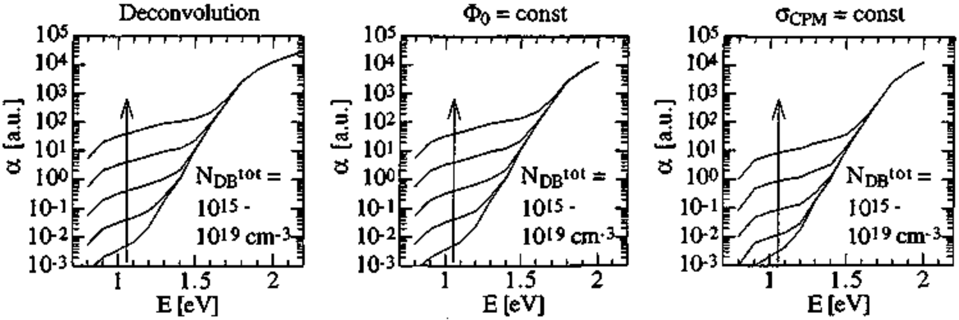

Variation of the total (integrated) **density of DB defects** N_{DB}^{tot} (dangling bonds).

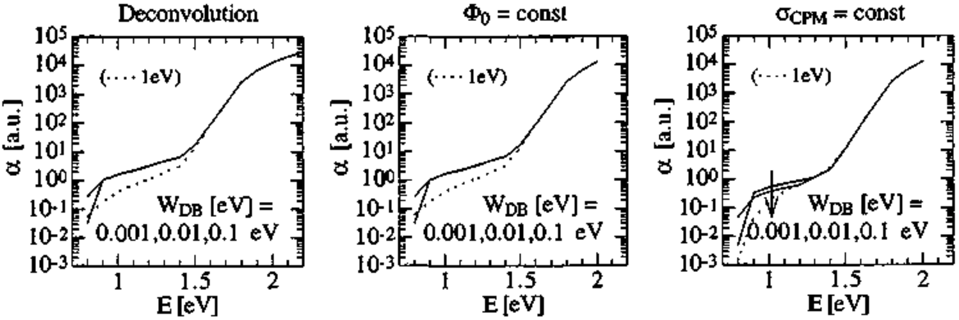

Variation of the **half width of the DB defect peak** W_{DB} (dangling bonds).

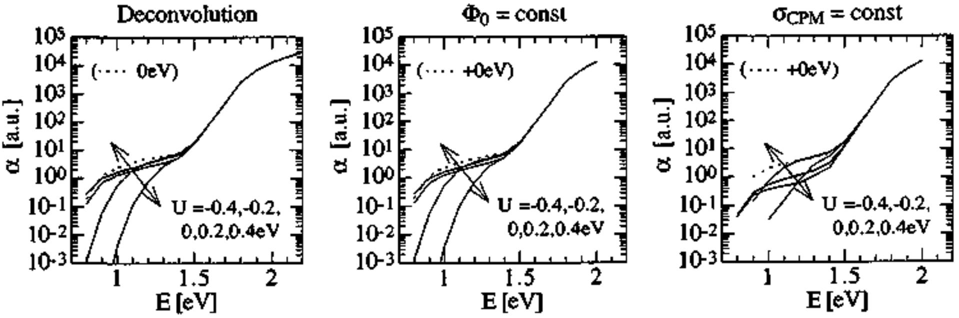

Variation of the finite **correlation energy** U of the DB defects (dangling bonds).

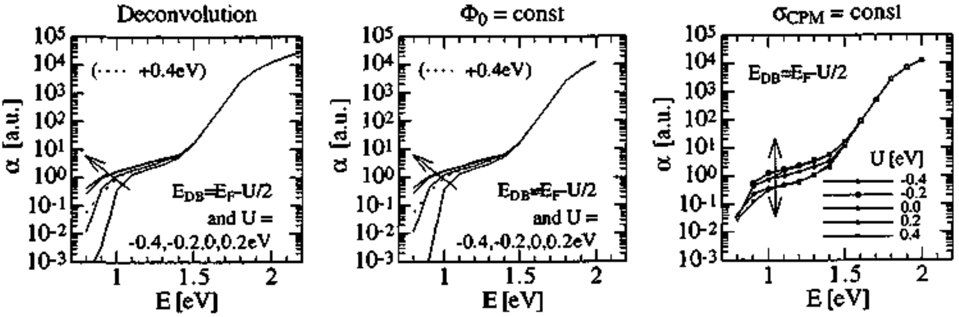

Variation of the **correlation energy** U <u>and</u> of the **defect position** E_{DB} with $E_F = E_{DB} + U/2$.

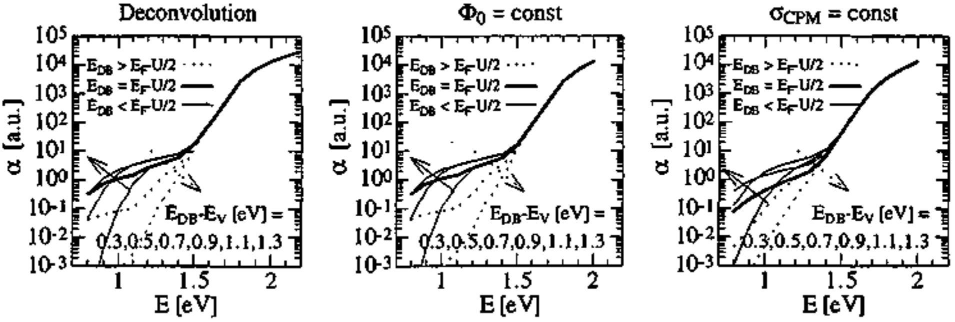

Variation of the **defect position** E_{DB}.

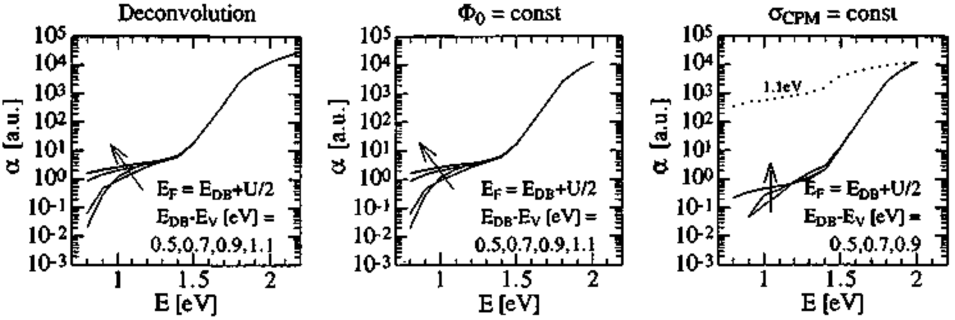

Variation of the **defect position** E_{DB} and the **Fermi position** E_F with $E_F = E_{DB} + U/2$.

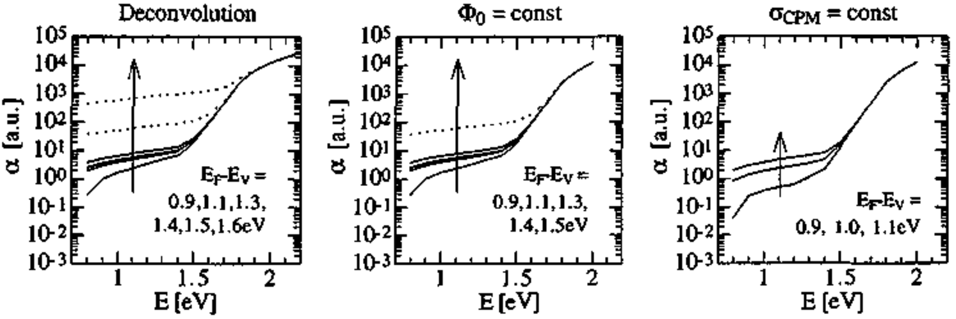

Variation of the **Fermi position** E_F to the conduction band.

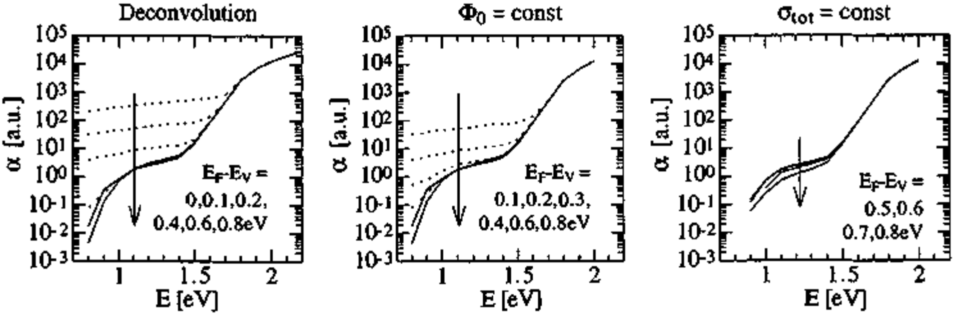

Variation of the **Fermi position** E_F to the valence band.

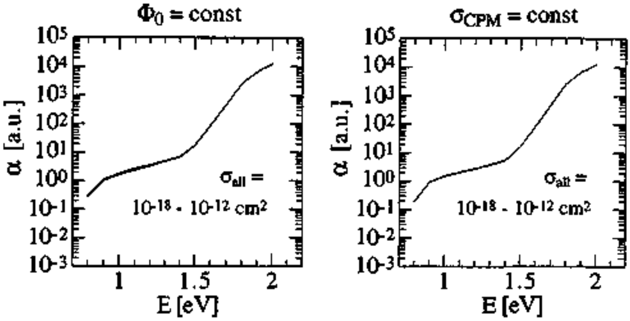

Variation of the **capture cross section** $\sigma_{all} \equiv \sigma_t = \sigma^0 = \sigma^{+/-}$;

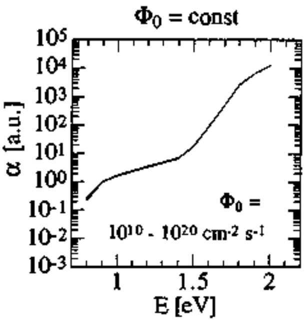

of the **PDS photon flux** Φ_0.

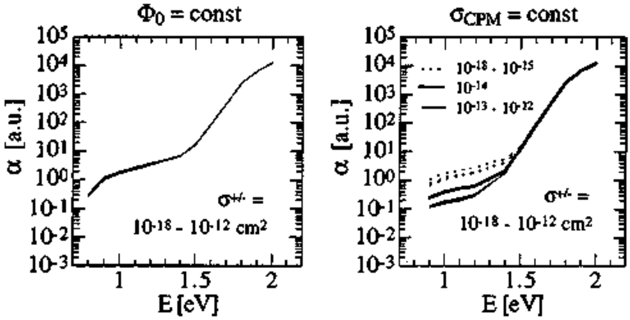

Variation of the **charged DB capture cross section** $\sigma^{+/-}$;

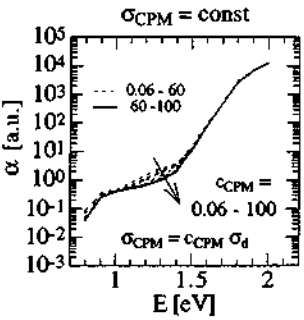

of the **CPM factor** c_{CPM}.

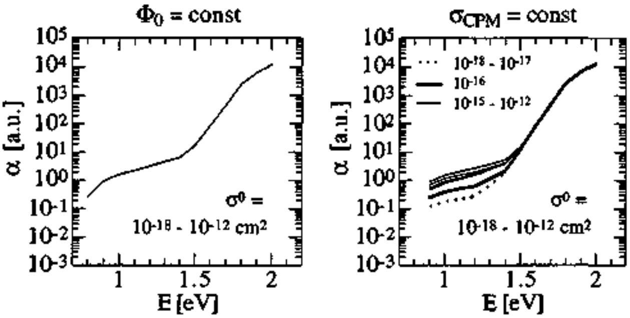

Variation of the **neutral DB capture cross section** σ^0;

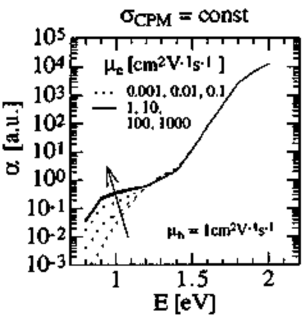

of the **electron mobility** μ_e.

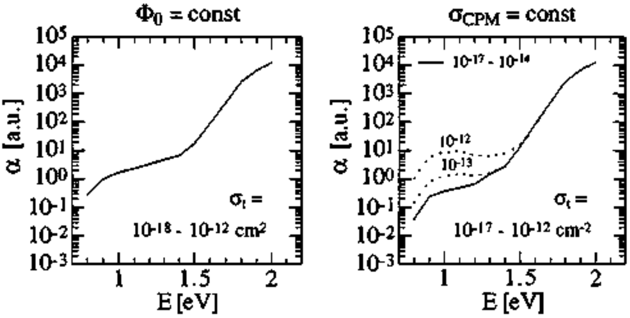

Variation of the **localised band capture cross section** σ_t;

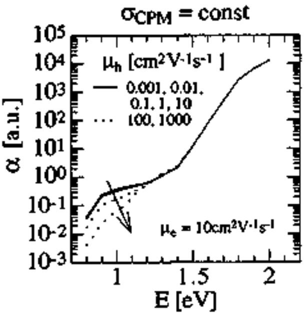

of the **hole mobility** μ_h.

C7. Details on numerical "PDS" analysis at steady state equilibrium (SETs 2 a-d)

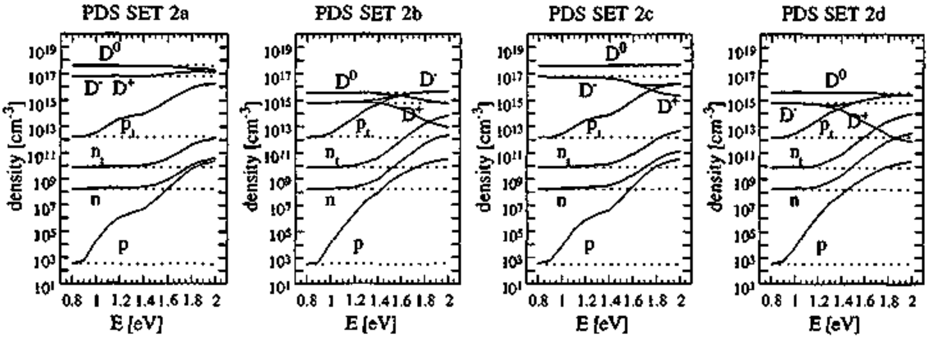

Fig.C7-1: charge densities of "PDS" (dashed lines = thermal equilibrium).

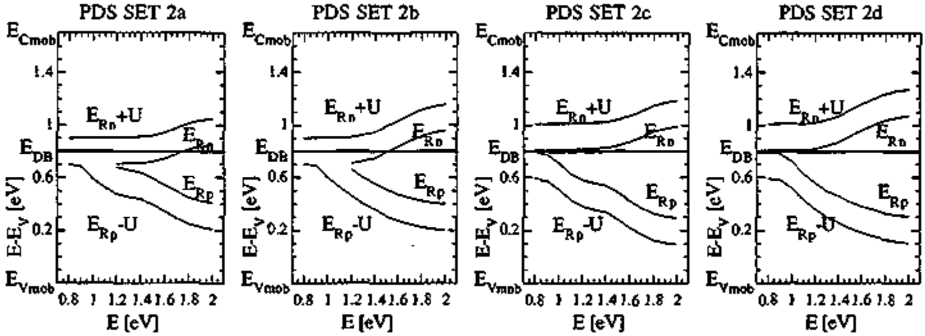

Fig.C7-2: recombination levels E_{Rn} and E_{Rp} of "PDS".

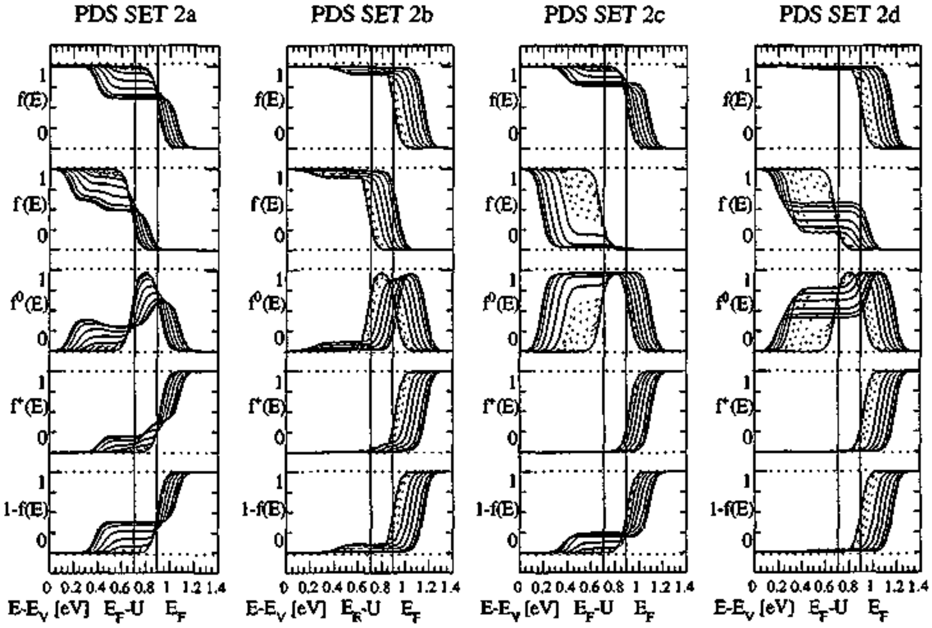

Fig.C7-3: occupation functions of "PDS" (Notation: full lines = thermal equilibrium and $\hbar\omega = 1.5 - 2.0$eV at steady-state equilibrium; dashed lines = $\hbar\omega = 0.8 - 1.4$eV at steady-state equilibrium).

PDS SET2a

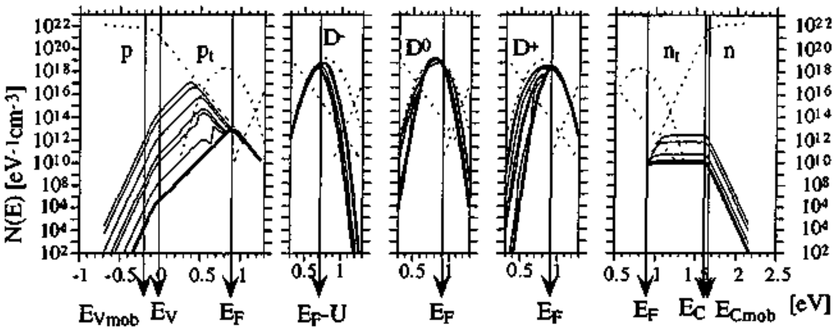

PDS SET2b

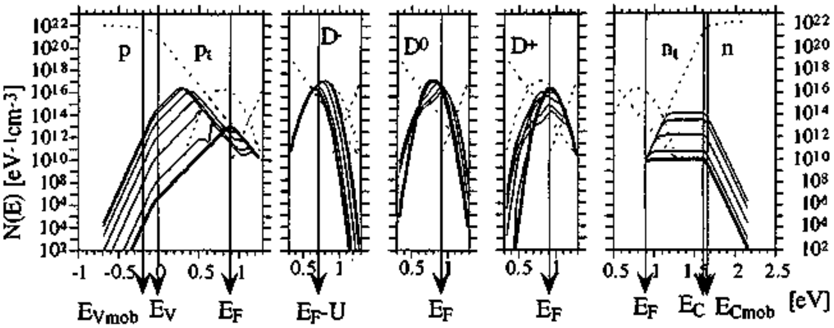

PDS SET2c

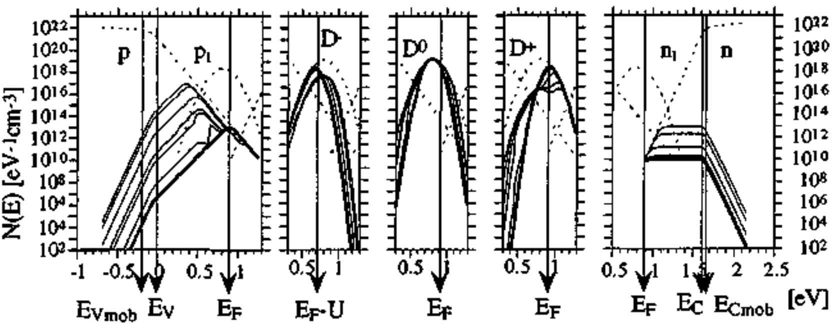

PDS SET2d

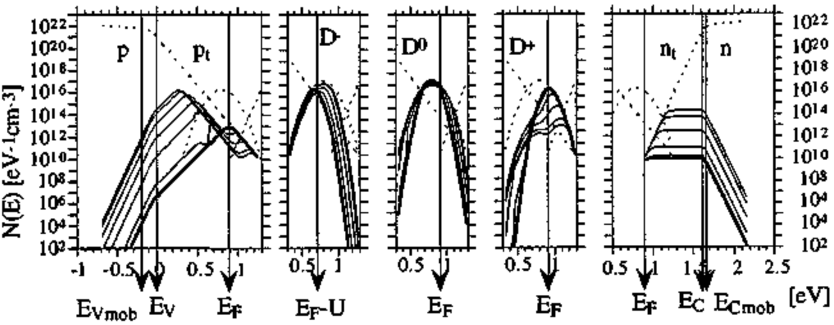

Fig.C7-4: DOS occupation of "PDS" ($\hbar\omega$ = 1, 1.2, 1.4, 1.8, 2eV).

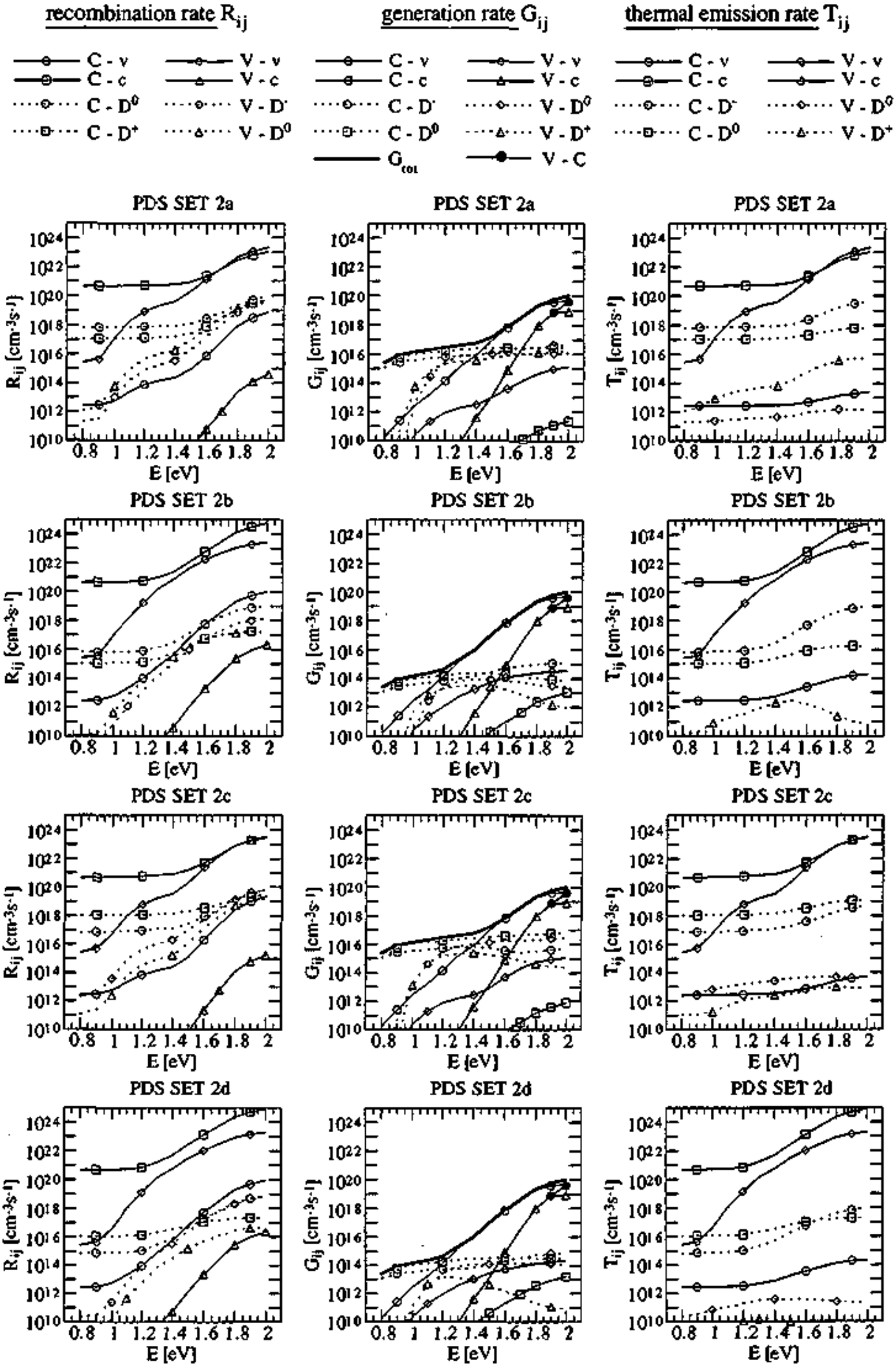

Fig.C7-5: partial rates of "PDS" (bold = total generation rate G_{tot}).

C8. Details on numerical "CPM" analysis at steady state equilibrium (SETs 2 a-d)

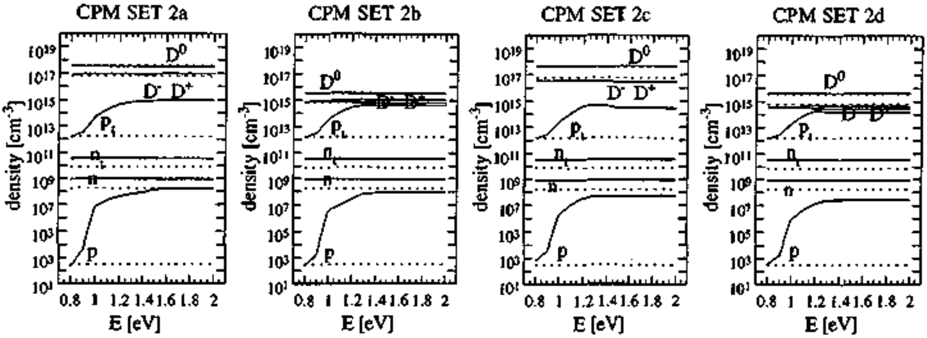

Fig.C8-1: charge densities of "CPM" (dashed lines = thermal equilibrium).

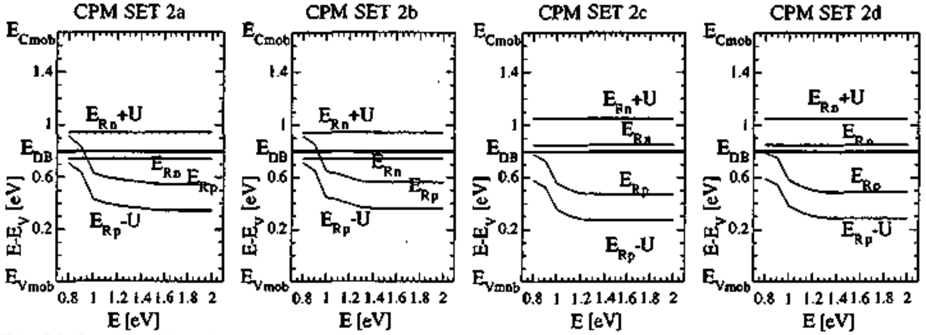

Fig.C8-2: recombination levels E_{Rn} and E_{Rp} of "CPM".

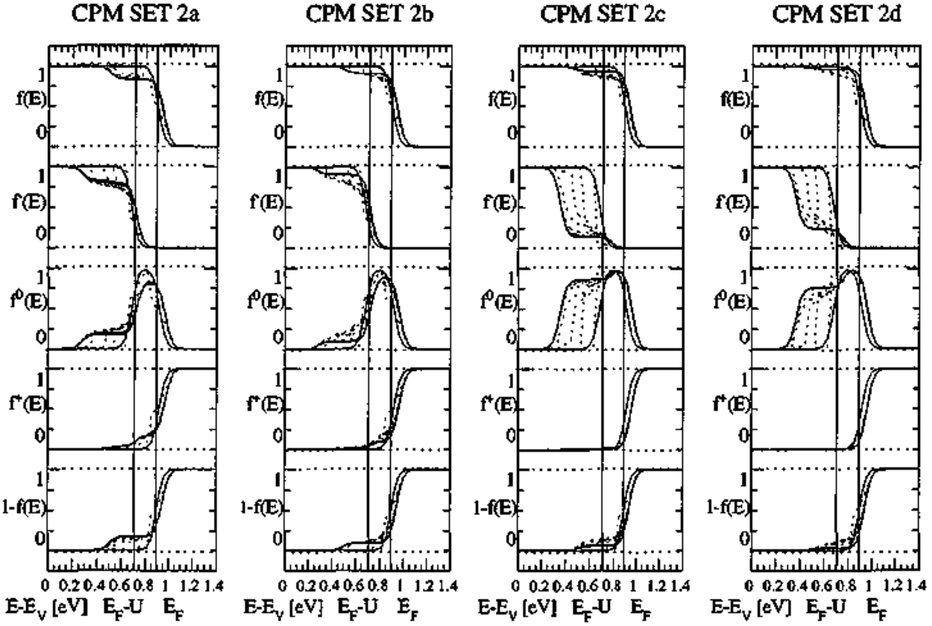

Fig.C8-3: occupation functions of "CPM" (Notation: full lines = thermal equilibrium and $\hbar\omega = 1.5-2.0$eV at steady state equilibrium; dashed lines = $\hbar\omega = 0.8-1.4$eV at steady state equilibrium).

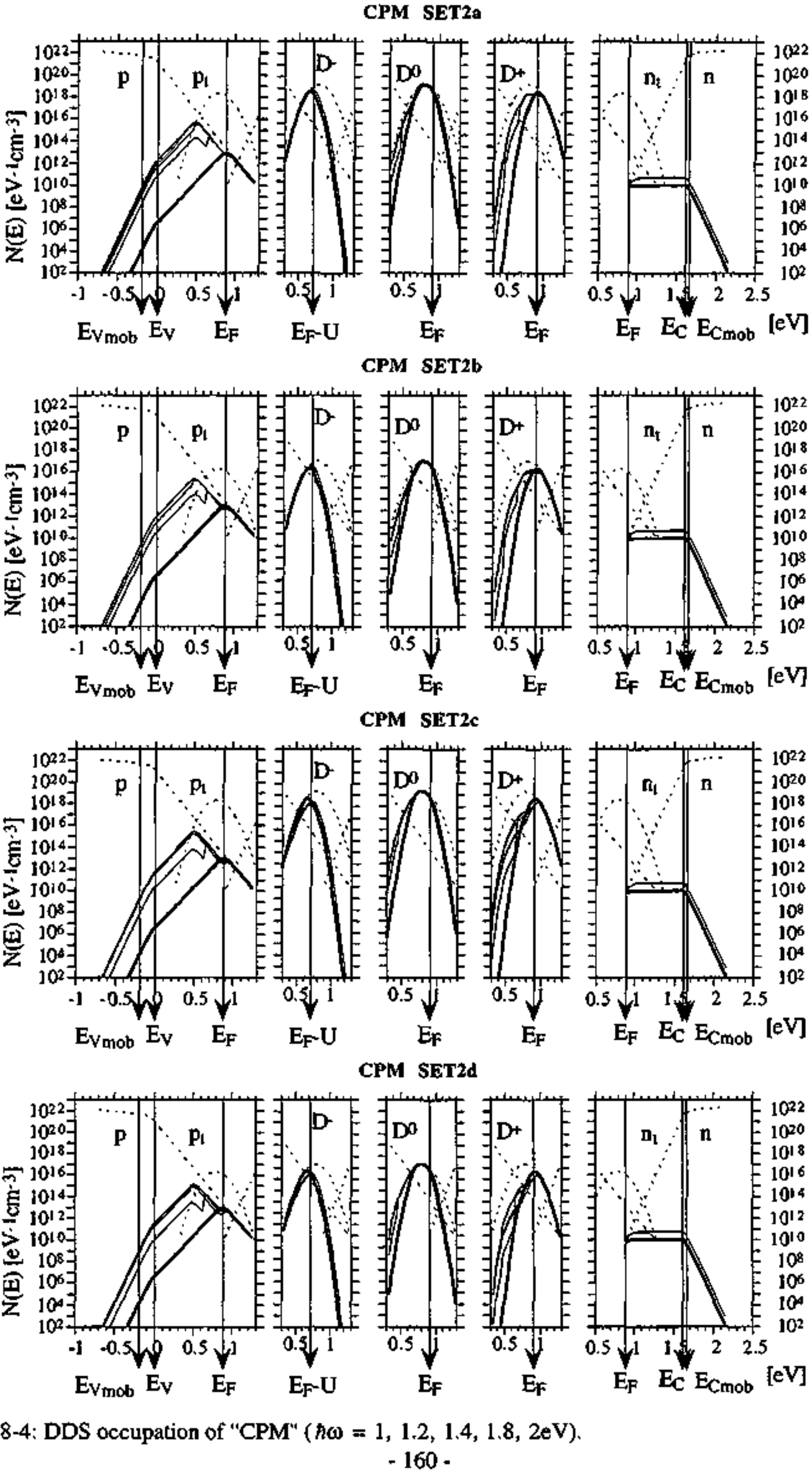

Fig.C8-4: DDS occupation of "CPM" ($\hbar\omega$ = 1, 1.2, 1.4, 1.8, 2eV).

C9. Details on numerical conductivity analysis at steady-state equilibrium (SETs 2a-d)

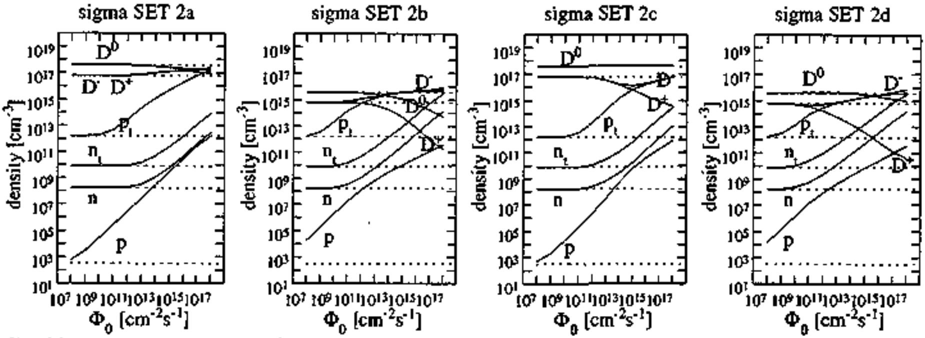

Fig.C9-1: charge densities of "sigma" ($\hbar\omega$ = 1.9eV) (dashed lines = thermal equilibrium).

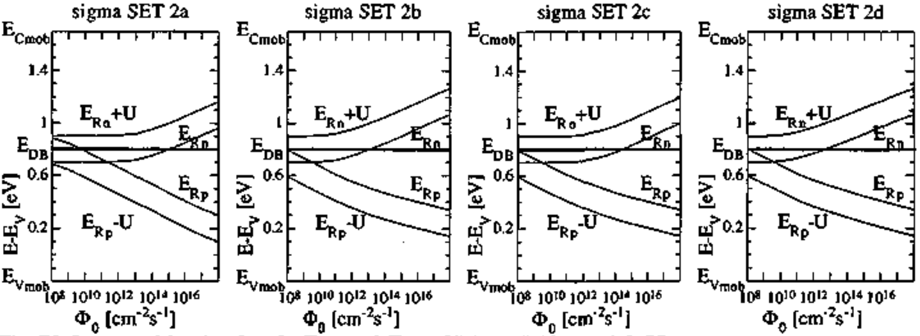

Fig.C9-2: recombination levels E_{Rn} and E_{Rp} of "sigma" ($\hbar\omega$ = 1.9eV).

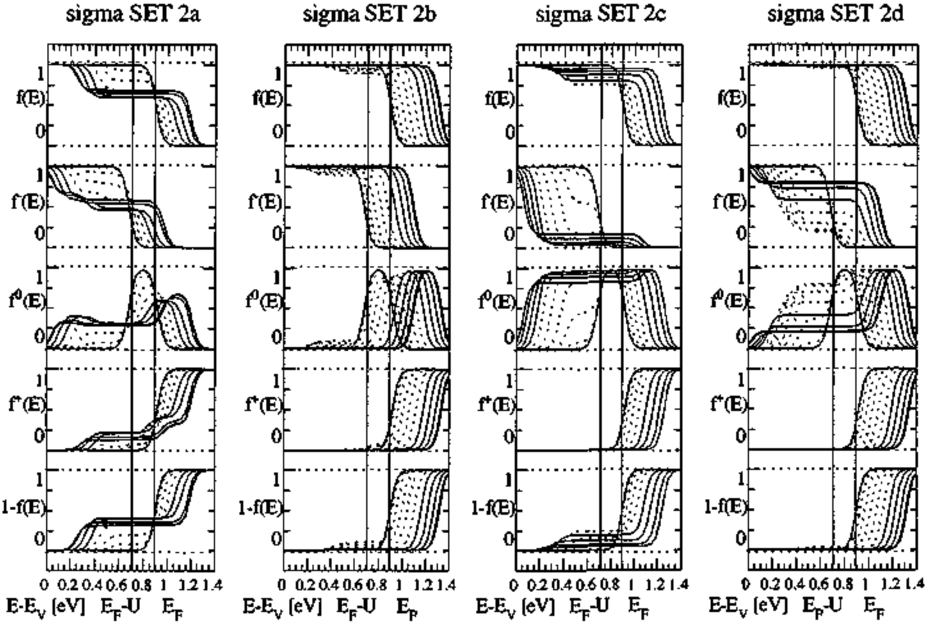

Fig.C9-3: occupation functions of "sigma" ($\hbar\omega$ = 1.9eV) (Notation: full lines = thermal equilibrium and $\Phi_0 = 10^{18} - 10^{20}$ cm^{-2}s^{-1} at steady state equilibrium; dashed lines = $\Phi_0 = 10^8 - 10^{18}$ cm^{-2}s^{-1} at steady state equilibrium).

sigma SET2a

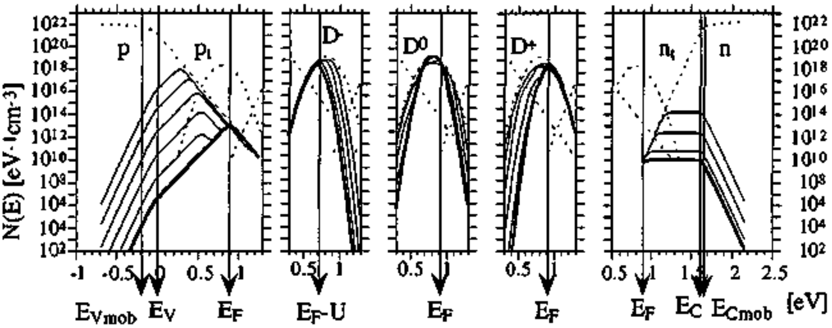

sigma SET2b

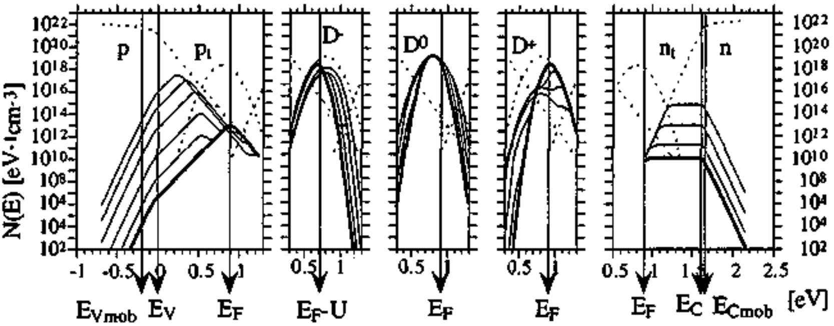

sigma SET2c

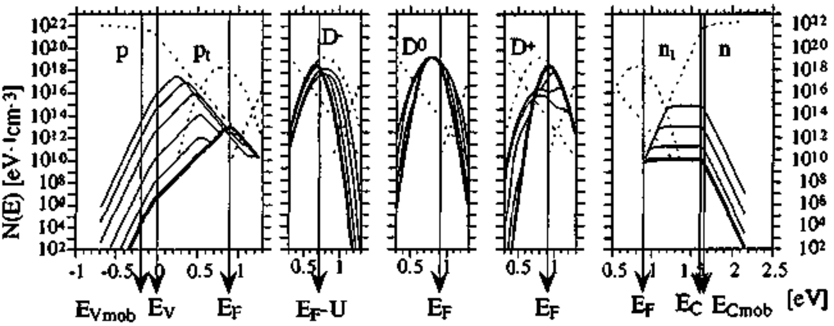

sigma SET2d

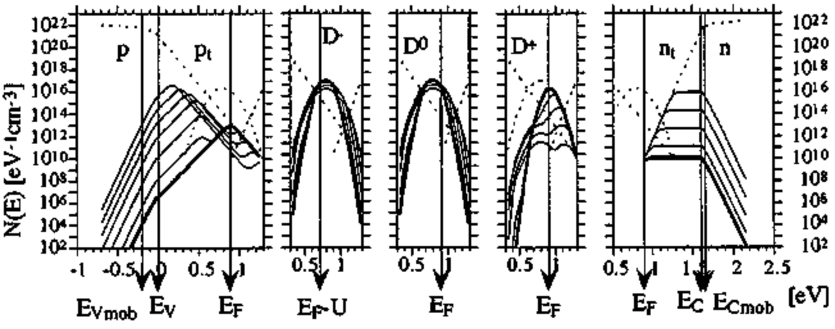

Fig.C9-4: DOS occupation of "sigma" ($\hbar\omega$ = 1.9eV, $\Phi_0 = 10^8, 10^{10}, 10^{12}, 10^{14}, 10^{16}, 10^{18}$ $cm^{-2}s^{-1}$).

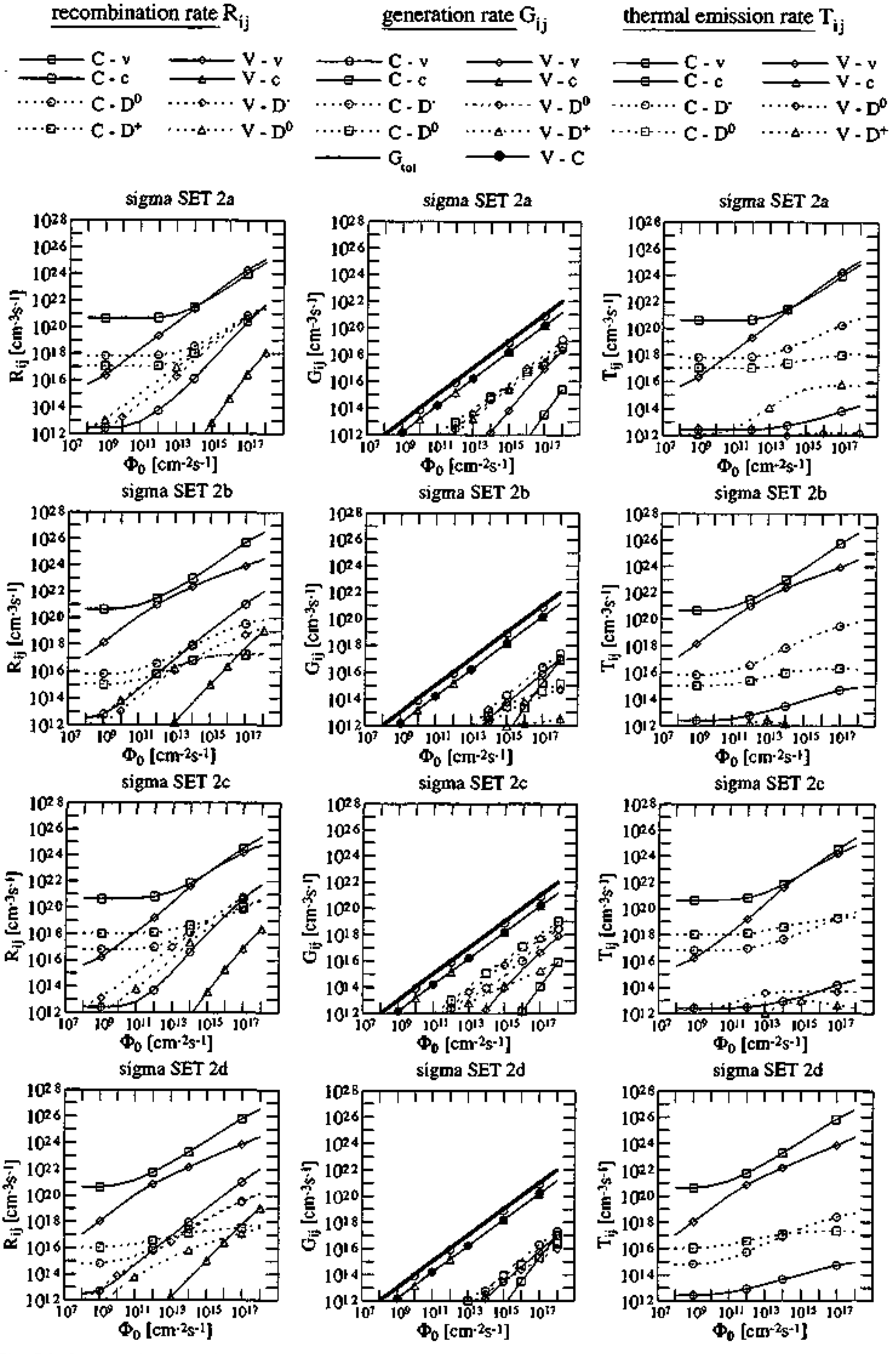

Fig.C9-5: partial rates of "sigma" with $\hbar\omega$ = 1.9eV (bold = total generation rate G_{tot}).

C10. Numerical analysis of the conductivity at steady state equilibrium (SETs 1-4 a-d)

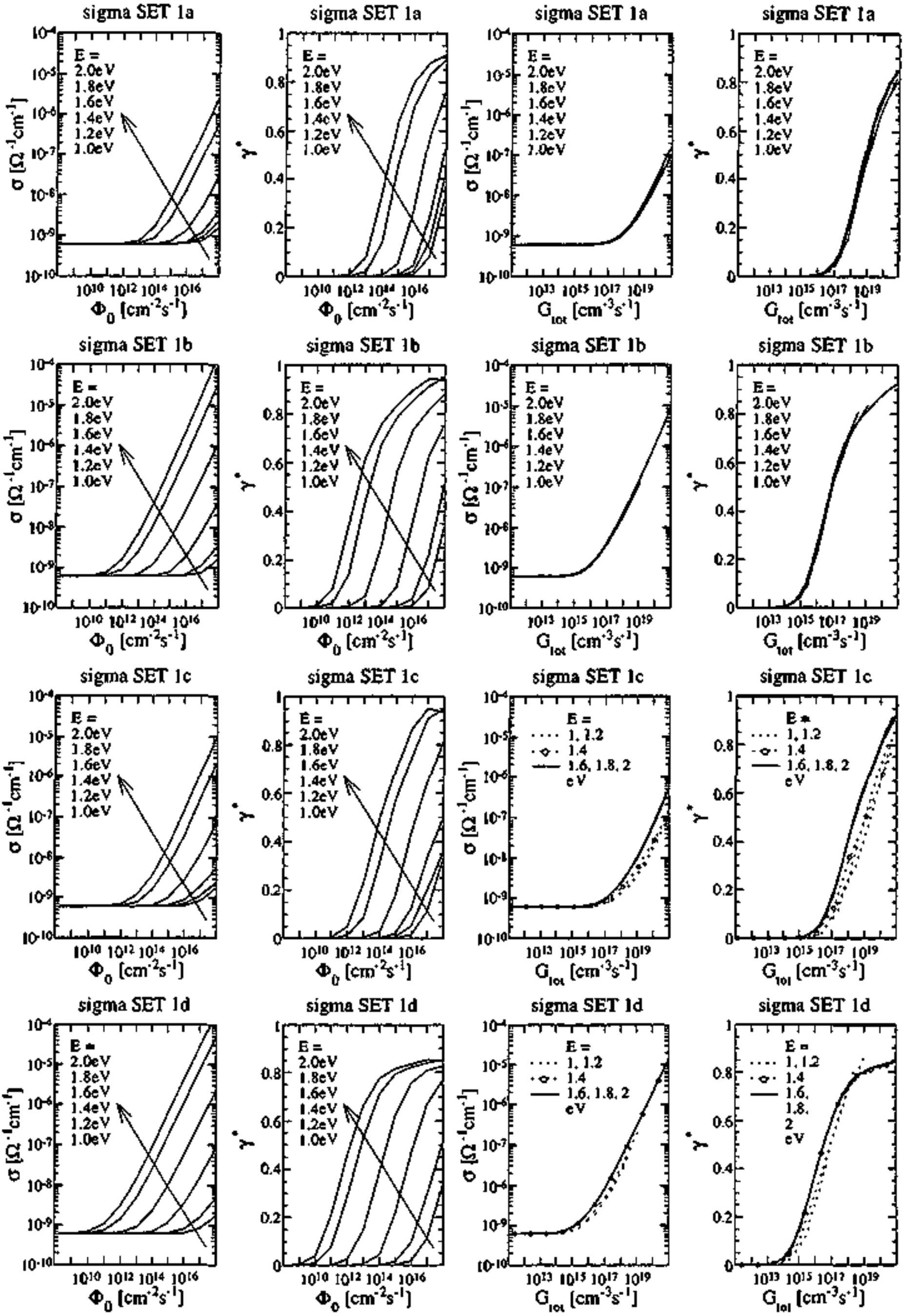

Fig.C10-1: conductivity $\sigma_{tot}(\Phi_0)$ and $\sigma_{tot}(G_{tot})$, as well as the corresponding power law factor $\gamma^*(\Phi_0)$ and $\gamma^*(G_{tot})$ of "sigma" SET 1a-d.

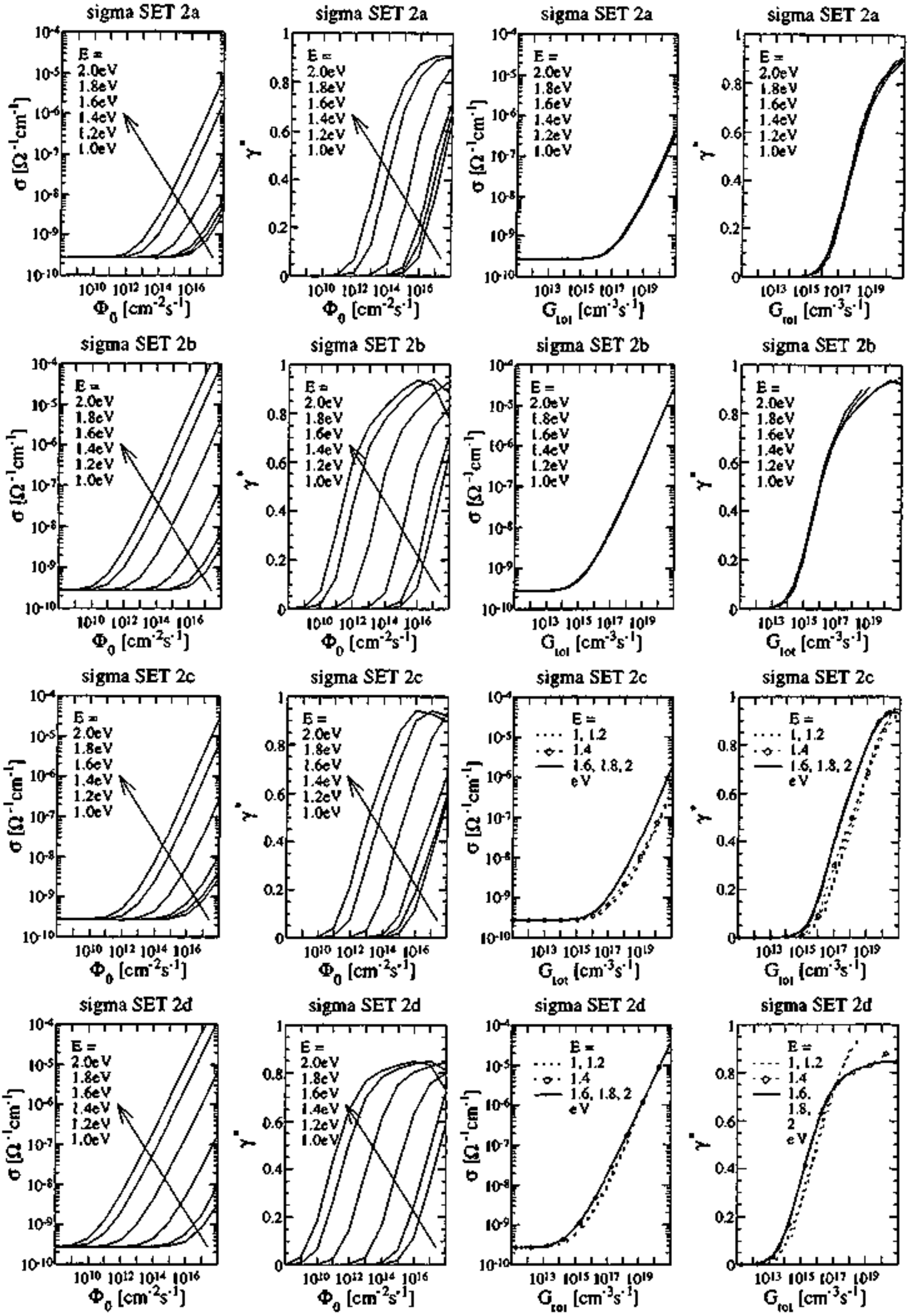

Fig.C10-2: conductivity $\sigma_{tot}(\Phi_0)$ and $\sigma_{tot}(G_{tot})$, as well as the corresponding power law factor $\gamma^*(\Phi_0)$ and $\gamma^*(G_{tot})$ of "sigma" SET 2a-d.

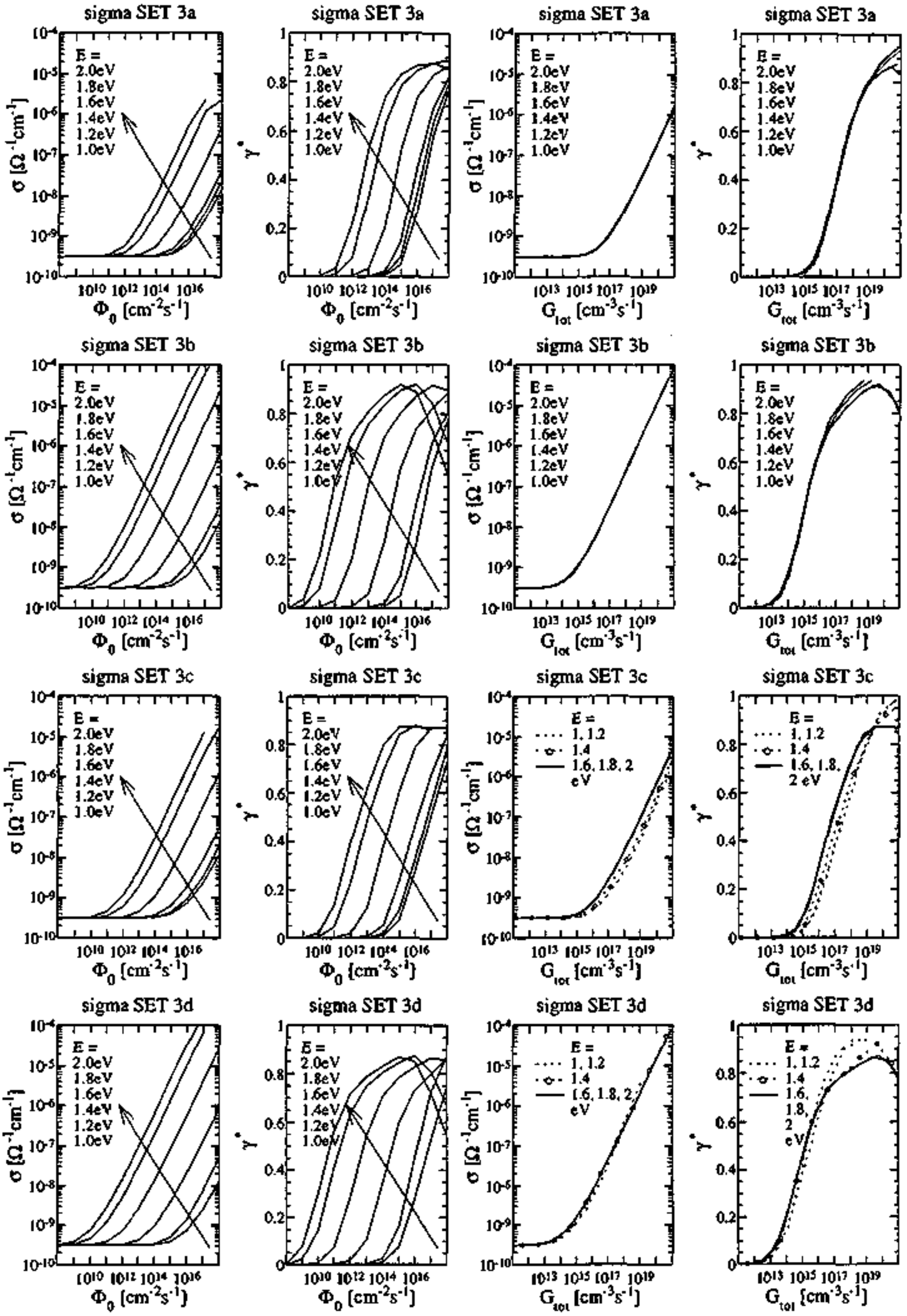

Fig.C10-3: conductivity $\sigma_{tot}(\Phi_0)$ and $\sigma_{tot}(G_{tot})$, as well as the corresponding power law factor $\gamma^*(\Phi_0)$ and $\gamma^*(G_{tot})$ of "sigma" SET 3a-d.

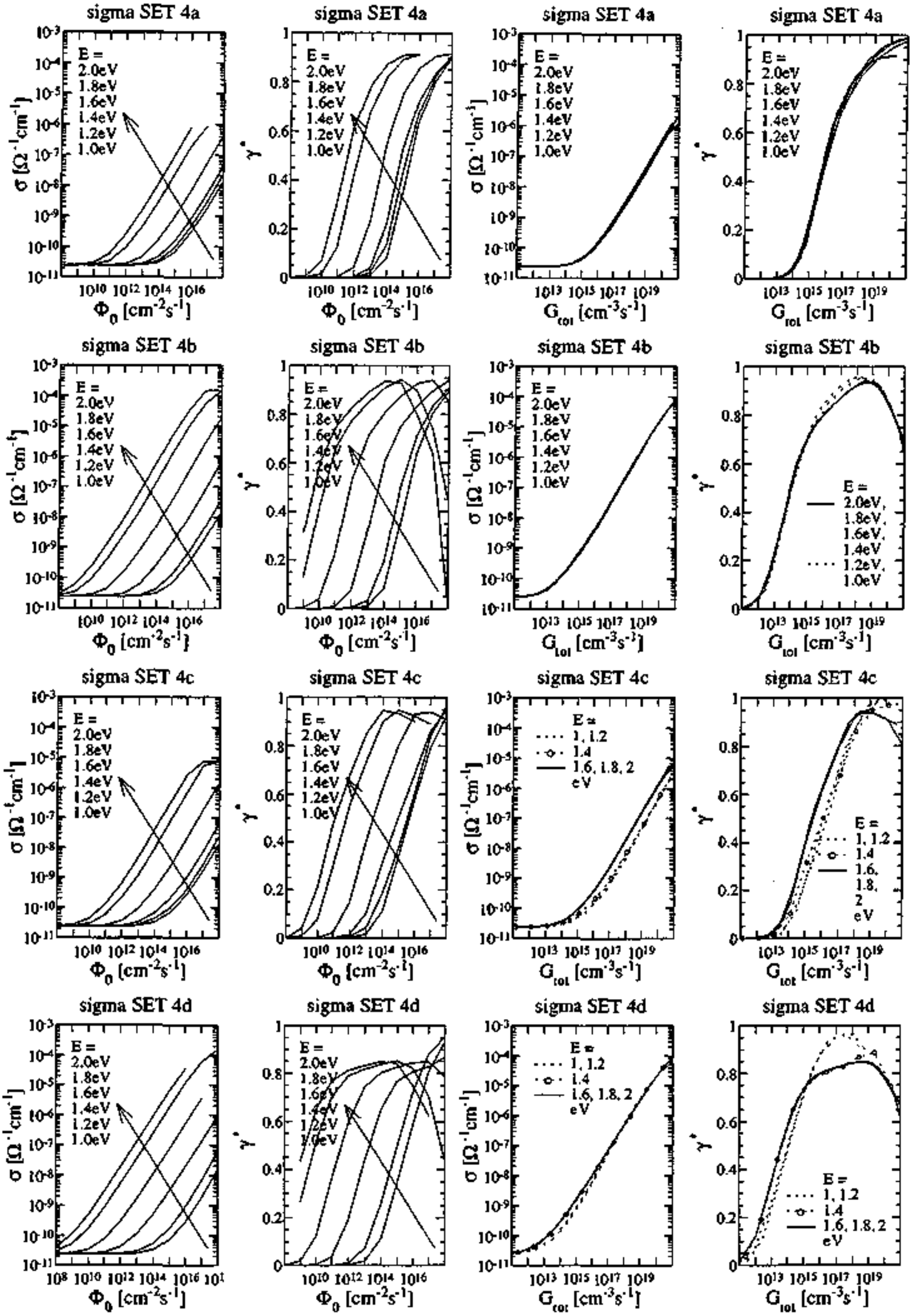

Fig.C10-4: *conductivity* $\sigma_{tot}(\Phi_0)$ *and* $\sigma_{tot}(G_{tot})$, as well as the corresponding power law factor $\gamma^*(\Phi_0)$ and $\gamma^*(G_{tot})$ of "sigma" SET 4a-d.

Appendix D: Notation

a) Abbreviations

a-Si:H	amorphous hydrogenated silicon
c-Si	crystalline silicon
μc-Si	micro-crystalline silicon
CPM	Constant Photocurrent Method
PDS	Photothermal Deflection Spectroscopy
ESR	Electron Spin Resonance measurements
DOS	standard density of state
CB	parabolic conduction band
CBT	exponential conduction band tail
VB	parabolic valence band
VBT	exponential valence band tail
DB	dangling bonds
D^+	positively charged dangling bond (atomic core)
D^0	neutral dangling bond (occupied by one electron)
D^-	negatively charged dangling bond (occupied by two electrons)
$D^{0/+}$	dangling bond peak in the two-peak picture at E_{DB}
$D^{0/-}$	dangling bond peak in the two-peak picture at $E_{DB}+U$
A	(optical) transition between delocalised states
B	(optical) transition between delocalised valence band states and localised states
C	(optical) transition between localised states and delocalised conduction band states
D	(optical) transition between localised states (here suppressed)
I	region, where G_a dominates
II	region, where G_{ap} dominates
III	region, where G_p dominates
IV	region, where G_a+G_p dominates
HDS	high discretisation set
LDS	low discretisation set

b) Roman alphabet

C	gas dopant ratio during deposition
C_0	proportionality factor between the absorption and the JDOS (optical matrix element R^2)

C_1	proportionality factor between the absorption and the JDOS (optical matrix element P^2)
c_0	speed of light
c_{CPM}	ratio between the CPM conductivity and the dark conductivity
d	thickness d of the material / sample
E	energy
E_a	activation energy of the dark conductivity
E_F	Fermi level position (thermal equilibrium)
E_{DB}	middle energy of the deep defect peak (dangling bonds)
E_d	defect position of a Dirac-function defect
E_g	bandgap
E_g^{opt}	optical bandgap
E_g^{mob}	mobility gap
E_g^*	photon energy of the Cody plot with $z_1(\hbar\omega) = 0$
E_C	edge of the parabolic conduction band
E_V	edge of the parabolic valence band
E_{Cmob}	mobility edge of the conduction band
E_{Vmob}	mobility edge of the valence band
E_{tn}	quasi-Fermi-level for trapped electrons
E_{tp}	quasi-Fermi-level for trapped holes
E_{In}	optical "ionisation" energy to the conduction band
E_{Ip}	optical "ionisation" energy to the valence band
E_{Rn}	upper "recombination" level of a defect **with** a finite correlation energy U
E_{Rp}	lower "recombination" level of a defect **with** a finite correlation energy U
E_{Gn}	upper "generation" level of a defect without a finite correlation energy
E_{Gp}	lower "generation" level of a defect without a finite correlation energy
E_C^0	characteristic tail slope of the exponential conduction band tail
E_V^0	characteristic tail slope of the exponential valence band tail
E_C^{tail}	connection point of $N_{CB}(E)$ with $N_{CBT}(E)$
E_V^{tail}	connection point of $N_{VB}(E)$ with $N_{VBT}(E)$
E_γ	parameter used for the discretisation
E_i	energy of the occupied electron states
E_j	energy of the non-occupied electron states
e_{bb}^{ph}	band-to-band generation probability (transition type A)
e_n^{th}, e_{nU}^{th}	thermal emission probability of negative charge carriers
e_p^{th}, e_{pU}^{th}	thermal emission probability of positive charge carriers
e_n^{ph}, e_{nU}^{ph}	defect-to-band generation probability of negative charge carriers (transition type C) (also called optical emission probabilities of negative charge carriers)
e_p^{ph}, e_{pU}^{ph}	defect-to-band generation probability of positive charge carriers (transition type B) (also called optical emission probabilities of positive charge carriers)

e_n, e_{nU}	thermal plus optical emission probability of negative charge carriers
e_p, e_{pU}	thermal plus optical emission probability of positive charge carriers
f, f(E)	occupation function
$f^+(E)$	occupation function of positively charged dangling bonds
$f^0(E)$	occupation function of neutral dangling bonds
$f^-(E)$	occupation function of negatively charged dangling bonds
$f_e(E)$	electron occupation function of a defect with a finite correlation energy
$f_{ch}(E)$	DB charge occupation function
$f_c(E)$	occupation function of the localised conduction band at steady state equilibrium
$f_v(E)$	occupation function of the localised valence band at steady state equilibrium
$\hat{f}(\chi)$	correction function of the effective DOS
G	generation rate
G_{CPM}	generation rate at the CPM working point
G(x)	local generation rate
G_{tot}	total generation rate
$G_{tot}(\hbar\omega)$	spectrally dependent total generation rate
$G_{ij}(\hbar\omega)$	partial generation rate of the standard DOS (i = C,V; j = c, v, +, 0, -)
$G_{bb}(\hbar\omega)$	band-to-band generation rate ($G_A(\hbar\omega)$) caused by transitions A
$G_d(\hbar\omega)$	defect-to-band generation rate ($G_{BC}(\hbar\omega)$) caused by transitions B and C
G_n	defect-to-band generation rate caused by transition C (defect without a finite correlation energy)
G_p	defect-to-band generation rate caused by transition B (defect without a finite correlation energy)
G_{np}	defect-to-band generation rate caused by transitions B and C (defect without a finite correlation energy)
H	Hamiltonian
h, $\hbar$	Plank's constant
$\hbar\omega$	photon energy
$\hbar\omega_c$	specific photon energy for the calibration of PDS
$\hbar\omega_W$	photon energy $\hbar\omega_W$ of the single energy absorption α_W
I	measured current
I_{CPM}	measured CPM current
I_d	measured dark current (at thermal equilibrium)
I_{ph}	measured photo current (lm-mode)
I_{tot}	measured total current (cw-mode)
I_0	incident light intensity
I_0^{cpm}	light intensity used for CPM
$J(\hbar\omega)$	joint density of states (JDOS)
$J_A(\hbar\omega)$	partial joint density of states (JDOS) of transitions of type A
$J_B(\hbar\omega)$	partial joint density of states (JDOS) of transitions of type B

$J_C(\hbar\omega)$	partial joint density of states (JDOS) of transitions of type C
$J_D(\hbar\omega)$	partial joint density of states (JDOS) of transitions of type D
$J^{ij}(\hbar\omega)$	partial joint density of the standard DOS ($i = C,V$; $j = c, v, +, 0, -$)
K, K_U	ratios which determinate the occupation function at steady state equilibrium
$\hat{K}$, $\hat{K}_U$	ratios K and K_U, neglecting the thermal emission and generation probabilities
k	Boltzmann's constant
$\hat{k}$	occupation $f(E)$, neglecting the thermal emission and generation probabilities
$\hat{k}^+$	occupation $f^+(E)$, neglecting the thermal emission and generation probabilities
$\hat{k}^0$	occupation $f^0(E)$, neglecting the thermal emission and generation probabilities
$\hat{k}^-$	occupation $f^-(E)$, neglecting the thermal emission and generation probabilities
k_d	used for the expression of G_n, G_p and G_{np} (defect without a finite correlation energy)
k_L	ratio of $10^4\,W / L$ of a coplanar contact
L	coplanar contact length
m	particle mass
m_e	electron rest mass
$\tilde{m}_e^*$	effective DOS mass for electrons in the conduction band
$\tilde{m}_h^*$	effective DOS mass for holes in the valence band
$\tilde{m}^*$	effective conductivity mass
$N(E)$	DOS of the free electrons
$N_{occ}(E)$	occupied electron states
$N_{non}(E)$	non-occupied electron states
$N_{CB}(E)$	DOS of the parabolic conduction band
$N_{VB}(E)$	DOS of the parabolic valence band
$N_{CBT}(E)$	DOS of the exponential conduction band tail
$N_{VBT}(E)$	DOS of the exponential valence band tail
N_C^0	bending parameter of the parabolic conduction band
N_V^0	bending parameter of the parabolic valence band
N_C^{tail}	DOS at the connection point of $N_{CB}(E)$ with $N_{CBT}(E)$
N_V^{tail}	DOS at the connection point of $N_{VB}(E)$ with $N_{VBT}(E)$
$N_{CB/CBT}(E)$	DOS of the conduction band
$N_{VB/VBT}(E)$	DOS of the valence band
$N_C(E)$	DOS of the delocalised conduction band states
$N_V(E)$	DOS of the delocalised valence band states
$N_c(E)$	DOS of the localised conduction band tail states
$N_v(E)$	DOS of the localised valence band tail states
$N_C^*(E)$	used for the expression of the thermal emission probability (e_n^{th}, e_{nU}^{th})
$N_V^*(E)$	used for the expression of the thermal emission probability (e_p^{th}, e_{pU}^{th})
N_{Cmob}	DOS at the mobility edge of the conduction band
N_{Vmob}	DOS at the mobility edge of the valence band
N_{Cmob}^{eff}	effective DOS at the mobility edge of the conduction band

N_{Vmob}^{eff}	effective DOS at the mobility edge of the valence band
N_d	defect density of a Dirac-function defect
$N_{DB}(E)$	Gaussian shaped deep defect peak (dangling bonds)
N_{DB}^{tot}	total (integrated) density of defects (dangling bonds)
N_{DB}^{-}	negatively charged dangling bond density
N_{DB}^{0}	neutral dangling bond density
N_{DB}^{+}	positively charged dangling bond density
N_S	ESR dangling bond spin density
N_{ion}	ionised defect densities
N_{min}	minimum value of the DOS for the numerical analysis
n	charge carrier density above the mobility edge of the conduction band
n_t	charge density in the localised conduction band tail states
$\bar{n}$, $\bar{n}_U$	capture probability of negative charge carriers
n_0	refraction index of a-Si:H
$\mathbf{P}$	momentum operator
P^2	average square momentum matrix element (optical matrix element)
p	charge carrier density below the mobility edge of the valence band
p_t	charge density in the localised valence band tail states
$\bar{p}$, $\bar{p}_U$	capture probability of positive charge carriers
Q_{tot}	total charge density
$Q_{tot}(E_F)$	total charge density at thermal equilibrium
$Q_{tot}(n,p)$	total charge density at steady state equilibrium
R_{tot}	total recombination rate
R_{bb}	band-to-band recombination rate
R_d	defect recombination rate
R_{ij}	partial recombination rate of the standard DOS (i = C,V; i = c, v, +, 0, -)
$\mathbf{R}$	dipole operator
R^2	average square dipole matrix element (optical matrix element)
R_0	reflection coefficient of a-Si:H / air interface
R_1	reflection coefficient of a-Si:H / glass interface
r_{DB}	capture cross section ratio of the charged to uncharged DB states
r_{DB}^{t}	capture cross section ratio of the localised band tail states to the uncharged DB states
$s_{PDS}(\hbar\omega)$	detected PDS signal
T	temperature
T_S	deposition substrate temperature
$\bar{T}$	averaged transmission
T_{min}	minimum values of the transmission
T_{max}	maximum values of the transmission
T_{tot}	total thermal emission rate
T_{bb}	band-to-band thermal emission rate

T_d	defect thermal emission rate
T_{ij}	partial thermal emission rate of the standard DOS (i = C,V; i = c, v, +, 0, -)
t	time
U	applied voltage (chapter 1)
U	correlation energy of a defect (chapter 2 and chapter 3)
W	coplanar contact width
W_{DB}	half-width of the deep defect peak (dangling bonds)
Y_1, Y_2	parameters of the discretisation
Z_n	used for the expression of E_{Gn}
Z_p	used for the expression of E_{Gp}
$z_0(\hbar\omega)$	function for the Cody plot
z_d, z_{dU}	correlation factors of a defect with a finite correlation energy U

c) Greek alphabet

α	absorption, absorption coefficient
$\alpha(x)$	local absorption coefficient
$\alpha(\hbar\omega)$	absorption, absorption coefficient
$\alpha_{th}(\hbar\omega)$	absorption spectrum at thermal equilibrium
$\alpha_{CPM}(\hbar\omega)$	CPM spectrum
$\alpha_{PDS}(\hbar\omega)$	PDS spectrum
$\alpha_{DB}(\hbar\omega)$	dual-beam spectrum
α_{dd}	deep defect absorption value
$\overline{\alpha}_I$	integrated excess absorption
α_W	single energy absorption at a specific photon energy $\hbar\omega_W$
β	= 1 / (kT)
γ	power law exponent (lm-mode), also called Rose factor
γ^*	power law exponent (cw-mode)
γ_{CPM}, γ^*_{CPM}	power law exponent at the CPM "working point"
Δn_0	change in the refraction index of a-Si:H
Δx	change in the position of the PDS probe beam
ε_c	threshold energy of the mobility edge of the conduction band
ε_v	threshold energy of the mobility edge of the valence band
η	microscopic quantum efficiency
θ_n	ratio of the optical matrix element and the capture cross section in the expression of E_{Gn}
θ_p	ratio of the optical matrix element and the capture cross section in the expression of E_{Gp}
θ_{DB}	ratio of the optical matrix element and the neutral DB capture cross section
λ	wave length

μ_e	average mobility at the mobility edge of the conduction band
μ_h	average mobility at the mobility edge of the valence band
ν	chopper frequency (lm-mode)
v_{th}	thermal velocity
v_n	thermal velocity of negative charge carriers
v_p	thermal velocity of positive charge carriers
ξ_d^*	voltage power law factor (dark current)
ξ	voltage power law factor (photo current)
ξ^*	voltage power law factor (total current)
ρ_A	atomic density
σ	conductivity
σ_d	dark conductivity / conductivity at thermal equilibrium
σ_{tot}	total conductivity (cw-mode)
σ_{ph}	photo conductivity (lm-mode)
σ_{CPM}	conductivity at the CPM working point
σ_0	prefactor of the measured dark conductivity
σ^0	capture cross section of neutral dangling bond states
$\sigma^{+/-}$	capture cross section of charged dangling bond states
σ_t	capture cross section of any localised band tail states
σ_{ion}	capture cross section based on the ionised scattering theory
σ_n	electron capture cross section of positively charged dangling bond states
σ_{nU}	electron capture cross section of neutral dangling bond states
σ_p	hole capture cross section of neutral dangling bond states
σ_{pU}	hole capture cross section of negatively charged dangling bond states
σ_{nc}	electron capture cross section of localised conduction band tail states
σ_{pc}	hole capture cross section of localised valence band tail states
σ_{nv}	electron capture cross section of localised conduction band tail states
σ_{pv}	hole capture cross section of localised valence band tail states
Φ_0	incident photon flux
$\Phi(x)$	local photon flux
χ	threshold energy ε in terms of kT
χ_c	threshold energy ε_c in terms of kT
χ_v	threshold energy ε_v in terms of kT

Appendix E: References

a) Chapter 1

[Asano 93] A.Asano, Y.Ichikawa, H.Sakai, J. of Non-Crystalline Solids, 164-166 (1993) 905

[Brandt 91] M.S.Brandt, M.Stutzmann, J. of Non-Crystalline Solids, 137&138 (1991) 211

[Curtins 89] H.Curtins, M.Favre, in Advances in Disordered Semiconductors Vol.1a, edited by H.Fritzsche, Word Scientific (1989) 329

[DeVore 56] H.B.DeVore, Phys.Rev. 102 (1956) 86

[Favre 91] M.Favre, A.Shah, J.Hubin, E.Bustarret, M.A.Hachicha, S.Basrour, J. of Non-Crystalline Solids, 137&138 (1991) 335

[Favre 94/1] M.Favre, thesis, University of Neuchâtel, 1994

[Fischer 94] D.Fischer, thesis, University of Neuchâtel, 1994

[Fiorini 93] P.Fiorini, M.Petracca, S.Korepanov, L.Fornarini, A.Mittiga, G.Grillo, J. of Non-Crystalline Solids, 164-166 (1993) 379

[Hoheisel 91] M.Hoheisel, O.Stika, J.Kocka, J.of Non-Crystalline Solids, 137&138 (1991) 615

[Jackson 81] W.B.Jackson, N.M.Amer, A.C.Boccara, D.Fournier, Appl.Opt. 20 (1981) 1333

[Kocka 89] J.Kocka, M.Vanecek, A.Triska, in Advances in Disordered Semiconductors Vol.1a, edited by H.Fritzsche, Word Scientific (1989) 297

[Kroll 93] U.Kroll, J.Meier, M.Goetz, A.Howling, J.L.Dorier, J.Dutta, A.Shah, Ch.Hollenstein, J. of Non-Crystalline Solids, 164-166 (1993) 59

[J.Z.Liu 93] J.Z.Liu, G.Lewen, J.P.Conde, P.Roca i Cabarrocas, J. of Non-Crystalline Solids, 164-166 (1993) 383

[H.N.Liu 93] H.N.Liu, Y.L.He, F.Wang, S.Grebner, J. of Non-Crystalline Solids, 164-166 (1993) 1005

[Mettler 93/2] A.Mettler, N.Wyrsch, A.Shah, J. of Non-Crystalline Solids, 164-166 (1993) 427

[Mettler 93/3] A.Mettler, N.Wyrsch, M.Goetz, A.Shah, Tech.Digest, PVSEC-7, Nagoya (1993) 603; Solar Energy Materials and Solar Cells, 34-35 (1994)

[Mittiga 90] A.Mittiga, P.Fiorini, M.Sebastiani, S.Korepanow, F.Evangelisti, Proc. of the 21th IEEE PVSEC, Orando (1990) 1465

[Nonomura 93] S.Nonomura, T.Nishiwaki, E.Nishimura, S.Hasegawa, T.Itoh, S.Nitta, Tech.Digest, PVSEC-7, Nagoya (1993) 607; Solar Energy Materials and Solar Cells, 34-35 (1995)

[Overhof 89] H.Overhof, P.Thomas, Hydrogenated amorphous silicon, Springer-Verlag, 1989

[Pierz 87] K.Pierz, B.Hilgenberg, H.Mell, G.Weiser, J. of Non-Crystalline Solids, 97&98 (1987) 91

[Pirz 90] K.Pierz, thesis, University of Marburg, Germany, 1990

[Prasad 91] K.Prasad, thesis, University of Neuchâtel, 1991

[Rose 63] A.Rose, concepts in photoconductivity and allied problems, 1963, Interscience Publishers, John Wiley & Sons

[Rübel 91] H.Rübel, W.Frammelsberger, R.Geyer, B.Scheppat, P.Lechner, M.Gorn, N.Kniffler, Proc. of the 10th E.C. PSEC, Lisbon (1991) 350

[Rübel 91] H.Rübel, W.Frammelsberger, P.Lechner, N.Kniffler, J.of Non-Crystalline Solids, 137&138 (1991) 1169

[Santos 91] P.V.Santos, W.B.Jackson, R.A.Street, AIP Converence proceedings 234, Amorphous silicon materials and solar cells, Denver (1991) 51

[Sasaki 93] M.Sasaki, S.Okamoto, Y.Hishikawa, S.Tsuda, S.Nakano, Tech.Digest, PVSEC-7, Nagoya (1993) 605
To be published in Solar Energy Materials and Solar Cells 34-35 (1995)

[Sauvain 93] E.Sauvain, A.Mettler, N.Wyrsch, A.Shah, Solid State Comm., 85 (1993) 219

[Shah 93] A.Shah, J.Hubin, E.Sauvain, P.Pipoz, N.Beck, N.Wyrsch, J. of Non-Crystalline Solids, 164-166 (1993) 485

[Sladek 92] P.Sladek, Y.Bouizem, M.L.Thèye, P.Roca i Cabarrocas, Proc. of the 11th E.C. PSEC, Montreux (1992) 710

[Sladek 93] P.Sladek, M.L.Thèye, L.Chahed, J. of Non-Crystalline Solids, 164-166 (1993) 363

[Stradins 93] P.Stradins, M.Q.Tran, H.Fritzsche, J. of Non-Crystalline Solids, 164-166 (1993) 175

[Stutzmann 87] M.Stutzmann, D.K.Biegelsen, R.A.Street, Phys.Rev.B 35 (1987) 5666

[Stutzmann 91] M.Stutzmann, J.Nunnenkanp, M.S.Brandt, A.Asano, M.C.Rossi, J. of Non-Crystalline Solids, 137&138 (1991) 231

[Street 82] R.A.Street, Phys.Rev.Lett., 49 (1982) 1187

[Street 91] R.A.Street, Hydrogenated amorphous silicon, Cambridge University Press, 1991

[Swanepoel 83] R.Swanepoel, J. Phys.E: Sci. Instrum., 16 (1983) 1214

[Urbach 53] F.Urbach, Phys.Rev. 92 (1953) 1324

[Vanecek 81] M.Vanecek, J.Kocka, J.Stuchlik, A.Triska, Solid State Comm., 39 (1981) 1199

[Vanecek 91/1] M.Vanecek, visit at IMT, University of Neuchâtel, Feb.1991

[Vanecek 91/2] M.Vanecek, J.Holoubek, A.Shah, M.Brêchet, A.Mettler, Proc. of the 10th E.C. PSEC, Lisbon (1991) 196

[Wronski 82] C.R.Wronski, B.Abeles, T.Tiedje, G.D.Cody, Solid State Comm., 44 (1982) 1423

[Wyrsch 91] N.Wyrsch, F.Finger, T.J.McMahon, M.Vanecek, J. of Non-Crystalline Solids, 137&138 (1991) 347

[Wyrsch 92] N.Wyrsch, thesis, University of Neuchâtel, 1992

[Zhou 91] T.X.Zhou, S.S.Hegedus, C.M.Fortmann, Proc. of the MRS Symp. 219 (1991) 451

b) Chapter 2

[Adler 76] D.Adler, Phys. Rev. Letters, 36 (1976) 1197

[Anderson 75] P.W.Anderson, Phys.Rev.Letters, 34 (1975) 953

[Bar-Yam 86] Y.Bar-Yam, D.Adler, J.D.Joannopoulos, Phys. Rev. Lett. 57 (1986) 467

[Cody 84] G.D.Cody, Semiconductors and Semimetals, Vol. 21B, p.16, Editor J.I.Pankove, Academic Press (1984)

[Favre 94/1] M.Favre, thesis, University of Neuchâtel, 1994

[Hubin 94] J.Hubin, thesis, University of Neuchâtel, 1994

[Jackson 85] W.B.Jackson, S.M.Kelso, C.C.Tsai, J.W.Allen, S.-J.Oh, Phys.Rev.B, 31 (1985) 5187

[Kireev 75] P.S.Kireev, Semiconductor Physics, Mir Publishers, Moscow, 1975

[Kivelson 79] S.Kivelson, C.D. Gelatt, Phys. Rev. B 19 (1979) 5160

[Kosarev 93] A.I.Kosarev, private communication, IMT Neuchâtel 1993

[Kroll 93] U.Kroll, J.Meier, M.Goetz, A.Howling, J.L.Dorier, J.Dutta, A.Shah, Ch.Hollenstein, J. of Non-Crystalline Solids, 164-166 (1993) 59

[Ley 84] L.Ley, in: Topics in Applied Physics, Hydrogenated Amorphous Silicon II, edited by J.D. Joanopoulos and G.Lukovsky, Springer Verlag, (1984) 61

[Milnes 73] A.G.Milnes, Deep impurities in semiconductors, John Wiley&Sons, 1973

[Mittiga 90] A.Mittiga, P.Fiorini, M.Sebastiani, S.Korepanow, F.Evangelisti, 21th. IEEE Photovoltaic spec. conf, Orando, (1990) 1465

[Mott 79] N.F.Mott, E.A. Davis, Electronic processes in non-crystalline materials, Clarendon Press Dxford, 1979

[Okamoto 77] H.Okamoto, Y.Hamakawa, Solid State Comm. 24 (1977) 23

[Overhof 89] H.Overhof, P. Thomas, Hydrogenated amorphous silicon, Springer-Verlag, 1989

[Sah 58] C-T.Sah, W.Shockley, Phys.Rev. 109 (1958) 1103

[Schweitzer 81] L.Schweitzer, M.Grünewald, H.Dersch, J.of physique 10 (1981) C4-827

[Schumm 93] G.Schumm, J. of Non-Crystalline Solids, 164-166 (1993) 317

[Shockley 52] W.Shockley, W.Read, Phys.Rev. 87 (1952) 835

[Smith 89] Z.E.Smith, S.Wagner, in Advances in Disordered Semiconductors Vol.1a, edited by H.Fritzsche, Word Scientific (1989) 409

[Street 91] R.A.Street, Hydrogenated amorphous silicon,Cambridge University Press, 1991

[Tauc 66] J.Tauc, R.Grigorovici, A.Vancu, Phys.Status Solidi 15 (1966) 627
[Taylor 72] G.Taylor, J.Simmons, J.of Non-cryst. solids 8-10 (1972) 940
[Thomas 93] P.Thomas, private communication, IMT Neuchâtel 1993
[Vaillant 86] F.Vaillant, D.Jousse, Phys.Rev.B 34 (1986) 4088
[Vanecek 81] M.Vanecek, J.Kocka, J.Stuchlik, A.Triska, Solid State Comm., 39 (1981) 1199
[Vanecek 93] M.Vanecek, private communication, Praha 1993
[Winer 90] K.Winer, Phys. Rev. B 41 (1990) 12150
[Wyrsch 92] N.Wyrsch, thesis, University of Neuchâtel, 1992

c) Chapter 3

[Adler 76] D.Adler, Phys. Rev. Letters, 36 (1976) 1197
[Anderson 75] P.W.Anderson, Phys.Rev.Letters, 34 (1975) 953
[Bube 92] R.Bube, L.Benatar, M.Grimbergen, D.Redfield, J. Appl. Phys., 72 (1992) 5766
[Cody 84] G.D.Cody, in Semiconductors and Semimetals, edited by J.Pankove (Academic, New York, 1984), 21B, p.20
[Dawson 92] R.M.Dawson, Y.M.Li, M.Gunes, D.Heller, S.Nag, R.W.Collins, C.R.Wronski, Mat. Res. Soc. Symp. Proc. 258 (1992) 595
[Dersch 81] H.Dersch, J.Stuke, J.Beichler, Phys.Sol. B 105 (1981) 265
[Elliott 90] S.R.Elliott, Physics of amorphous materials, Longman Group 1990
[Favre 91] M.Favre, A.Shah, J.Hubin, E.Bustarret, M.A.Hachicha, S.Basrour, J. of Non-Crystalline Solids, 137&138 (1991) 335
[Favre 94/2] M.Favre, private communication, IMT Neuchâtel 1994
[Jackson 82] W.B.Jackson, N.M. Amer, Phys.Rev.B 25 (1982) 5559
[Jackson 85] W.B.Jackson, S.M.Kelso, C.C.Tsai, J.W.Allen, S.-J.Oh, Phys.Rev.B, 31 (1985) 5187
[Lee 89] S.Lee, S.Kumar, C.R.Wronski, J. of Non-Cryst. Solids 114 (1989) 316
[Ley 87] I.Hirabayashi, K.Winer, L.Ley, J. of Non-Crystalline Solids 97&98 (1987) 87
[Lucovsky 65] G.Lucovsky, Solid State Comm. 3 (1965) 299
[Mittiga 90] A.Mittiga, P.Fiorini, M.Sebastiani, S.Korepanow, F.Evangelisti, 21th. IEEE Photovoltaic Spec. Conf, Orando, (1990) 1465
[Street 91] R.A.Street, Hydrogenated amorphous silicon,Cambridge University Press, 1991
[Overhof 89] H.Overhof, P. Thomas, Hydrogenated amorphous silicon, Springer-Verlag, 1989
[Platz 93] R.Platz, R.Brüggemann, G.H.Bauer, J. of Non-Crystalline Solids, 164-166 (1993) 355
[Stutzmann 85] M.Stutzmann, Festschrift for Prof. H.Fritzsche, Chicago (1985)

[Stutzmann 87] M.Stutzmann, Phil.Mag. B 56 (1987) 63
[Vaillant 86] F.Vaillant , D.Jousse, Phys.Rev.B 34 (1986) 4088
[Vaillant 88] F.Vaillant, D.Jousse, J.-C.Bruyere, Phyl. Mag. B, 57 (1988) 649
[Vanecek 81] M.Vanecek, J.Kocka, J.Stuchlik, A.Triska, Solid State Comm., 39 (1981) 1199
[Vanecek 83] M.Vanecek, J.Kocka, J.Stuchlik, Z.Kozisek, O.Stika, A.Triska, Solar Energy Mat. 8 (1983) 411
[Wyrsch 91] N.Wyrsch, F.Finger, T.J.McMahon, M.Vanecek, J. of Non-Cryst. Solids, 137&138 (1991) 347
[Wyrsch 92] N.Wyrsch, thesis, University of Neuchâtel, 1992
further references: see tab.1 in chapter 2

d) Appendix

[Adler 76] D.Adler, Phys. Rev. Letters, 36 (1976) 1197
[Ashcroft 87] N.W.Ashcroft, N.D.Mermin, Solid State Physics, 1987, p.586
[Bube 92] R.Bube, L.Benatar, M.Grimbergen, D.Redfield, J. Appl. Phys., 72 (1992) 5766
[Dalal 90] V.L.Dalal, R.D.Knox, Proc. of the MRS Symp. 192 (1990) 713
[Finger 90] F.Finger, internal communication, IMT, University of Neuchâtel, 1990
[Goetz 93] M.Goetz, IMT, University of Neuchâtel, 1993
[Gu 86] B.Gu, D.Han, C.Li, S.Zhao, Phil.Mag.B, 53 (1986) 321
[Hegedus 88] S.S.Hegedus, J.M.Cebulka, Proc. of the 20th IEEE PVSEC, Las Vegas (1988) 186
[Hubin 94] J.Hubin, thesis, University of Neuchâtel, 1994
[Jackson 82] W.B.Jackson, N.M.Amer, Phys.Rev.B 25 (1982) 5559
[Kireev 75] P.S.Kireev, Semiconductor Physics, Mir Publishers, Moscow, 1975
[Kocka 88] J.Kocka, M.Vanecek, O.Stika, Q.D.Tring, J.Smchlik, A.Triska, Proc. of the 8th E.C. PSEC, Florence (1988) 724
[Kroll 93] U.Kroll, J.Meier, M.Goetz, A.Howling, J.L.Dorier, J.Dutta, A.Shah, Ch.Hollenstein, J. of Non-Crystalline Solids, 164-166 (1993) 59
[Mettler 93/1] A.Mettler visited M.Vanecek, University of Prague, April 1993
[Mettler 93/2] A.Mettler, N.Wyrsch, A.Shah, J. of Non-Crystalline Solids, 164-166 (1993) 427
[Mittiga 90] A.Mittiga, P.Fiorini, M.Sebastiani, S.Korepanow, F.Evangelisti, Proc. of the 21th IEEE PVSEC, Orando (1990) 1465
[Pipoz 93] P.Pipoz, N.Wälchli, H.Beck, A.Shah, J. of Non-Crystalline Solids, 164-166 (1993) 525
[Rose 63] A.Rose, concepts in photoconductivity and allied problems, 1963, Interscience Publishers, John Wiley & Sons

[Rübel 89] H.Rübel, M.Gorn, B.Scheppat, R.Geyer, P.Lechner, N.Kniffler, Proc. of the MRS Symp. 149 (1989) 465

[Sauvain 93] E.Sauvain, A.Mettler, N.Wyrsch, A.Shah, Solid State Comm., 85 (1993) 219

[Smith 78] R.A.Smith, Semiconductors, Cambridge University Press, 2nd edition 1978

[Vanecek 91/1] M.Vanecek, visit at IMT, University of Neuchâtel, Feb.1991

[Wyrsch 91] N.Wyrsch, F.Finger, T.J.McMahon, M.Vanecek, J. of Non-Cryst. Solids, 137&138 (1991) 347

e) Prologue

[Chittick 69] R.C.Chittick, J.H.Alexander, H.F.Sterling, J. Electrochemical Soc. 116 (1969) 77

[Carlson 76] D.E.Carlson, C.R.Wronski, Appl. Phys. Lett. 28 (1976) 671

[Spear 76] W.E.Spear, P.G.LeComber, Phil. Mag. B33 (1976) 935

[Staebler 77] D.L.Staebler, C.R.Wronski, Appl. Phys. Lett. 31 (1977) 292

[Vanecek 81] M.Vanecek, J.Kocka, J.Stuchlik, A.Triska, Solid State Comm., 39 (1981) 1199

ACKNOWLEDGEMENTS

I am greatly indebted to Prof. Dr. A.V.Shah for supervising this dissertation. I would also like to acknowledge Prof. Dr. H.Beck and Dr. N.Wyrsch for many constructive discussions and comments. I especially wish to thank Dr. M.Vanecek for the fruitful interaction at Prague and Neuchâtel. Last, but not least, I would like to thank my colleagues, the secretaries and the staff of the technical, mechanical and electronical offices for their collaboration and the pleasant atmosphere at the institute.

* * *